The Extended Tisserand-Poincaré graph for multi-body trajectory design

Mattia Pugliatti

Technische Universiteit Delft

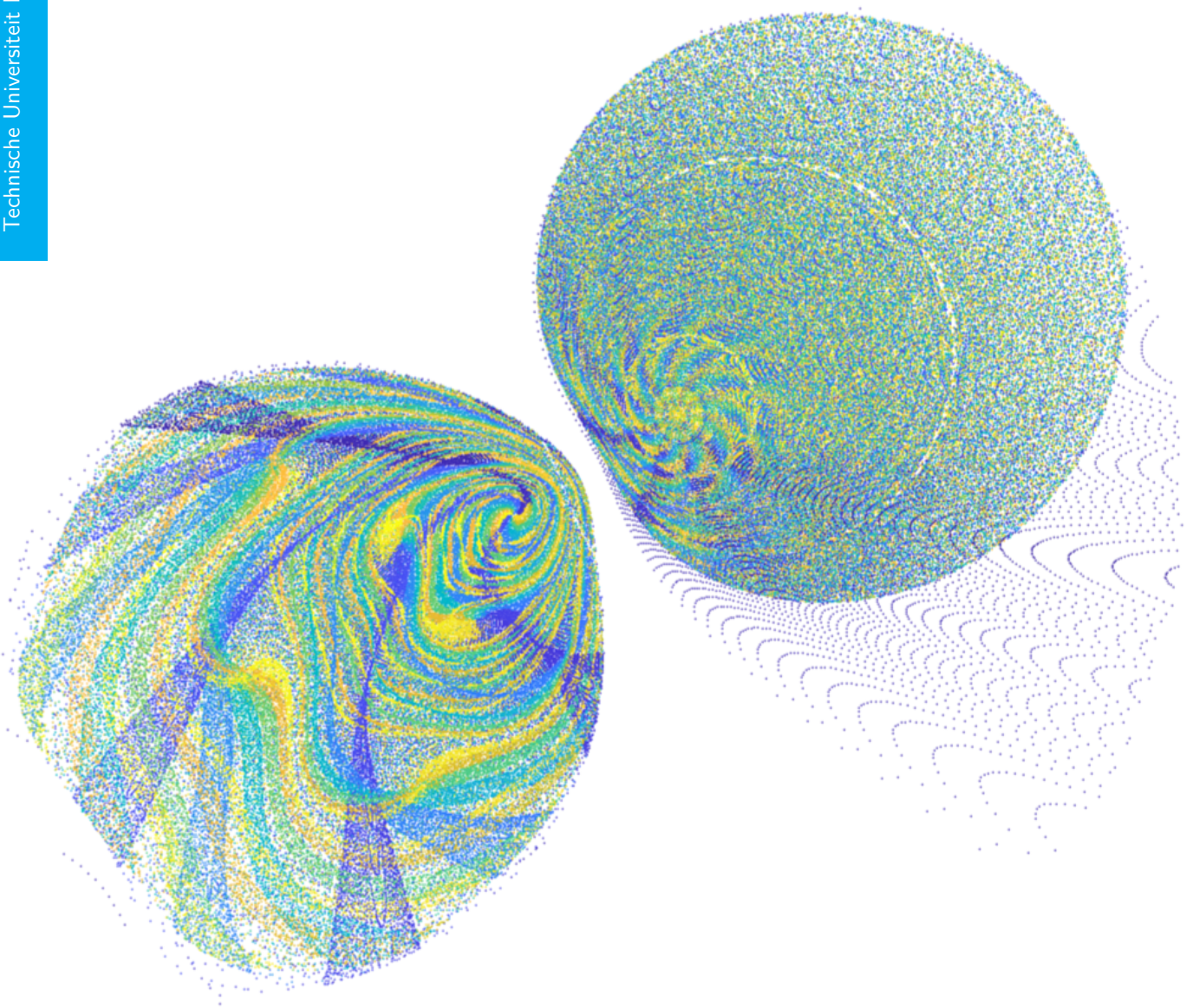

TU Delft Delft University of Technology

Challenge the future

THE EXTENDED TISSERAND-POINCARÉ GRAPH FOR MULTI-BODY TRAJECTORY DESIGN

by

Mattia Pugliatti

in partial fulfillment of the requirements for the degree of

Master of Science
in Aerospace Engineering

at Delft University of Technology,
to be defended publicly on Wednesday March 28, 2018 at 9:00.

Student number :	4522680	
Thesis committee:	Dr. D. M. Stam,	TU Delft (chairholder)
	ir. R. Noomen,	TU Delft (supervisor)
	ir. Y. Liu,	TU Delft (supervisor)
	Dr. ir. W. T. van Horssen,	TU Delft
	Prof. Dr. Y. Kawakatsu,	ISAS/JAXA (external supervisor)

This thesis is confidential and cannot be made public until June 30, 2018.

The work here presented has been carried out at Institute of Space and Astronautical Science, part of the Japan Aerospace Exploration Agency. Their hospitality is here acknowledged.

You don't choose your passions,
your passions choose you.

Jeff Bezos

ACKNOWLEDGMENTS

Since I was not alone in this endeavor I would like to take a moment to thank all the people that have supported me during this astonishing period of my life.

First, I would like to thank my supervisors from TU Delft, Ron Noomen and Yuxin Liu. Our weekly meetings have been a source of inspiration and encouragement that guided and pushed me through the entire project. Thank you for your availability, support and opinions both on professional and personal matters.

I am deeply grateful to professor Yasuhiro Kawakatsu for his hospitality at JAXA. Thank you for giving me the enormous possibility to work in such a thriving environment, thank you for guiding me with your technical experience and for having involved me in the mission design teams of EQUULEUS and DESTINY. It has been a huge honor.

I would also like to thank Dr. Stefano Campagnola from JPL for his excellent mentorship. Without your contribution and help this work would have been much poorer. The inspiration you provided guided me throughout the research.

Japan will always have a special place in my heart and so will be for the incredible persons I have met here. I would like to thank the members of Kawakatsu laboratory and the other people at ISAS that have made this experience the best that one could imagine. In particular let me thank the colleagues and friends who I shared the office with, who have patiently endured my turbulent coding sessions, and all the members of the EQUULEUS and DESTINY teams. A special thank goes to Stefano B. , without you such experience would have missed something important. Thank you for your fundamental support as a colleague but most importantly as a friend.

I would also like to thank my friends spread over Europe that never failed to make me feel their support despite the distance. In particular I would like to thank the 'Bombers', especially Giovanni and Livio, but also my close old friends from Milan, in particular Stefano T. and Luca who never failed to make me laugh during the years I have spent abroad.

Lastly I would like to thank my family, because since the beginning they have always put my education before everything. Without you all this would have not been possible. Mother, you can now put away the thesis and sip some coffee contemplating the sunset with some heroic posture, as there is no chance you will understand a single word after this page, apologies for that.

ありがとうございます

Mattia Pugliatti
Milan, February 2018

CONTENTS

NOMENCLATURE

CONSTANTS

Symbol	Description	Value	unit
AU	Astronomical unit	149597870660	m
G	Universal gravitational constant	6.67259×10^{-11}	$m^3/kg\ s^2$
μ_{Earth}	Earth gravitational parameter	398600.441×10^9	m^3/s^2
μ_{Europa}	Europa gravitational parameter	3202.739×10^9	m^3/s^2
$\mu_{Jupiter}$	Jupiter gravitational parameter	$126686534.922 \times 10^9$	m^3/s^2
μ_{Moon}	Moon gravitational parameter	4902.834×10^9	m^3/s^2
μ_{Sun}	Sun gravitational parameter	$132712440041.939 \times 10^9$	m^3/s^2
R_{Earth}	Earth radius	6378000	m
R_{Europa}	Europa radius	1561000	m
$R_{Jupiter}$	Jupiter radius	69911000	m
R_{Moon}	Moon radius	1738000	m
R_{Sun}	Sun radius	600000000	m

Table 1: Constants taken from [1],[2] and [3].

PARAMETERS CIRCULAR RESTRICTED THREE-BODY PROBLEM

System	μ	**DU** [m]	**VU** [m/s]	**TU** [s]
Earth-Moon	$1.21506683 \times 10^{-2}$	384405000	1024.54023475108	375197.563708557
Sun-Earth	$3.00348090844352 \times 10^{-6}$	149597870700	29784.7352120705	5022635.576071
Sun-Jupiter	$9.53683889576763 \times 10^{-4}$	778400000000	13063.5614375152	59585588.7939285
Jupiter-Europa	$2.52801752854173 \times 10^{-5}$	671080000	13739.8999551929	48841.694785876

Table 2: Parameters taken from [4],[1] or derived.

PARAMETERS BICIRCULAR RESTRICTED FOUR-BODY PROBLEM

System	$\mathbf{m_S}$ $[\mathbf{m_E} + \mathbf{m_M}]$	$\mathbf{a_S}$ $[\mathbf{a_M}]$	$\mathbf{w_S}$ $[-]$
Sun-Earth-Moon	328900.54	388.81114	0.925195985520347

Table 3: Parameters taken from [5].

LATIN SYMBOLS

Symbol	Description	Unit
a	Semi-major axis	[-] or m
a_E	Earth semi-major axis	[-] or m
a_{Eur}	Europa semi-major axis	[-] or m
a_J	Jupiter semi-major axis	[-] or m
a_M	Moon semi-major axis	[-] or m
A	Position rotation matrix	[-]
B	Velocity rotation matrix	[-]
C_{ijk}	Jacobi constant in the ijk frame	[-] or m^2/s^2
C_{Li}	Jacobi constant of the $i-th$ Lagrange libration point	[-] or m^2/s^2
d	Distance	[-] or m
DU	Distance normalization parameter	m
e	Eccentricity	[-]
E_i	Energy with respect to the $i-th$ body	[-] or m^2/s^2
f_i	Explicit function with respect the $i-th$ body	[-]
F_i	Implicit function with respect the $i-th$ body	[-]
h_i	Angular momentum with respect to the $i-th$ body	[-] or m/s^2
$\mathbf{H}_i$	Angular momentum vector with respect to the $i-th$ body	[-] or m/s^2
i	Inclination	rad
I_{sp}	Specific impulse	s
J_{ijk}	Jacobi integral in the ijk frame	[-] or m^2/s^2
L_i	$i-th$ Lagrange libration point	[-]
m	Number of spacecraft revolutions	[-]
m_i	Mass of the $i-th$ point	[-] or kg
n	Number of body revolutions	[-]
$P(i)$	P-th point	[-]
P_i	Residual function with respect to $i-th$ body	[-] or m^2/s^2
$\mathbf{r}$	Position vector	[-] or m
r	Position magnitude	[-] or m
R	Radial distance	[-] or m
R_{SOI}	Sphere of influence radius	[-] or m
r_a	Apocenter radius	[-] or m
r_a^{cr}	Critical apocenter radius	[-] or m
r_c	Circular orbit radius	[-] or m
r_p	Pericenter radius	[-] or m
r_p^{cr}	Critical pericenter radius	[-] or m
r_1	Distance from the primary P1	[-] or m
r_2	Distance from the secondary P2	[-] or m
S_i	Family of Poincaré sections about the $i-th$ body	[-]
t	Time	[-] or s
T_i	Tisserand parameter with respect to the $i-th$ body	[-] or m^2/s^2
T_1^{cl}	Classical Tisserand parameter	[-] or m^2/s^2
T_{L_i}	Tisserand parameter of the L_i Lagrange point	[-] or m^2/s^2
TU	Time normalization parameter	s
U	Potential function	[-]
$\mathbf{v}$	Velocity vector	[-] or m/s
V	Velocity magnitude	[-] or m/s
$\mathbf{V}_\infty$	Hyperbolic excess velocity	m/s
VU	Velocity normalization parameter	m/s
x,y,z	Position components	[-] or m
$\dot{x},\dot{y},\dot{z}$	Velocity components	[-] or m/s
$\ddot{x},\ddot{y},\ddot{z}$	Acceleration components	[-] or m/s^2
X,Y,Z	Axes of synodic frame	[-] or m
$\mathbf{X}$	State vector	[-] or m and m/s

Table 4: Latin symbols.

GREEK SYMBOLS

Symbol	Description	Unit
α	Mass coefficient in the BR4BP	[-]
α	Flyby pump angle	rad
Δ	Difference	[-]
ΔV	Velocity change	m/s
ξ,η,ς	Position components in inertial frame	[-] or m
$\dot{\xi}$,$\dot{\eta}$,$\dot{\varsigma}$	Velocity components in inertial frame	[-] or m/s
θ	True anomaly	rad
θ	Angle between synodic and inertial frames	rad
θ^{syn}	Angle of the synodic velocity	rad
θ^{in}	Angle of the inertial velocity	rad
θ, Ψ	Azimuth and elevation angles of the synodic velocity	[rad]
μ_i	Body i gravitational constant	m^3/s^2
μ	Mass parameter of the CR3BP	[-]
ω	Argument of pericenter	rad
ω_3	Angular coefficient in the BR4BP	rad
Ω	Right ascension of the ascending node	rad

Table 5: Greek symbols.

ABBREVIATIONS

ARTEMIS	Acceleration, Reconnection, Turbulence and Electrodynamics of the Moon's Interaction with the Sun
BOL	Begin Of Life
BR4BP	Bi-circular Restricted Four-Body Problem
CR3BP	Circular Restricted Three-Body Problem
DESTINY	Demonstration and Experiment of Space Technology for INterplanetary voYage
DST	Dynamical System Theory
EM	Earth-Moon
EME2000	Earth Mean Equator and Equinox of J2000
EM-1	Exploration Mission 1
EMLi	Earth-Moon L_i point
EOL	End Of Life
EQUULEUS	EQuilibriUm Lunar-Earth 6U Spacecraft
ER3BP	Elliptical Restricted Three-Body Problem
ESA	European Space Agency
ETP-graph	Extended Tisserand-Poincaré graph
GTO	Geostationary transfer orbit
ICPS	Interim Cryogenic Propulsion Stage
IP1D	Inertial P1-centered Dimensional
ISAS	Institute of Space and Astronautical Science
JAXA	Japan Aerospace Exploration Agency
JE	Jupiter-Europa
JPL	Jet Propulsion Laboratory
LEOP	Launch and Early Orbit Phase
MATLAB	MATrix LABoratory
MBA	Main Belt Asteroid
MGA	Multiple Gravity Assist
NASA	National Aeronautics and Space Administration
NEO	Near Earth Object
NRHO	Near Rectilinear Halo Orbit
QSS	Quasi-Spherical Surface
SB	Synodic Barycenter
SE	Sun-Earth
SELi	Sun-Earth L_i point
SJ	Sun-Jupiter
SLS	Space Launch System
SMART-1	Small Missions for Advanced Research in Technology-1
SOI	Sphere Of Influence
SP1	Synodic P1-centered
SRP	Solar Radiation Pressure
T-graph	Tisserand graph
THEMIS	Time History of Events and Macroscale Interactions during Substorms
TOF	Time Of Flight
TP-graph	Tisserand-Poincaré graph
VEEGA	Venus-Earth-Earth Gravity Assist
ZVC	Zero velocity curve
WSB	Weak Stability Boundary
2BP	Two-Body Problem
3BP	Three-Body Problem
4BP	Four-Body Problem

ABSTRACT

The decision on the dynamical model used to design a spacecraft's trajectory is a fundamental choice influenced by many factors. The complexity of such a model affects the accuracy of the designed trajectory but also the difficulty of the design process. One approach to simplify this task consists of splitting the trajectory design process into two phases. In the first phase a first-guess reference trajectory is generated through the usage of a simple dynamical model considering the most important forces in the system. In the second phase this reference trajectory is taken and refined with the addition of the perturbing forces that have been neglected in the first phase. The success of this approach depends on the proper sharing of the perturbing forces between the two phases. In this sense the backbone of the trajectory is designed in the first phase and it is fundamental that in this phase the main forces are taken into account to not avoid to consider them as negative perturbing effects in the second phase, that often is performed using an optimization technique.

The research covered in this report is focused on the first phase of this process, in particular for what concerns the gravitational influences generated by multiple bodies. In this sense the simplest dynamical model that could be used considers only the gravitational influence of the main attracting body. Such model however is not able to capture interesting and useful phenomena existing in a more realistic multi-body environment that allow to save a considerable amount of ΔV. This aspect is of crucial importance for missions such as EQUULEUS and DESTINY, whose limited ΔV capabilities need to be compensated by a clever design process actively exploiting both lunar and solar perturbation effects.

This is achieved in this research through the usage of a patched Circular Restricted Three-Body Problem model describing the motion of the spacecraft under the influence of two primaries at a time. Such a patched model is an approximated model that represents the trajectory of a spacecraft under the influence of three bodies. A graphical technique called Tisserand-Poincaré graph exploits this dynamical model to design trajectories in several multi-body environments. The applicability of this technique however is strongly tied to the definition of the so-called Tisserand parameter. The latter however exists only about the primary, limiting the patching between different Circular Restricted Three-Body Problems to those systems sharing the most attracting body such as the Jupiter-Europa-Ganymede or Sun-Earth-Jupiter systems. To overcome this limitation, that would make it impossible to apply the same technique in the Sun-Earth-Moon system for the EQUULEUS and DESTINY missions, the theoretical framework of the technique is extended in this research. In particular a modified version of the Tisserand parameter defined about the secondary that possesses the same constancy property of the classical Tisserand parameter but on a specifically defined family of Poincaré sections is derived. The concept of the modified Tisserand parameter is based on a relationship between the parameter and the Jacobi constant of the system that can be expressed by the fundamental equation $J = T + P$. The new parameter and associated Poincaré sections are used to characterize the Earth-Moon and Sun-Earth systems. Through the usage of a graphical tool, the definition of the modified parameter and the definition of a specific family of Poincaré sections, both solar and lunar perturbations are characterized and exploited in the trajectory design process in the multi-body environment. A database approach to be used for the EQUULEUS trajectory design in a quasi-four body problem is developed. Databases of flyby trajectories about the Moon and Jupiter in the Earth-Moon and Sun-Jupiter CR3BP models are also developed. A standard patching procedure is tested in the Sun-Jupiter-Europa environment to demonstrate a capture trajectory about Jupiter.

1

INTRODUCTION

This chapter introduces the research performed by the author during his 8 months period stay at ISAS/JAXA in Sagamihara, Japan. In Section 1.1 a brief description of the state of the art is presented. In Section 1.2 the main research questions and relative sub-questions are presented, followed up by the research goals and sub-goals. In conclusion the structure of the whole report is provided in Section 1.3.

1.1. STATE OF THE ART

The research presented in this report is focused on orbital mechanics, in particular on the trajectory design process of first-guess solutions in a multi-body environment. This work has been encouraged by JAXA for an application on the EQUULEUS and DESTINY missions. The limited ΔV capabilities of these missions, together with the necessity to actively take into account solar, Earth's and lunar gravitational influences, make the whole trajectory design process a complex task. The current state of the art of the design strategies of EQUULEUS and DESTINY is described in [6][7] and [8] respectively. The task is particularly challenging for EQUULEUS due to its piggyback nature, demanding certain flexibility in the design process. In such a case a grid-search technique is adopted to generate a set of first-guess trajectories in a full ephemeris model. This set is later used by an optimizer refining it with the addition of corrective maneuvers and higher-order perturbation effects. The overall design procedure can be lengthy, heavily relying on numerical propagation. There is therefore a strong interest to reduce the computational effort, especially in the generation of first-guess solutions. As illustrated in [9], both lunar and solar perturbation effects play a fundamental role in these missions. The benefits from the latter have been qualitatively illustrated with the usage of a graphical technique called Tisserand-Poincaré graph.

Such a technique has been presented for the first time in [10] and uses a dynamical model called Circular Restricted Three-Body Problem (CR3BP) and a parameter derived from it called Tisserand parameter to perform the patching between trajectories in different dynamical systems. In this way it is possible to approximate the trajectory under the gravitational influences of three bodies as a patched trajectory computed considering two bodies at a time. This graphical technique however is valid only under certain assumptions, most of which are tied to the definition of the Tisserand parameter. Because of these assumptions the technique as it is cannot be applied to a system such as the Sun-Earth-Moon system. It is for this reason that the core of this work is the extension of the theoretical framework sustaining the Tisserand-Poincaré graphical tool through the derivation of a modified Tisserand parameter that overcomes the limitations of the classical one. The second main objective is to leverage such a parameter to design trajectories using patched CR3BP models that share the same body as primary and secondary. A trajectory under the influence of the Sun, Earth and Moon will therefore be approximated by Sun-Earth and Earth-Moon CR3BP patched models. These trajectories will serve as first-guess solutions for an optimizer that will be working with a full ephemeris model to generate the final trajectory. The idea is that the coupling between the optimizer and the first-guess tool will increase the overall efficiency of the trajectory design process. From an industrial perspective this is of special interest for EQUULEUS and DESTINY, but it can be applied to all other missions for which multi-body effects like in a Sun-Earth-Moon system play a role.

A challenge is set by the desire of the author to develop the tool for the generation of first-guess trajectories for the spatial case of the CR3BP, that is often considered in literature only in its planar formulation [10][9][11][12]. From the characteristics of the EQUULEUS and DESTINY operational orbits [7][8], and from the recommendations in [7] it is clear that a spatial analysis will result in a more realistic trajectory design tool, also providing deeper insight into the solar perturbation effects on the Tisserand-Poincaré graph.

1.2. RESEARCH QUESTION, AIMS AND OBJECTIVES

Following the state of the art introduced in the previous section the main research questions and related subquestions are presented in this section, together with the research goals and sub-goals.

1. *What are the characteristics of a modified Tisserand parameter defined about the secondary under the assumptions of the Circular Restricted Three-Body Problem?*

    (a) *What are the similarities and differences of the modified Tisserand parameter with respect to the classical one?*

    (b) *How are the Tisserand level sets obtained from the modified Tisserand parameter represented in the Tisserand-Poincaré graph?*

    (c) *How can solar perturbation effects be explained through the usage of the modified Tisserand parameter?*

    (d) *What are the limitations of the modified version of the Tisserand parameter?*

    (e) *Which alternative applications can be found for the modified Tisserand parameter?*

2. *How can the modified Tisserand parameter be used to develop a trajectory design tool in the Sun-Earth-Moon patched CR3BP?*

    (a) *What potential does the modified Tisserand parameter show for the trajectory design in the CR3BP model?*

    (b) *What mathematical tools are necessary in order to exploit the parameter for the trajectory design in a multi-body environment?*

    (c) *Is the tool capable to explain the results existing in literature?*

    (d) *How easily can the tool be used to describe the spatial effects of solar perturbations?*

    (e) *How accurate is the tool when compared to higher-order fidelity dynamical models?*

    (f) *What is the performance compared to the state of the art trajectory design strategy used for EQUULEUS and DESTINY?*

    (g) *Are there any other similar scenarios that would benefit from the usage of the tool?*

From these research questions the following research objectives are set:

1. *Develop an efficient trajectory design tool in the patched CR3BP model by using a combination of propagation technique, the Tisserand-Poincaré graph and the modified Tisserand parameter.*

    (a) *Develop all the necessary mathematical tools to implement the CR3BP model.*

    (b) *Develop a new theoretical framework that extends the validity of the Tisserand parameter in the vicinity of the secondary body.*

    (c) *Implement and characterize the usage of a newly defined Poincaré section.*

    (d) *Understand and develop a way to introduce Sun's perturbation in the Earth-Moon CR3BP*

    (e) *Understand the spatial dynamics of the Sun's perturbing effects.*

    (f) *Develop a tool to generate fist-guess trajectories in the Sun-Earth-Moon system.*

1.3. REPORT STRUCTURE

The report is divided into ten chapters, with supplementary material collected in four appendices. Besides this introduction chapter, the historical background of fundamental missions that have exploited multi-body dynamics is presented in Chapter 2, together with a brief explanation of the author's work on EQUULEUS and DESTINY during his stay at JAXA. The theoretical background of the research is discussed in Chapter 3. In Chapter 4 the derivation of the modified Tisserand parameter is presented, together with the definitions of the Poincaré sections that will be used throughout the report. In Chapter 5 the Tisserand level sets obtained with the usage of the modified Tisserand parameter are represented in the Tisserand-Poincaré graph. In this chapter also the graphical patching between the Sun-Earth and Earth-Moon CR3BP models is illustrated. In Chapter 6 a specific type of Poincaré section is used to investigate what kind of dynamical insight these sections are able to represent for the planar cases of the Sun-Earth and Earth-Moon CR3BP models. A tool to design trajectories in the spatial case of the Sun-Earth-Moon system that can be used for EQUULEUS and DESTINY is developed in Chapter 7. In Chapters 8 and 9 additional applications are presented to investigate flyby effects with the Moon and Jupiter and to illustrate a method to design a trajectory in the Sun-Jupiter-Europa system making use of the tools derived in the report. Finally, Chapter 10 provides the main findings of this research and possible other areas of investigation for future studies.

2

HISTORICAL BACKGROUND

In the following chapter a brief historical background is presented about the most important missions which have been exploiting multi-body dynamics effects in the low-energy regime.

First, three historical missions have been chosen that are representative of the Japan Aerospace Exploration Agency (JAXA), European Space Agency (ESA) and National Aeronautics and Space Administration (NASA) approaches to low-energy transfer trajectories. Each of these correspond to a mission representing a milestone for this type of trajectories. Hiten will be discussed in Section 2.1 as an example of an exterior transfer in the Earth-Moon system. Successively the Small Missions for Advanced Research in Technology-1 (SMART-1) will be briefly presented in Section 2.2 as an example of interior transfer in the Earth-Moon system. The Acceleration Reconnection Turbulence and Electrodynamics of the Moon's Interaction with the Sun (ARTEMIS) will be presented in Section 2.3 as an example of the first exterior transfer to reach a Halo orbit in the Earth-Moon system.

In addition to these historical missions JAXA's EQUULEUS and DESTINY missions will be briefly presented in Sections 2.4 and 2.5. These missions are currently designed at the Institute of Space and Astronautical Science (ISAS) and are presented here because of the considerable amount of effort the author has spent working on the trajectory design process of these missions during his stay at ISAS/JAXA.

2.1. HITEN

The Hiten mission represents a milestone in low-energy transfer techniques applied for lunar missions. Designed as a technology demonstration mission to enable JAXA's future lunar and planetary missions, two spacecraft were involved: a primary one called Hiten and a secondary one called Hagoromo [13],[14]. While the latter one was designed to enter into a lunar orbit, the first one was originally designed to work as a communication relay from a highly elliptical orbit with respect to Earth.

According to the original schedule, Hiten demonstrated the areobraking technique with two maneuvers on March 19 and 30, 1991. These reduced the spacecraft velocity by 1.7 and 2.8 m/s respectively, resulting in apogee decreases of about 8665 and 14000 km [1]. After the completion of this phase the mission was changed due to a failure on-board the secondary spacecraft soon after release. Hagoromo was not being able to be inserted into a lunar orbit anymore, so it was decided to use Hiten itself for this purpose. The small amount of propellant left on-board the spacecraft however made it impossible for the spacecraft to achieve such a goal with a conventional transfer technique. To reach a lunar orbit a recently developed technique designed by Edward Belbruno and James Miller [15], the Weak Stability Boundary (WSB), was employed. Making use of this concept and exploiting Sun's gravitational perturbation, lunar flybys and small corrective maneuvers, the spacecraft was finally put in a temporary capture orbit about the Moon on October 2, 1991.

The transfer trajectory so designed took relatively long compared to a conventional one such as a Hohmann transfer, five months instead of three days [1]. The ΔV saved by correctly exploiting the multi-body dynamics in the low-energy regime however allowed the transfer to happen in the first place. The savings also allowed

Hiten to explore the Sun-Earth fourth and fifth Lagrange libration point regions (SEL4 and SEL5), investigating the presence of trapped dust particles. The mission concluded when the spacecraft was purposely crashed into the lunar surface on April 10, 1993. Deemed as a success after the failure of the secondary spacecraft, it was the first time a low-energy transfer had been used to reach an orbit about the Moon.

2.2. SMART-1

SMART-1 was an ESA spacecraft launched on September 2003 as a technology demonstration mission. The main scientific goal of the mission was to perform research about the Moon's surface chemistry and investigate the presence of ice in the south pole lunar region. Being launched into a Geostationary Transfer Orbit (GTO) the spacecraft parking orbit had a perigee of 655 km and an apogee of 35890 km. In order to reach the Moon a combination of orbit raising maneuvers and low-energy transfer techniques was employed. By carefully designing thrusting arcs and exploiting the effects of the Moon's gravitational perturbation the spacecraft apogee and perigee were increased in one year to 300000 and 170000 km respectively, while the inclination was increased from 6.9° to 12° [1]. Lunar resonance phases also played a fundamental role in the trajectory design, widening out the spiraling of the orbit raising phase. The spacecraft was captured by the Moon at an altitude of about 60000 km on November 14, 2004. Correction maneuvers were executed thereafter to insert the spacecraft into the nominal polar orbit about the Moon, from where the scientific phase of the mission started. The transfer phase to reach such orbit lasted 1.5 years, but allowed for important savings in ΔV [1]. The mission concluded by purposely crashing the spacecraft on the Moon's surface on September 3, 2006.

It is important to underline that multi-body dynamics was exploited in a different way for the SMART-1 mission than for Hiten. In the latter one Sun's gravitational influence played a key role to modify the spacecraft trajectory. On the contrary in SMART-1 this was merely a disturbing effect as the main source of perturbation exploited by SMART-1 was the Moon. This played a crucial role in the design of a transfer strategy based on resonance effects.

2.3. ARTEMIS

ARTEMIS is the name of the extended phase of the Time History of Events and Macroscale Interactions during Substorms mission (THEMIS), a NASA mission that took place between 2007 and 2010, involving five identical Earth-orbiting spacecraft. Towards the end of this mission an extended phase was proposed for the two outermost spacecraft, P1 and P2, that were re-assigned to study the Earth's magnetotail and solar wind from about 60 Earth radii.

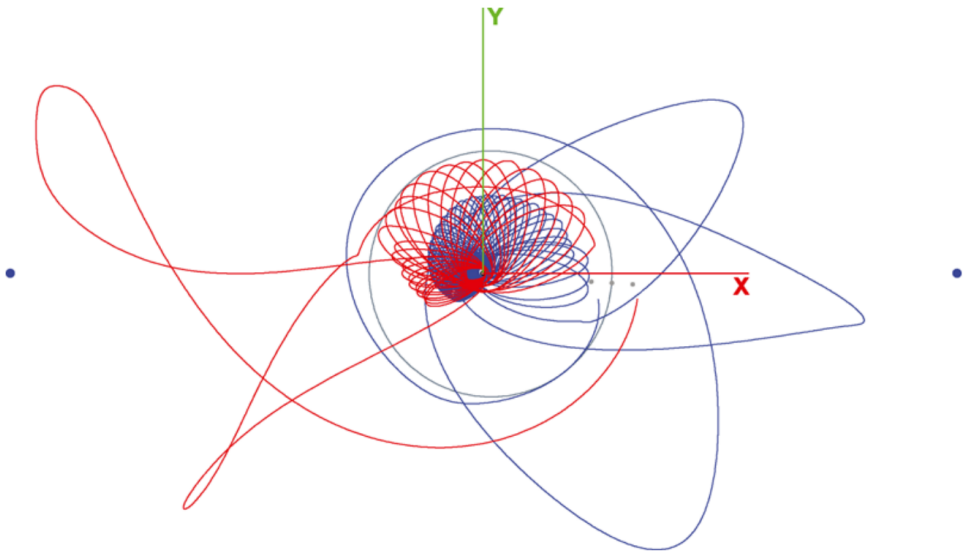

Figure 2.1: ARTEMIS trajectories in the SP2 frame of the Sun-Earth system. The red and blue lines show the P1 and P2 trajectories while the Moon's orbit is shown in gray. Blue dots represents SEL1 and SEL2 while the gray ones the EML1 and EML2 at particular epochs [16].

Because of the limited amount of propellant on-board of the spacecraft, it was decided to exploit a low-energy transfer to reach this goal. In order to do that however several limitations given by the spacecraft design needed to be taken into account. Amongst the most relevant ones from a trajectory design point of view are the need to never exceed 2 million kilometers distance from Earth to be able to communicate with the spacecraft, and to always have the Sun in view during the thrusting maneuvers [16].

By taking into account these and other factors listed in [16] a two-year transfer trajectory that exploited Sun's and Moon's perturbation had been designed to reach Halo orbits around the Earth-Moon first and second Libration Points (EML2 and EML1). It was the first and only time up to now [7] to successfully navigate and perform stationkeeping operations in lunar libration orbits. As of February 2018 the spacecraft are still operational.

2.4. EQUULEUS

EQUULEUS is a Japanese 6-units cubesat that is being designed by a team of students and researchers in cooperation between the Institute of Space and Astronautical Sciences (ISAS) and the University of Tokyo. The name of the spacecraft is an acronym that refers to the constellation of the little horse or foal and stands for Equilibrium Lunar-Earth point 6U Spacecraft. The spacecraft is set for launch in October 2018 as a piggyback on the maiden flight of NASA's Space Launch System (SLS), during Exploration Mission 1 (EM1).

2.4.1. MISSION DESIGN

A comprehensive analysis of the mission can be found in [7]; only the most relevant aspects will be briefly introduced here. EQUULEUS features three main objectives:

- **Trajectory control:** To demonstrate low-energy trajectory design and control techniques in the Sun-Earth-Moon perturbed region.
- **Earth plasmasphere and radiation environment:** To image Earth's plasmasphere and to measure the surrounding plasma distribution in order to better understand the radiation environment in the region of space around Earth.
- **Lunar flashes:** Investigate the size, distribution, influx rate and daily variations of meteoroids impact on the far side of the Moon, essential both to understand the Solar System evolution and to assess eventual risks posed to human activities in cis-lunar space.

These objectives will be achieved during four different phases of the mission, illustrated schematically in Figure 2.2.

Figure 2.2: Different phases of the EQUULEUS mission [7].

The observation phase (4) will be performed from a Near Rectilinear Halo Orbit (NRHO) about the EML2 point, while the investigation on the radiation environment will be done during the transfer phase (3) [7].

EQUULEUS limited ΔV capability makes the overall trajectory design process quite challenging. The spacecraft is in fact a 6U cubesat with a nominal wet mass of only 14 kg. A 4 mN thrusting capability can generate up to 0.3 mm/s^2, enabled by a water propulsive system with an I_{sp} of 70 s and a propellant mass of 1.47 kg. The total ΔV budget available is only 80 m/s. More details of the EQUULEUS spacecraft can be found in [7], they will not be discussed here since the focus of this report is more on the trajectory design process rather than the spacecraft itself.

Another important aspect of EQUULEUS is due to its nature as secondary payload onboard the Interim Cryogenic Propulsion Stage (ICPS) adapter of the SLS. Separation conditions are not under direct control of the EQUULEUS team and are dependent on the main EM-1 mission. From a mission perspective this translates into two challenges regarding the energy and timing of the trajectory after separation. The geometric configuration of the Sun-Earth-Moon system basically repeats itself after a lunar month. The trajectory design process of EQUULEUS is dependent on this configuration, since the mission will extensively use flybys and Sun's perturbation phases as an active design technique to save ΔV. This means that a too wide launch window, e.g. 2-3 weeks, could dramatically change the nominal trajectory of EQUULEUS, since it will dramatically change the Sun-Earth-Moon configuration of phase (1). Moreover the ICPS is designed to be set into an escape trajectory from the Earth-Moon system for decommissioning reasons. For EQUULEUS this means that right after separation it is important to execute a maneuver to avoid escaping the system. The direction and magnitude of this initial ΔV_1 determine the global trajectory and is one of the crucial design parameters of the trajectory design process, as will be illustrated in the next section.

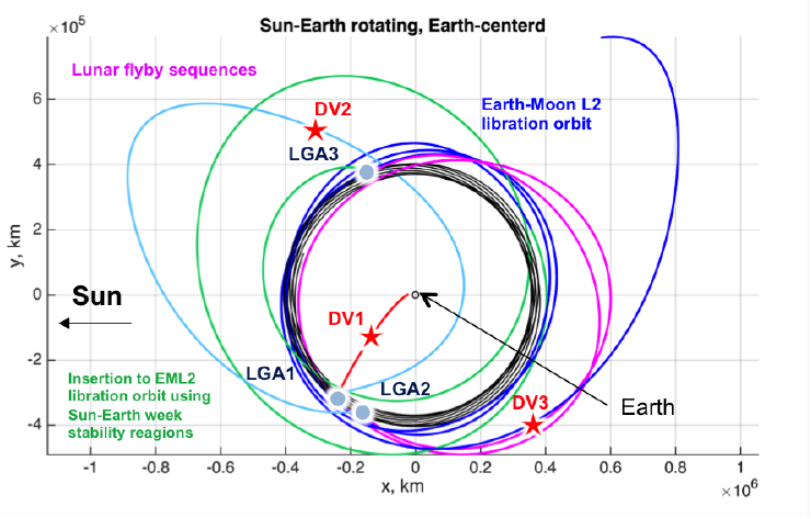

Figure 2.3: EQUULEUS nominal trajectory with an SLS launch on October 7, 2018 [7]. The trajectory is represented in the Sun-Earth synodic reference frame. The red, light blue, pink, green and blue trajectories represent successive phases of the mission represented in Figure 2.2.

2.4.2. TRAJECTORY DESIGN

The design of the transfer phase of EQUULEUS represents the most challenging and difficult phase of the mission for several reasons [7]. The limited ΔV capabilities, uncertain launch conditions, multiple lunar flybys and Sun's gravitational perturbations are all factors that make the trajectory design process a complex task. A detailed analysis of this process is illustrated in [6], while [17] focuses more on the design of the Halo orbit for the observation campaign. In this section the overall trajectory design process will be illustrated, as part of the work the author of this report performed during his stay at ISAS/JAXA.

Due to the complexity the design of the EQUULEUS trajectory is divided into several smaller blocks. These are part of a two-step process: a first-guess step and a refinement step [7]. Hereby a brief description of the tasks of the blocks:

- **Forward Propagation:** From the initial state and time given by NASA, a ΔV_1 is simulated to perform a search-grid analysis. From these initial states trajectories are propagated forward in time for about one year using the jPRO[1] propagation scheme in a full-ephemeris model considering the Sun, Earth and Moon gravitational influences. Spherical harmonics of Earth and Moon are also considered for a brief part of the propagation. The apogee states and epochs are saved into a database.
- **Halo Generation:** Quasi-periodic Halo orbits about EML2 are computed using a full-ephemeris model in the Halo-generation module.

[1] jPRO is a propagation tool implemented in jTOP, a trajectory optimization tool widely used in Kawakatsu laboratory.

- **Backward Propagation:** Trajectories are propagated backward in time from certain epoch and states of the nominal Halo orbit chosen for operations. Apogee states and epochs are saved in a database.
- **Apogee Patching:** The previously saved apogee states and epochs from forward and backward propagations are confronted. Only those within a certain position and velocity mismatch (50000 km and 100 m/s) are chosen and ranked based on a fictitious ΔV.
- **Trajectory Generation:** From this set a number of promising first-guess trajectories are selected. The whole state and epoch history of these trajectories is generated from initial to arrival condition on the Halo orbit. This have not been saved during the propagation phases for size issues.
- **Eclipse:** The duration of possible eclipse phases is checked to make sure certain mission requirements are respected. Only those trajectories satisfying these requirements are selected.
- **Optimization:** The pool of best first-guess trajectories are optimized using jTOP. After a final eclipse check, one of these trajectories is selected as the best nominal trajectory for EQUULEUS mission.

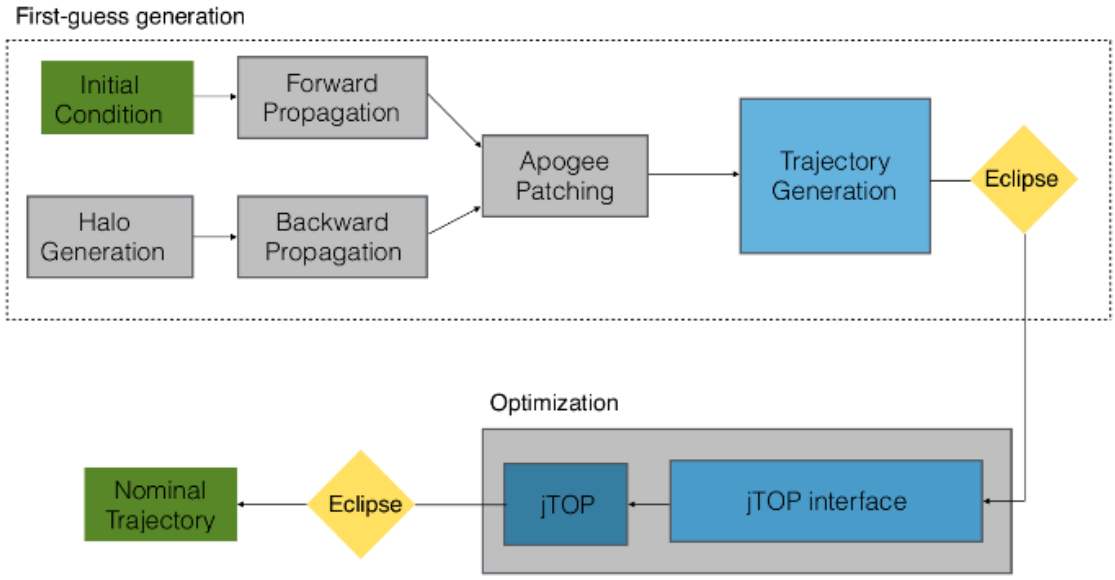

Figure 2.4: Schematic of the overall trajectory design process for the EQUULEUS trajectory.

It is noteworthy to mention that the most computationally intensive phases are the forward and backward propagations. For what concerns the backward propagation the actual strategy envisions the creation of a database of trajectories stemmed from the same Halo orbit at different epochs.

Figure 2.5 shows a selection of the 200 best trajectories computed in the first-generation step for an old initial condition of the EQUULEUS mission. Figure 2.6 shows the best of these trajectories in terms of ΔV_{Patch}. In both cases the trajectories are represented in the Earth mean equator and equinox of J2000 reference frame (EME2000) centered on Earth.

During his stay at ISAS/JAXA the author of this report has performed work on the forward propagation block and on the the code maintenance of the first-guess generation step of the toolbox. In the first case the tasks addressed the speed up of the block with the usage of a different propagation scheme in combination with parallelization capabilities and the introduction of higher-order perturbations into the dynamical model. Due to the sensitivity of the data of the EQUULEUS mission, all the trajectories represented in this report refer to old initial conditions or test cases that have been already presented in literature. The latest trajectory of the EQUULEUS mission is therefore not presented in this report, as well as certain data about the mission that will not be disclosed. An analysis of EQUULEUS trajectory with the TP-graph is presented in Appendix D.

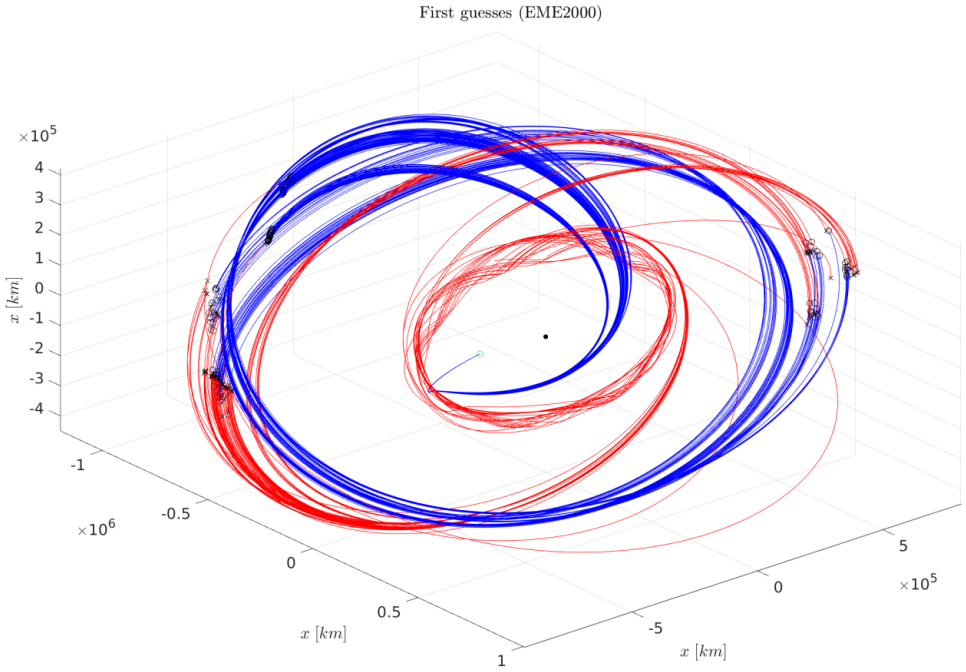

Figure 2.5: Example of the 200 best trajectories computed in the first-guess generation step. Blue and red curves are respectively forward and backward trajectories. Patching positions are highlighted by black crosses and circles while the starting position is represented by a green circle.

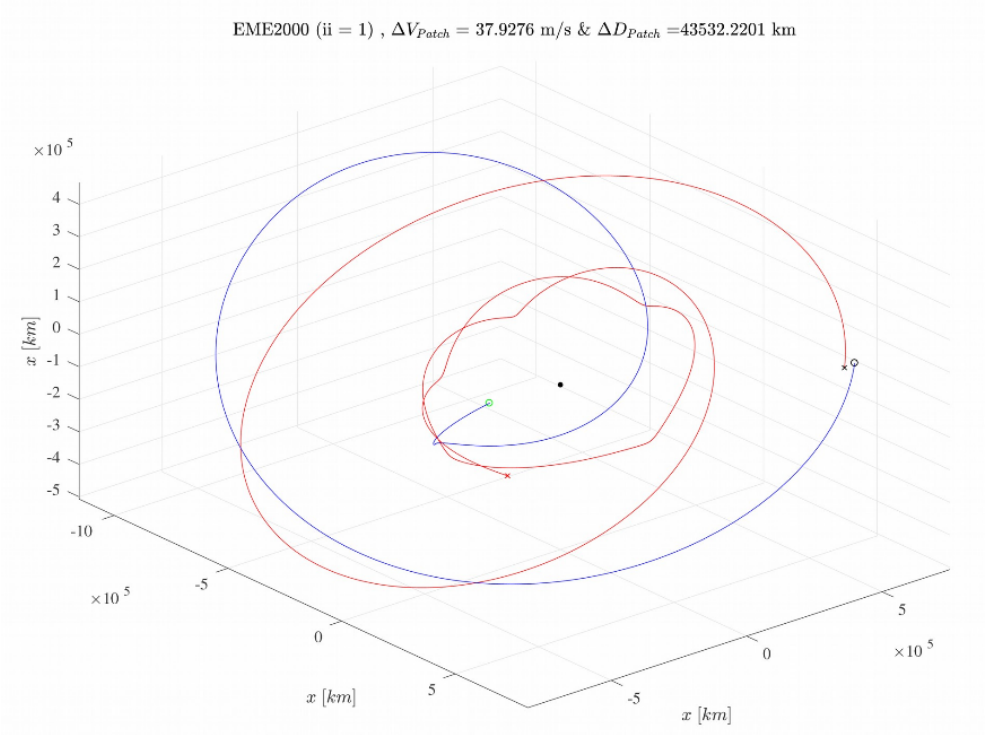

Figure 2.6: Representation of the trajectory with the lowest ΔV_{Patch} from the ones represented in Figure 2.5. Green and red points are initial and final conditions respectively, the black symbols represent the patching positions.

2.5. DESTINY

DESTINY is a Japanese interplanetary low-thrust and low-cost mission that is being designed by ISAS/JAXA as a technology demonstration mission for future deep space missions. The name of the mission stands for Demonstration and Experiment of Space Technology for INterplanetary voYage. The launch will take place in 2022 from the Tanegashima Space Center using a dedicated Epsilon-4 vehicle [8].

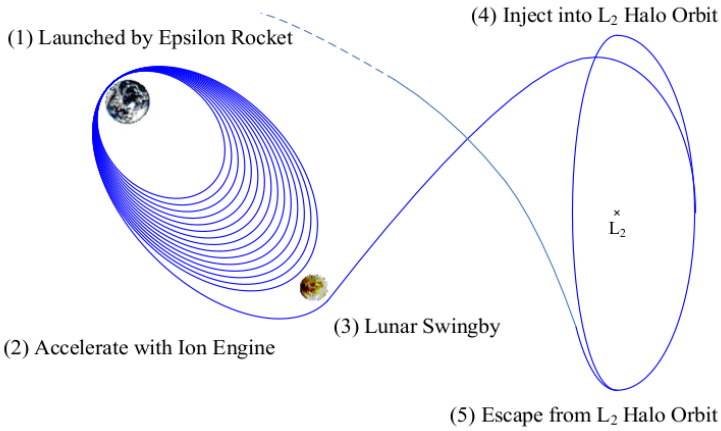

Figure 2.7: Five different phases of DESTINY mission [8].

2.5.1. MISSION DESIGN

The spacecraft will have a wet mass of about 400 kg and will be three-axis controlled. Two retractable solar panels will provide about 2930 W at EOL. The spacecraft propulsive system is derived from Hayabusa's μ10 thrusters. The newly developed μ20 thruster will allow the spacecraft to reach an acceleration of 10^{-4} m/s^2, a ΔV of 5 km/s with a thrust of 40 mN. The I_{sp} of the system is 3800 s and the propellant mass of Xenon is estimated to be around 50 kg. Amongst the most relevant technologies DESTINY will be testing, there will be the ultra-lightweight solar panel, the large-scale ion engine μ20, advanced thermal control and communication systems, autonomous on-board operations and orbit determination under low-thrust operation. More details about the spacecraft design and the mission can be found in [8].

2.5.2. TRAJECTORY DESIGN

The DESTINY trajectory will be characterized by five different phases:

- The spacecraft is injected into a highly elliptical trajectory with perigee and apogee altitudes of 230 and 29000 km.
- After 30 days in this orbit the spacecraft starts an orbit raising phase that will bring it to an apogee altitude of approximately 300000 km after 1.5 years from launch.
- A lunar swingby phase is used both to widen out the last spiraling part of the trajectory and to efficiently change the orbit inclination to that of the Moon's orbit. Successive flybys are designed either to increase or decrease the energy of the spacecraft.
- The spacecraft is injected into a Halo orbit about the SEL2 point.
- The spacecraft escapes the region in proximity of the Earth and starts the interplanetary trajectory towards the asteroid 3200-Phaeton, that will be closely studied during a flyby event. Other additional flyby targets are under selection for the extended phase of the mission [8].

There are currently two scenarios under discussion; one foresees the spacecraft to reach the SEL2 Halo orbit and then to escape while another scenario uses a direct escape trajectory after the swingby phase. The latter case defines the DESTINY+ mission.

The current work that has been performed in the DESTINY team is related to the generation of first-guess trajectories in the lunar swingby phase. The approach used is thoroughly illustrated in [9] and is based on a database of Moon-to-Moon transfer legs computed in the Sun-Earth planar CR3BP. By patching several of these legs, first-guess trajectories can be generated that make use of multiple flyby events with the Moon to increase or decrease the spacecraft energy. Some preliminary results of this technique for both EQUULEUS and DESTINY missions are illustrated in [9]. Note that this approach actually inspired the author of this report to develop a similar technique that considers instead a specifically defined Poincaré section as patching surface. This will be discussed in Chapter 7.

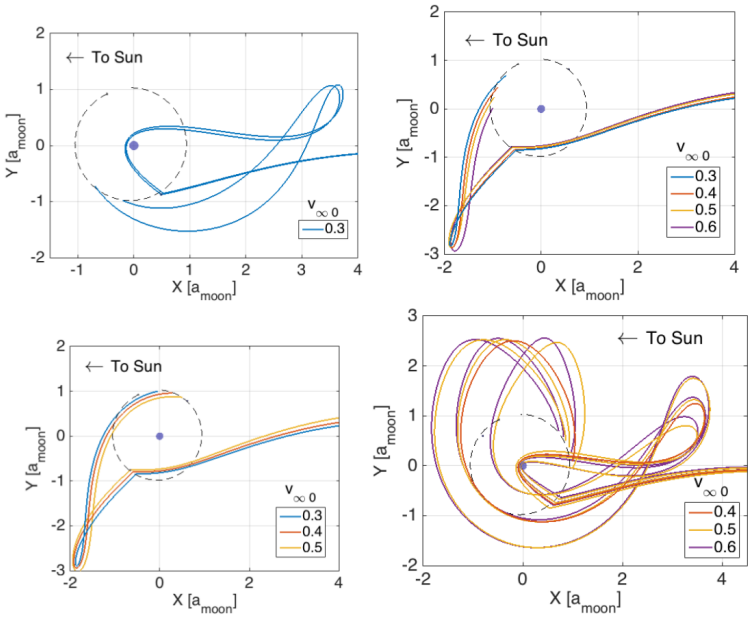

Figure 2.8: Example of the last flyby legs of the DESTINY mission obtained from a query on the database defined in [9].

3

THEORY

In this chapter the theoretical background of the research work is illustrated. In Section 3.1 the trajectory design approach is briefly illustrated. In Section 3.2 the dynamical models that will be used in the report are presented. In Sections 3.3 and 3.4 multi-body dynamic effects such as lunar flybys and solar perturbation events are described. A few fundamental concepts from dynamical system theory that will be used in the report are illustrated in Section 3.5. The Tisserand parameter is presented in Section 3.6, while its application as graphical tool is discussed in Section 3.7.

3.1. FIRST-GUESS AND OPTIMIZATION PROCESSES

The decision of the dynamical model used to design a spacecraft's trajectory is a fundamental choice influenced by many factors. The complexity of such a model affects the accuracy of the designed trajectory but also the difficulty of the design process. An approach to simplify this task consists into splitting the trajectory design process into two phases. In the first phase a first-guess reference trajectory is generated through the usage of a simple dynamical model considering the most important forces in the system. In the second phase such a reference trajectory is taken and refined with the addition of the perturbing forces that have been neglected in the first phase. The success of this approach depends on the proper sharing between the two phases of the perturbing forces considered.

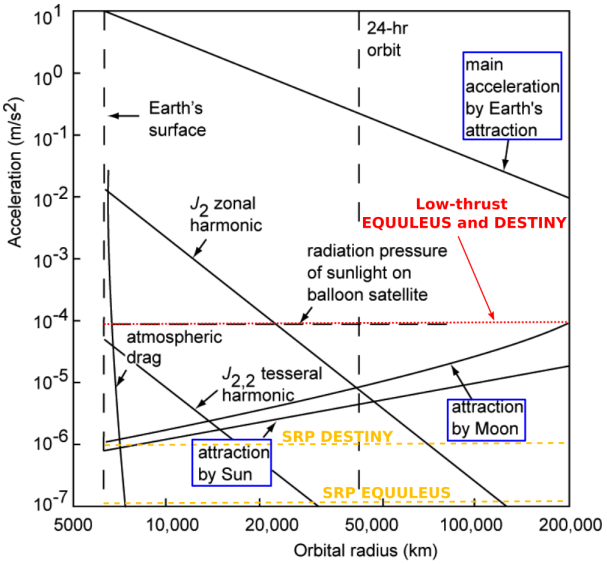

Figure 3.1: Magnitude of perturbing forces as function of orbital radius, sketch adapted from [1]. The solar radiation pressure (SRP) perturbing acceleration of EQUULEUS and DESTINY has been added using a reflectivity coefficient of 1.8.

The backbone of the trajectory is designed in the first phase and it is fundamental that in such a phase only the main perturbing forces that keep the model simple are considered. These depend on the mission scenario and can be evaluated thanks to sketches as the one in Figure 3.1, representing the main perturbing forces in the vicinity of Earth. For example for missions such as EQUULEUS and DESTINY it is possible to see from Figure 3.1 that only gravitational perturbations and thrust effects are expected to give important contributions.

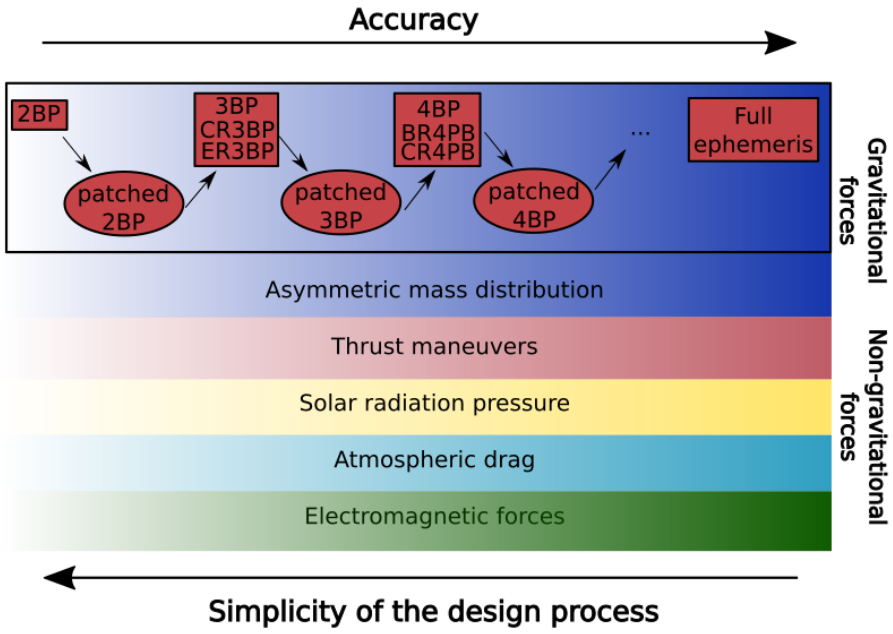

Figure 3.2: Sketch of the trajectory design process. The choice of the dynamical model to use is fundamental. The left-right gradient of each perturbing force is representative of the complexity of the model considered for that particular force. In a preliminary analysis, when generating first-guess solutions, the sketch will be traversed vertically in the left region with the usage of simple but inaccurate models. At successive iterations the complexity of the dynamical model is refined to increase the accuracy.

A schematic of the trajectory design approach is illustrated in Figure 3.2. Note that the research presented in this report is focused on the generation of first-guess trajectories considering only the gravitational influence generated by multiple bodies.

3.2. DYNAMICAL MODELS

In this section three different dynamical models that have been used in this research are presented. As discussed in the previous section these are all pertaining to dynamical models considering gravitational influences only. First the two-body problem (2BP) will be briefly introduced in Section 3.2.1, from which the notion of osculating orbital elements is adopted. Then the main dynamical model of the research, the CR3BP, is discussed at length in Section 3.2.2. In this section also the main notation used throughout the report is introduced. Finally in Section 3.2.3 the Bicircular Restricted Four-Body Problem (BR4BP) is briefly introduced.

Note that the two latter dynamical models do not comply with Newton's laws, since they force the bodies in the model to have a certain type of motion by neglecting mutual attraction between them. The error committed is however small and these model are universally considered as very efficient in giving a simple insight into the dynamics of the multi-body environment.

As it is possible to see from Figure 3.2, the higher the number of bodies considered, the higher the accuracy of the trajectory and complexity of the design process. Rushing to consider the highest number of bodies however is not the only possibility to increase the accuracy of a model. An alternative is presented by patching two different dynamical model in a region where they both exert an equal influence on the spacecraft trajectory. With such an approach a trajectory under the influence of $N+1$ bodies is computed using N bodies at a

time, decreasing the overall complexity and reaching a compromise between the two dynamical models. To design trajectories in the Sun-Earth-Moon system such a patching approach will be used. Its application has already been demonstrated to be successful as it is possible to see for Hiten's trajectory design illustrated in [5].

3.2.1. TWO-BODY PROBLEM

The relative motion of a spacecraft about a larger body (such as a planet or a moon) can be described by the following equation:

$$\ddot{\mathbf{r}} = -\mu \frac{\mathbf{r}}{r^3} \tag{3.1}$$

The solution of such an equation of motion is referred to as Keplerian motion or a Keplerian orbit, and describes a conic section with the massive body located in one of the focal points. To describe such a conic section in three dimensions a set of six orbital elements can be used. One of the most used ones is constituted by the semi-major axis a, the eccentricity e, the inclination i, the right ascension of the ascending node Ω or $RAAN$, the argument of pericenter ω and the true anomaly θ.

a is responsible for the energy and size of the Keplerian orbit, while e determine the shape. The remaining four orbital elements describe its orientation in space.

In a Keplerian orbit these elements will be constant, however considering other perturbations will make them vary with time. In such a case they are defined as osculating orbital elements. Throughout this report a set of three osculating orbital elements will be of fundamental use. These will be the pericenter radius $r_p = a(1-e)$, the apocenter radius $r_a = a(1+e)$ and the inclination i.

3.2.2. CIRCULAR RESTRICTED THREE-BODY PROBLEM

The Circular Restricted Three-Body Problem (CR3BP) is a specific case of a Three-Body Problem characterized by the following assumptions:

- The mass of two bodies ($P1$ and $P2$) is much larger than the mass of the third body (P). As a consequence the gravitational influence exerted by P on $P1$ and $P2$ can be neglected.
- The two massive bodies ($P1$ and $P2$) move in coplanar circular orbits about the barycenter of the system. The motion of body P is not confined to this plane.

Throughout this report the author will refer to "primaries" intending $P1$ and $P2$ together, while "primary" and "secondary" will be used to address $P1$ and $P2$ singularly. Assuming the motion of $P1$ and $P2$ to be known, the purpose is to determine the motion of the third body P, which in engineering applications is assumed to be the spacecraft.

REFERENCE FRAMES

Two different reference frames can be used in the description of the motion of body P in the CR3BP; these are the psuedo-inertial and synodic reference frames. These two reference frames are represented in Figure 3.3. O is the origin and barycenter of the system, around which the primaries move in circular orbits. The inertial reference frame is the red one defined by the ξ, η and ς axes, the latter one being perpendicular to the orbital plane of the primaries. This reference frame is inertial for what concerns the orientation of its axes, that stay fixed in time, but is not for what concerns its origin, hence the term pseudo-inertial. When this is centered on the primaries in fact it moves in a circular motion, and such a reference frame would not satisfy the first principle of dynamics and could not be properly defined as inertial. In this report, as well as in most of the existing literature, the term pseudo will be discarded to facilitate the comprehension. The synodic reference frame is a co-rotating reference frame with axes X, Y and Z, represented by the blue axes if Figure 3.3. The X-axis is aligned with $P1$ and $P2$, positive towards $P2$, the Y-axis is perpendicular to the X-axis and the Z-axis coincides with the ς-axis. The synodic reference frame is rotating with respect to the inertial one about the Z/ς-axis with a constant rate $\dot{\theta}$.

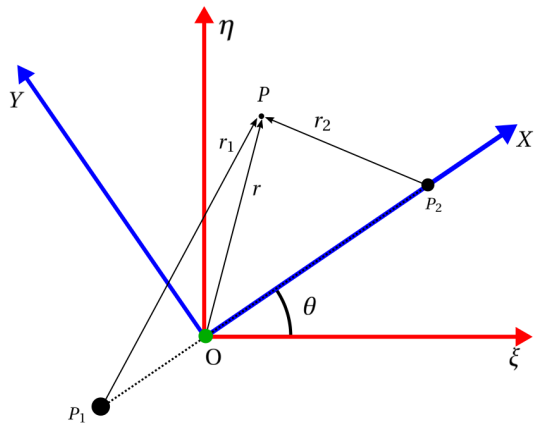

Figure 3.3: Synodic reference frame XYZ (blue) and inertial reference frame $\xi\eta\varsigma$ (red) centered on the barycenter of the system (O). The Z and ς axes coincide and are not represented.

The system is often normalized with respect to a normalization parameter μ, the value of which can be changed in order to model different three-body systems. This parameter relates the primary and secondary masses and distances as follow:

$$m_1 + m_2 = 1 \quad ; \quad m_1 = 1 - \mu \quad ; \quad m_2 = \mu \tag{3.2}$$

$$OP1 + OP2 = 1 \quad ; \quad OP1 = \mu \quad ; \quad OP_2 = 1 - \mu \tag{3.3}$$

m_1 and m_2 being the masses of the primaries and $OP1$ and $OP2$ their distances from the barycenter. In many cases is also important to dimensionalize and give a physical importance to quantities by using the dimensionalization parameters DU,VU and TU, corresponding respectively to the distance, velocity and time units of the specific CR3BP system considered. DU is often taken as a parameter defining the system while TU and VU can be computed as:

$$TU = \sqrt{\frac{DU^3}{G(m_1 + m_2)}} \quad \text{and} \quad VU = \frac{DU}{TU} \tag{3.4}$$

where G is the universal gravitational constant. In the majority of the existing literature the synodic and inertial reference frames are considered centered in the barycenter of the system. However in this report reference frames centered on the primaries will be extensively used. To facilitate the discussion the following notation will be used when referring to a generic quantity A_{ijk}:

- i: refers to the reference frame being synodic (S) or inertial (I).
- j: refers to the reference frame's origin, barycenter (B), primary (P1), secondary (P2) or any chosen point (P_i).
- k: refers to the dimensionality; if the quantity is described using physical units (D) the index is used, if not is omitted.

So for example the position vector $\mathbf{r}$ in Figure 3.3 expressed in adimensional units in the synodic reference frame centered in the barycenter will be named $\mathbf{r}_{SB}$ while the corresponding quantity in the inertial one $\mathbf{r}_{IB}$. If the notation is omitted it will be explained in the text.

COORDINATE TRANSFORMATION

In the following section the coordinate transformation equations will be briefly illustrated, as they will be extensively used throughout the report. The 6×1 state vector will be represented by the symbol $\mathbf{X}$, followed by the information of the reference frame with respect to which its components are expressed. The state vector

can be decomposed in a position vector of dimension 3×1 named $\mathbf{r}$ and a velocity one of 3×1 named $\mathbf{v}$. The complete state transformation equations are now introduced with an example to pass from $\mathbf{X}_{SB}$ to $\mathbf{X}_{IP_iD}$. First the state can be transformed by considering a different origin but remaining in the synodic reference frame. Let's fix for example such an origin on the point P_i of coordinates $((P_i)_x, (P_i)_y, (P_i)_z)$ expressed in the SB reference frame. The state in SP_i can be computed as:

$$\mathbf{X}_{SP_i} = \mathbf{X}_{SB} - \begin{bmatrix} (P_i)_x \\ (P_i)_y \\ (P_i)_z \\ 0 \\ 0 \\ 0 \end{bmatrix} \tag{3.5}$$

In order to transform the state from $\mathbf{X}_{SP_i}$ to $\mathbf{X}_{IP_i}$ the following rotation matrices need to be defined:

$$A = \begin{bmatrix} cos\theta & -sin\theta & 0 \\ sin\theta & cos\theta & 0 \\ 0 & 0 & 1 \end{bmatrix} \quad \text{and} \quad B = \frac{dA}{dt} = \dot{\theta} \begin{bmatrix} -sin\theta & -cos\theta & 0 \\ cos\theta & -sin\theta & 0 \\ 0 & 0 & 0 \end{bmatrix} \tag{3.6}$$

The transformation matrix to pass from a synodic to inertial state can be expressed by the matrix T_{S2I} and vice-versa by the matrix T_{I2S} so defined[1]:

$$T_{S2I} = \left[\begin{array}{c|c} A & 0_{3\times3} \\ \hline B & A \end{array}\right] \quad \text{and} \quad T_{I2S} = \left[\begin{array}{c|c} A^T & 0_{3\times3} \\ \hline B^T & A^T \end{array}\right] \tag{3.7}$$

where the T denotes the transpose operation. By using these matrices the state can be expressed as $\mathbf{X}_{IP_i} = T_{S2I}\mathbf{X}_{SP_i}$. The distance, velocity and time units defined in Equation 3.4 are then used to give a dimensionality to both the state vector and epoch:

$$\mathbf{X}_{IP_iD} = \begin{bmatrix} DU \begin{bmatrix} x \\ y \\ z \end{bmatrix}_{IP_i} \\ VU \begin{bmatrix} \dot{x} \\ \dot{y} \\ \dot{z} \end{bmatrix}_{IP_i} \end{bmatrix} \quad \text{and} \quad t_{IP_iD} = TU\left[t_{IP_i}\right] \tag{3.8}$$

By substituting $(P_i)_x = -\mu$ and $(P_i)_y = (P_i)_z = 0$ it is possible to derive the canonical transformation existing in literature to transform from SB to IP1D.

EQUATIONS OF MOTION

The equations of motion expressed in the SB frame are [1]:

$$\begin{cases} \ddot{x} = 2\dot{y} + x - \dfrac{1-\mu}{r_1^3}(\mu + x) + \dfrac{\mu}{r_2^3}(1 - \mu - x) \\ \ddot{y} = -2\dot{x} + y - \dfrac{1-\mu}{r_1^3}y - \dfrac{\mu}{r_2^3}y \\ \ddot{z} = -\dfrac{1-\mu}{r_1^3}z - \dfrac{\mu}{r_2^3}z \end{cases} \tag{3.9}$$

where $r_1 = \sqrt{(\mu + x)^2 + y^2 + z^2}$ and $r_2 = \sqrt{(x - 1 + \mu)^2 + y^2 + z^2}$ are the distances from the primaries presented in Figure 3.3.

JACOBI'S INTEGRAL

The only analytic integral of motion in the CR3BP is called the Jacobi's integral. In its simplest formulation it is expressed in the SB reference frame as:

$$J_{SB}\left(x, y, z, \dot{x}, \dot{y}, \dot{z}\right) = x^2 + y^2 + \frac{2\left(1-\mu\right)}{\sqrt{(\mu + x)^2 + y^2 + z^2}} + \frac{2\mu}{\sqrt{(x - 1 + \mu)^2 + y^2 + z^2}} - (\dot{x}^2 + \dot{y}^2 + \dot{z}^2) + \mu(1 - \mu) \tag{3.10}$$

[1] The reader can verify that $T_{S2I}T_{I2S} = I$, making use of the fact that $BA^T + AB^T = 0_{3\times3}$ by substituting the terms in Equation 3.6.

The term $\mu(1-\mu)$ is often used to simplify the analysis of the Hill surfaces, that will be introduced in the next section. Often there is an ambiguity between the Jacobi integral considered as a function and the Jacobi constant considered as a scalar quantity representing the value of such a function evaluated for a particular state.

$$\left(x, y, z, \dot{x}, \dot{y}, \dot{z}\right) \in \mathbb{R}^6 \; : \; J\left(x, y, z, \dot{x}, \dot{y}, \dot{z}\right) = C \in \mathbb{R}^1 \tag{3.11}$$

The first can be seen as a function depending on a six dimensional vectorial state, the latter is a scalar quantity representative of the specific energy level considered in the model and is obtained by the evaluation of the function for a specific state of the spacecraft. In this report I will refer to the Jacobi integral to the function $J\left(x, y, z, \dot{x}, \dot{y}, \dot{z}\right)$ while I will refer to the Jacobi constant to its value C.

HILL'S SURFACES

A Hill's surface is defined as the. region of space where the velocity of point P is zero. For certain values of the Jacobi constant C different surfaces can be identified, hence the plural. These surfaces are important to discern between regions of space that are potentially accessible from those which are not. The equation describing Hill's surfaces can be simply derived by taking Equation 3.10 and imposing $V = \sqrt{\dot{x}^2 + \dot{y}^2 + \dot{z}^2} = 0$; for this reason they are often also called Zero Velocity Curves (ZVC). Expressed in the SB reference frame this can be written as an implicit function:

$$x^2 + y^2 + \frac{2\left(1-\mu\right)}{\sqrt{(\mu+x)^2 + y^2 + z^2}} + \frac{2\mu}{\sqrt{(x-1+\mu)^2 + y^2 + z^2}} - C_{SB} + \mu(1-\mu) = 0 \tag{3.12}$$

A representation of the Hill's surfaces for three different values of C_{SB} can be seen in Figure 3.4. When these are projected in the XY-plane they appear as curves, in such a case it is important not to confuse them with the black areas represented in Figure 3.4, as these only express the areas impossible to reach, while the surfaces correspond to the border of these regions.

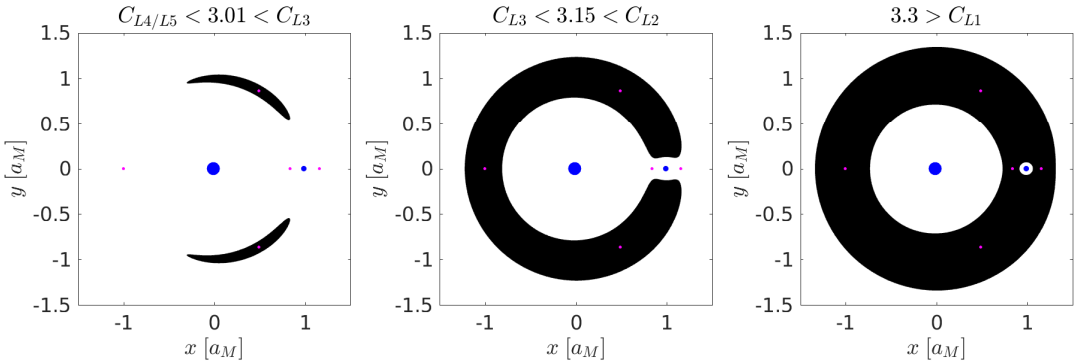

Figure 3.4: ZVC and forbidden areas in the XY-plane for three different cases of the Jacobi constant. The primaries are represented as blue points, the primary being bigger than the secondary. The five Lagrange libration points are represented by pink points.

As it is possible to note from Equation 3.12 and from Figures 3.4 and 3.5, Hill's surfaces are symmetric with respect to the XY and XZ-planes. A 3D representation of these surfaces is illustrated in Figure 3.5. As shown before the surface shapes can be changed by varying the Jacobi constant C. In particular there are four different values for which these touch or separate from each other: $C_{L1}, C_{L2}, C_{L3}, C_{L4/L5}$ .These separation points are all located on the XY-plane and their coordinates define five different equilibrium points called Lagrange libration points.

LAGRANGE LIBRATION POINTS

Five equilibrium points exist in the CR3BP and these are called Lagrange libration points. All of them are contained in the XY-plane, three of them (L_1, L_2, L_3) are called *collinear* as they lay on the X-axis of the SB reference frame, while the remaining two (L_4, L_5) are called *equilateral* since they form an equilateral triangle with the primaries. By defining a potential function $U(x, y, z)$ as [1]:

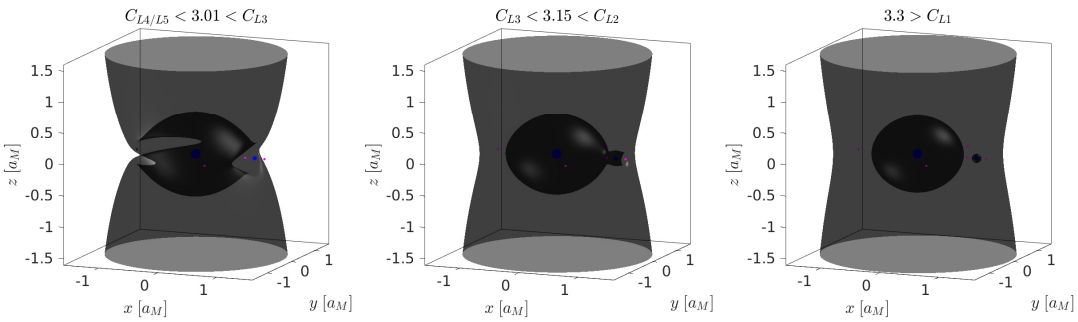

Figure 3.5: Hill's surfaces in 3D for the three different cases used in Figure 3.4. Note that in this figure only the surface is represented, while the inaccessible region has not been filled as in Figure 3.4.

$$U(\mathbf{r}_{SB}) = \frac{\left(x^2+y^2\right)}{2} + \frac{1-\mu}{r_1} + \frac{\mu}{r_2} + \frac{1}{2}\mu(1-\mu) \tag{3.13}$$

the Lagrange libration points are defined such that $\frac{\partial U}{\partial x} = \frac{\partial U}{\partial y} = \frac{\partial U}{\partial z} = 0$. The equations of motion can also be written by using the potential function as:

$$\ddot{x} - 2\dot{y} = \frac{\partial U}{\partial x} \quad \text{and} \quad \ddot{y} + 2\dot{x} = \frac{\partial U}{\partial y} \quad \text{and} \quad \ddot{z} = \frac{\partial U}{\partial z} \tag{3.14}$$

By starting from one libration point with $\mathbf{V} = 0$, it is then possible to see that the spacecraft would not experience any acceleration with respect to the synodic frame.

MOTION ABOUT COLLINEAR LIBRATION POINTS

The are several types of motion about the Lagrange libration points. The most used ones for observation missions are the ones relative to the collinear points, that are briefly illustrated here. It is important to remember that while a Keplerian orbit develops about a physical body such as a planet or a moon, orbiting a libration point means to orbit an empty mathematical point. Three big families of such orbits about the collinear points exist:

- **Lyapunov orbits:** It is a class of periodic two-dimensional orbits contained in the XY-plane.
- **Lissajous orbits:** A class of three-dimensional orbits for which the periodicity in the XY-plane is different from the one in the Z-direction. They can be described as slowly changing elliptical orbits.
- **Halo orbits:** It is a class of closed-loop orbits generated by a particular case of Lissajous orbits when the motion in the XY-plane is coupled with the one in the Z-component. The orbit develops on a plane inclined with respect to the XY-plane. A NRHO is a particular type of Halo orbit that develops almost entirely out-of-plane and that approaches the Moon at close distance with a nearly-stable behavior.

3.2.3. BICIRCULAR RESTRICTED FOUR-BODY PROBLEM

The Bicircular Restricted Four-Body Problem (BR4BP) is a simplified version of the four-body problem and a natural extension of the CR3BP taking into account a fourth body. In such a model three massive bodies $P1$,$P2$ and $P3$ and a point mass P are considered such that $m_{P3} >> m_{P1} >> m_{P2} >> m_P$. $P3$ and the barycenter of the $P1-P2$ system are assumed to be moving in circular orbits about their common barycenter with mutual separation d_2. $P1$ and $P2$ are assumed as well to be moving in circular orbits about their common barycenter with mutual separation d_1 such that $d_1 < d_2$. All masses except for P are assumed to be moving in the same plane.

The equations of motion of the BR4BP are now presented in normalized units in the synodic reference frame of the $P1-P2$ system. Each acceleration component can be decomposed into two terms. The reader will recognize the first of these terms in the square brackets to be the one of the CR3BP model, these are the terms

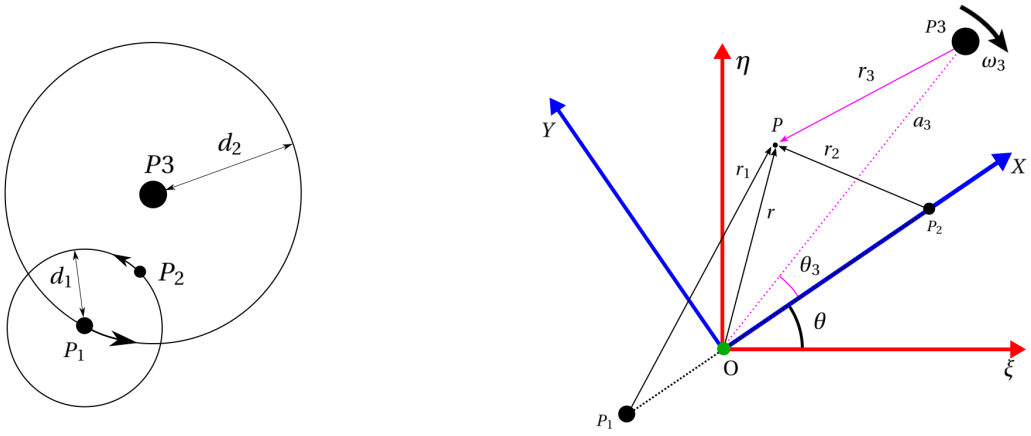

Figure 3.6: On the left, schematic of the BR4BP model geometry, adapted from [5]. On the right, synodic reference frame XYZ (blue) and inertial reference frame $\xi\eta\varsigma$ (red) centered in the barycenter of the $P1-P2$ system (O), with the addition of the fourth point mass $P3$. Adapted from Figure 3.3.

accounting for the $P1-P2$ system alone. The additional term is dependent on the geometric properties and physical characteristics of $P3$. The equations of motion[2] are [5]:

$$\begin{cases} \ddot{x} = \left[2\dot{y} + x - \dfrac{1-\mu}{r_1^3}(\mu+x) + \dfrac{\mu}{r_2^3}(1-\mu-x)\right] - \dfrac{\mu_3}{r_3^3}x + \dfrac{\mu_3}{r_3^3}(1-\alpha)x_3 \\ \ddot{y} = \left[-2\dot{x} + y - \dfrac{1-\mu}{r_1^3}y - \dfrac{\mu}{r_2^3}y\right] - \dfrac{\mu_3}{r_3^3}y + \dfrac{\mu_3}{r_3^3}(1-\alpha)y_3 \\ \ddot{z} = \left[-\dfrac{1-\mu}{r_1^3}z - \dfrac{\mu}{r_2^3}z\right] - \dfrac{\mu_3}{r_3^3}z \end{cases} \tag{3.15}$$

where $\alpha = \frac{m_3}{a_3^3}$, $r_3 = \sqrt{(x-x_3)^2+(y-y_3)^2+z^2}$ and $\mu_3 = m_3$. The motion of $P3$ about the barycenter of the $P1-P2$ system is described by a circle with radius $a_3 = d_2$. The coordinates (x_3, y_3, z_3) of point $P3$ will therefore be $(a_3 cos(\theta_3), a_3 sin(\theta_3), 0)$, where $\theta_3 = -\omega_3 t + \theta_{3_0}$, θ_{3_0} being the initial angle between $P3$ and the x-axis of the $P1-P2$ synodic reference frame. The parameters a_3,m_3 and ω_3 represent the normalized semi-major axis, mass and angular velocity of the fourth body P3 with respect to normalized units of the $P1-P2$ system.

By comparing Equations 3.15 and 3.9 it is possible to see that the insertion of the fourth body has the important effect of introducing a term in these equations that is depending on time: the position of the body $P3$. The BR4BP is therefore a non-autonomous system. An important consequence of this property is the non-existence of an analytic integral of motion; in such a model the Jacobi integral is not a constant function but varies with time, as it is possible to see in Appendix D.

In this report the BR4BP model of the Sun-Earth-Moon system will be used as a valid continuous counterpart of the patched CR3BP approach that will be adopted in Chapter 7. In such a case the BR4BP of the Sun-Earth-Moon system will be used with the following set of values [5]:

$$m_3 = 328900.54 \qquad a_3 = 388.81114 \qquad \omega_3 = 0.925195985520347 \tag{3.16}$$

3.3. FLYBY EFFECTS

In this section the flyby phenomenon will be discussed. The theory behind it is well known and has been applied to space missions since many years by now. As a result an abundant amount literature exists on the topic. Most notably [18] investigated the celestial mechanics of the gravity assist in the patched 2BP

[2] The equations of motion given in [5] are valid for the 2D case and are extended in this report for the 3D one.

approximation, [19] numerically analyzed and classified families of gravity-assist trajectories in the CR3BP, [11] investigated the flyby in the planar CR3BP and developed a tool, the flyby map, derived from the Keplerian map and the Tisserand graph useful to design trajectories in the Jupiter environment, [20] analyzed the phenomenon in the Earth-Moon CR3BP and have developed a method to design double Lunar swingby trajectories.

The gravity assist or flyby effect is a phenomenon deriving from the multi-body problem formulation. However to simplify the analysis often a reduced dynamical model is used such as a patched 2BP or a CR3BP. By considering Figure 3.3 the secondary of the system is considered as the flyby body while the primary is the main body. By using a patched 2BP approximation we would generally consider a flyby trajectory as an hyperbolic trajectory about the flyby body within the sphere of influence (SOI) with respect to the primary. Such a hyperbolic trajectory develops on a plane that is not necessarily oriented as the body's orbit plane. The velocity of the flyby body will be $\mathbf{V}_{FB}$, while its projection onto the plane of the hyperbolic trajectory would be $\mathbf{V}^*_{FB}$. The effect of the flyby from the perspective of the primary corresponds to a bending of the spacecraft velocity by what is called a deflection angle or pump angle α. The spacecraft velocities at entrance and exit of the SOI are referred to as ingoing and outgoing hyperbolic excess velocities $\mathbf{V}^+_\infty$ and $\mathbf{V}^-_\infty$. These vectors are the same in magnitude V_∞ but are oriented in different ways, and in this different orientation lays the flyby effect. Figure 3.7 represents a schematic of the flyby effectt.

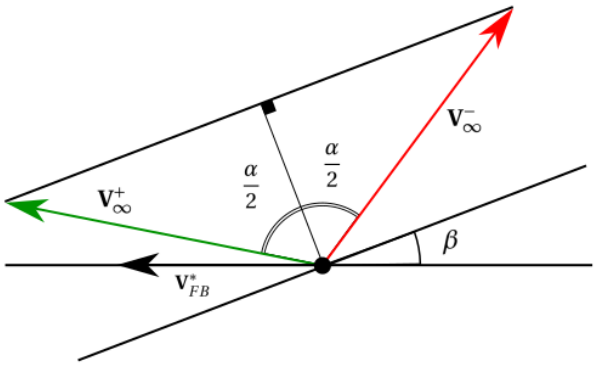

Figure 3.7: Sketch of the velocity vectors that characterize the flyby effect. The ingoing and outgoing asymptotic excess velocities (red and green respectively) are presented, as are the flyby body projected velocity V^*_{FB}, the pump angle α and the angle β.

β represents the angle between the hyperbolic trajectory pericenter vector and the flyby body velocity vector. The change in the orientation of the velocity from the perspective of the primary corresponds to a proper ΔV in the patched approximation. This ΔV can be easily computed by considering the vectorial difference between the spacecraft final and initial velocity vectors and correspond to $\Delta\mathbf{V} = \mathbf{V}^+_\infty - \mathbf{V}^-_\infty$. Applying this formula on the sketch in Figure 3.7 it is possible to quantify the magnitude of the ΔV given by the swingby as:

$$\Delta V = 2V_\infty sin\left(\frac{\alpha}{2}\right) \tag{3.17}$$

This ΔV represents a change in the velocity of the spacecraft with respect to the primary and thus in the kinetic energy of the spacecraft with respect to the main body. By assuming the potential energy to be approximately constant within the limited region of the SOI of the flyby body, we can conclude that in such a model the flyby effect corresponds to a discontinuous change in the Keplerian energy of the spacecraft ΔE_1. This change can be quantified as [1]:

$$\Delta E_1 = V^*_{FB}\Delta V cos\beta = 2V^*_{FB}V_\infty sin\left(\frac{\alpha}{2}\right)cos\beta \tag{3.18}$$

The change in the spacecraft specific energy derives from the flyby body itself; when a spacecraft acquires energy through a swingby the flyby body loses the same amount and vice versa. This ΔE_1 is exploited by the spacecraft, but is too small to cause any quantifiable effect on the secondary, given its mass compared to the that of the spacecraft. Using the vis-viva equation it would be possible to quantify the change on the

semi-major axis [3] caused by the flyby [1]:

$$\Delta\left(\frac{1}{a}\right) = -\frac{2}{\mu_2}\Delta E_1 = -\frac{4}{\mu_2}V_{FB}^* V_\infty sin\left(\frac{\alpha}{2}\right)cos\beta \tag{3.19}$$

From these equations very simple but fundamental conclusions can be derived on the flyby's effects:

- The spacecraft total energy will decrease if the spacecraft passes ahead of the planet ($90° < \beta < 270°$). The decrease would be maximum for $\beta = 180°$, when the spacecraft pericenter vector would be aligned to the planet's velocity vector.
- The spacecraft total energy will increase if the spacecraft passes behind the planet ($-90° < \beta < 90°$). The increase would be maximum for $\beta = 0°$, when the spacecraft pericenter vector would be opposite with the planet's velocity vector.
- Having specified β and V_∞, ΔE_1 would be maximum if V_{FB}^* is maximum. This is the case when the plane of the flyby trajectory and the flyby body orbit coincides and $V_{FB}^* = V_{FB}$.
- Assuming $V_{FB}^* = V_{FB}$, ΔE_1 is affected by two parameters that depend on the flyby body: μ_2 and V_{FB}.
- Having specified β and V_∞, ΔE_1 will be zero if $V_{FB}^* = 0$. This is the case when the flyby trajectory and the flyby body's orbit plane are perpendicular with respect to each other. In reality the flyby will have effects on the inclination of the trajectory.

By using the patched 2BP approximation a very simple model of the flyby phenomenon can be derived. In such an approximation the minor body essentially rotates the velocity vector of the spacecraft by a bending angle that is dependent on the flyby altitude. The flyby is therefore seen as a discontinuous change in the velocity, energy and semi-major axis as described in Equations 3.17, 3.18 and 3.19. In reality since the flyby happens under the continuous influence of n bodies, such a discontinuity does not exist. The discontinuity is the effect introduced by the usage of a patched approximation that is capable to easily describe a multi-body dynamic phenomenon that would require at least three bodies (considering also the spacecraft) for a sufficient characterization. By removing this approximation and using the CR3BP it would be possible to investigate these changes in a continuum way but still avoid the complexity involved in a typical n-body problem. In this sense the work in [20] bridges the gap between the patched 2BP and CR3BP and offers an easy-to-understand characterization of the events involved.

By considering the Earth-Moon planar CR3BP, the total energy of the spacecraft E with respect to the barycenter of the synodic reference fame can be computed. This can then be differentiated to obtain the instantaneous energy change as [20]:

$$\frac{dE}{dt} = \mu(1-\mu)y\left(\frac{1}{\left(\sqrt{(\mu+x)^2+y^2}\right)^3} - \frac{1}{\left(\sqrt{(x-1+\mu)^2+y^2}\right)^3}\right) \tag{3.20}$$

By inspecting this equation it is possible to see the existence of two loci such that $\frac{dE}{dt} = 0$: $x = \frac{1}{2} - \mu$ and $y = 0$. These conditions split the SB frame into four different regions in which the sign of $\frac{dE}{dt}$ is invariant. As it is possible to see in Figure 3.8 $\frac{dE}{dt}$ is relatively flat apart from the region in proximity of the primaries. A closer view of the region in the vicinity of the Moon can be seen in Figure 3.9.

From these figures it is possible to see that the spacecraft energy will suffer a dramatic change only in the proximity of the primaries. It is such a dramatic variation that defines the flyby effect.

In the work of [20] a formula is also proposed to quantify the ΔE caused by the flyby. Since a direct integration over time of Equation 3.20 is difficult to perform for an arbitrary orbit in the CR3BP, in [20] a 2BP approximation in the vicinity of the Moon has been assumed. With such an assumption the energy variation generated by the flyby in the CR3BP has been estimated to be:

[3] the term $\frac{1}{a}$ is used to avoid singularities.

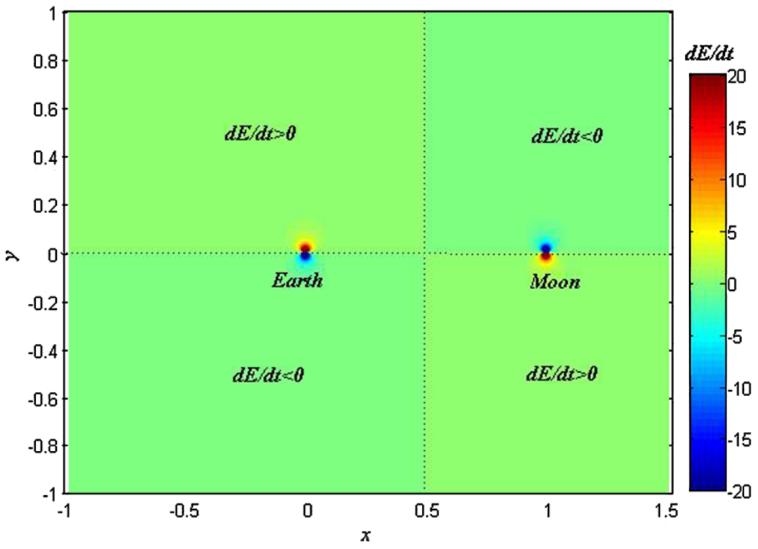

Figure 3.8: Distribution of $\frac{dE}{dt}$ in the Earth-Moon SB reference frame [20]. The variation is relatively flat in most of the region of the Earth-Moon system. Relevant variations are present in the proximity of the primaries, Earth and Moon in the case considered.

$$\Delta E = -\frac{2\mu(1-\mu)}{v_p r_p} sin(\theta_{out}) sin(\beta) \tag{3.21}$$

where v_p is the velocity of the spacecraft at pericenter distance r_p with respect to the flyby body and θ_{out} is the true anomaly of the outgoing position at the SOI with the Moon. Note that by decreasing v_p we would enhance the flyby effect, suggesting that a flyby in the low-energy regime could be exploiting this phenomenon at its maximum. Numerical integration [20] also shows two important results: flyby events can be categorized into four categories depending on the energetic characteristics of the trajectories before and after the event and that there is a difference in the absolute energy variation generated by a prograde and retrograde flybys, the first ones being more effective than the latter.

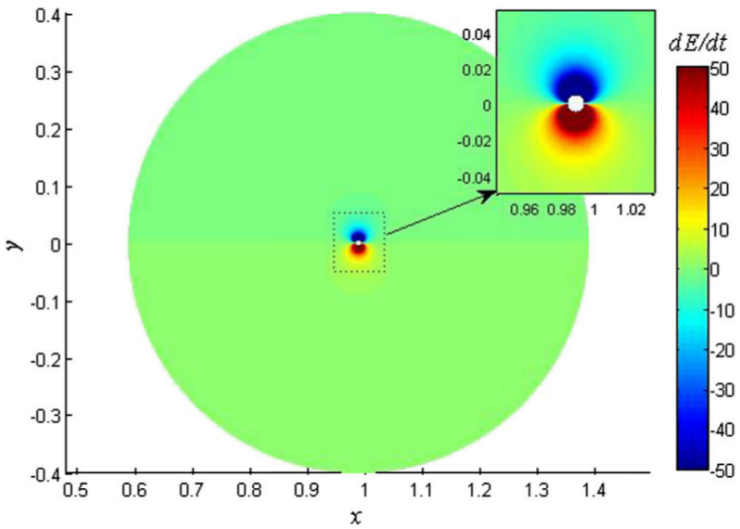

Figure 3.9: Distribution of $\frac{dE}{dt}$ in the vicinity of the Moon in the SB frame [20]. A passage ahead or behind the Moon (upper or lower region about the Moon) will correspond to a negative and positive energy variation respectively. This behavior was already described in the patched 2BP by Equation 3.18.

This result in particular has been highlighted already in [11], which identified the existence of two families of flybys called Type I or direct and Type II or retrograde in the planar CR3BP. In [11] it is argued that Type I flybys exist for all energy levels and are more efficient than type II flybys, whose existence is guaranteed only at high energy levels. Another difference between Type I and Type II is that in the latter case the spacecraft can access both sides of the flyby body. In this sense the work in [11] connects between the low-energy regime, where direct flybys can be approximated by a tool called Keplerian map, and the high-energy regime, where both direct and retrograde flybys are approximated by the patched 2BP as discussed before.

A detailed analysis of the flyby effects in the spatial CR3BP of the Sun-Jupiter and Earth-Moon systems will be presented in Chapter 8. This would be an addition to the body of science about the understanding of the flyby effect in a multi-body environment in the light of the new framework developed in this report.

Note that in this discussion, and for the rest of the report, the flyby will be treated purely from a gravitational point of view; non-gravitational perturbations will therefore be neglected.

3.4. SUN'S PERTURBATION EFFECTS

In the previous section the flyby effects have been described. These have been generated by the perturbing forces of the secondary disturbing the motion of the spacecraft about the primary. In this section the complementary situation will be discussed, as the perturbing forces generated by the primary disturbing the motion of the spacecraft about the secondary will be briefly analyzed. As the name of the section suggests the focus will be put on the Sun's perturbation effects.

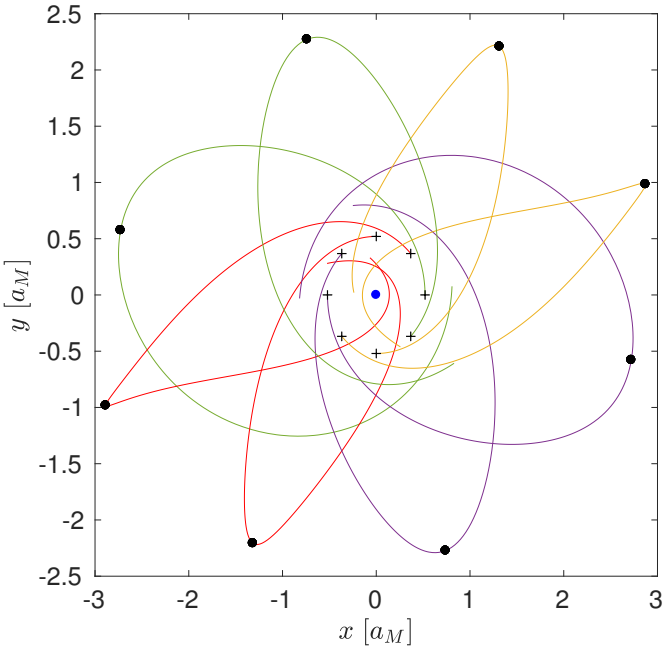

Figure 3.10: Example of the Sun's perturbing effects on eight trajectories propagated in the Sun-Earth CR3BP for about one orbital revolution from different initial points (+ symbols) at 200000 km from Earth (blue circle). The trajectories are represented in the $SP2$ frame of the Sun-Earth CR3BP, a value of $C = 3.00092$ has been used for the propagation. Four different colors categorize the trajectories depending on the quadrant of the apocenters (black dots) in this reference frame.

Sun's perturbing forces can play a fundamental role in providing free ΔV to a spacecraft. As seen in Chapter 2 this is a crucial aspect in the trajectory design of missions such as Hiten, ARTEMIS and EQUULEUS that exploit an exterior low-energy transfer. For the latter mission the desired aspects of a trajectory exploiting Sun's perturbation are extensively discussed in [9] through the usage of a graphical tool called the Extended

Tisserand-Poincaré graph that will be introduced in Section 3.7.3.

The key effects caused by the Sun's gravity are related to a change in the Keplerian energy and angular momentum with respect to the secondary body considered as main attractor. In a 2BP these quantities would be constant, however due to the third-body perturbations in the CR3BP they are not. This phenomenon is widely reported in literature for orbits in the same plane, most notably in [21]. To illustrate it eight different trajectories have been propagated in the Sun-Earth CR3BP from initial conditions at 200000 km from Earth. These trajectories are represented in Figure 3.10 in the $SP2$ frame about Earth, with axes expressed in Moon semi-major axis units. Two important effects can be seen from this figure: the trajectories seem to display a general symmetry with respect to the origin of the $SP2$ reference frame, these have drastically different behaviors depending on the position of the apogees. For example trajectories in the $I°$ and $III°$ quadrants reduce their perigees after an excursion away from the Earth-Moon system, trajectories in the $II°$ and $IV°$ quadrants express the opposite behavior. By inspecting the Keplerian energy E_2 and angular momentum H_2 with respect to Earth in Figure 3.11 their differences became even more clear. The derivation of the formulas used to compute E_2 and H_2 in the $SP2$ reference frame are provided in Appendix B.

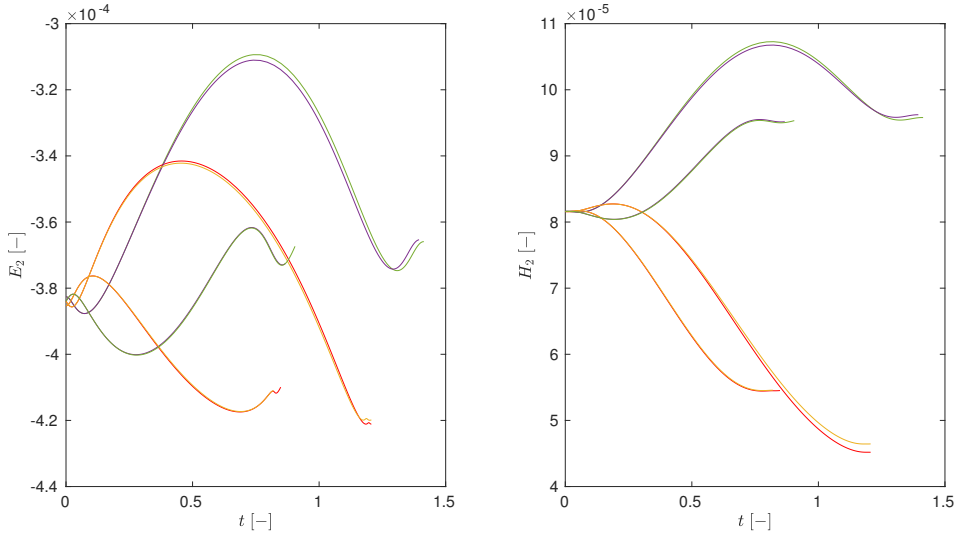

Figure 3.11: Representation of the variation of Keplerian energy E_2 (left) and angular momentum H_2 (right) of the eight trajectories illustrated in Figure 3.10, colors are corresponding.

Four global trends can be discerned in the variation of E_2 and H_2 illustrated in Figure 3.11. As it is possible to see from the colors these four trends are dependent on the quadrants and on the symmetry properties illustrated before. Trajectories in the $I°$ and $III°$ quadrants (respectively the orange and red ones) display an overall reduction of both E_2 and H_2, that correspond in a reduction of the perigee radii after one orbital revolution about Earth. On the contrary the trajectories in the $II°$ and $IV°$ quadrants (respectively the purple and green ones) display an overall increase of both E_2 and H_2, that correspond in an increase of the perigee radii after one orbital revolution about Earth. In Figure 3.11 it is possible to see a small difference between E_2 or H_2 for trajectories within the same group. This is due to the fact that in the CR3BP there is not an exact symmetric relation about P2, as is clear also from Figure 3.12.

The mechanism that is describing this phenomenon can be easily explained by looking at Figure 3.12. Four different trajectories are taken from Figure 3.10 and superimposed over a sketch of the combined gravitational and centrifugal forces in the Sun-Earth system, neglecting Earth influences for simplicity. These are represented by the black flux lines. The Sun is located on the far left region of the graph. The trajectories are assumed to be moving in counterclockwise direction. A trajectory with an apogee in the $I°$ or $III°$ quadrants will be generally experiencing a 'dragging' force that can be compared to a $\Delta V < 0$. On the contrary a trajectory in the $II°$ and $IV°$ quadrants will be experiencing a 'boosting' force that can be compared to a $\Delta V > 0$.

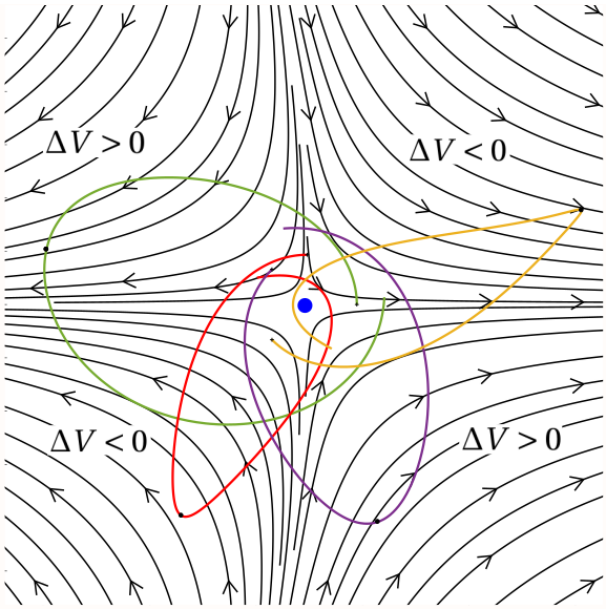

Figure 3.12: Sketch of the Sun's perturbing effect in the Sun-Earth CR3BP. The Sun is on the left part of the graph. All trajectories move in counterclockwise direction. The behavior in the four quadrants can be explained by the way the combined Sun and centrifugal forces act in the four quadrants of the $SP2$ frame.

Such ΔV is particularly effective also considering the amount of time that the spacecraft spends in the region perturbed by the combined Sun and centrifugal forces. Given the time it can significantly build up, causing the variations on E_2 and H_2 described before. In the case of a trajectory in the $I°$ or $III°$ quadrants the effects can be so profound to invert the motion of the spacecraft from prograde to retrograde.

To conclude, since this ΔV is generated from the multi-body dynamics of the system, it is essentially for free. The only major drawback lays on a bigger flight time associated with the trajectory excursion outside the vicinity of the Earth-Moon system. From this brief discussion it is clear why taking these effects actively into account in the trajectory design process can become a crucial aspect to save the overall ΔV of a mission.

3.5. DYNAMICAL SYSTEM THEORY

Dynamical System Theory (DST) is a mathematical theory that makes use of models based on differential equations in order to describe the behavior of complex dynamical systems. It has found a successful application for the qualitative analysis of the long-term behavior of dynamical systems [1]. In this section only the most fundamental concepts from DST used in the report are illustrated, the interested reader is referred to [22] for a more detailed discussion.

3.5.1. AUTONOMOUS AND NON-AUTONOMOUS SYSTEM

A system of first-order differential equations can be expressed in the following forms [22]:

$$\dot{\mathbf{x}} = \mathbf{f}(\mathbf{x}, t) \quad \text{or} \quad \dot{\mathbf{x}} = \mathbf{f}(\mathbf{x}) \tag{3.22}$$

$$\mathbf{x}(t_0) = \mathbf{x}_0 \tag{3.23}$$

where t is an independent variable representing time, $\mathbf{f}$ is a vector function, continuous in t and $\mathbf{x}$ such that $\mathbf{f}: G \to \mathbb{R}^n$ and G is an open subset of $\mathbb{R}^{n+1}$. $\mathbf{x}(t)$ represents a vector function that is the solution of the differential equation, if continuously differentiable, with $\mathbf{x} \in D \subset \mathbb{R}^n$.

If time is an explicit variable of the function **f**, then the system is called non-autonomous (the first form in Equation 3.22). If this is not the case the system is called autonomous (the second form of Equation 3.22).

Any n^{th}-order differential equation can be transformed in an n^{th}-order system of first-order differential equations as illustrated in Equation 3.22. By applying such a procedure to the equations of motion of the CR3BP and BR4BP, respectively Equations 3.9 and 3.15, two systems of six first-order differential equations can be written. By comparing them with Equation 3.22 these systems can be classified as autonomous and non-autonomous. The consequences of such a classification have already been discussed in Sections 3.2.2 and 3.2.3.

3.5.2. POINCARÉ MAP

The phase space can be defined as that subset $D \subset \mathbb{R}^n$ where the solution of the differential equation $\mathbf{x}(t)$ is defined. In such a space the behavior of the variables that compose the state $\mathbf{x}(t)$ that are parametrized by the independent variable t is described. By varying t a point moves in the phase space describing what is referred to as an orbit. For an autonomous system it is possible to demonstrate that orbits do not intersect in the phase space in finite time based on the existence and uniqueness theorem [22].

A Poincaré map is a powerful tool that provides insight into the dynamics of a system. It does that by providing a portrait of the phase space through the usage of a Poincaré section, a subspace of lower dimension $V \subset \mathbb{R}^{n-1}$. Such a section is transversal to the flow of the system, meaning that orbits do not intersect the section V tangentially.

The map is also referred to as first recurrence map if only the first intersections of the orbits emanating from the section V are recorded. In general if an orbit started from the point $\mathbf{x_0} \in V$ return to intersect V in the point $P(\mathbf{x_0}) \in V$, then the point is said to be mapped by P:

$$P : V \rightarrow V \tag{3.24}$$

The mapped point $P(\mathbf{x_0}) \in V$ found after mapping $\mathbf{x_0}$ can be mapped again. The second mapping is called $P^2(\mathbf{x_0})$ and so on for increasing orders. For the mapping procedure to be successful no critical points of the system must be considered by the Poincaré section.

Note that in this report the term map will be referred both to the mapping process defined by P in equation 3.24 and to the representation of the mapped points in a subset of the phase space. The latter serves as a discrete representation of a dynamical system, being one dimension smaller than the original system. Periodic and quasi-periodic orbits of the original system are enhanced in a Poincaré map, since many properties of these types of orbits are preserved in the mapping process. For this reason a Poincaré map is a fundamental tool to analyze a dynamical system in a simpler way. Poincaré maps will be extensively used in Chapter 6, alongside Poincaré sections defined in Section 4.5.

3.6. TISSERAND PARAMETER

The Tisserand parameter is a mathematical expression named after François Félix Tisserand, a 19th-century French astronomer. The formula first appeared in his work *Traité de mécanique céleste* [23] in 1896 as a derivation from the Jacobi integral in the CR3BP. Several alternative formulations exist in literature, but all of them are a rearrangement of the original formula. Amongst the most used ones there are:

$$T(a,e,i) = \frac{DU}{a} + 2\sqrt{\frac{a(1-e^2)}{DU}}cos(i) \tag{3.25}$$

$$T(a,e,i) = \frac{\mu_1}{a} + \frac{2}{TU}\sqrt{\mu_1 a\left(1-e^2\right)}cos(i) \tag{3.26}$$

where a is the semi-major axis, e is the eccentricity and i is the inclination of the trajectory. DU is the distance normalization parameter, while μ_1 is the primary mass parameter of the CR3BP in consideration. The difference between Equations 3.25 and 3.26 is a direct consequence of an assumption on the TU parameter

of the CR3BP and will be explained in detail in Section 4.2. Note that the inclination is referred to the inclination of the orbit with respect to the orbital plane of the primaries of the CR3BP taken into consideration. The parameter is often presented as a function of r_a and r_p instead of a and e if elliptic orbits are taken in consideration. The transformation is immediate by considering that $r_a = a(1+e)$ and $r_p = a(1-e)$, so that $a = \frac{r_a+r_p}{2}$ and $e = \frac{r_a-r_p}{r_a+r_p}$. By substituting these expressions into Equation 3.26 we obtain:

$$T(r_a, r_p, i) = \frac{2\mu_1}{r_a + r_p} + \frac{2}{TU}\sqrt{2\mu_1 \frac{r_a r_p}{r_a + r_p}} cos(i) \tag{3.27}$$

Other well-known alternative formulations of the Tisserand parameter are the one that shows the decomposition into Keplerian energy E_1 and angular momentum H_1 with respect to the primary and the one that shows the relationship with the hyperbolic excess velocity v_∞ [10] for high-energy levels:

$$T(E_1, H_1, i) = -2E_1 + \frac{2}{TU} H_1 cos(i) \tag{3.28}$$

$$T(v_\infty) = 3 - v_\infty^2 \tag{3.29}$$

The Tisserand parameter is derived from the CR3BP and it always refers to the primary of the system. The derivation of the classical parameter and of a new modified parameter that breaks this assumption will be illustrated in Chapter 4. These assumptions are:

- **The mass parameter μ of the CR3BP is small**: The distance of an object from the primary can be approximated as the distance from the barycenter and the secondary can be assumed to be moving in a circular orbit about the primary.
- **The object is considered far from the minor body**: its trajectory can be approximated in the 2BP as a Keplerian orbit about the primary as main attractor.

Whenever these assumptions are satisfied the Tisserand parameter can be used as a valid alternative to the Jacobi constant. In this sense the Tisserand parameter in certain cases is more practical than the Jacobi integral since it is depending only on three variables against the six necessary to evaluate the latter. Because of this reduction in complexity and relative simplicity the Parameter has found a large number of applications.

In the original consideration the parameter has been used in the Sun-Jupiter system to determine if possible comets disturbed by Jupiter's gravitational influence were objects already observed and cataloged. Since the comets orbit could have been heavily influenced by flyby effects with Jupiter, there was the necessity to determine if an observed comet was actually a perturbed one that was already discovered or was a new one. The Tisserand parameter could do that because of its property to remain approximately constant after a flyby, given the assumptions explained before. By comparing the Tisserand parameter of previously observed comets with the one of the 'new' one it was possible to determine if two objects were the same comet or no. The following comparison took the name of Tisserand criterion, because it involved the comparison between the parameters of two possibly different objects. The success of this application relies on the fact that during a flyby the orbital elements a,e,i are scrambled, but their combination into the Tisserand parameter returns the same value, that is conserved after the flyby.

Although it was originally applied to the Sun-Jupiter CR3BP, the parameter can be adapted to any CR3BP of interest, given that its assumptions are still valid. The parameter has found applications mainly in astrodynamics and astronomy, amongst them the most important ones [1]:

- In astronomy the Tisserand parameter considering Jupiter as perturbing body can be used to categorize bodies into families. For example it is used to distinguish between asteroids ($T > 3$), comets ($2 < T < 3$) and a group of minor planets called Damocloids ($T < 2$).
- In astronomy it is used to determine if an observed orbiting body is the same as one previously observed whose motion has been perturbed by swingby effects with a planet.
- In astrodynamics the conservation of the parameter can be used to constrain the achievable flyby effects.

The latter application will be discussed in detail in the next section.

3.7. TISSERAND GRAPH AND ITS VARIANTS

The usage of the parameter for astronomical applications has been particularly successful since the 19th century, however it was only until recent time that the parameter found another successful application in the design of multiple gravity assist (MGA) trajectories. By developing a graphical tool based on the parameter different techniques have been developed in the past 20 years to design trajectories in a multi-body dynamics environment. What follows is a brief discussion that would like to clarify the differences between some variants of this graphical technique and their evolution in time. The techniques that will be presented here are the Tisserand graph (T-graph), the Tisserand-Poincaré graph (TP-graph) and the Extended Tisserand-Poincaré graph (ETP-graph).

3.7.1. TISSERAND GRAPH

The Tisserand graph has been developed in [12][24] as a tool to compute first-guess MGA trajectories with the purpose to reduce the computational effort in the design process of interplanetary trajectories. The T-graph uses two parameters to characterize a Keplerian orbit about the main attractor. The reference dynamical model of the graph is in fact the planar case of the patched 2BP. The most used parameters have been r_a and r_p, as well as the orbital period and the specific energy E_1. The most well-known graphs presented in literature are therefore the $r_a - r_p$, Period$-r_p$ and $E_1 - r_p$ Tisserand graphs. The first one is being used with circular and elliptic orbits while the latter is defined also for hyperbolic and parabolic orbits. The key elements of a T-graph are the curves at constant Tisserand parameter, also referred to as Tisserand level sets.

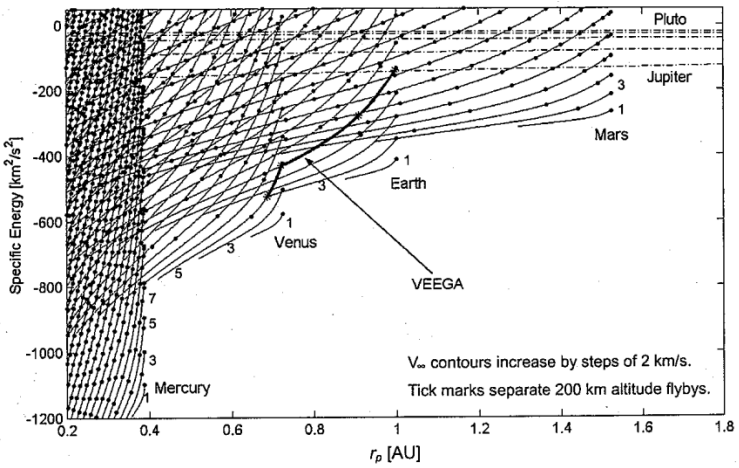

Figure 3.13: The $E_1 - r_p$ T-graph of the Solar System with a representation of the VEEGA sequence [12]. The level sets of the inner and some of the outer planets are represented. It is often preferred to show them in different graphs, as it is possible to see from the bad scaling of the contours of Jupiter and Pluto in the top part of the figure.

In the T-graph a Tisserand level set represents a contour line that contains orbits sharing the same Tisserand parameter. As it is possible to see from Equation 3.29 this corresponds also to the same escape velocity v_∞. Every point in the T-graph represents a Keplerian orbit about the main attractor. The flyby effects described in Section 3.3 are represented in a very simple way in the graph as a movement from one point to another, following a particular level. The movement itself is not causal, but it is constrained on the Tisserand level set and its magnitude is depending on a set flyby altitude. Thick points are often introduced to the graph to highlight the maximum excursion that is possible to achieve in a single flyby event due to such altitude limitation. When the level sets of different bodies intersect with each other a transfer opportunity opens, as the orbit in two different systems share the same energetic level. It is important to remind that this opportunity in reality is just potential, since it derives only from energetic considerations that do not take into account the phasing of the bodies. Nonetheless it can be used to constrain a flyby sequence from an energy-wise point of view. Figure 3.13 shows the $E_1 - r_p$ T-graph for the Solar System, with the contours of inner and some of the outer planets.

The T-graph so defined can be efficiently used to explore the search space for candidate flyby trajectories and most importantly to understand which are the best sequences of flyby planets. Such sequences are often constrained or chosen by some previous experience, they themselves are not a variable in the trajectory design process. The T-graph however offers a simple and inexpensive way to investigate them. Figure 3.14 shows the Venus-Earth-Earth Gravity Assist sequence (VEEGA) in the Period$-r_p$ T-graph. At launch the spacecraft is positioned on a relatively low energy contour (Earth, $v_\infty = 3$ km/s), however from the properties of this contour the trajectory can be easily patched through flyby maneuvers with higher energy contours of other bodies. A flyby with Venus and a double flyby with Earth shift the orbit upward first on a Venus contour (Venus, $v_\infty = 5$ km/s) and finally into an Earth one (Earth, $v_\infty = 9$ km/s) intersecting Jupiter (Jupiter, $v_\infty = 6$ km/s). In this case it is possible to see how efficient the Venus flyby is to move the spacecraft from the 3 to 9 km/s contour with respect to Earth, allowing a much lower escape velocity than the one originally needed to reach Jupiter.

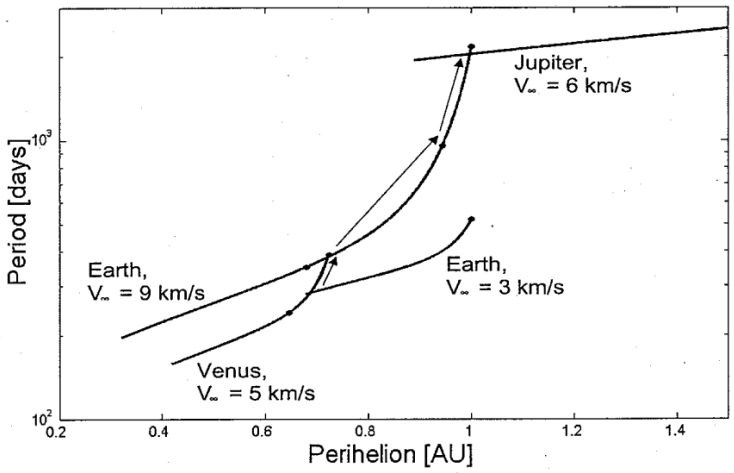

Figure 3.14: Representation of a VEEGA trajectory in a Period$-r_p$ T-graph [12]. A number of Tisserand level sets of Earth, Venus and Jupiter are represented at different v_∞. By looking at the flyby sequence in the graph it is easy to understand the mechanism behind it from an energy perspective.

The design process envisioned in [12] for MGA trajectories in the Solar System is made by two parts called finding and solving. In the finding step first-guess trajectories are generated by the application of an algorithmic search on the graph. The purpose of this phase is to identify the most promising sequences of flyby planets to use, pruning them on the basis of energy considerations only. The contour intersections are discretized and constitute a network of nodes at different energy levels. The network is traversed from an initial set of nodes close to the launch condition to the final condition. Only trajectories satisfying a criterion based on the estimated time of flight are taken into consideration as first-guess trajectories for the next step, the solving phase. In this step the first-guess trajectories are propagated and optimized in a higher-fidelity dynamical model. This step is necessary to produce a realistic nominal trajectory.

3.7.2. TISSERAND-POINCARÉ GRAPH

The TP-graph is a natural extension of the T-graph that has been designed in [25][10]. While the T-graph uses the patched 2BP, the TP-graph reference dynamical model is the patched CR3BP. The graph is built by plotting the osculating orbital elements of points intersecting a Poincaré section defined in a planar CR3BP in the $r_a - r_p$ graph together with the Tisserand level sets. The Poincaré section chosen in [10] is the negative x-axis of the SP1 frame and is chosen to take osculating orbital elements of trajectories that are far from the secondary and can therefore be approximated as Keplerian orbits with respect to the primary.

Since patched CR3BP models are used in the TP-graph, the Tisserand level sets can extend well beyond the region in which v_∞^2 is defined in the patched 2BP. For example the sets for which $T > 3$, that would be characterized by $v_\infty^2 < 0$ (physically inconsistent) in the 2BP assumption, become accessible regions of the graph in the CR3BP model. With this fundamental property [10] successfully demonstrated the potential of the technique for applications in the low-energy regime. An important result presented in [10] is that with the

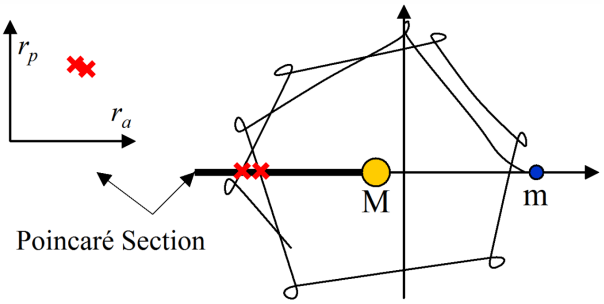

Figure 3.15: Schematic of how points in the TP-graph are drawn from a Poincaré section on the negative x-axis of the SP1 reference frame [10].

TP-graph it is possible to see that ballistic transfers between the moons of Jupiter are possible from an energetic point of view in the low-energy regime. The opposite conclusion could have not been derived by the usage of a patched 2BP and associated T-graph.

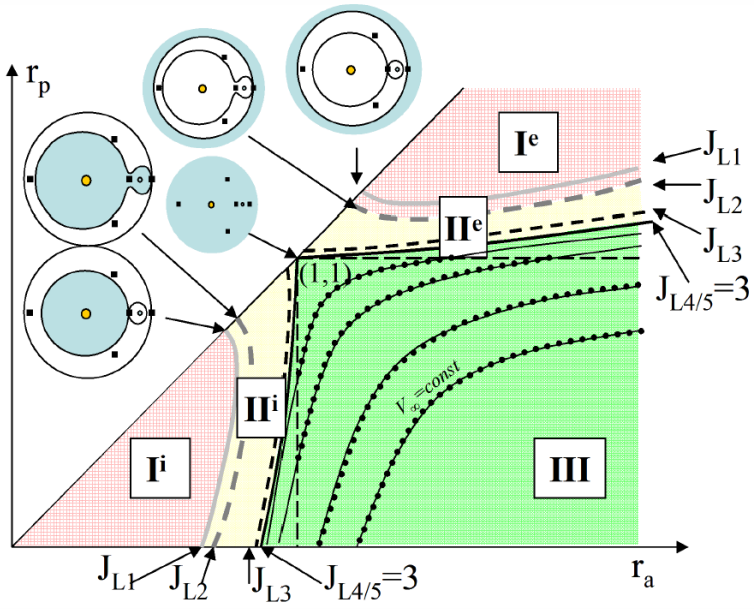

Figure 3.16: TP-graph with associated regions of motion in the CR3BP [10]. I^i and I^e are regions that do not allow a transfer trajectory to the secondary. II^i and II^e allow such a transfer from the primary or from the exterior region. In the region III the entire space is accessible to the spacecraft.

The anatomy of the TP-graph is illustrated in Figure 3.16. The Tisserand level sets represented have been computed by applying Equation 3.25 in the planar and prograde case ($i = 0°$). Several level sets are depicted, however the most important are the ones associated to the Jacobi constant C of the Lagrange libration points ($C_{L1}, C_{L2}, C_{L3}, C_{L4/L5}$ introduced in Section 3.2.2). These sets divide the TP-graph into regions that are accessible or not depending on the configuration of the Hill's surfaces associated to that energy levels. In [10] three regions are characterized from the perspective of a transfer trajectory between secondaries of different CR3BP models. Region I is delimited on the lower part of the graph by C_{L1} and on the upper part by C_{L2}. From the associated ZVC it is possible to see that a point taken in these regions would not be able to reach the secondary with a ballistic trajectory as it will be confined in a region about the primary (I^i) or in a region outside the system due to the closure of the $L2$ neck (I^e). Region II is delimited from region I to $C_{L4/L5}$, in this case the secondary is accessible from the inner region (II^i) with the $L1$ neck open (even with the $L2$ neck closed) or from the outer region with an open $L2$ neck (II^e). Lastly in region III any point can energetically

access the secondary. A subregion of III is given by the conditions $r_p < 1$ and $r_a > 1$. This subregion represents the original portion of the graph that can be represented by the T-graph. It is therefore immediate to understand that the extension of the TP-graph by using a CR3BP model has unlocked the possibility to reach very high apocenters also with low v_∞. This capability is at the basis of the low-energy transfer technique.

To design transfers between Europa and Ganymede, where the multi-body dynamics is relevant, a patched CR3BP approach is developed in [10] that makes use of the TP-graph. The trajectory is divided into phases where only one minor body at a time affects the motion of the spacecraft as the secondary, while the primary (Jupiter) does not change. A search-grid is performed by propagating forward and backward in time from different points on the initial and final orbits about Europa and Ganymede in the different CR3BP models with fixed values of C. The intersection states on the Poincaré section are recorded (as well as their epochs) and represented in the TP-graph. The patching between trajectories in the Jupiter-Europa and Jupiter-Ganymede CR3BP is performed in the graph. In this sense the graph is important because it easily displays different CR3BP systems at different values of Jacobi constant C, showing at which orbital elements a patching between two systems can be executed in a ballistic way. In this example the TP-graph has been used as a simple patching technique between different CR3BP's that share the same primary body. However in this case numerical propagation was necessary to compute trajectories in the CR3BP that can be much more complex than a conic-shaped Keplerian orbit.

3.7.3. EXTENDED TISSERAND-POINCARÉ GRAPH

The ETP-graph is a natural extension of the TP-graph proposed in [9] in order to include in a qualitative analysis the Sun's perturbation effects into the TP-graph. The latter graph considers CR3BP systems that share the same primary but have different secondaries such as the Jupiter-Europa-Ganymede or the Sun-Earth-Jupiter and so forth. The reason for this constraint relies on a fundamental limitation of the Tisserand parameter introduced in Section 3.6: The Tisserand parameter is defined about the primary and it is only in the vicinity of the primary that it possesses its constancy property.

One of the categorical assumptions for its derivation was to consider the parameter only far from the secondary. In literature this has been put into practice by taking into account the region outside the SOI of the secondary [12] or the negative x-axis of the $SP1$ reference frame [10]. When considering the Sun-Earth-Moon system a fundamental problem arises: the two CR3BP's do not share the same primary, indeed they share the same body (Earth) once as a primary (Earth-Moon CR3BP) and once as a secondary (Sun-Earth CR3BP). For this reason the Tisserand parameter has not found an application for these type of systems. In Chapter 4 a modified parameter that overcomes this limitation is derived. In this section the state of the art of the ETP-graph is discussed.

Given this crucial obstacle the analysis performed in [9] is just qualitative, because it simply assesses the potential effects of Sun's perturbing forces into the ETP-graph of the Earth-Moon system to investigate upon their usage for the EQUULEUS and DESTINY missions. Nonetheless the addition of the Sun's perturbations can justify the new naming of the graph as Extended TP-graph or ETP-graph. Two different approaches are investigated in [9]: an analytical and a numerical one. The analytical approximation takes into consideration Gauss form of the Lagrange planetary equations and uses the Sun's third-body attraction as perturbing force. By integrating the differential form of the instantaneous change of a and e over one revolution it is possible to estimate the discrete variations Δa and Δe assuming small variations with respect to an unperturbed trajectory [9]:

$$\Delta a \approx 0 \tag{3.30}$$

$$\Delta e = \frac{15\pi}{2\mu} a^3 e \sqrt{1-e^2}\, sin2\left(\omega_p - \theta\right) \tag{3.31}$$

where the angle θ is half the rotation of the apsis line in the synodic reference frame along the orbit and the term $\omega_p - \theta$ can be considered as a representative argument of pericenter. The complete analysis is presented in [9] and will not be reproduced here. Two important results are already visible from Equations 3.30 and 3.31. First, that the effects of Sun's perturbing force are Sun-kicks acting on the ETP-graph as lines of

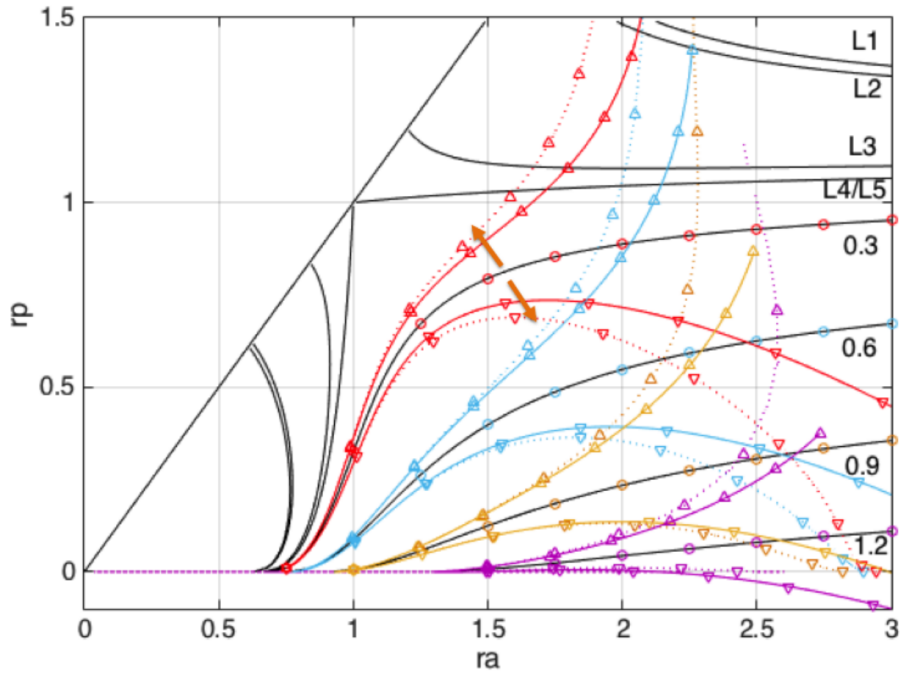

Figure 3.17: Effect of the Sun's perturbations in the ETP-graph of the Earth-Moon system described by an analytical approximation (continuous lines) and numerical analysis (dashed lines) [9]. Axes are expressed in Moon semi-major axis units. By taking points on the Tisserand level sets and performing the analytical and numerical analysis, the effect of the Sun's perturbations is estimated for one orbital revolution. Triangle symbols are introduced to facilitate the analysis for specific points on the graph. The Tisserand level sets for the Lagrange points and for different cases of v_∞ are illustrated in the ETP-graph. In the latter case the values are represented on the right part of the graph (0.3, 0.6, 0.9 and 1.2).

slope -1, since from Equation 3.30 it holds that $\Delta r_p = -\Delta r_a$. Second, from Equation 3.31 it is possible to see a sinusoidal term that depends on two times the average argument of pericenter $(\omega_p - \theta)$. This term is the one that explains the quadrant behavior of Sun's perturbation effects already described in detail in Section 3.4. The applicability of the results from this analytic approximation however can be put into question due to the fact that the integrations of the equation to obtain Δa and Δe has been done assuming constant orbital elements over one revolution and small variations with respect to the unperturbed trajectories. As underlined in [9] this is not really applicable in this case. To compute the achievable maximum deviation a numerical technique that makes use of a small optimization procedure considering the argument of pericenter as optimization variable is performed in [9]. The overall effects of these analyses can be seen in Figure 3.17.

As explained in Section 3.4 and as clearly illustrated in Figure 3.17, the effects of Sun perturbations will play a crucial role in providing free kicks on the trajectories of both EQUULEUS and DESTINY. From Figure 3.17 it is possible to see that for apogees above 1.2 Moon semi-major axis these effects start to play a crucial rule [9].

4

TISSERAND PARAMETERS

In this chapter the derivation of the classical Tisserand parameter introduced in Chapter 4 will be presented together with the derivation of a modified Tisserand parameter. The classical Tisserand parameter will be refereed to the expressions introduced in Section 3.6 that describe a parameter about the primary of the system. The modified parameter derived in this chapter however will be defined about the secondary of the system, hence the distinction between the two parameters.

In Section 4.1 the Jacobi integral will be expressed in a generic inertial P_i centered reference frame. This will be the starting point to derive both the classical and the modified Tisserand parameters. The derivations of these parameters are illustrated in Sections 4.2 and 4.3 respectively. A comparison between the two parameters is illustrated for a trajectory in the Earth-Moon system in Section 4.4. In Section 4.5 a class of Poincaré sections that can be used in the TP-graph is characterized. Amongst these the specific Poincaré sections that will be used throughout the report are defined. Finally Section 4.6 concludes the discussion with the main findings in the chapter. Appendix will summarize the main expressions derived in this chapter. Note that the mathematical derivations will heavily rely on the notation introduced in Section 3.2.2.

4.1. JACOBI INTEGRAL'S TRANSFORMATIONS

The expression of the Jacobi integral in the SB frame (Equation 3.10)is well known in literature, it is however of little use when working in other frames. When this is the case it is necessary to perform a series of transformations to express the state of the spacecraft in the SB frame in order to proceed with the evaluation of the Jacobi integral. However since in this report the SB frame will rarely be used, a different approach is adopted. Instead of transforming the states, the integral will be transformed to be expressed in coordinates of other frames. The notation used here will be the same as introduced in Section 3.2.2, so for example the integral expressed in coordinates of the $SP1D$ frame will be referred to as J_{SP1D} in short or $J(\mathbf{X}_{SP1D})$ in full.

In this section a general expression of the Jacobi integral in different frames will be presented in a parametric form depending on the position of the frame's origin. For what concerns the derivation of the Tisserand parameters we are interested to express J_{IP1D} and J_{IP2D}. The transformations involved to pass from SB to the generic IP_iD frame are now presented separated in three different steps: from SB to SP_i, then to IP_i, and finally to IP_iD.

4.1.1. FROM J_{SB} TO J_{SP_i}

Let us first consider the expression of the Jacobi integral in the SB frame already presented in Equation 3.10 and repeated here for better understanding:

$$J_{SB} = \frac{2(1-\mu)}{r_1} + \frac{2\mu}{r_2} + \left(x^2+y^2\right) - \left(\dot{x}^2+\dot{y}^2+\dot{z}^2\right) + \mu(1-\mu) \tag{4.1}$$

where r_1 and r_2 are the distances of the point P from the primaries and $\mathbf{X}_{SB} = [x\ y\ z\ \dot{x}\ \dot{y}\ \dot{z}]^T$ is the state in the SB frame.

To express this integral as a function of the state in the SP_i frame a coordinate transformation as the one presented in Equation 3.5 needs to be performed. To simplify the analysis while keeping it always generic the translation from barycenter to the generic point P_i is done assuming such a point to be positioned on the x-axis, such that its coordinates are $(d,0,0)$ in the SB frame. Since the barycenter, primaries and the collinear points lay on this axis, the assumption does not represent a limitation for the cases of interest. By using Equation 3.5 the state can be transformed from SP_i to SB and vice versa:

$$\mathbf{X}_{SB} = \mathbf{X}_{SP_i} + \begin{bmatrix} d \\ 0 \\ 0 \\ 0 \\ 0 \\ 0 \end{bmatrix} \tag{4.2}$$

Applying this transformations to the elements of the integral expressed by Equation 4.1 we can write:

$$\begin{aligned} (x^2+y^2)_{SB} &= (x+d)^2 + (y)^2 \\ &= (x^2+y^2) + d^2 + 2xd \end{aligned} \tag{4.3}$$

$$(\dot{x}^2+\dot{y}^2+\dot{z}^2)_{SB} = (\dot{x}^2+\dot{y}^2+\dot{z}^2) \tag{4.4}$$

where the left-hand side of these equations are intended in the SB frame while the right-hand ones are expressed in the SP_i frame. Since r_1 and r_2 are relative distances from the primaries they will not be transformed until the very end to not further complicate the analysis. By substituting these terms into Equation 4.1 we can write the Jacobi integral expressed as a function of the state in the SP_i frame as:

$$J_{SP_i} = 2\frac{1-\mu}{r_1} + 2\frac{\mu}{r_2} + (x^2+y^2) - (\dot{x}^2+\dot{y}^2+\dot{z}^2) + 2xd + d^2 + \mu(1-\mu) \tag{4.5}$$

where $\mathbf{X}_{SP_i} = [x\ y\ z\ \dot{x}\ \dot{y}\ \dot{z}]^T$ is now the state of the point P in the SP_i frame.

4.1.2. FROM J_{SP_i} TO J_{IP_i}

The state is now transformed to be expressed in the inertial frame IP_i. In order to do that the transformation matrix T_{I2S} in Equation 3.7 is used to express the synodic state as a function of the inertial one. The transformation can be written in short notation as $\mathbf{X}_{SP_i} = T_{I2S}\mathbf{X}_{IP_i}$ or component-by-component as:

$$\begin{cases} x_{SPi} = xcos\theta + ysin\theta \\ y_{SPi} = -xsin\theta + ycos\theta \\ z_{SPi} = z \\ \dot{x}_{SPi} = (\dot{y}-x)\,sin\theta + (y+\dot{x})\,cos\theta \\ \dot{y}_{SPi} = (\dot{y}-x)\,cos\theta - (y+\dot{x})\,sin\theta \\ \dot{z}_{SPi} = \dot{z} \end{cases} \tag{4.6}$$

Note that the state $\mathbf{X}_{IP_i} = [x\ y\ z\ \dot{x}\ \dot{y}\ \dot{z}]^T$ is now the one expressed on the right-hand side of the equations, that is the arrival state of the transformation. It follows that the following terms of Equation 4.5 can be transformed:

$$\begin{aligned} (x^2+y^2)_{SP_i} &= (xcos\theta + ysin\theta)^2 + (-xsin\theta + ycos\theta)^2 \\ &= x^2cos^2\theta + y^2sin^2\theta + 2xycos\theta sin\theta + x^2sin^2\theta + y^2cos^2\theta - 2xycos\theta sin\theta \\ &= x^2 + y^2 \end{aligned} \tag{4.7}$$

$$\begin{aligned}(\dot{x}^2+\dot{y}^2+\dot{z}^2)_{SP_i} &= (\dot{y}-x)^2 sin^2\theta + (y+\dot{x})^2 cos^2\theta + 2(\dot{y}-x)(\dot{x}+y) sin\theta cos\theta + ... \\ &+ (\dot{y}-x)^2 cos^2\theta + (y+\dot{x})^2 sin^2\theta - 2(\dot{y}-x)(\dot{x}+y) sin\theta cos\theta + ... \\ &+ \dot{z}^2 \\ &= (\dot{x}^2+\dot{y}^2+\dot{z}^2) + (y^2+x^2) + 2(y\dot{x}-\dot{y}x)\end{aligned} \tag{4.8}$$

Note that since the distance from the origin is the same in the two frames, the first transformation does not introduce new terms. As expected by substituting these expressions into the Jacobi integral in Equation 4.5, we obtain the Jacobi integral as a function of the state in the IP_i frame:

$$J\left(\mathbf{X}_{IP_i},\theta\right) = 2\frac{1-\mu}{r_1} + 2\frac{\mu}{r_2} + 2\left(x\dot{y}-y\dot{x}\right) - (\dot{x}^2+\dot{y}^2+\dot{z}^2) + 2d\left(xcos\theta + ysin\theta\right) + d^2 + \mu(1-\mu) \tag{4.9}$$

Note that this time the integral is also a function of the angle θ, that is the angle between the synodic and inertial frames at the time of the transformation. This is an important effect as this angle is often used with an abuse of notation in literature as the time variable of the system, thus transforming the integral also into a function of time.

4.1.3. FROM J_{IP_i} TO J_{IP_iD}

The last step is the dimensionalization of the normalized quantities that appear in the integral. A generic CR3BP can be specified by the choice of the mass parameter μ and then be dimensionalized by the usage of three parameters: DU,VU and TU. These are often taken from tables but depending on the assumptions made to obtain them different numerical errors might be introduced, as all the variables that define the CR3BP have specific relations with each other. In order to avoid committing these errors in this report a CR3BP system is defined by three parameters:

$$DU \quad \mu_1 \quad \mu \tag{4.10}$$

where DU is the distance between the primaries expressed in m, μ_1 is the gravitational parameter of the primary expressed in m^3/s^2 and μ is the mass parameter of the system. The latter is related to the mass of the primaries of the system as follow:

$$\frac{\mu_1}{\mu_1+\mu_2} = 1-\mu \quad \text{and} \quad \frac{\mu_2}{\mu_1+\mu_2} = \mu \tag{4.11}$$

where μ_2 is the gravitational parameter of the secondary. From these equations and from the fact that the primaries move in circular orbits about the barycenter of the system, the following set of relations can be derived:

$$\mu_2 = \mu_1\frac{\mu}{1-\mu} \quad \text{and} \quad TU = \sqrt{\frac{DU^3}{\mu_1+\mu_2}} \quad \text{and} \quad VU = \frac{DU}{TU} \tag{4.12}$$

From these relations it is possible to see that by choosing a set of DU, μ_1 and μ, the corresponding VU,TU and μ_2 of the system can be derived. As said before this is preferred to the practice of defining DU,TU and VU upfront and can help avoiding numerical errors. By applying these relationships each term of the Jacobi integral in Equation 4.9 is analyzed:

$$\left(2\frac{1-\mu}{r_1}\right)_{ad} = 2\frac{\mu_1}{r_1}\frac{DU}{\mu_1+\mu_2} \tag{4.13}$$

$$\left(2\frac{\mu}{r_2}\right)_{ad} = 2\frac{\mu_2}{r_2}\frac{DU}{\mu_1+\mu_2} \tag{4.14}$$

$$\left(2\left(x\dot{y}-y\dot{x}\right)\right)_{ad} = 2\frac{1}{DUVU}\left(x\dot{y}-y\dot{x}\right) \tag{4.15}$$

$$\left(\dot{x}^2+\dot{y}^2+\dot{z}^2\right)_{ad} = \frac{1}{VU^2}\left(\dot{x}^2+\dot{y}^2+\dot{z}^2\right) \tag{4.16}$$

$$\left(2d\left(xcos\theta+ysin\theta\right)\right)_{ad} = 2\frac{d}{DU^2}\left(xcos\theta+ysin\theta\right) \tag{4.17}$$

$$\left(d^2\right)_{ad} = \frac{d^2}{DU^2} \tag{4.18}$$

$$\left(\mu\left(1-\mu\right)\right)_{ad} = \frac{\mu_1\mu_2}{\left(\mu_1+\mu_2\right)^2} \tag{4.19}$$

Both the left and right-hand sides of these equations are in adimensional units. However the combination of normalization parameters that make these expressions adimensional (ad) is exposed on the right-hand side of the equations. The integral J_{IP_i} can be transformed with these normalization parameters as:

$$\begin{aligned} J^*\left(\mathbf{X_{IP_iD}},\theta\right) =& 2\frac{\mu_1}{r_1}\frac{DU}{\mu_1+\mu_2} + 2\frac{\mu_2}{r_2}\frac{DU}{\mu_1+\mu_2} + 2\frac{1}{DUVU}\left(x\dot{y}-y\dot{x}\right) - \frac{1}{VU^2}\left(\dot{x}^2+\dot{y}^2+\dot{z}^2\right) + \\ &+ 2\frac{d}{DU^2}\left(xcos\theta + ysin\theta\right) + \frac{d^2}{DU^2} + \frac{\mu_1\mu_2}{\left(\mu_1+\mu_2\right)^2} \end{aligned} \tag{4.20}$$

where the state $\mathbf{X}_{IP_iD} = [x\ y\ z\ \dot{x}\ \dot{y}\ \dot{z}]^T$ and the parameter d are expressed in dimensional units. Because this integral is expressed as a function of the state in dimensional units but with the normalization parameters into it, the integral evaluation (the Jacobi constant) is still adimensional, hence the symbol * is used. To make it dimensional it is necessary to multiply $J^*_{IP_iD}$ by VU^2. By using Equations 4.11 and 4.12 this term can be written as:

$$VU^2 = \frac{DU^2}{TU^2} = \frac{\mu_1+\mu_2}{DU} \tag{4.21}$$

by multiplying it on the right-hand side of $J^*_{IP_iD}$ it is possible to obtain the final expression of the Jacobi integral in dimensional units:

$$\begin{aligned} J\left(\mathbf{X_{IP_iD}},\theta\right) =& 2\frac{\mu_1}{r_1} + 2\frac{\mu_2}{r_2} + 2\frac{1}{TU}\left(x\dot{y}-y\dot{x}\right) - \left(\dot{x}^2+\dot{y}^2+\dot{z}^2\right) + \\ &+ 2\frac{d}{TU^2}\left(xcos\theta + ysin\theta\right) + \frac{d^2}{TU^2} + VU^2\frac{\mu_1\mu_2}{\left(\mu_1+\mu_2\right)^2} \end{aligned} \tag{4.22}$$

We now possess the general expression of the Jacobi integral in the IP_iD frame centered on a point P_i. By specifying its position on the x-axis of the SB frame this general formula can be adapted to any specific case of interest. By moving P_i on the primaries it is very simple to obtain J_{IP1D} and J_{IP2D}. These will represent the starting points for the derivations illustrated in Sections 4.2 and 4.3.

4.1.4. SUMMARY

The generic equations of the Jacobi integrals dependent on the states expressed in different frames are briefly summarized here. Although these integrals are rarely found in literature, they will be widely used in this report and for this reason they are represented here for clarity:

$$\begin{cases} J_{SP_i} = 2\dfrac{1-\mu}{r_1} + 2\dfrac{\mu}{r_2} + (x^2+y^2) - (\dot{x}^2+\dot{y}^2+\dot{z}^2) + 2xd + d^2 + \mu\left(1-\mu\right) \\ J_{IP_i} = 2\dfrac{1-\mu}{r_1} + 2\dfrac{\mu}{r_2} + 2\left(x\dot{y}-y\dot{x}\right) - (\dot{x}^2+\dot{y}^2+\dot{z}^2) + 2d\left(xcos\theta+ysin\theta\right) + d^2 + \mu(1-\mu) \\ J_{IP_iD} = 2\dfrac{\mu_1}{r_1} + 2\dfrac{\mu_2}{r_2} + 2\dfrac{1}{TU}\left(x\dot{y}-y\dot{x}\right) - \left(\dot{x}^2+\dot{y}^2+\dot{z}^2\right) + 2\dfrac{d}{TU^2}\left(xcos\theta+ysin\theta\right) + \dfrac{d^2}{TU^2} + VU^2\dfrac{\mu_1\mu_2}{\left(\mu_1+\mu_2\right)^2} \end{cases} \tag{4.23}$$

where the components of the states are expressed in SP_i,IP_i and IP_iD frames respectively. The parametric distance of the point $P_i = (d,0,0)$ is expressed in normalized units in the SB frame in the first two equations while it is expressed in dimensional units in the SBD frame in the latter equation.

4.2. CLASSICAL TISSERAND PARAMETER

The parameters introduced in Section 3.6 by Equations 3.25 to 3.29 are classified as different versions of the classical Tisserand parameter. In this section the derivation of such a parameter will be discussed in detail.

4.2.1. DERIVATION

As explained in Section 3.6 the Tisserand parameter is an approximation of the Jacobi constant that derives from the CR3BP formulation. The starting point of its derivation is therefore the Jacobi integral expressed in the $IP1D$ frame. The integral J_{IP1D} can be easily obtained by substituting the position of the primary as point P_i in Equation 4.22. The substitution is performed by setting $d = -\mu DU$ in this expression. The terms affected by this parameter are $\frac{d}{TU^2}$ and $\frac{d^2}{TU^2}$, by considering Equations 4.11 and 4.12 they can be written as:

$$\begin{aligned}\frac{d}{TU^2} &= \frac{-\mu DU}{TU^2} \\ &= -\frac{\mu DU}{\frac{DU^3}{\mu_1+\mu_2}} \\ &= -\frac{\mu_2}{\mu_1+\mu_2}\frac{\mu_1+\mu_2}{DU^2} \\ &= -\frac{\mu_2}{DU^2}\end{aligned} \tag{4.24}$$

$$\begin{aligned}\frac{d^2}{TU^2} &= \frac{\mu_2}{DU^2}\mu DU \\ &= \frac{\mu_2}{DU}\frac{\mu_2}{\mu_1+\mu_2} \\ &= \frac{\mu_2^2}{DU\frac{DU^3}{TU^2}} \\ &= \frac{\mu_2^2}{DU^2VU^2}\end{aligned} \tag{4.25}$$

By substituting these expressions into Equation 4.22 the Jacobi integral J_{IP1D} can be expressed as:

$$J(\mathbf{X_{IP1D}},\theta) = 2\frac{\mu_1}{r_1} + 2\frac{\mu_2}{r_2} + 2\frac{1}{TU}\left(x\dot{y} - y\dot{x}\right) - V^2 - 2\frac{\mu_2}{DU^2}\left(xcos\theta + ysin\theta\right) + \frac{\mu_2^2}{DU^2VU^2} + VU^2\frac{\mu_1\mu_2}{\left(\mu_1+\mu_2\right)^2} \tag{4.26}$$

where V is the velocity of the spacecraft $V = \sqrt{\dot{x}^2+\dot{y}^2+\dot{z}^2}$ in this frame. The aim of the derivation is to decompose this integral into two different functions. The first one will be the Tisserand parameter and it will be depending on a combination of osculating orbital elements or properties of Keplerian orbits. The second one will be a residual function depending on the position of the spacecraft. The fact that this residual function is small in a region of space far from the secondary will justify the classical Tisserand parameter being a good approximation of the Jacobi constant under certain assumptions, as expressed in Section 3.6. As explained in that section the whole derivation is based on two fundamental assumptions, the first of which is that:

1. **A region of space is considered where the primary acts as the main attractor.**

This condition derives from the necessity to define the osculating orbital elements with respect to the primary and is often expressed by considering the spacecraft far from the secondary. In [25][10][11] this is put into practice by considering the negative x-axis of the $SP1$ frame, while in [12] it is simply not contemplated in the patched 2BP approximation since the spacecraft is influenced by a single main attractor at a time. The assumption to be able to express the orbital elements of an osculating Keplerian orbit will make it possible to use the vis-viva and angular momentum equations. From the equations in Appendix B these can be written as:

$$2E_1 = V^2 - \frac{2\mu_1}{r_1} = -\frac{\mu_1}{a} \tag{4.27}$$

$$(H_1)_z = H_1 cos(i) = \sqrt{\mu_1 a\left(1-e^2\right)} cos(i) = x\dot{y} - y\dot{x} \tag{4.28}$$

assuming the state to be expressed in the $IP1D$ frame as $\mathbf{X}_{IP1D} = [x\ y\ z\ \dot{x}\ \dot{y}\ \dot{z}]^T$. Note that the z-component of the angular momentum is considered for the derivation. a,e,i are the osculating semi-major axis, eccentricity and inclination of the trajectory with respect to the primary. The inclination is computed with respect to the $P1P2$ orbital plane. By substituting these expressions into Equation 4.26 we obtain:

$$\begin{aligned} J_{IP1D}(\mathbf{X_{IP1D}}, \theta) &= -2E_1 + 2\frac{\mu_2}{r_2} + 2\frac{1}{TU} H_1 cos(i) - 2\frac{\mu_2}{DU^2}\left(xcos\theta + ysin\theta\right) + \frac{\mu_2^2}{DU^2 VU^2} + VU^2 \frac{\mu_1\mu_2}{\left(\mu_1+\mu_2\right)^2} \\ &= \left[-2E_1 + 2\tfrac{1}{TU} H_1 cos(i)\right] + \left[2\tfrac{\mu_2}{r_2} - 2\tfrac{\mu_2}{DU^2}\left(xcos\theta + ysin\theta\right) + \tfrac{\mu_2^2}{DU^2 VU^2} + VU^2 \tfrac{\mu_1\mu_2}{\left(\mu_1+\mu_2\right)^2}\right] \end{aligned} \tag{4.29}$$

Already at this stage it is possible to observe a decomposition of the Jacobi integral into two functions. The reader will recognize the first term to be the Tisserand parameter expressed in Equation 3.28 while the second term is a residual function only depending on the position of the spacecraft in $IP1D$ and the angle θ. The reader can also recognize that the term $\left(xcos\theta + ysin\theta\right)$ in $IP1D$ frame is indeed the x-component in the $SP1$ frame, as is possible to see from Equation 4.6. The term in the first square brackets cannot be considered the Tisserand parameter yet, as it has not been demonstrated that the second square brackets is a small quantity far from the secondary.

The derivation can now follow two different paths that will lead to slightly different formulations. This depends whether or not an approximation on the TU parameter is adopted. The TU parameter can be written from Equation 4.12 as:

$$TU = \sqrt{\frac{DU^3}{\mu_1+\mu_2}} = \sqrt{\frac{DU^3}{\mu_1}} \frac{1}{\sqrt{1+\frac{\mu_2}{\mu_1}}} \tag{4.30}$$

Since $\mu_1 >> \mu_2$ it is possible to see that there is room for approximations that will simplify the general expression of the parameter. Both the approximated and non-approximated cases will be now briefly discussed.

APPROXIMATION ON TU

From Equation 4.30 it is possible to see that assuming $x = \frac{\mu_2}{\mu_1}$ and since $\mu_1 >> \mu_2$ for the systems considered in engineering applications, a series expansion at $x = 0$ can be used to approximate the term $\frac{1}{\sqrt{1+x}}$ as :

$$\frac{1}{\sqrt{1+x}} = 1 - \frac{x}{2} + \frac{3x^2}{8} - \frac{5x^3}{16} + \frac{35x^4}{128} + O(x^5) \tag{4.31}$$

here expressed up to the 4th order. It is a common practice in literature to stop at the first order [10][1] of the series expansion. Such practice translates into the following assumption in the derivation:

2. **The mass parameter μ of the CR3BP is small.**

As a consequence the distance of the spacecraft to the primary can be approximated as the distance to the barycenter of the system and the secondary can be assumed to be moving in a circular orbit about the primary. By assuming $TU \approx \sqrt{\frac{DU^3}{\mu_1}}$ for a system with a small μ from Equation 4.30, an error $O\left(\frac{\mu_2}{\mu_1}\right) = O\left(\frac{\mu}{1-\mu}\right)$ is introduced. For the Earth-Moon system this would be roughly an error of 1% on the TU parameter introduced by the approximation. Depending on the cases this can be acceptable or not. The reason why the approximation is used is because it allows to further simplify Equation 4.29 by removing the μ_1 parameter from the square root of the Tisserand term and to put it as a small multiplier in front of the second square bracket. The Tisserand term of Equation 4.29 can be simplified as:

$$\begin{aligned} T_1(a,e,i) &= \frac{\mu_1}{a} + 2\frac{1}{TU}\sqrt{\mu_1 a\left(1-e^2\right)}cos(i) \\ &= \frac{\mu_1}{a} + 2\sqrt{\frac{\mu_1^2 a\left(1-e^2\right)}{DU^3}}cos(i) \\ &= \frac{\mu_1}{DU}\left[\frac{DU}{a} + 2\sqrt{\frac{a(1-e^2)}{DU}}cos(i)\right] \end{aligned} \tag{4.32}$$

Substituting this result into Equation 4.29 we obtain:

$$\begin{aligned} J_{IP1D}(\mathbf{X_{IP1D}},\theta) &\approx \frac{\mu_1}{DU}\left[\frac{DU}{a} + 2\sqrt{\frac{a(1-e^2)}{DU}}cos(i)\right] + \left[2\frac{\mu_2}{r_2} - 2\frac{\mu_2}{DU^2}\left(xcos\theta + ysin\theta\right) + \frac{\mu_2^2}{DU^2VU^2} + VU^2\frac{\mu_1\mu_2}{(\mu_1+\mu_2)^2}\right] \\ \frac{DU}{\mu_1}J_{IP1D}(\mathbf{X_{IP1D}},\theta) &\approx \left[\frac{DU}{a} + 2\sqrt{\frac{a(1-e^2)}{DU}}cos(i)\right] + \frac{\mu_2}{\mu_1}\left[2\frac{DU}{r_2} - 2\frac{1}{DU}\left(xcos\theta + ysin\theta\right) + \frac{\mu_2}{DUVU^2} + \frac{1}{\left(1+\frac{\mu_2}{\mu_2}\right)}\right] \end{aligned} \tag{4.33}$$

Given that the order of magnitude of the terms in the second square brackets is smaller than that of the ones in first square brackets and as a result of being far from the secondary ($r_2 > DU$) in a system with a small mass parameter $\mu_1 >> \mu_2$, the term $\frac{\mu_2}{\mu_1}$ acts as a small multiplier for the second square brackets. For this reason the second square brackets are neglected. Moreover the term $\frac{DU}{\mu_1} = \frac{1}{VU^2}$, since it has been assumed that $TU \approx \sqrt{\frac{DU^3}{\mu_1}}$. The end result is that the Tisserand parameter with the normalized semi-major axis is a good approximation of the Jacobi constant expressed in normalized units $J_{IP1} = \frac{1}{VU^2}J_{IP1D}$:

$$J_{IP1} \approx \frac{DU}{a} + 2\sqrt{\frac{a\left(1-e^2\right)}{DU}}cos(i) \tag{4.34}$$

This Tisserand parameter is the one introduced in Equation 3.25 and used in [9][10][11][25].

NO APPROXIMATION ON TU

When the TU parameter is not approximated from Equation 4.30, then the derivation continues. From Equations 4.27 to 4.29 the following equation can be written:

$$J_{IP1D}(\mathbf{X_{IP1D}},\theta) = \left[\frac{\mu_1}{a} + 2\frac{1}{TU}\sqrt{\mu_1 a\left(1-e^2\right)}cos(i)\right] + \left[2\frac{\mu_2}{r_2} - 2\frac{\mu_2}{DU^2}\left(xcos\theta + ysin\theta\right) + \frac{\mu_2^2}{DU^2VU^2} + VU^2\frac{\mu_1\mu_2}{(\mu_1+\mu_2)^2}\right] \tag{4.35}$$

Two functions are therefore identified by the two square brackets. The first represents the Tisserand parameter about the primary T_1 and the second one a residual function P_1. The Tisserand function is depending on the osculating orbital elements a,e and i, but other sets may be chosen depending on the necessity. P_1 is depending on the position of the spacecraft in the $IP1D$ frame as well as on the angle θ between synodic and inertial frames, that with an abuse of notation is often used to represent the time variable. The result is that the Jacobi integral can be decomposed into two functions, one depending on the osculating orbital elements and the other depending on position coordinates and time:

$$J(\mathbf{X_{IP1D}},\theta) = T_1(a,e,i) + P_1(\mathbf{r}_{IP1D},\theta) \tag{4.36}$$

Note that the velocity part of the state vector is hidden in the osculating orbital elements, as can be seen from Equation 4.27. As it is not possible to make the simplifications introduced by the approximation on TU, an analysis of the components of the residual function P_1 is necessary to determine whether or not this function is acceptably small in a region of interest of the CR3BP model.

4.2.2. RESIDUAL ANALYSIS

In this section the analysis is focused on the residual term P_1 of Equation 4.36. This can be written in the $IP1D$ frame as:

$$P_1\left(\mathbf{r}_{IP1D},\theta\right)=\left[2\frac{\mu_2}{r_2}-2\frac{\mu_2}{DU^2}\left(xcos\theta+ysin\theta\right)+\frac{\mu_2^2}{DU^2VU^2}+VU^2\frac{\mu_1\mu_2}{\left(\mu_1+\mu_2\right)^2}\right] \tag{4.37}$$

The analysis however is much more simple when considering the residual expressed in the $SP1$ frame. Making use of the normalization equations and rotation matrices defined before the residual function can be easily expressed in the $SP1$ frame as:

$$P_1\left(\mathbf{r}_{SP1}\right)=\frac{2\mu}{\sqrt{(x-1)^2+y^2+z^2}}-2\mu x+\mu^2+\mu\left(1-\mu\right) \tag{4.38}$$

The function is composed of four terms, two are functions of the spacecraft position in the SPI frame while the other two are constant terms. For the rest of the analysis the four terms in Equation 4.38 will be referred from left to right with the letters A,B,C and D. A trajectory in the Earth-Moon CR3BP model is used to illustrate the variation and magnitude of the terms composing the residual function P_1

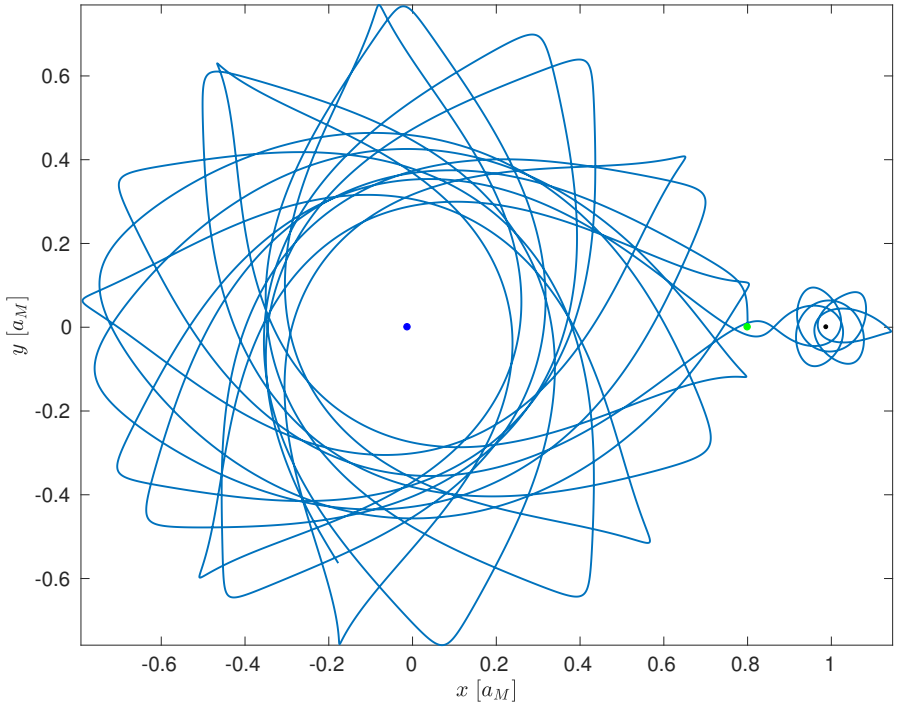

Figure 4.1: Trajectory in the Earth-Moon CR3BP in the SB frame, initial state at $\mathbf{X}^0_{SB}=[0.8\ 0\ 0\ 0\ 0.17\ 0]^T$, $C_{SB}=3.18514418060237$. The initial state is represented by a green dot, while the blue and black dots represent the primaries. Is it possible to see that for a brief part of the trajectory the spacecraft is temporarily captured by the Moon.

The trajectory represented in Figure 4.1 is for most of the time under the influence of the primary as main attractor. The secondary influence however is not negligible and at a certain point it leads to a temporary capture about the Moon. Figure 4.2 represents the behavior of the four terms of the residual function $P_1\left(\mathbf{r}_{SP1}\right)$.

It is possible to see that the variable terms A and B are essentially working in opposition. The A term is depending on the inverse of the distance with respect to the secondary, so when the spacecraft gets close to the secondary the term exhibits large fluctuations. Eventually the spacecraft is temporarily captured by the secondary. In such a case A exhibits large fluctuations that are not balanced by B, reaching a value of over 1.2. Considering that $C_{SB}\approx 3.185$ the discrepancy between the Tisserand and the Jacobi generated by the residual

function is quite large in this phase. We can thus conclude that staying far from the secondary is a necessary condition to guarantee a small A term and thus a small value of the residual function P_1.

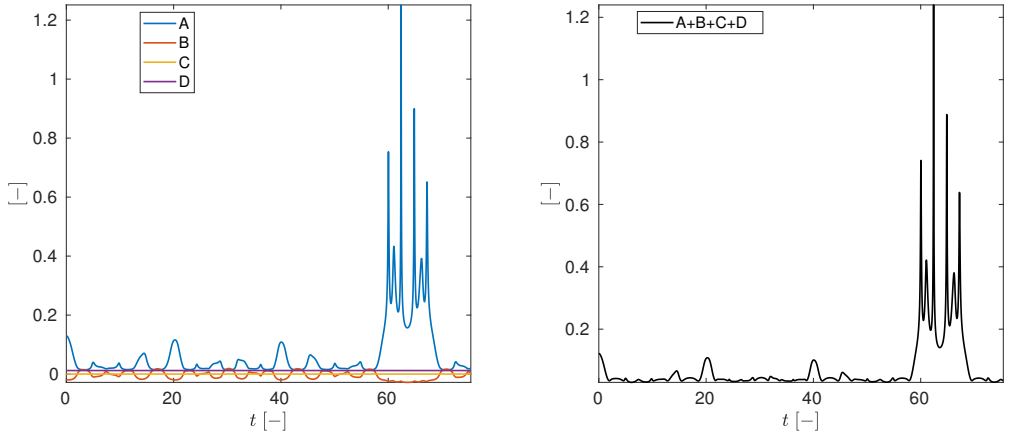

Figure 4.2: Behavior of the residual function P_1 (right) and decomposed in the four terms A,B,C and D (left). P_1 exhibits large fluctuations during the temporarily capture event at about $57 < t < 70$.

The behavior of the complementary Tisserand parameter is presented in Figure 4.6. The analysis over one trajectory has helped visualizing the singular contribution of the terms that compose the residual function, however a more universal analysis can be performed by considering the residual function over a region of interest of the CR3BP. By taking the planar case ($z = 0$) of $P_1(\mathbf{r}_{SP1})$ and plotting the value of the residual function over a region of space in the $SP1$ frame it is possible to obtain Figure 4.3.

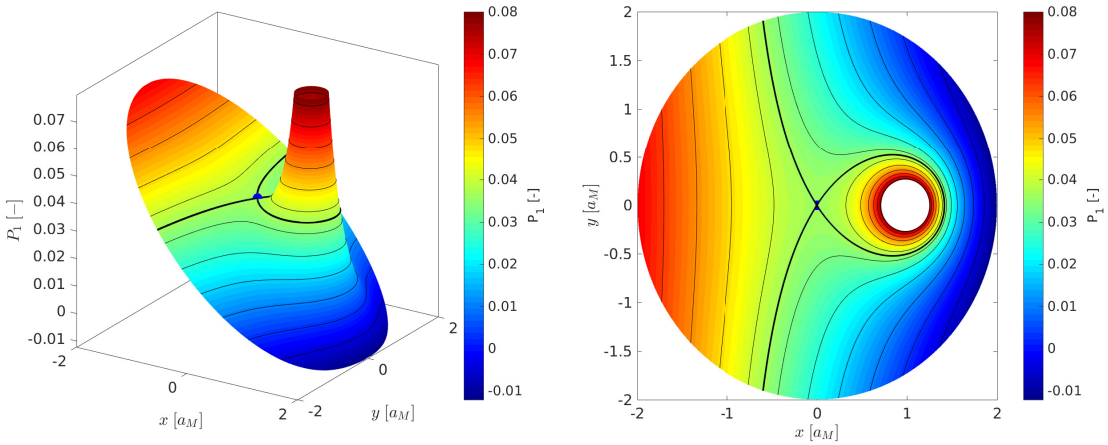

Figure 4.3: Value of the residual function P_1 over a region of space with $-2 < x < 2$ and $-2 < y < 2$ for the planar case in the $SP1$ frame. 3D representation on the left, xy projection on the right. Note that a portion of the surface in the proximity of the secondary has been removed to allow an easy understanding of the figures. Different contour levels can be identified, amongst which there is a contour intersecting the primary highlighted with a thick black line. This contour is characterized by $P_1(0,0,0) = 3\mu$. It is possible to see that since the primary is located on a saddle point of the residual surface P_1,the variation of the residual term in its proximity will be minimal. Since this variation is also applied to a small value of the residual, in this region the Tisserand parameter will be a good approximation of the Jacobi constant.

From Figure 4.3 it is possible to see the shape of the residual function in the planar case represented in the $SP1$ frame. As the residual function P_1 needs a mass parameter μ to be specified, the one for the Earth-Moon system has been used to obtain the figure. Note that the general shape of the residual is the same for the

CR3BP systems interesting for engineering applications. From the figure it is possible to see that the value of the residual function explodes in the region about the secondary. The term responsible for this behavior is $\frac{2\mu}{r_2}$, that has a singularity at the secondary position. This behavior was expected from the equation of the residual function, already observed in Figure 4.2 and is at the basis of the necessary condition to consider the Tisserand parameter only far from the secondary. This 'far' can now be quantified by looking at Figure 4.3, depending on the desired accuracy on the Tisserand parameter.

The most important result of this analysis however is given by the contour lines represented in figure. By definition these lines have a constant value of the residual function. However by guaranteeing a constant residual function, by the relation expressed in Equation 4.36, also constant Tisserand parameter is guaranteed over the contour line. By changing the contour level we would end up at a different Tisserand level, such that the sum between the Tisserand level and the contour level will always be equal to the Jacobi constant of the system considered. This property holds independently from the vicinity to the secondary. Indeed it is possible to see that there are also closed surfaces in the proximity of the secondary that have a constant Tisserand level. This fundamental result is used in Section 4.5 to define a new family of Poincaré sections to be used in the ETP-graph.

4.3. MODIFIED TISSERAND PARAMETER

In this section the derivation of a modified Tisserand parameter is presented. The parameter is called modified to justify the fact that it is defined about the secondary, whereas the classical Tisserand parameter is only defined about the primary. The two derivations are very similar, but possess a few fundamental differences that will be highlighted in this section. To the best of the author's knowledge a Tisserand parameter about the secondary has never been derived. This is because of a fundamental limitation of the classical Tisserand parameter that as seen before is defined only far from the minor body. The results presented in the previous section however show the existence of regions of space where the classical Tisserand parameter exhibits a homogeneous behavior independently of the vicinity to the secondary. This result is encouraging the search for similar properties for a Tisserand parameter defined about the secondary. Since many authors consider the Tisserand parameter constant by definition, the parameter about the secondary is differentiated by the modified adjective.

4.3.1. DERIVATION

The derivation of the modified Tisserand parameter can be considered complementary to the one of the classical parameter. The derivation starts from the Jacobi integral expressed in the $IP2D$ frame. The integral J_{IP2D} can be easily obtained by substituting the position of the secondary as point P_i in Equation 4.22, by setting $d = (1-\mu)\,DU$. The terms affected by this parameter are $\frac{d}{TU^2}$ and $\frac{d^2}{TU^2}$, by considering Equations 4.11 and 4.12 they can be written as:

$$\begin{aligned}\frac{d}{TU^2} &= \frac{(1-\mu)\,DU}{TU^2} \\ &= \frac{(1-\mu)\,DU}{\frac{DU^3}{\mu_1+\mu_2}} \\ &= \frac{\mu_1}{\mu_1+\mu_2}\frac{\mu_1+\mu_2}{DU^2} \\ &= \frac{\mu_1}{DU^2}\end{aligned} \tag{4.39}$$

$$\begin{aligned}\frac{d^2}{TU^2} &= \frac{\mu_1}{DU^2}(1-\mu)\,DU \\ &= \frac{\mu_1}{DU}\frac{\mu_1}{\mu_1+\mu_2} \\ &= \frac{\mu_1^2}{DU\frac{DU^3}{TU^2}} \\ &= \frac{\mu_1^2}{DU^2VU^2}\end{aligned} \tag{4.40}$$

Note the similarity of these terms with the ones in Equations 4.24 and 4.25, but with μ_2 replaced by μ_1. By substituting these expressions into Equation 4.22 the Jacobi integral J_{IP2D} can be expressed as:

$$J(\mathbf{X_{IP2D}},\theta) = 2\frac{\mu_1}{r_1} + 2\frac{\mu_2}{r_2} + 2\frac{1}{TU}\left(x\dot{y} - y\dot{x}\right) - V^2 + 2\frac{\mu_1}{DU^2}\left(xcos\theta + ysin\theta\right) + \frac{\mu_1^2}{DU^2VU^2} + VU^2\frac{\mu_1\mu_2}{\left(\mu_1+\mu_2\right)^2} \tag{4.41}$$

with V the velocity of the spacecraft in this frame. Also this time the Jacobi integral is decomposed as the sum of two functions. The first one is the modified Tisserand parameter, depending on a combination of osculating orbital elements or properties of Keplerian orbits. The second one is a residual function depending on the position of the spacecraft. Differently than the derivation of the classical Tisserand parameter, this time the residual term will not be generally small when considering a specific region of space since the influence of the primary is much larger than the one of the secondary. As a consequence the modified Tisserand parameter will not be a good approximation of the Jacobi constant. The fundamental assumption for the derivation of the modified Tisserand parameter is that:

1. **A region of space is considered where the secondary acts as the main attractor.**

Note that this condition is complementary to the one in the classical derivation that considered the primary as main attractor and thus considered regions of space far from the secondary. This time the situation is reversed as we are interested in a region of space where consistent osculating orbital elements with respect to the secondary can be derived. The assumption to be able to express the orbital elements of an osculating Keplerian orbit will allow possible to use the vis-viva and angular momentum equations, as expressed in Appendix B:

$$2E_2 = V^2 - \frac{2\mu_2}{r_2} = -\frac{\mu_2}{a} \tag{4.42}$$

$$(H_2)_z = H_2 cos(i) = \sqrt{\mu_2 a\left(1-e^2\right)}cos(i) = x\dot{y} - y\dot{x} \tag{4.43}$$

assuming the state to be expressed in the $IP2D$ reference frame as $\mathbf{X}_{IP2D} = [x\ y\ z\ \dot{x}\ \dot{y}\ \dot{z}]^T$. Note that the z-component of the angular momentum is considered for the derivation. a,e and i are the osculating semi-major axis, eccentricity and inclination of the trajectory with respect to the secondary. The inclination is computed with respect to the $P1P2$ orbital plane. By substituting these expressions into Equation 4.41 we obtain:

$$\begin{aligned}J_{IP2D}(\mathbf{X_{IP2D}},\theta) &= -2E_2 + 2\frac{\mu_1}{r_1} + 2\frac{1}{TU}H_2 cos(i) + 2\frac{\mu_1}{DU^2}\left(xcos\theta + ysin\theta\right) + \frac{\mu_1^2}{DU^2VU^2} + VU^2\frac{\mu_1\mu_2}{\left(\mu_1+\mu_2\right)^2} \\ &= \left[-2E_2 + 2\tfrac{1}{TU}H_2 cos(i)\right] + \left[2\tfrac{\mu_1}{r_1} + 2\tfrac{\mu_1}{DU^2}\left(xcos\theta + ysin\theta\right) + \tfrac{\mu_1^2}{DU^2VU^2} + VU^2\tfrac{\mu_1\mu_2}{(\mu_1+\mu_2)^2}\right] \\ &= \left[\tfrac{\mu_2}{a} + 2\tfrac{1}{TU}\sqrt{\mu_2 a\left(1-e^2\right)}cos(i)\right] + \left[2\tfrac{\mu_1}{r_1} + 2\tfrac{\mu_1}{DU^2}\left(xcos\theta + ysin\theta\right) + \tfrac{\mu_1^2}{DU^2VU^2} + VU^2\tfrac{\mu_1\mu_2}{(\mu_1+\mu_2)^2}\right]\end{aligned} \tag{4.44}$$

Also at this stage it is possible to see a decomposition of the Jacobi integral into two functions. The first one reminds us of the Tisserand parameter because it has the same expression. However in this case this term is

expressed as a function of the osculating orbital elements about the secondary body as main attractor. The second one is a residual function only depending on the position of the spacecraft in the $IP2D$ frame and the angle θ. Also in this case the term $\left(xcos\theta + ysin\theta\right)$ can be associated with the x-component in the $SP2$ frame, as it is possible to see from Equation 4.6. Note that an approach as the one in the classical derivation that relies on an approximation on TU would be failing in this case because all will be reduce to a multiplier $\frac{\mu_1}{\mu_2}$ that is not a small multiplier as $\frac{\mu_2}{\mu_1}$ in front of the second square brackets in Equation 4.44, since $\mu_1 >> \mu_2$. The decomposition of the Jacobi integral as the sum of two functions, one depending on osculating orbital elements and the other depending on position coordinates and time, can be written in short notation as:

$$J\left(\mathbf{X_{IP2D}},\theta\right) = T_2(a,e,i) + P_2(\mathbf{r}_{IP2D},\theta) \tag{4.45}$$

Since the modified parameter T_2 does not have constancy properties in a generic region of space (even in the vicinity of the secondary) the 'modified' adjective is used. In fact it can be argued that a Tisserand parameter is defined as that constant parameter that does not change after a flyby. To not create a conflict with this generic definition of the parameter, the new terminology is introduced. As it is not possible to make the simplifications introduced by the assumption on TU, an analysis of the components of the residual function P_2 is necessary to determine the behavior of this function in a region of interest of the CR3BP model.

4.3.2. RESIDUAL ANALYSIS

In this section the analysis is focused on the residual function P_2 of Equation 4.45. This can be written in $IP2D$ frame as:

$$P_2\left(\mathbf{r}_{IP2D},\theta\right) = \left[2\frac{\mu_1}{r_1} + 2\frac{\mu_1}{DU^2}\left(xcos\theta + ysin\theta\right) + \frac{\mu_1^2}{DU^2 VU^2} + VU^2\frac{\mu_1\mu_2}{\left(\mu_1+\mu_2\right)^2}\right] \tag{4.46}$$

Also in this case the analysis is much more simple when considering the residual function expressed in the $SP2$ frame. Making use of the normalization equations and rotation matrices presented before, the residual function can be easily expressed in such a frame as:

$$P_2\left(\mathbf{r}_{SP2}\right) = \frac{2\left(1-\mu\right)}{\sqrt{(x+1)^2+y^2+z^2}} + 2(1-\mu)x + (1-\mu)^2 + \mu\left(1-\mu\right) \tag{4.47}$$

As before this function is composed of four terms, whose behavior will now be analyzed for the same trajectory presented in Figure 4.1 for the analysis of the residual terms of the classical Tisserand parameter. For the rest of the section the four terms in Equation 4.47 will be referred to with the letters A,B,C and D from left to right. Their behavior is presented in Figure 4.4.

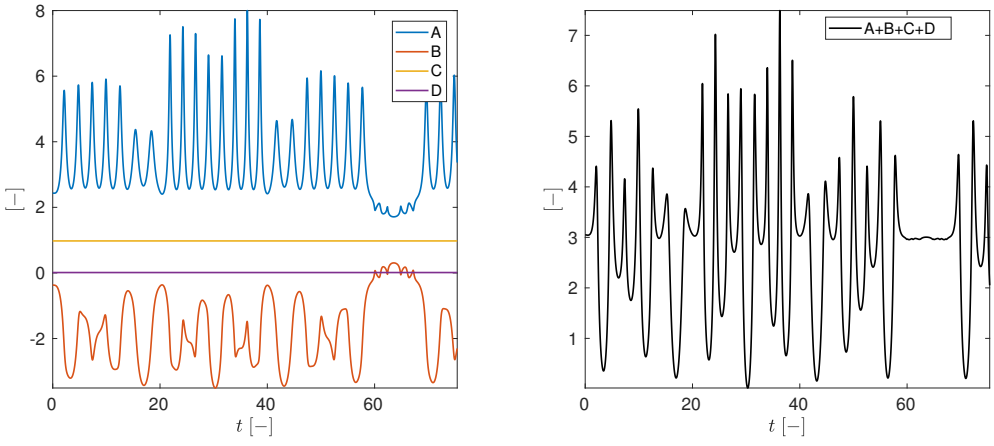

Figure 4.4: Behavior of the residual function P_2 (right) and decomposed in the four terms A,B,C and D (left) for the trajectory illustrated in Figure 4.1. P_2 exhibits large fluctuations during most of the time but not during the temporarily capture event at about $57 < t < 70$.

Also in this case it is possible to see that the two variable terms A and B have some sort of compensation between each other. This time however their fluctuations are much larger and happens at higher mean values

(in absolute sense) than the ones observed in the terms of P_1. The large fluctuations this time are dependent on the spacecraft being too close to the primary for most of the motion. By looking at the behavior of these terms, it is expected for the Tisserand parameter to have a much smaller value compared to the Jacobi constant. This time a paradoxical situation occurs where the residual function, and not the modified Tisserand parameter, is potentially a better approximation of the Jacobi integral. The behavior of the modified Tisserand parameter is presented in Figure 4.6. A more general analysis will now be presented considering the residual function P_2 over a region of interest in the planar CR3BP. By taking $P_2(\mathbf{r}_{SP2})$ with $z = 0$ and plotting the value of the function over a region of space in the $SP2$ frame it is possible to obtain Figure 4.5.

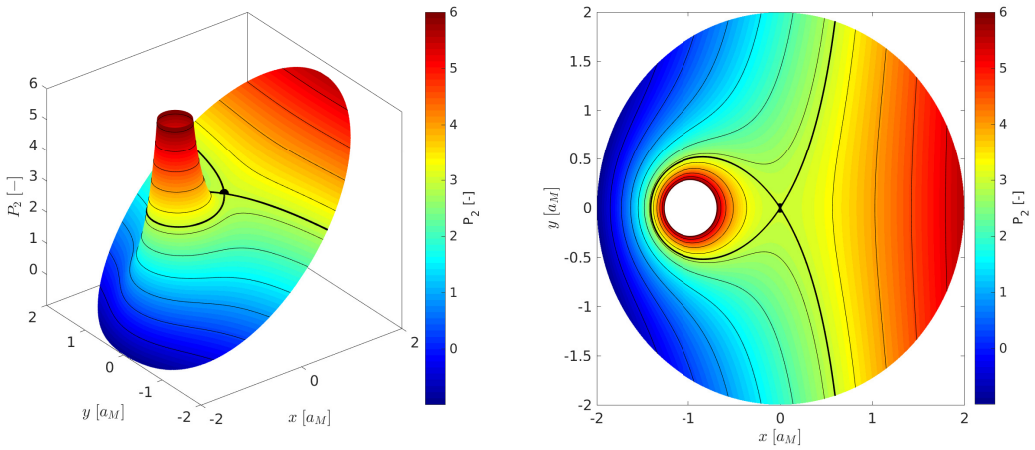

Figure 4.5: Value of the residual function P_2 over a region of space $-2 < x < 2$ and $-2 < y < 2$ for the planar case in the $SP2$ frame. 3D-representation on the left, xy-projection on the right. Note that a portion of the surface in the proximity of the primary has been removed to allow an easy understanding of the figures. Different contour levels can be identified, amongst which there is a contour intersecting the secondary highlighted with a thick black line. This contour is characterized by $P_2(0,0,0) = 3(1-\mu)$. It is possible to see that since the secondary is located on a saddle point of the residual surface P_2,the variation of the residual term in its proximity will be minimal. Since this variation is also applied to a large value of the residual, in this region the residual function will be a good approximation of the Jacobi constant.

From Figure 4.5 it is possible to see the shape of the residual function in the planar case represented in the $SP1$ frame. As the function needs a mass parameter μ to be specified, the one for the Earth-Moon system has been used. Note that the general shape of the residual is the same for the CR3BP systems interesting for engineering applications. The characteristics of the function P_2 are similar to those of P_1. In this case the residual function has a singularity point on the primary, but a fundamental difference exists with respect to the characteristics of P_1. As it is possible to see from the vertical scale in Figure 4.5, the value of the residual is generally not small and can reach multiple times the value of the Jacobi constant of the system considered. Note the difference in scale of P_2 vs P_1 in Figures 4.3 and 4.5. There is therefore no region in space for which the residual can be identified as a small quantity.

However a fundamental result can be observed also in this case. By focusing on the regions where the residual is constant rather than searching a region where it is small, one sees the presence of numerous contour lines. By definition these lines have a constant value of the residual function. But due to Equation 4.45, by guaranteeing a constant value of P_2 on a contour line we are also guaranteeing a constant value of T_2 on it, since their sum must always be equal to the Jacobi constant. By changing the contour level we would end up on a different modified Tisserand level, such that the sum of the modified Tisserand level and the contour level will always be equal to the Jacobi constant of the system considered. This property holds independently for the region in space considered as in principle any contour can be taken for the analysis. This crucial result plays a significant role in the definition of a family of Poincaré sections that possesses the property of having a constant modified Tisserand parameter. This will be of fundamental importance to represent multiple CR3BP models in the ETP-graph.

4.4. COMPARISON OF THE TISSERAND PARAMETERS

In this section the general behaviors of the Tisserand parameters presented in this chapter are briefly discussed. The parameters considered are:

$$\begin{cases} T_1^{cl} = \dfrac{DU}{a} + 2\sqrt{\dfrac{a\left(1-e^2\right)}{DU}}cos(i) \\ T_1 = \dfrac{\mu_1}{a} + 2\dfrac{1}{TU}\sqrt{\mu_1 a\left(1-e^2\right)}cos(i) \\ T_2 = \dfrac{\mu_2}{a} + 2\dfrac{1}{TU}\sqrt{\mu_2 a\left(1-e^2\right)}cos(i) \end{cases} \tag{4.48}$$

where the osculating orbital elements of T_1^{cl} and T_1 are with respect to the primary, while the ones of T_2 are with respect to the secondary. Figure 4.6 presents the variation of these parameters for the trajectory considered in Figure 4.1.

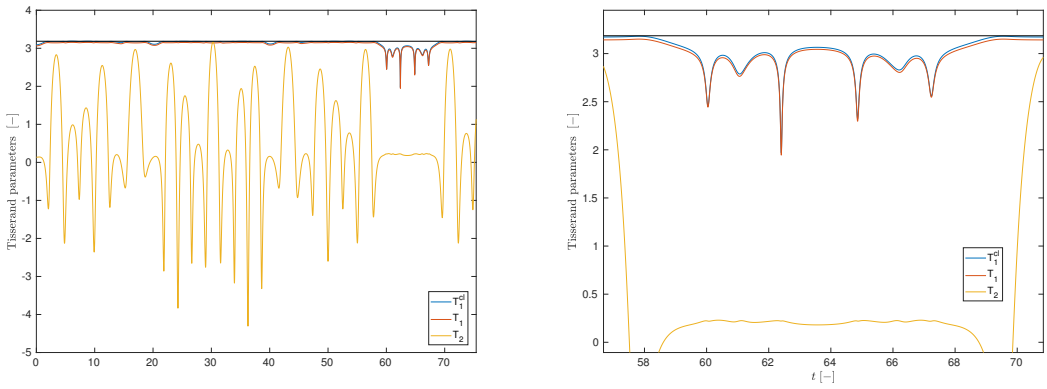

(a) (b)

Figure 4.6: On the left: behavior of the Tisserand parameters in Equation 4.48 for the trajectory represented in Figure 4.1. The value of the Jacobi constant is represented for reference by the black line with value $C_{SB} = 3.185$. On the right: zoom of the Tisserand parameters during the temporarily capture event. In this region both T_1^{cl} and T_1 exhibit large fluctuations, while T_2 exhibit a more regular behavior.

As it is possible to see from Figure 4.6 the parameters about the primary are about constant and equal to the Jacobi integral for most of the time, however during the temporarily capture event with the secondary they experience large variations. It is literally possible to see that these parameters fail to be a good approximation of the Jacobi constant in proximity of the secondary, as well expected from literature. Other minor variations of the parameters about the primary are visible in other points at which the trajectory gets closer to the secondary such as for $t = 20$ and $t = 40$. It is also possible to see the effect of the approximation of TU in the small difference between the two parameters with respect the primary. The modified Tisserand parameter on the other way exhibits very large variations when considered far from the secondary. It is possible to observe that this parameter becomes approximately constant during the temporarily capture event. This behavior however does not make the parameter a good approximation of the Jacobi constant; paradoxically in this case the residual function P_2 results to be a better approximation of the Jacobi constant. It appears that when considering the secondary T and P exchange roles.

For consistency in this report T_1^{cl} will not be considered and the author will be referring to T_1 and T_2 when discussing the Tisserand parameters about the primary and secondary, or classical and modified respectively.

4.5. POINCARÉ SECTION FAMILIES

As seen in the previous sections and from the planar visualization of the residual functions P_1 and P_2 in Figures 4.3 and 4.5, it is possible to select contour lines that have a constant value of the residual functions and thus constant values of the Tisserand parameters. In the planar case this corresponds to the identification of a family of curves in the XY-plane that has the same Tisserand parameter. This result can be extended in the

3D case by looking at the expressions of the residual functions P_1 and P_2 in Equations 4.38 and 4.47. A family of surfaces can be defined in the $SP1$ frame that has a constant Tisserand parameter about the primary. This family is expressed by the following implicit function S_1:

$$S_1 : \frac{2\mu}{\sqrt{(x-1)^2+y^2+z^2}} - 2\mu x + \mu^2 + \mu(1-\mu) - P^k = 0 \tag{4.49}$$

On the other hand a family of surfaces that has a constant modified Tisserand parameter about the secondary in the $SP2$ frame is defined by the following implicit function S_2:

$$S_2 : \frac{2(1-\mu)}{\sqrt{(x+1)^2+y^2+z^2}} + 2(1-\mu)x + (1-\mu)^2 + \mu(1-\mu) - P^k = 0 \tag{4.50}$$

In both cases the parametric term P^k determines the level set of the residual functions, thus the shape of S_1 and S_2 in space. As possible to see from Equations 4.49 and 4.50 both S_1 and S_2 families of surfaces are axial-symmetric with respect to the x-axis of the $SP1$ and $SP2$ frames. Moreover the shape of the family of S_1 functions is similar but inversed with respect to the shape of the S_2 family.

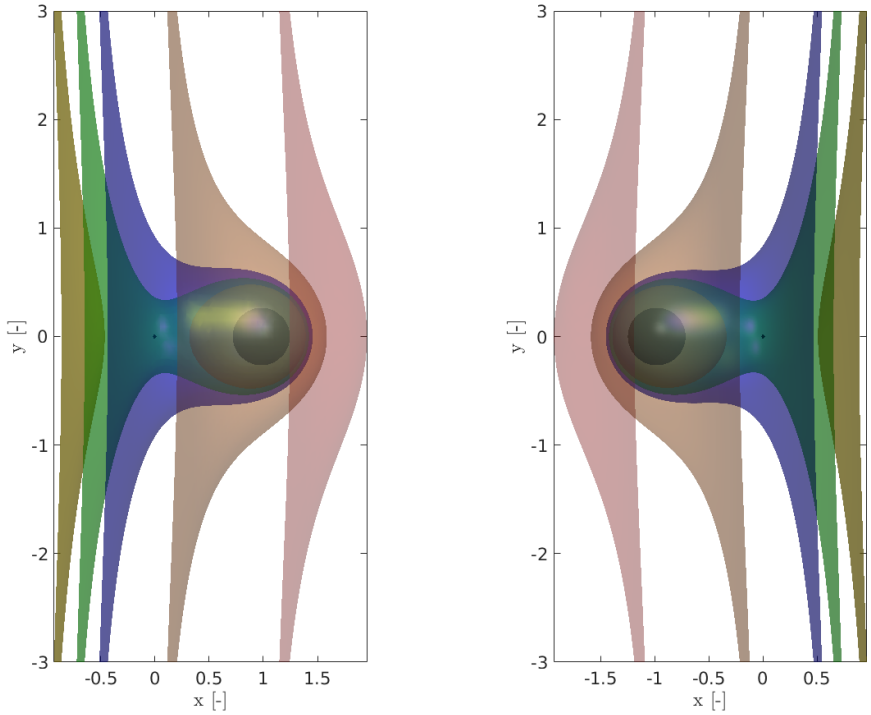

Figure 4.7: Example of six surfaces from the S_1 and S_2 families in the $SP1$ and $SP2$ frames respectively of the Earth-Moon system. On the left: family of S_1 for $P^k = [-0.01, 0.015, 0.03, 0.035, 0.04, 0.08]$. On the right: family of S_2 for $P^k = [-0.7, 1.2, 2.5, 2.85, 3.3, 6.5]$. These surfaces are represented in red, orange, blue, green, yellow and black from lower to higher values of P^k. Surfaces are completely open for low-values of P^k and separate into two parts, one open and one closed for higher value of P^k. The passage between these two configurations is represented by $P^k = 3\mu$ for S_1 and $P^k = 3(1-\mu)$ for S_2.

In Figure 4.7 example surfaces of the S_1 family are illustrated. Amongst these surfaces a special type is the one that passes from the primary. In this case it is very simple to compute the value of the parameter P^k for which this happens. By just evaluating P_1 in the origin we obtain $P_1(0,0,0) = 3\mu$. The surface so defined will be described in Section 4.5.1.

The same holds for S_2, since by setting $P^k = P_2(0,0,0) = 3(1-\mu)$ we obtain a single closed surface passing by the secondary. The surface so defined will be described in Section 4.5.2.

For high values of P^k a quasi-spherical surface about the secondary can be defined by S_1. This surface will be defined in Section 4.5.3 and then used as Poincaré section for the study of the flyby effects of the Moon and Jupiter in Chapter 8.

Note that by choosing these families of Poincaré sections for the analysis we are just substituting the shape of an arbitrary section that loosely satisfies certain assumptions (to be far from the primary or secondary) with a set of mathematical rigorously defined sections that satisfy a condition directly on the Tisserand parameter. There is a fundamental difference between a surface and the Poincaré section, since the latter can be defined in any subset of the phase-space, while the former is usually intended in the position portion of the phase-space. In this case since the residual terms are function of the position coordinates only, the Poincaré sections that are defined for the analysis are also surfaces and the two terms will be used together.

4.5.1. POINCARÉ SECTION ABOUT THE PRIMARY

In this section the Poincaré section about the primary that will be used in this report is defined. To obtain the section the term $P^k = 3\mu$ is substituted into S_1 to guarantee the passage of the surface through the primary. By substitution it is possible to simplify the equation of the section as the implicit function as:

$$F_1(x,y,z): \frac{1}{\sqrt{(x-1)^2+y^2+z^2}} - x - 1 = 0 \tag{4.51}$$

given that $\mu \neq 0$, where $F_1(x,y,z) = S_1(x,y,z)|_{P^k=3\mu}$. Note that by substituting $P^k = 3\mu$ we have obtained a surface that is not depending on the mass parameter μ of the system. It can be concluded that in any CR3BP considered the Poincaré surface passing by the primary that has the constant Tisserand parameter about the primary is defined in Equation 4.51 and that the condition that determines its passage is always driven by $P^k = 3\mu$, independently from the specific system considered. The shape of the surface expressed by equation 4.51 is represented in Figure 4.8.

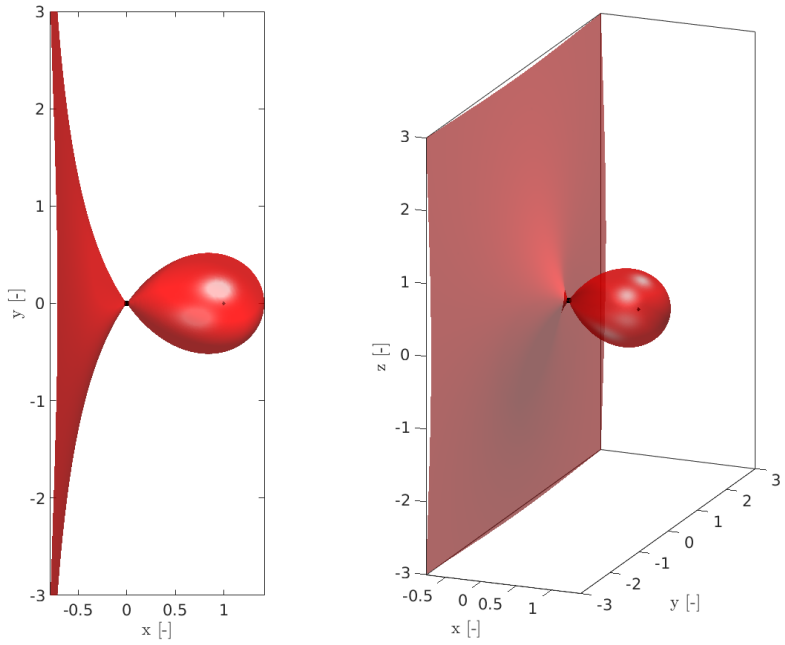

Figure 4.8: Poincaré section about the primary. On the left xy-view, while on the right xyz-view in the SP1 frame. Note that the section is passing by the primary at the origin of the $SP1$ frame and that it completely envelopes the secondary with a closed surface.

The domain of $F_1(x,y,z)$ is $D = \{(x,y,z) \in \mathbb{R}^3 \,|x > -1 \wedge (x,y,z) \neq (1,0,0)\}$. The total differential of the function F_1 is:

$$dF_1 = \frac{\partial F_1}{\partial x}dx + \frac{\partial F_1}{\partial y}dy + \frac{\partial F_1}{\partial z}dz \tag{4.52}$$

$$F_{1_x} = \frac{1-x}{\sqrt{(x-1)^2+y^2+z^2}^3} - 1 \tag{4.53}$$

$$F_{1_y} = \frac{-y}{\sqrt{(x-1)^2+y^2+z^2}^3} \tag{4.54}$$

$$F_{1_z} = \frac{-z}{\sqrt{(x-1)^2+y^2+z^2}^3} \tag{4.55}$$

Since dF_1 is continuous $\forall (x,y,z) \in D$, it is possible to conclude that $F_1 \in C^1$, $\forall (x,y,z) \in D$. The implicit function theorem is applied to understand which sufficient conditions ensure the conversion between the implicit function F_1 and its explicit counterpart f_1. The theorem for a two-variables case states that let $F : \mathbb{R}^{n+m} \to \mathbb{R}^m | F \in C^1$, such that $\mathbb{R}^{n+m}$ has coordinates (x,y). A point (a,b) is fixed such that $f(a,b) = c, c \in \mathbb{R}^m$. If the Jacobian matrix $J_{f,y}(a,b)$ is invertible, then there exists an open set U of R^n containing a and there exists a unique continuosly differentiable function $g : U \to \mathbb{R}^m$ such that:

- $g(a) = b$
- $f(x, g(x)) = c,\ \forall x \in U$
- $\dfrac{\partial g}{\partial x_j} = -J_{f,y}(x,g(x))^{-1}\frac{\partial f}{\partial x_j}(x,g(x))$

By applying the theorem is possible to see that if the implicit function $F_1(x,y,z) = 0$ satisfies certain local conditions on its partial derivatives, then it is possible to express such a function as an explicit one f_1. In this case $F_1 \in C^1$, so a point of coordinates (a,b,c) is fixed and the Jacobian matrix is evaluated at this point:

$$J(a,b,c) = \left[\frac{1-a}{\sqrt{(a-1)^2+by^2+c^2}^3} - 1\,,\ \frac{-b}{\sqrt{(a-1)^2+b^2+c^2}^3}\,,\ \frac{-c}{\sqrt{(a-1)^2+b^2+c^2}^3}\right] \tag{4.56}$$

It is possible to invert $F_{1_y}(a,b,c)$ or $F_{1_z}(a,b,c)$ only if $b \neq 0$ or $c \neq 0$ respectively. This means that it is possible to express an explicit function $y = f_1(x,z)$ that represents the implicit function F_1, $\forall (x,y,z) \in D \mid y \neq 0$. The same would be possible for a function $z = f_1(x,y)$, $\forall (x,y,z) \in D \mid z \neq 0$. It is then important to investigate upon the zeros of the explicit function f_1 to understand the points where it is not possible to map the implicit function into the explicit one. From Equation 4.51 it is easy to find the explicit function $y = f_1(x,z)$:

$$y = f_1(x,z) = \pm\sqrt{\frac{1}{(x+1)^2} - (x-1)^2 - z^2} \tag{4.57}$$

Finding the zeros of this function corresponds to solve the following equation parametrized by z:

$$x^4 + x^2(z^2-2) + 2xz^2 + z^2 = 0 \tag{4.58}$$

The points of coordinates $(x(z)_{1,2,3,4}, 0, z)$ are the ones where the sufficient condition of the implicit function theorem is not satisfied. Is important to remember that D was such that $x > -1$, this means that depending on z, certain $x(z)$ will be discarded because they are not belonging to the domain. In the planar case of the CR3BP, $z = 0$ and it is easy to see that $x(0)_1 = -\sqrt{2} \notin D$, $x(0)_2 = x(0)_3 = 0$, $x(0)_4 = \sqrt{2}$. Generally speaking the locus of points that does not satisfy the sufficient condition of the implicit function theorem can be seen in Figure 4.8 as the intersection of the Poincaré section and the xz-plane with $y = 0$.
An important result that derives from the implicit function theorem is the computation of the partial derivatives of the function $f_1(x,z)$:

$$\frac{\partial y}{\partial x} = \mp\frac{\frac{1}{(1+x)^3} + x - 1}{\sqrt{\frac{1}{(x+1)^2} - (x-1)^2 - z^2}} \tag{4.59}$$

$$\frac{\partial y}{\partial z} = \mp \frac{z}{\sqrt{\frac{1}{(x+1)^2} - (x-1)^2 - z^2}} \tag{4.60}$$

From these equations it is possible to see that $\frac{\partial y}{\partial x} = 0$ by solving $x\left(x^3 + 2x^2 - 2\right) = 0$, that gives as real solution $x = 0 \notin D$ and $x = 0.8393\ \forall z$ while $\frac{\partial y}{\partial z} = 0$ if $z = 0$. The value of the derivatives evaluated on the section is important to ensure the transversality condition between the trajectory and the Poincaré section defined by $f_1(x, y)$.

4.5.2. POINCARÉ SECTION ABOUT THE SECONDARY

In this section the Poincaré section about the secondary that will be used in the report is defined. To obtain the section the term $P^k = 3\left(1-\mu\right)$ is substituted into S_2 to guarantee the passage of the surface from the secondary. By substitution it is possible to simplify the equation of the section as an implicit function:

$$F_2(x, y, z) : \frac{1}{\sqrt{(x+1)^2 + y^2 + z^2}} + x - 1 = 0 \tag{4.61}$$

given that $\mu \neq 1$, where $F_2(x, y, z) = S_2(x, y, z)|_{P^k = 3(1-\mu)}$. Note that also in this case by substituting $P^k = 3(1-\mu)$ we have obtained a surface that is not depending on the mass parameter μ of the system. It can be concluded that in any CR3BP considered the Poincaré surface passing by the secondary that has the constant modified Tisserand parameter about the secondary is defined by Equation 4.61 and that the condition that determines its passage is always driven by $P^k = 3(1-\mu)$, independently from the specific system considered. The shape of the surface expressed by equation 4.61 is represented in Figure 4.9.

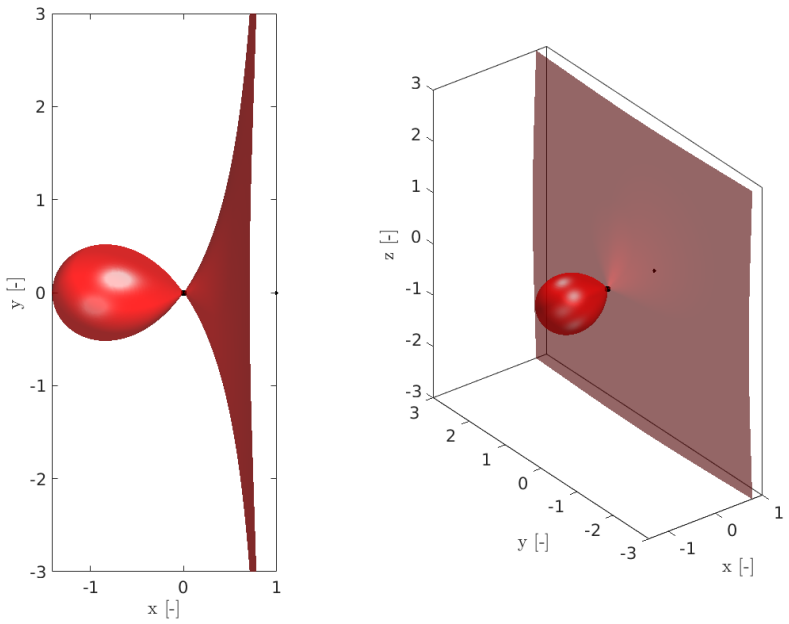

Figure 4.9: Poincaré section about the secondary in the SP2 frame. On the left xy-view, while on the right xyz-view. Note that the section is passing on the secondary at the origin of the $SP2$ frame and that it completely envelopes the primary with a closed surface.

The domain of $F_2(x, y, z)$ is $D = \left\{(x, y, z) \in \mathbb{R}^3 \,|\, x < 1 \wedge (x, y, z) \neq (-1, 0, 0)\right\}$. The total differential of the function F_2 is:

$$dF_2 = \frac{\partial F_2}{\partial x}dx + \frac{\partial F_2}{\partial y}dy + \frac{\partial F_2}{\partial z}dz \tag{4.62}$$

$$F_{2_x} = \frac{1+x}{\sqrt{(x+1)^2 + y^2 + z^2}^3} + 1 \tag{4.63}$$

$$F_{2_y} = \frac{-y}{\sqrt{(x+1)^2+y^2+z^2}^3} \tag{4.64}$$

$$F_{2_z} = \frac{-z}{\sqrt{(x+1)^2+y^2+z^2}^3} \tag{4.65}$$

Since dF_2 is continuous $\forall(x,y,z) \in D$, it is possible to conclude that $F_2 \in C^1$, $\forall(x,y,z) \in D$. At this point the implicit function theorem is applied in a similar way as it was used before to characterize the Poincaré section about the primary. The Jacobian matrix evaluated on a point (a,b,c) is:

$$J(a,b,c) = \left[\frac{1+a}{\sqrt{(a+1)^2+by^2+c^2}^3} + 1\,,\ \frac{-b}{\sqrt{(a+1)^2+b^2+c^2}^3}\,,\ \frac{-c}{\sqrt{(a+1)^2+b^2+c^2}^3} \right] \tag{4.66}$$

It is possible to invert $F_{2_y}(a,b,c)$ or $F_{2_z}(a,b,c)$ only if $b \neq 0$ or $c \neq 0$ respectively. This means that it is possible to express an explicit function $y = f_2(x,z)$ that represents the implicit function F_2, $\forall(x,y,z) \in D \mid y \neq 0$. The same would be possible for a function $z = f_2(x,y)$, $\forall(x,y,z) \in D \mid z \neq 0$. From Equation 4.61 it is easy to find the explicit function $y = f_2(x,z)$:

$$y = f_2(x,z) = \pm\sqrt{\frac{1}{(1-x)^2} - (1+x)^2 - z^2} \tag{4.67}$$

The zeros of this function correspond to the solutions of the following equation parametrized by z:

$$x^4 + x^2(z^2-2) - 2xz^2 + z^2 = 0 \tag{4.68}$$

In the planar case of the CR3BP, $z = 0$ and it is easy to see that $x(0)_1 = -\sqrt{2}$, $x(0)_2 = x(0)_3 = 0$, $x(0)_4 = \sqrt{2} \notin D$. As done before the locus of points that does not satisfy the sufficient condition of the implicit function theorem can be seen in Figure 4.9 as the intersection of the Poincaré section and the xz-plane with $y = 0$.
The partial derivatives of $f_2(x,z)$ are:

$$\frac{\partial y}{\partial x} = \mp\frac{-\frac{1}{(1-x)^3} + x + 1}{\sqrt{\frac{1}{(1-x)^2} - (1+x)^2 - z^2}} \tag{4.69}$$

$$\frac{\partial y}{\partial z} = \mp\frac{z}{\sqrt{\frac{1}{(1-x)^2} - (1+x)^2 - z^2}} \tag{4.70}$$

From these equations is possible to see that $\frac{\partial y}{\partial x} = 0$ solving the equation $x\left(x^3 - 2x^2 - 2\right) = 0$, that gives as real solution $x = 0 \notin D$ and $x = -0.8393$ $\forall z$. $\frac{\partial y}{\partial z} = 0$ if $z = 0$. Also in this case the value of the derivatives evaluated on the section is important to ensure the trajectory to pass the Poincaré section transversely.

4.5.3. QUASI-SPHERICAL SURFACE ABOUT THE SECONDARY

From Figure 4.7 it is possible to see that for high values of the parameter P^k the Poincaré sections described by Equation 4.49 are quasi-spherical surfaces about the secondary. This type of Poincaré sections will be used in Chapter 8 to study the flyby effects of the Moon and Jupiter with the Tisserand parameter about the primary. To define these sections, the following P^k parameter has been chosen by using Equation 4.38:

$$P^k = P_1(1+R_{SOI},0,0) = \frac{2\mu}{R_{SOI}} - 2\mu(1+R_{SOI}) + \mu^2 + \mu\left(1-\mu\right) \tag{4.71}$$

where R_{SOI} is the radius of the SOI about the secondary. Substituting this into Equation 4.49 it is possible to obtain the implicit function of the quasi-spherical section (QSS) that will be used as Poincaré section for the 3D flyby analysis:

$$QSS_1\left(x,y,z\right): \frac{1}{\sqrt{(x-1)^2+y^2+z^2}} - x + 1 + \left(R_{SOI} - \frac{1}{R_{SOI}}\right) = 0 \tag{4.72}$$

4.6. CONCLUSIONS

In this section the derivation of the Tisserand parameters T_1 and T_2 has been discussed. In particular a modified Tisserand parameter T_2 about the secondary has been derived. In both cases the Jacobi integral J has been decomposed into two functions, one being the Tisserand parameter T depending on the osculating orbital elements and the other being a residual function P depending on the spacecraft position in the synodic frame considered:

$$J = T + P \tag{4.73}$$

where the Tisserand parameters expressed in dimensional units can be defined as:

$$\begin{cases} T_1 = \dfrac{\mu_1}{a} + 2\dfrac{1}{TU}\sqrt{\mu_1 a\left(1-e^2\right)}cos(i) \\ T_2 = \dfrac{\mu_2}{a} + 2\dfrac{1}{TU}\sqrt{\mu_2 a\left(1-e^2\right)}cos(i) \end{cases} \tag{4.74}$$

or in adimensional units as:

$$T_k = \frac{\mu^*}{a} + 2\sqrt{\mu^* a\left(1-e^2\right)}cos(i) \quad \text{where} \quad \mu^* = \begin{cases} 1-\mu & \text{if} \quad k=1 \\ \mu & \text{if} \quad k=2 \end{cases} \tag{4.75}$$

From the expression of the residual functions P_1 and P_2 in Equations 4.47 and 4.38 respectively, it has been possible to determine families of Poincaré sections with constant Tisserand parameters. This is of crucial importance especially for T_2. By selecting a Poincaré section from the S_2 family it is possible to use a modified Tisserand parameter about the secondary that possesses on this section the same constancy properties exhibited by the classical Tisserand parameter.

Three different Poincaré sections that guarantee the relationship presented in Equation 4.73 are chosen for the analysis in the report. These sections are a fundamental step towards the patching of CR3BP models such as the Sun-Earth-Moon or Sun-Jupiter-Europa that share the same body as primary and secondary. In the next chapter the properties of the ETP-graph that is obtained by the usage of the Tisserand parameters on these sections will be illustrated.

5

EXTENDED TISSERAND-POINCARÉ GRAPH

In this chapter the characteristics of the TP-graphs obtained with the new formulations of the Tisserand parameters derived in the previous chapter will be discussed. First the case of the $r_a - r_p$ TP-graph will be characterized in Section 5.1, while the case of the $r_a - r_p - i$ TP-graph will be discussed in Section 5.2. Since these are using two and three variables respectively, they will be addressed as the $2D$ and $3D$ cases. The ETP-graph will be discussed in detail in Section 5.3 as the merging between two different TP-graphs. To conclude the chapter Section 5.4 sums up the main findings.

To generalize the analysis of the TP-graph the following expression of the parameters in dimensional units is used:

$$T_* = \frac{2\mu_*}{r_a + r_p} + \frac{2}{TU}\sqrt{2\mu_* \frac{r_a r_p}{r_a + r_p}} cos(i) \tag{5.1}$$

where the symbol $*$ is used to represent one of the primaries considered, as done in Equations 4.74 and 4.75. The osculating orbital elements are expressed in dimensional units, as well as the gravitational constant of the main attracting body μ_*. Note that the characterization will be performed in the region with $r_a > 0$ and $r_p > 0$, pertaining to circular and elliptic osculating orbits in the $r_a - r_p$ and $r_a - r_p - i$ TP-graphs. Also note that the formulation of the parameter shall not interfere with the representation of the osculating orbital elements in the graph, but is fundamental for the evaluation of the parameter and for the representation of the Tisserand level sets in the graphs. Finally, although the mathematical characterization will be universally valid for both T_1 and T_2 of any CR3BP considered, the graphs illustrated in the figures are necessarily obtained for a real case. This will be the Earth-Moon CR3PB and in such a case the T_1 parameter will be used and the graph will be limited in the region $0 < r_a < 5$ and $0 < r_p < 5$, in the portion for which $r_a \geq r_p$.

5.1. 2D GRAPH

In this section the characteristics of the $r_a - r_p$ TP-graph will be discussed for a planar trajectory. The generic expression of the Tisserand parameter can be written from Equation 5.1 as:

$$T_* = \frac{2\mu_*}{r_a + r_p} \pm \frac{2}{TU}\sqrt{2\mu_* \frac{r_a r_p}{r_a + r_p}} \tag{5.2}$$

By considering the planar case it is necessary to distinguish between prograde and retrograde trajectories, hence the $\pm$ in front of the second term of the parameter. By using this expression as an implicit function, the following Tisserand level sets can be plotted in the graph.

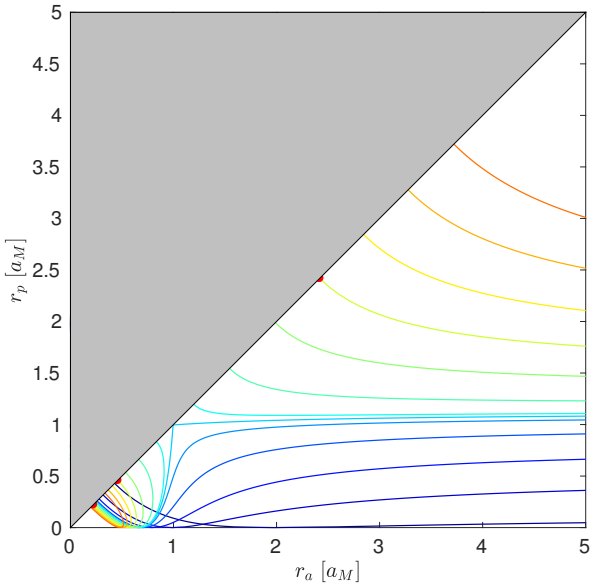

Figure 5.1: Tisserand-level sets plotted in r_a-r_p TP-graph for the planar case using T_1 in the Earth-Moon CR3BP. The Tisserand level sets are arranged alongside the color spectrum from low (blue) to high (red) values. Both retrograde and prograde regions of the level sets are displayed (see text for explanation). The area colored in gray denotes the impossible condition for a point to have a pericenter greater than its apocenter. The three red points represent the intersections with the $r_a = r_p = r_c$ line highlighted in Figure 5.2.

It is possible to see in Figure 5.1 that for high values of T_*, corresponding to the low-energy regime, the level sets are divided into two parts: one in the bottom-left and the other in the top-right area of the graph. In the first case the level sets are essentially closed curves, while they are open in the latter case. Generally there exist three intersection points between the level set and the line $r_a = r_p = r_c$. This line represents the condition for a circular trajectory, for which the evaluation of the Tisserand parameter can be used for classification purposes. By substituting $r_a = r_p = r_c$ into Equation 5.2 and solving for r_c these intersection points can be computed by solving the following cubic equation:

$$r_c^3\left(\frac{4\mu_*}{TU^2}\right) - r_c^2\left(T_*^2\right) + r_c\left(2T_*\mu_*\right) - \mu_*^2 = 0 \tag{5.3}$$

For high values of T_* there exist three distinct solutions to this equation, two in the prograde and one in the retrograde region of the level set. The passage between retrograde and prograde occurs in the graph at a critical point:

$$\begin{cases} r_p^{cr} = 0 \\ r_a^{cr} = \dfrac{2\mu_*}{T_*} \end{cases} \tag{5.4}$$

At this condition $H_* = 0$. For $r_a < r_a^{cr}$ the level set is describing a retrograde motion, while it is describing a prograde motion for $r_a > r_a^{cr}$. The points on the level set taken in proximity of this critical points generally correspond to collision trajectories with the body $*$ considered. The collision condition cannot generally be related to the pericenter being smaller than the body's radius, since the orbital elements are osculating and the collision event might not occur if large fluctuations of the orbital elements are expected, i.e. if the osculating orbital elements are taken very far from the body considered.

By decreasing the value of T_* the level sets in the bottom-left move upward while the ones in the top-right move downward. When $T_* = 3\left(\frac{\mu_*}{TU}\right)^{\frac{2}{3}}$ the two parts of the level sets touch each other approximately about the point with $r_a = r_p = 1$ in Figure 5.1. This condition is expressed by Equation 5.18 and will be clear from the 3D-characterization performed in the next section. At this condition there exist two distinct intersection points with the $r_a = r_p$ line, one in the prograde and the other in the retrograde region. By further decreasing T_* we enter in the high-energy realm, where we find the same curves used in the T-graph and with the 2BP

approximation. At these levels only one intersection occurs with the $r_a = r_p$ line and this is in the retrograde region. Figure 5.2 shows the relationship between the intersection coordinate r_c on the $r_a = r_p$ line as a function of the Tisserand level set for both prograde and retrograde regions just described at different levels of T_*.

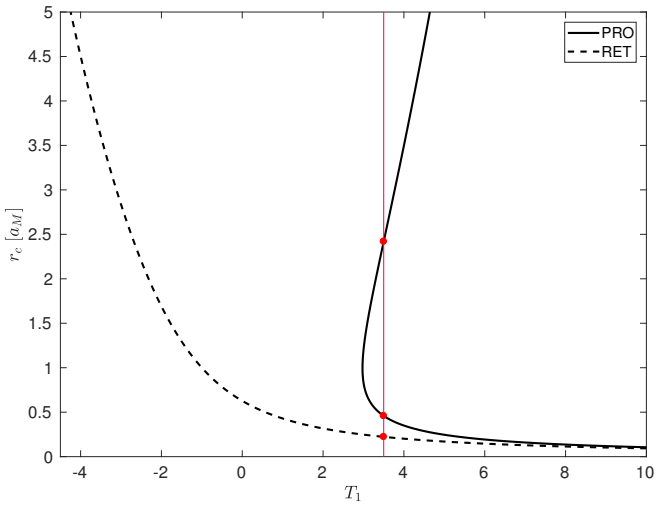

Figure 5.2: Sketch of the relationship between the intersection coordinate r_c on the $r_a = r_p$ line as a function of the Tisserand level set value for both prograde and retrograde regions. The three red points highlighted in this figure are also represented in the TP-graph in Figure 5.1.

It is possible to see that for high values of T_* (T_1 in this case for the EM system used to produce Figure 5.1) two of the three intersections occur close to each other but in the retrograde and prograde regions. As a consequence in this case the level sets in the bottom-left part of the graph can be approximated by lines of slope -1. This is a fundamental result that will play a crucial role in the characterization of the ETP-graph and will be discussed in detail in Section 5.3.

Another phenomenon that is possible to spot from Figure 5.1 is that for higher r_a the prograde region of the level sets become shallower. From Equation 5.2 it is possible to demonstrate the existence of a horizontal asymptote in the graph:

$$\lim_{r_a \to \infty} T_* = \frac{2}{TU}\sqrt{2\mu_* r_p} \tag{5.5}$$

from which it follows that the horizontal asymptote is represented by the line:

$$r_p^{\infty} = \frac{T_*^2 TU^2}{8\mu_*} \tag{5.6}$$

By choosing a specific CR3BP (fixing TU and μ_*) each level set possesses a horizontal asymptote, which is shifter upward when higher values of T_* are considered, as already illustrated in Figure 5.1. Another important feature of the graph is represented by resonance curves. As demonstrated in [10] these are lines of slope -1 described by the following equation when considering a constant $n : m$ resonance:

$$r_p = -r_a + 2\left(\frac{n}{m}\right)^{\frac{2}{3}} \tag{5.7}$$

where n is the number of body revolutions and m is the number of spacecraft revolution. The intersection between one of these lines and a Tisserand level set can be found by solving the following quadratic equation obtained by the combination of Equations 5.2 and 5.7:

$$r_a^2[-\mu] + r_a\left[2\mu DU\left(\frac{n}{m}\right)^{\frac{2}{3}}\right] - \left[-\frac{DUTU^2}{4}\left(\frac{n}{m}\right)^{\frac{2}{3}}\left(T - \frac{\mu}{DU\left(\frac{n}{m}\right)^{\frac{2}{3}}}\right)^2\right] \tag{5.8}$$

Amongst the large number of level sets that can be used in the TP-graph, the ones associated with the Lagrange libration points have important implications. Since these sets are associated to specific regions of space that are energetically accessible or not to the spacecraft, as discussed in Section 3.2.2, they are important to understand whether the spacecraft is in the desired energy state or not. These particular level sets are illustrated in Figure 5.3 for two different definition of Tisserand parameters.

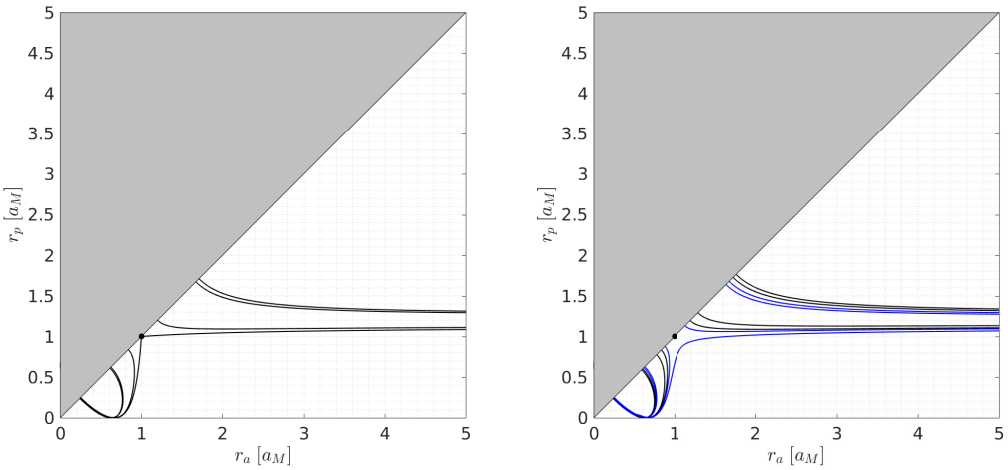

Figure 5.3: On the left: Level sets of $T_{L_1}, T_{L_2}, T_{L_3}$ and T_{L_4/L_5} using T_1^{cl} defined in Equation 4.48 for the Earth-Moon system. The sets are displayed from the outer to the inner region respectively. On the right: Level sets of $T_{L_1}, T_{L_2}, T_{L_3}$ and T_{L_4/L_5} using T_* defined in Equation 5.2 in the Earth-Moon system. The black curves display the sets when $T_{L_i} \approx J_{L_i}$, however since the relationship $J = T + P$ has been derived, the blue curves represent the level sets associated with the exact value of T_{L_i}, that is computed by adding the residual constant for the Poincaré section considered (3μ in this case) to the Jacobi constant value.

The level sets displayed in Figure 5.3 are computed with two different techniques. The one displayed on the left make use of the classical Tisserand parameter T_1^{cl} defined in Equation 4.48. In this case the approximation $T_{L_i} \approx J_{L_i}$ is used to represents the level sets in the graph as in [10],[9]. The graph on the right shows the level sets computed using the parameter T_1 defined in Equation 5.2. The level sets in black are yet computed with the approximation $T_{L_i} \approx J_{L_i}$, the ones in blue however are computed making use of the exact relationship between Tisserand and Jacobi integral $J = T + P$ derived in the previous section. In the latter case the value of the residual function P is related to the specific Poincaré section used to represent the osculating orbital elements. As it is possible to see that the difference between these different ways to represent the level sets is quite important, hence the necessity to discern between these cases. If not specified the blue level sets will be used in this report to represent the energy levels of the Lagrange libration points.

5.2. 3D GRAPH

In this section the characteristics of the $r_a - r_p - i$ TP-graph will be discussed. The generic expression of the Tisserand parameter can be written from Equation 5.1 as:

$$T_* = \frac{2\mu_*}{r_a + r_p} + \frac{2}{TU}\sqrt{2\mu_* \frac{r_a r_p}{r_a + r_p}} cos(i) \tag{5.9}$$

where the symbol $*$ is used to represent both T_1 and T_2 for a certain CR3BP specified by the TU normalization parameter. To better understand the shape of the level sets for the 3D case, two examples are illustrated in Figures 5.4 and 5.6 in 3D views, while their representations from different perspectives can be seen in Figures 5.5 and 5.7 respectively.

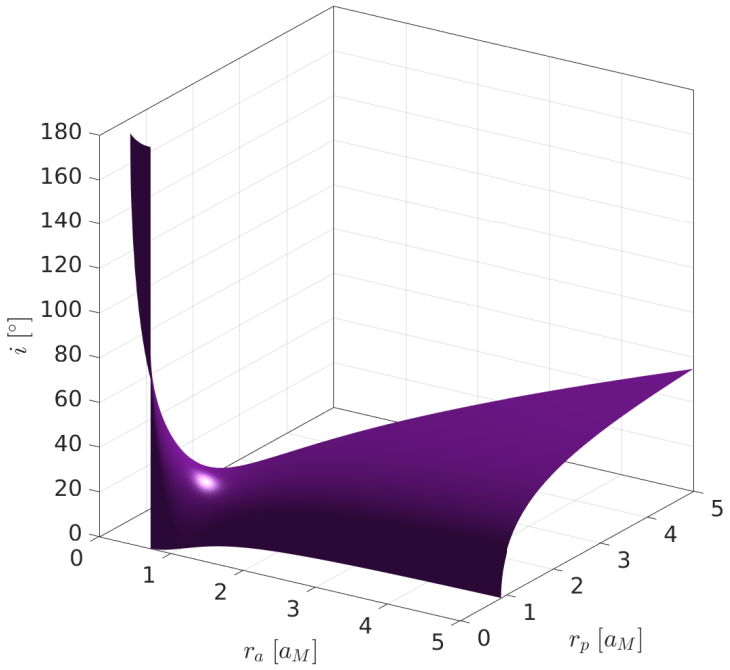

Figure 5.4: Tisserand level set in the $r_a - r_p - i$ TP-graph for the Earth-Moon system. The level set illustrated is $T_1 = 2.7635479951$ for a Poincaré section with $P_1 = 3\mu$.

The level sets, that in the 2D case are contour lines, are now surfaces within the $r_a - r_p - i$ volume of the TP-graph. A continuous surface is presented in Figures 5.4 and 5.5, while a separated one is presented in Figures 5.6 and 5.7. Once again the differentiation between these cases is represented by the condition expressed by Equation 5.18 that will be derived in this section. By looking at these figures it is possible to see that the portion reserved for retrograde motion ($i > 90°$) is much smaller than the one for prograde motion ($i < 90°$). Moreover while the latter seems to be distributed at higher values of r_a and r_p, retrograde motion only seems possible in the proximity of the body considered.

The general behavior of the surface can be easily characterized by looking at the five functions that define its borders in the graph. The functions f_1 and f_2 describe the characteristics of the level sets in the planar case for prograde and retrograde trajectories respectively. For these functions the level sets are described by the following implicit functions:

$$f_1 : T_* = \frac{2\mu_*}{r_a + r_p} + \frac{2}{TU}\sqrt{2\mu_* \frac{r_a r_p}{r_a + r_p}} \tag{5.10}$$

$$f_2 : T_* = \frac{2\mu_*}{r_a + r_p} - \frac{2}{TU}\sqrt{2\mu_* \frac{r_a r_p}{r_a + r_p}} \tag{5.11}$$

The characteristics of these have already been discussed in Section 5.1 and will not be repeated here. The interface line that connect these two functions in the 3D case is represented by the vertical line of Equation 5.4:

$$f_3 : r_a = \frac{2\mu_*}{T_*} \tag{5.12}$$

Note that in the 2D case this value differentiates between retrograde and prograde motion in a discrete way. However as it is possible to see from Figures 5.4 and 5.6, this distinction is not that clear in the 3D case.

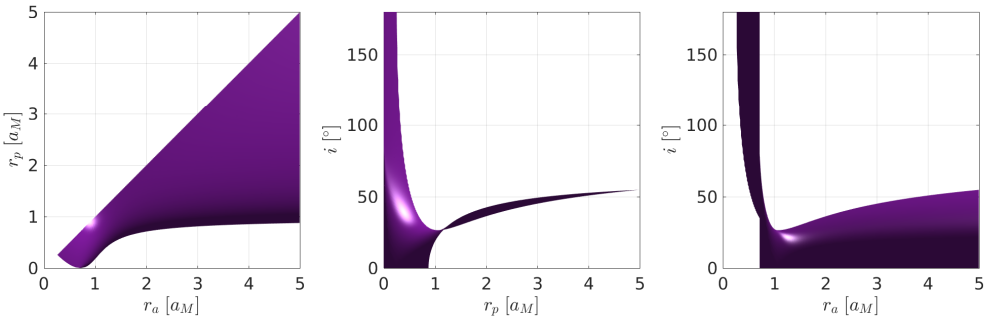

Figure 5.5: Different views of the Tisserand level set for the Earth-Moon system. The level set illustrated is $T_1 = 2.7635479951$ for a Poincaré section with $P_1 = 3\mu$.

The other two functions are f_4 and f_5. The first results from the intersection between the level set and the maximal value of r_a considered in the graph (five in this case). The latter is the intersection between the level set and the $r_a = r_p = r_c$ plane. These functions can be written in explicit form by considering that they develop entirely on the $r_a = 5$ and $r_a = r_p = r_c$ planes respectively:

$$f_4 : i(r_p) = acos\left[\frac{TU}{2}\frac{\left(T_* - \frac{2\mu_*}{r_a+r_p}\right)}{\sqrt{2\mu_*\frac{r_a r_p}{r_a+r_p}}}\right] \tag{5.13}$$

$$f_5 : i(r_c) = acos\left[\frac{TU}{2}\frac{\left(T_* - \frac{\mu_*}{r_c}\right)}{\sqrt{\mu_* r_c}}\right] \tag{5.14}$$

The analysis of f_5 reveals important properties of the level set in the 3D case. It is possible to clearly see the shape of this function from the $r_p - i$ views in Figures 5.5 and 5.7. The function has a maximum for low values of r_c, then a minimum point about $r_c \approx 1$ and finally shows a steady increase for higher values of r_c. By investigating f_5 for $r_c \to +\infty$ we obtain:

$$\lim_{r_c \to +\infty} f_5 = \frac{\pi}{2} \tag{5.15}$$

This proves an important characteristic of the level set that was only observed from the figures, that the region of retrograde motion is only possible closer to the body considered. Since the maximum of the surface in the prograde region will be located in the top-right part of the surface in the graph, and since it has been just demonstrated that this point can asymptotically reach only a polar orbit, there are no other regions of inversion of motion other than the one in proximity of the body considered. This is true when considering ballistic trajectories in the elliptic and circular regions and neglecting thrusting maneuvers.

The maximum of f_5 is equal to π and can be located by solving Equation 5.3 and considering only the solution in the retrograde region. The minimum point of f_5 can be computed by considering:

$$\frac{\partial f_5}{\partial r_c} = TU\frac{T_* r_c - 3\mu_*}{2r_c^2\sqrt{\mu_* r_c\left(1 - \frac{TU^2(\mu_* - T_* r_c)^2}{\mu_* r_c^3}\right)}} = 0 \quad \text{for} \quad r_c = \frac{3\mu_*}{T_*} \tag{5.16}$$

This condition corresponds to a point in the graph with the following coordinates of (r_a, r_p, i):

$$\left(\frac{3\mu_*}{T_*}, \frac{3\mu_*}{T_*}, acos\left[\frac{TU}{\mu_*}\left(\frac{T_*}{3}\right)^{\frac{3}{2}}\right]\right) \tag{5.17}$$

In particular this minimum point has a zero component of the inclination when the Tisserand level set is chosen to be:

$$T_* = 3\left(\frac{\mu_*}{TU}\right)^{\frac{2}{3}} \tag{5.18}$$

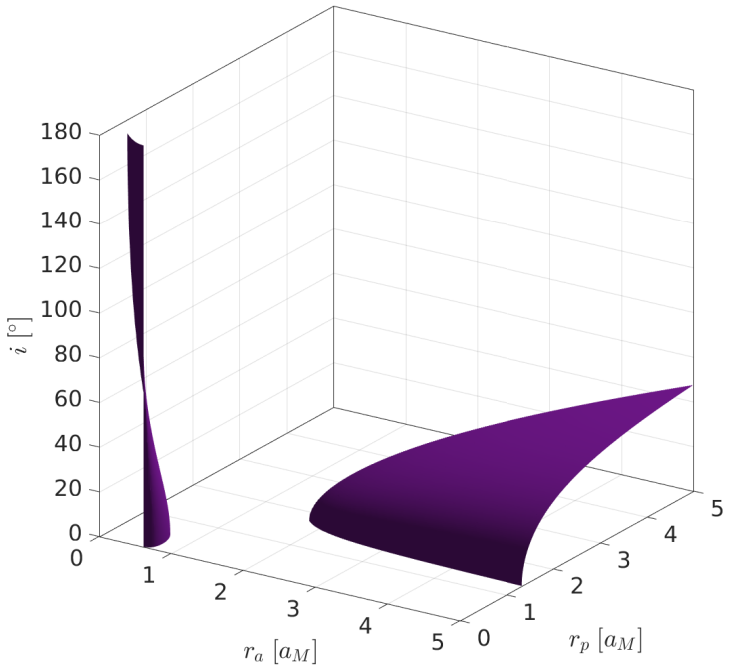

Figure 5.6: Tisserand level set in the $r_a - r_p - i$ TP-graph for the Earth-Moon system. The level set illustrated is $T_1 = 3.2$ for a Poincaré section with $P_1 = 3\mu$.

When this level set is chosen then the coordinates of the minimum of f_5 becomes:

$$\left(\frac{3\mu_*}{T_*}\,,\,\frac{3\mu_*}{T_*}\,,\,0\right) = \left(\frac{DU\mu_*}{\left[\mu_*^2\mu_1(1+\frac{\mu_2}{\mu_1})\right]^{\frac{1}{3}}}\,,\,\frac{DU\mu_*}{\left[\mu_*^2\mu_1(1+\frac{\mu_2}{\mu_1})\right]^{\frac{1}{3}}}\,,\,0\right) \approx (DU\,,\,DU\,,\,0)\,|_{\mu_*=\mu_1} \tag{5.19}$$

where the definition of TU as normalization parameter has been used. The reader can therefore imagine this critical point to be the passage between a single continuous surface as the one represented in Figure 5.4 to one divided into two parts as in Figure 5.6. This point represents this passage for both the 2D and the 3D cases, but as it is possible to see it can only be derived by considering the 3D case. The coordinates in Equation 5.19 explain why the point has been observed about the point $(1,1)$ in the 2D case for T_1 and demonstrate that such a point could be located on a different location when considering T_2.

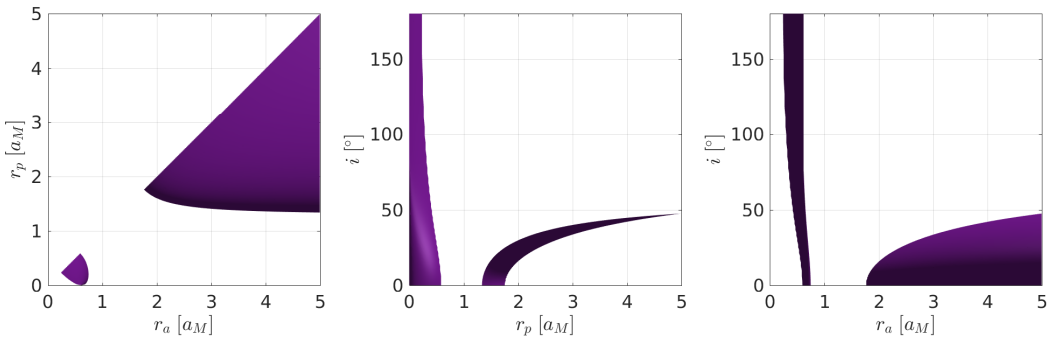

Figure 5.7: Different views of the Tisserand level set for the Earth-Moon system. The level set illustrated is $T_1 = 3.2$ for a Poincaré section with $P_1 = 3\mu$.

3D TP-graphs are generally not used for trajectory design in the CR3BP for the associated difficulty to design a trajectory in a spatial graph. Moreover assuming a planar motion for the spacecraft is often a good approximation of the real trajectory. This is not the case for missions such as EQUULEUS and DESTINY, that are expected to exhibit important out-of-plane components in their trajectories. In these cases the inclination parameter of the trajectory needs to be taken into account. Some examples of Tisserand level sets in the $r_a - r_p - i$ TP-graph can be seen in [10] for some planets of the Solar System and for the Moons of the Jovian system. In [10] some minor bodies are also presented in the 3D TP-graph. From this perspective the $r_a - r_p - i$ graph can be used to easily represent the characteristics of the minor bodies of the Solar System. By taking the data of the osculating orbital elements from the JPL Small-Body Database [1] of about 740000 minor bodies Figures 5.8 to 5.10 are obtained.

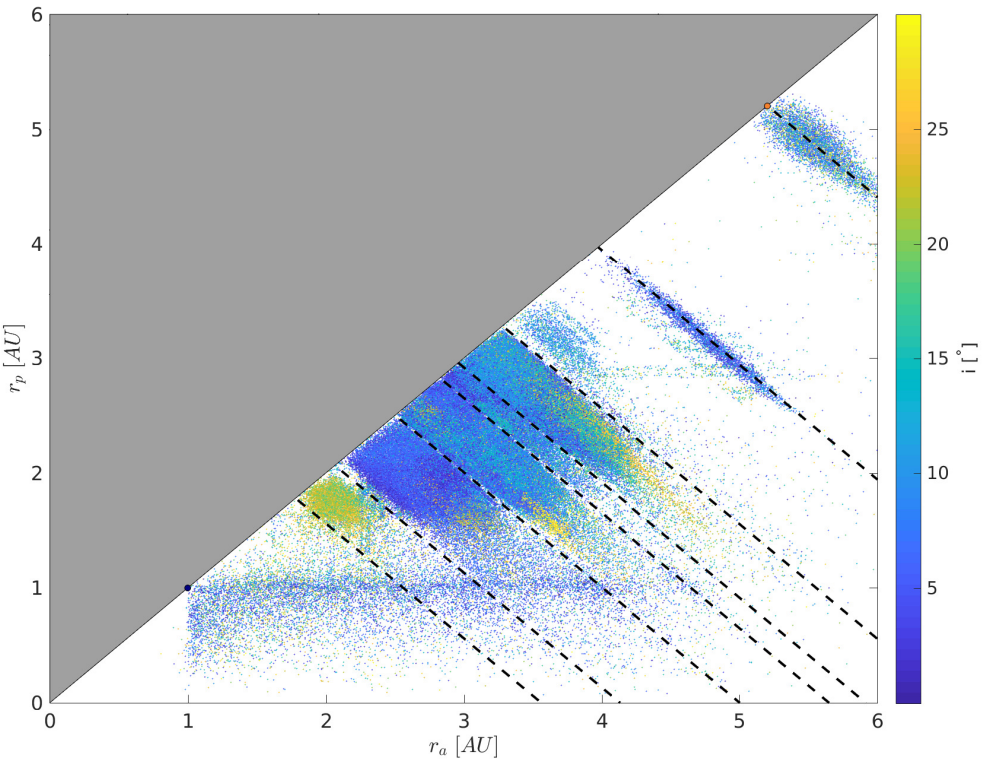

Figure 5.8: $r_a - r_p$ TP-graph with the discovered minor bodies of the Solar System up to 6 AU. The inclination of the bodies is represented by colors. In this figures only those with $i < 30°$ have been shown. Earth's orbit is represented by a blue dot, while Jupiter's by an orange one. The black dashed lines represent some resonance levels with the latter. From bottom to top they are the: 5 : 1, 4 : 1, 3 : 1, 5 : 2, 7 : 3, 2 : 1, 3 : 2 and 1 : 1 resonances.

The graph are reproduced here either directly in the 3D volume of the TP-graph as in Figure 5.9 or in a 2D projection on the $r_a - r_p$ plane with the inclination component represented by colors as in Figures 5.8 and 5.10.

Figures 5.8 and 5.9 represent the minor bodies within 6 AU from the Sun and with an inclination smaller than 30°. This corresponds to about 99.2% of the minor bodies in the database. In these cases the graph is an effective tool to have an overall visualization of the minor bodies distribution and orbital characteristics. The properties they exhibit in these graphs can be used to categorize them, as will be briefly discussed now. In both figures it is possible to distinguish between three classes of asteroids: NEOs (Near Earth Object), MBAs (Main Belt Asteroid) and Trojan asteroids.

[1] https://ssd.jpl.nasa.gov/sbdb_query.cgi#x, last accesed on September 5, 2017

NEOs pose a direct threat to Earth due to their osculating orbital elements being close to those of Earth's orbit. In the graph they can be observed about those lines determined by $r_a = 1$ and $r_p = 1$. The distribution of objects is denser along these lines due to the fact that objects crossing Earth's orbit might be easier to detect. On the other hand very few NEOs are observed for $r_a < 1$ and $r_p < 1$. This might be due to the geometric difficulty to observe them due to their angular vicinity to the Sun. NEOs population is usually subdivided into four categories depending on perihelia and aphelia, the interested reader may consult [2].

Trojan asteroid trajectories develop around the $L4$ and $L5$ triangular Lagrange libration points of the Sun-Jupiter CR3BP. Since they are in a $1:1$ resonance with Jupiter, it is possible to locate them on such a resonance line on the top-right part of the graphs.

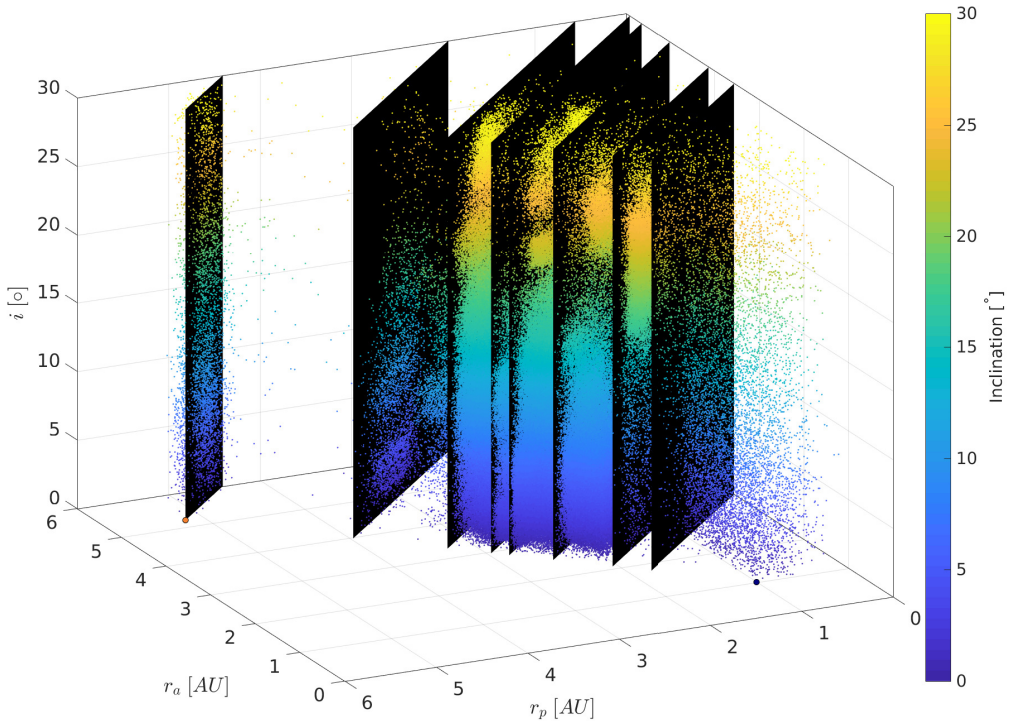

Figure 5.9: $r_a - r_p - i$ TP-graph with the discovered minor bodies of the Solar System up to 6 AU. The inclination of the bodies is represented by colors. In this figure only those with $i < 30°$ have been shown. The black planes represent the resonances with Jupiter, from bottom to top they represent the: $5:1, 4:1, 3:1, 5:2, 7:3, 2:1, 3:2$ and $1:1$ resonances.

In general resonance phenomena with Jupiter play a crucial role in the subdivision of asteroids in different categories and this is easily observed for the MBAs. These stretch across the graph between Mars and Jupiter orbits. Their distribution however is not homogeneous but is interrupted by several gaps, known as Kirkwood gaps, caused by resonance interactions with Jupiter. The most prominent ones are the $4:1$, $3:1$, $5:2$, $7:3$ and $2:1$ resonances [2]. Resonance phenomena may act differently in the inner and outer asteroid belt, for example on the contrary of the gaps observed before, there exist regions such as the $3:2$ and $4:3$ resonances where we can find a stable population of asteroids [2]. Usually an asteroid in the outer belt is perturbed so heavily by Jupiter to suffer a close approach with the giant planet and is scattered to interstellar space. These resonance regions however give stability to these asteroids by avoiding these encounters to happen [2]. In general the MBAs observed in Figure 5.9 show many groupings of asteroids with similar osculating orbital elements. These similar properties are used to categorize them, the full categorization is not illustrated here.

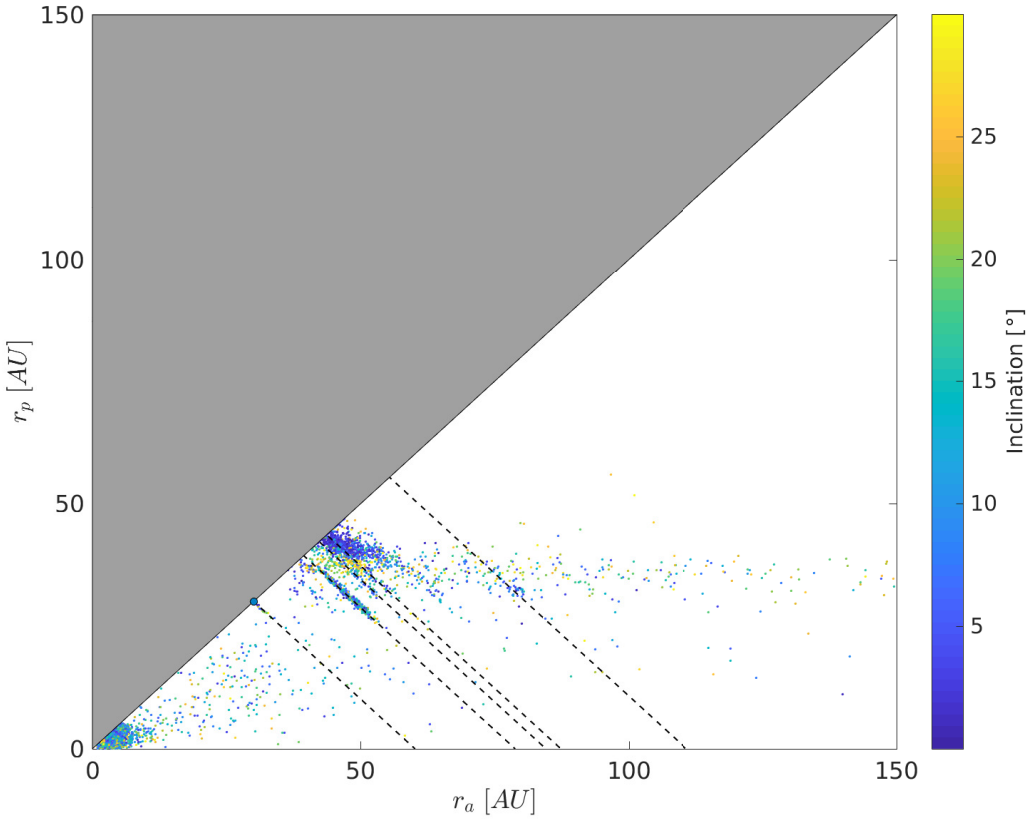

Figure 5.10: $r_a - r_p$ TP-graph with the discovered minor bodies of the Solar System up to 150 AU. The inclination of the bodies is represented by colors. In this figure only those with $i < 30°$ have been shown. The black dashed lines represent the resonance lines with Neptune, represented by the blue point. From bottom to top they represent the: 1 : 1, 2 : 3, 5 : 3, 7 : 4, 2 : 5 resonances.

Most of the small bodies of the Solar System are trans-Neptunian objects, characterized by orbits laying entirely or partially beyond Neptune's distance [2]. Due to their distances however these objects are very difficult to observe, hence in the database used only a small portion of these object is cataloged. For example in the database used to plot these figures only 3440 out the 740000 cataloged bodies (about 0.005%) have $r_a > 6$ AU. Many of the trans-Neptunian objects exhibit resonance phenomena with Neptune, as can be seen in Figure 5.10. Pluto and many other objects occupy the 2 : 3 resonance region and are called Plutinos, other populated regions are the 3 : 5, 4 : 7, 1 : 2 and 2 : 5 resonances [2].

5.3. ETP-GRAPH

In this section a different version of the qualitative ETP-graph [9] is presented that makes use of the findings on the Tisserand parameters discussed in the previous chapter. In this section the focus is put on the Sun-Earth and Earth-Moon CR3BP models, as they share Earth as a secondary and primary respectively. For the rest of the section the author will refer in short notation to the Earth-Moon system as EM and for the Sun-Earth system as SE. The expressions of the two Tisserand parameters T_1 and T_2 are:

$$\begin{cases} T_1 = \dfrac{2\mu_{Earth}}{r_a + r_p} + \dfrac{2}{TU_{EM}} \sqrt{2\mu_{Earth} \dfrac{r_a r_p}{r_a + r_p}} cos(i) \\ T_2 = \dfrac{2\mu_{Earth}}{r_a + r_p} + \dfrac{2}{TU_{SE}} \sqrt{2\mu_{Earth} \dfrac{r_a r_p}{r_a + r_p}} cos(i) \end{cases} \tag{5.20}$$

The two parameters refer to the same body, Earth, as main attractor to which the osculating orbital elements are referred. For this reason the μ of the Tisserand parameters are substituted to μ_{Earth}. The parameters are

therefore identical in each term except for the normalization parameter of the two CR3BP models, TU_{EM} and TU_{SE}. The Tisserand level sets that are generated from the planar case of these equations are illustrated in Figure 5.11.

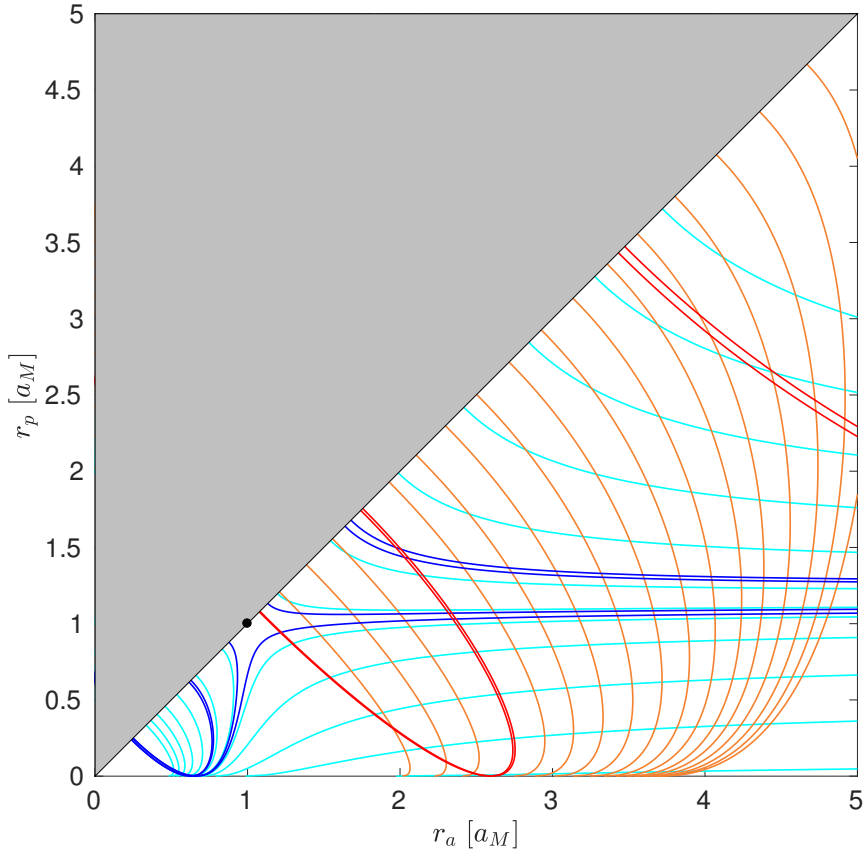

Figure 5.11: Tisserand level sets of the EM (blue and cyan) and SE (red and orange) systems. The level sets associated to the Lagrange points are represented in blue and red respectively, while generic level sets are represented in cyan and orange. The generic level sets are represented only for the prograde region to avoid confusion in the graph, while the Lagrange sets are represented both in the prograde and retrograde regions. The black dot is used as a reference for the osculating orbital elements of the Moon's orbit about Earth in the graph.

From this figure it is possible to understand the fundamental effects caused by the TU term in both parameters, especially in T_2. As said before the expressions of both parameters in the two systems are identical except from the value of TU used and for the systems considered $TU_{SE} \approx 13.4 TU_{EM}$. The result is that the level sets of T_2 almost preserve their shapes to the ones of T_1, but result scaled in the graph by a scaling factor of about $\frac{TU_{SE}}{TU_{EM}} \approx 13.4$. This scaling factor makes the level sets of the SE system to naturally develop on a bigger portion of the graph with respect to the level sets of the EM system. By closer inspection of Figure 5.11 the reader can realize that the level sets of the SE represented in this figure are essentially the scaled versions of the level set already presented in the lower-left part of the EM system.

A similar scaling effect has been observed in the classical T-graph when representing inner and outer planets of the Solar System in the same graph, as possible to see in Figure 3.13. However due to the non-existance of T_2 the same phenomenon has never been observed for a system such as the Sun-Earth-Moon system. The findings of the previous chapter overcome this limitation and for the first time allow an energetic representation of the level sets of two CR3BP models that share the same body as primary and secondary.

In this ETP-graph it is therefore possible to see the combined effects of Sun's perturbations and lunar flybys with respect to osculating orbital elements about Earth. It is interesting to observe that the prograde region of the level sets associated with $L1$ and $L2$ of the SE system intersects the prograde region of the level sets of all Lagrange points of the EM system. This is essentially describing well-known transfers between Lagrange points of different CR3BP models. On the other hand only the retrograde region of the level sets of the SE system associated with $L3$ and $L4$ are intersecting the ones of the EM system. These intersections however occur in the EM system in the prograde region, making the intersection unfeasible. In a certain region of the graph the level sets of the SE system act as lines of slopes -1 while they present a tail about the r_p axis. Both characteristics can be observed in the ETP-graph obtained in the qualitative analysis conducted in [9].

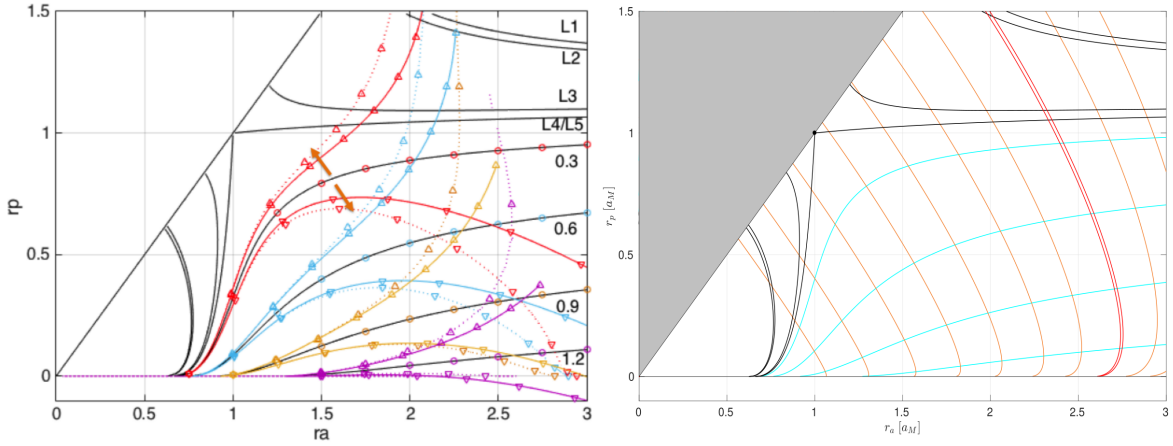

Figure 5.12: Comparison between different ETP-graphs. On the left: ETP-graph used in [9] with the Sun's perturbation described by an analytical approximation (continuous lines) and numerical analysis (dashed lines). On the right: ETP-graph produced with the modified Tisserand parameters derived in this report to reproduce Sun's perturbations. Note that the level sets of the EM system have been reproduced using the technique illustrated in Figure 5.3 (left) for comparison.

In Figure 5.12 the results presented in this report are confronted with the ones known in literature. As already discussed in Section 3.7.3, the results computed in [9] are the effect of an analytical approximation of the Lagrange planetary equations and from the application of a numerical technique. They represent the variation of the osculating orbital elements obtained by these two techniques after one orbital revolution. The level sets obtained in this report with the modified Tisserand parameter on the other hand are only energy level sets, thus they cannot show which points can be reached after one orbital revolution. However they elegantly explain the observed slopes of the level sets that have been approximated by Equation 5.3 and represented in Figure 5.2. Moreover by a closer inspection of Figure 5.12 it is possible to observe that for example the Sun's perturbation effects on the purple level set generate the tail structure close to the r_p axis. In light of the structure of the level sets illustrated in Figure 5.11 such a phenomenon is a natural characteristic of the level sets for low energies.

It is important to underline once more the crucial role played by the TU term in the derivation, without which the modified parameter would not exist and the scaling effect would not be possible in the ETP-graph. Following the classical derivation and the simplification assumptions this result would not have been visible.

Figure 5.13 shows an example of an intersection between two level sets of the SE and EM systems in the 3D EPT-graph. The intersection between the two surfaces can be found by solving the system expressed in Equation 5.20:

$$\begin{cases} r_p = \dfrac{\mu \pm \sqrt{\mu^2 - \left[\dfrac{T_1 - T_2}{2\left(\frac{1}{TU_1} - \frac{1}{TU_2}\right)cos(i)}\right]^2 \left[T_1 - \dfrac{T_1 - T_2}{1 - \frac{TU_1}{TU_2}}\right]}}{\left[T_1 - \dfrac{T_1 - T_2}{1 - \frac{TU_1}{TU_2}}\right]} \\ r_a = \dfrac{r_p \left[\dfrac{T_1 - T_2}{2\left(\frac{1}{TU_1} - \frac{1}{TU_2}\right)cos(i)}\right]^2}{2\mu r_p - \left[\dfrac{T_1 - T_2}{2\left(\frac{1}{TU_1} - \frac{1}{TU_2}\right)cos(i)}\right]^2} \end{cases} \tag{5.21}$$

Such results can be easily adapted for the planar case to determine the intersection between two level sets in the 2D ETP-graph.

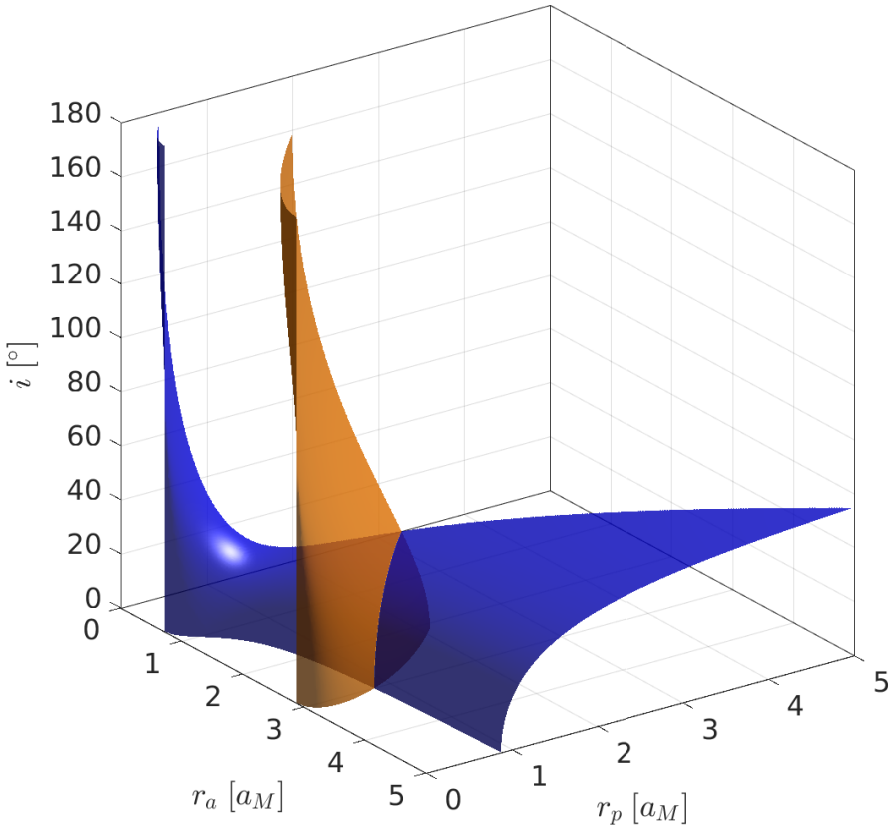

Figure 5.13: 3D ETP-graph with the level sets of the EM (blue) and SE (orange) systems. T_1 = 2.7635479951, while T_2 = 0.0008099999, corresponding to C_{EM} = 2.8 and C_{SE} = 3.00080098955727. The intersection between the two surfaces happens entirely in the prograde region.

From Figures 5.11 and 5.13 it is possible to see the powerful effect of Sun's perturbation to change the Jacobi integral of the EM system. Moreover as the SE surfaces are much more contained than the EM ones, prograde and retrograde motions could be simpler to connect on the SE level sets. This could explain the well known effect of these perturbations to change the sense of motion of a spacecraft. By looking at these figures it is possible to understand how this effect can be used as powerful tool to access previously denied regions of the TP-graph, literally allowing a movement across the level sets of the EM system.

5.4. CONCLUSIONS

In this chapter the Tisserand parameters T_1 and T_2 that have been derived in the previous chapter are used to display the Tisserand level sets in the TP-graph and ETP-graph. The latter is just a combination of multiple TP-graphs that allow the inclusion of Sun's perturbation.

Since the formulation of the two parameters is the same, the analysis has been carried out in this chapter for a generic Tisserand parameter $T*$ that can be used to describe both T_1 and T_2. All the results and mathematical formulations derived for $T*$ can be simply adapted to the level set described by T_1 or T_2 by simple substitutions. In this way both characteristics of the Tisserand level sets of these parameters in their corresponding TP-graphs have been characterized.

A crucial result illustrated in this chapter is that by combining the Tisserand level sets of the EM and SE systems into a single ETP-graph, we are able to produce a graph with Tisserand level sets that shows similarity with a qualitative analysis existing in literature [9]. The analysis performed in this chapter shows that the ETP-graph obtained by combining the level sets of T_1 and T_2 is capable to explain all the phenomenon described in previous frameworks associated with Sun's perturbing effects on the osculating orbital elements in the ETP-graph. This fundamental result has been achieved thanks to the different TU normalization parameters in the SE and EM CR3BP models. This difference acts as a scaling factor for the level sets represented in the ETP-graph in a similar way observed in T-graphs such as the one in Figure 3.13.

6

POINCARÉ MAPS

In this chapter the Poincaré sections defined by Equations 4.51 and 4.61 in Chapter 4 will be characterized in the planar cases of the Earth-Moon and Sun-Earth CR3BP models. The purpose of this chapter is to characterize the sections and the dynamics they are able to capture. The results of the EM system will be presented in Section 6.1 while the one of the SE system in Section 6.2; to conclude the chapter Section 6.3 illustrates the most important findings of this chapter. Additional material on derivations and maps that have not been included in this chapter can be found in Appendix E.

Numerous techniques make use of Poincaré maps to patch planar trajectories from different systems. For this reason the investigation of Poincaré maps obtained by using the sections defined in this report is interesting. Unfortunately fewer techniques that work in the spatial case exist and their application for the models considered in this report did not generate the desired results. Nonetheless the investigation in the planar case performed in this chapter will give important insight into the dynamics these sections are able to represent. In order to generate the maps in this chapter the following procedure has been adopted:

1. A value of the Jacobi constant C_{SB} is arbitrarily chosen.
2. As it is possible to see from the xy-view of the sections in Figures 4.8 and 4.9, the sections can be divided by four quadrants in the planar case of the SP1 and SP2 frames respectively. Only the portions of the sections in the II° quadrant are used to produce the maps. A total of 500 points are uniformly distributed in these portions between a minimum distance equal to Earth radius and a maximum distance of $5a_M$.
3. For each state the magnitude of the synodic velocity is computed from the expression of the Jacobi integral J_{SB}.
4. This velocity is then oriented in space with an angular separation of 1° for each position on the sections, ensuring that the transversality condition is not violated. This correspond to 358 angles for each position, for a total of 179000 propagation states that are therefore considered at each energy level.
5. The initial states are propagated forward in time for about six months in the EM system, while they are propagated backward and forward for about one year in the SE system.
6. The states and epochs of the intersection events with the sections are recorded. Collisions with Earth and/or Moon and escape events are also recorded, and whenever they occur the propagation is interrupted.

By following this procedure the characteristics of the intersection states and epochs in the Poincaré sections are recorded. The analysis of the results for the EM and SE systems will now be illustrated.

6.1. EARTH-MOON SYSTEM

Classical Poincaré maps obtained by plotting the $x\dot{y}$ or $\dot{x}y$ components of the states do not show any particular features. Interesting features however are possible to see by using $\dot{x}\dot{y}$ maps. Two of these are illustrated for the interior and exterior regions respectively in Figures 6.1 and 6.2.

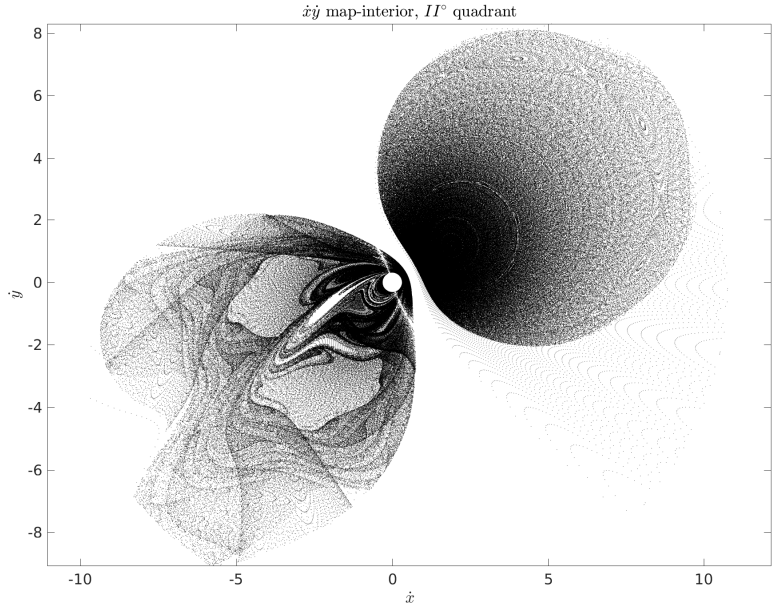

Figure 6.1: $\dot{x}\dot{y}$ map for points in the interior region obtained with $C = 2.91200302955986$ and $P_1 = 3\mu$, considering the Poincaré section in the II° quadrant of the SP1 frame.

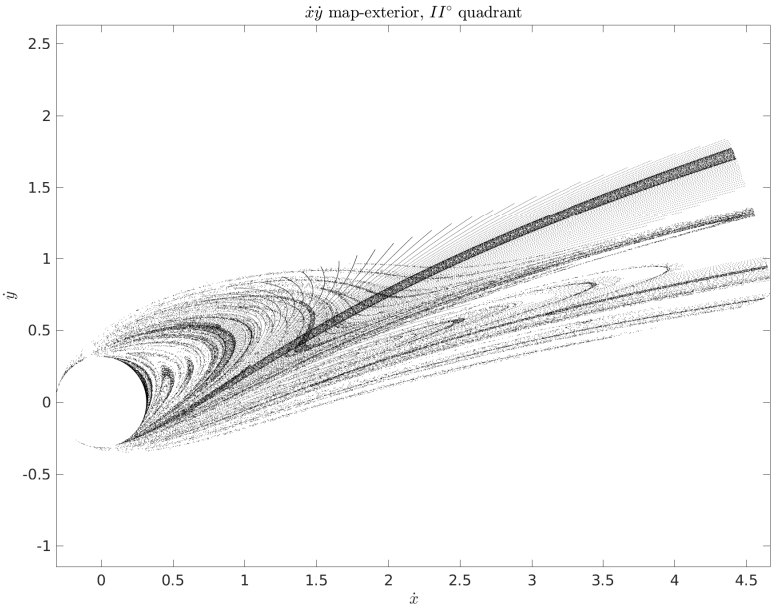

Figure 6.2: $\dot{x}\dot{y}$ map for points in the exterior region obtained with $C = 2.91200302955986$ and $P_1 = 3\mu$, considering the Poincaré section in the II° quadrant of the SP1 frame.

These maps are obtained in the EM system by using the components of the synodic velocity of the intersection states. In order to be able to reconstruct the full state from the map however it is necessary to differentiate between interior and exterior region. Figure 6.3 shows these two regions on the section considered to obtain the maps in Figures 6.1 and 6.2.

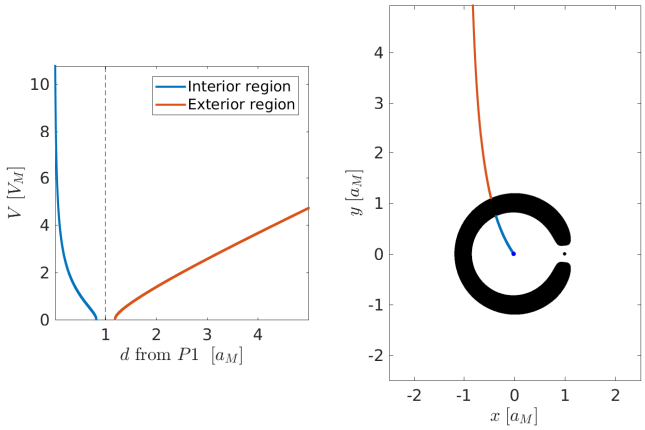

Figure 6.3: On the left: Visualization of the magnitude of the synodic velocity as a function of the distance from the primary for points taken on the Poincaré section. Note that the function has a minimum in proximity of the secondary distance, but goes to $+\infty$ for $d \to 0$ and $d \to +\infty$. On the right: Representation of exterior and interior regions in the position phase space, together with a representation of the Hill's surface at such energy level.

Since each map is tied to a value of C_{SB} (and P_1, defining the Poincaré section considered) by taking any point $\dot{x}, \dot{y}$ from an undifferentiated map there would exist two sets of solutions for the position on the section that could have these velocity components. As it is possible to see from Figure 6.3 there are two values of distances from P_1 with the same magnitude of synodic velocity, making it impossible to reconstruct the exact state of a point represented on the map. To avoid this ambiguity the sections are differentiated between interior or exterior points.

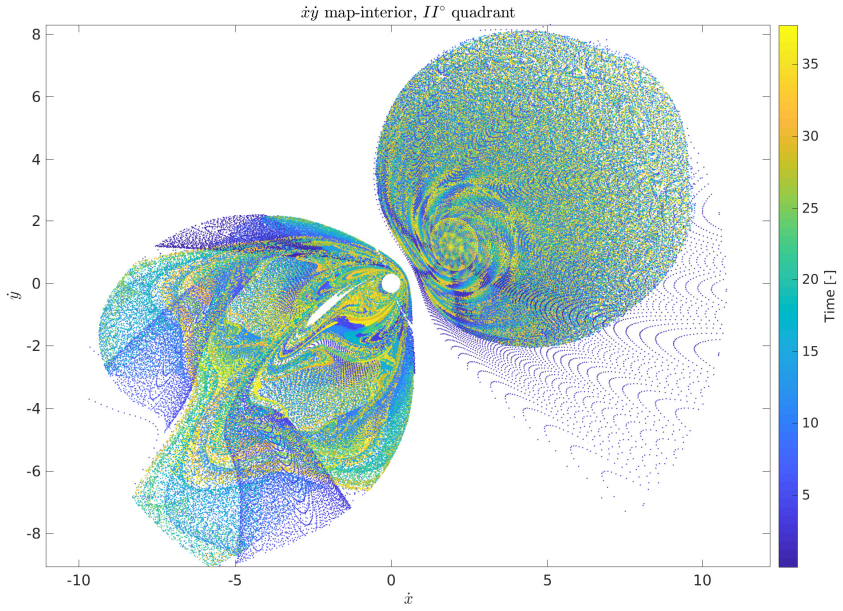

Figure 6.4: $\dot{x}\dot{y}$ map for points in the interior region obtained with $C = 2.91200302955986$ and $P_1 = 3\mu$, considering the Poincaré section in the II° quadrant of the SP1 frame. Colors represent the intersection epochs with the section.

The maps in Figures 6.1 and 6.2 have numerous interesting features. First of all it is possible to observe a very neat separation of the points in the interior map into two different regions. These are approximately contained in the I° and III° quadrants of these plots and characterize retrograde and prograde motion respectively. Inspecting the retrograde region, it is possible to see the presence of various tori as well as numerous resonance lines and chaotic regions between them. All these features seem to be centered on a particular velocity state that will be discussed later in this section. This region is much more organized than its prograde counterpart, which exhibits a more chaotic behavior. The white spots at the center of the maps are caused by the minimum achievable synodic velocity, that is a function of the energy level considered in the maps.

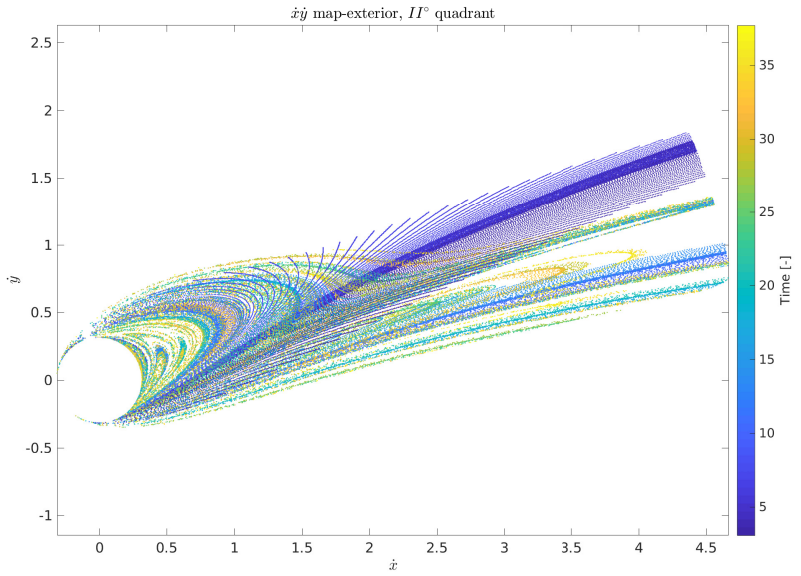

Figure 6.5: $\dot{x}\dot{y}$ map for points in the exterior region obtained with $C = 2.91200302955986$ and $P_1 = 3\mu$, considering the Poincaré section in the II° quadrant of the SP1 frame. Colors represent the intersection time with the section.

The regularity of both maps is disturbed by a number of points that traverse the map. These can be identified from Figures 6.4 and 6.5 as the blue points in the maps. Since these points occur quite early during the propagation and are located in a region with relatively high velocity, they correspond to hyperbolic trajectories traversing the system very quickly or to collision trajectories with Earth. The latter can be seen in the interior map both in the prograde and retrograde regions, while the first ones are clearly visible in the exterior map.

A close inspection of the interior map can be seen in Figure 6.6. From this figure it is possible to observe the net separation at low velocities between retrograde and prograde regions. The white band in the prograde region in this figure is due to the transversality condition imposed on the Poincaré section. From Figure 6.6 it is also possible to observe resonance: concentric lines in the retrograde region (upper right) centered on a point with coordinates about $\dot{x} = 2$ and $\dot{y} = 1$. This particular point in the map corresponds to a stable retrograde circular orbit about Earth whose characteristics are fundamental to understand a unique phenomenon caused by the Poincaré section used.

The characteristics of the Tisserand level sets have already been presented in Chapter 5. By looking at Figure 5.1 it is possible to see that the retrograde region of the level sets extends in a very limited portion of the graph and that it behaves in a similar way as resonance lines, that have slopes of -1 in the TP-graph. By choosing a Poincaré section that has the property of having a constant Tisserand parameter we are essentially considering points that are all lying on the same Tisserand level set. The author therefore believes that such a carefully designed section exalt the natural alignment existing between retrograde level sets and resonance lines, enhancing the properties of stable retrograde trajectories in the Poincaré maps just presented. The centered tori in fact turned out to be circular trajectories whose characteristics are determined by the intersection of

the Tisserand level sets considered in the map and the line $r_a = r_p = r_c$ in the TP-graph. All other tori around the center have resonances similar to the one of this specific orbit.

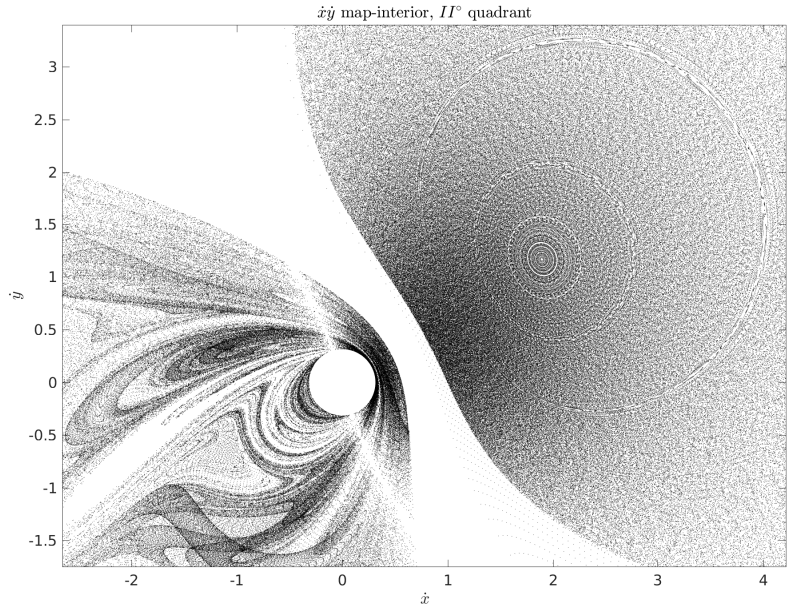

Figure 6.6: Zoomed $\dot{x}\dot{y}$ map for points in the interior region obtained with $C = 2.91200302955986$ and $P_1 = 3\mu$, considering the Poincaré section in the II° quadrant of the SP1 frame.

This phenomenon is also occurring for prograde trajectories at specific energy levels, since as seen in Figure 5.1 there exist level sets aligned to lines of slopes -1 also in the prograde region of the level set. The very cover of this report is such a case with tori both in the retrograde and prograde portions of the map. Other tori can be observed in the prograde region also for the additional maps presented in Appendix E. An enhanced version of the features of the interior map is represented in Figure 6.7 by making use of the symmetries of the CR3BP and representing the intersection points with the section from both the II° and III° quadrants.

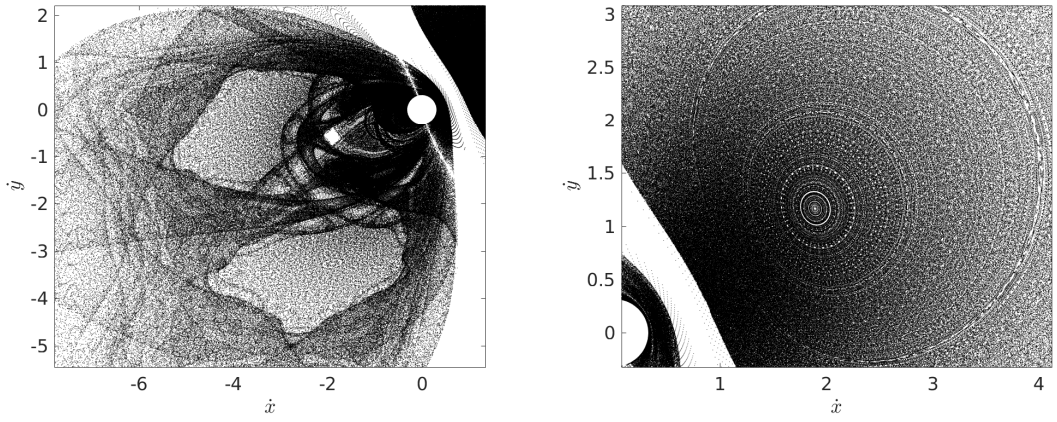

Figure 6.7: Enhanced interior $\dot{x}\dot{y}$ map obtained exploiting symmetry properties in the CR3BP and representing the intersection points with the Poincaré section in the II° and III° quadrants. The focus is put on the prograde region (left) and retrograde region (right) to enhance characteristics of period trajectories in the map.

This map considers double the points of a classical maps and its sole purpose is to highlight the characteristics of periodic orbits. Note that the map is technically incorrect since the representation of points from both the II° and III° quadrants does not allow for a unique reconstruction of the state. Nonetheless it is used here only to illustrate more clearly the difference between the structure of the tori in the prograde and retrograde regions. In the latter a torus can be located at the point of coordinate $\dot{x} = 2$, $\dot{y} = 1.3$ while in the former two tori are identifiable within the sea of chaos at the points of coordinates $\dot{x} = -2$, $\dot{y} = -3$ and $\dot{x} = -4$, $\dot{y} = -0.5$.

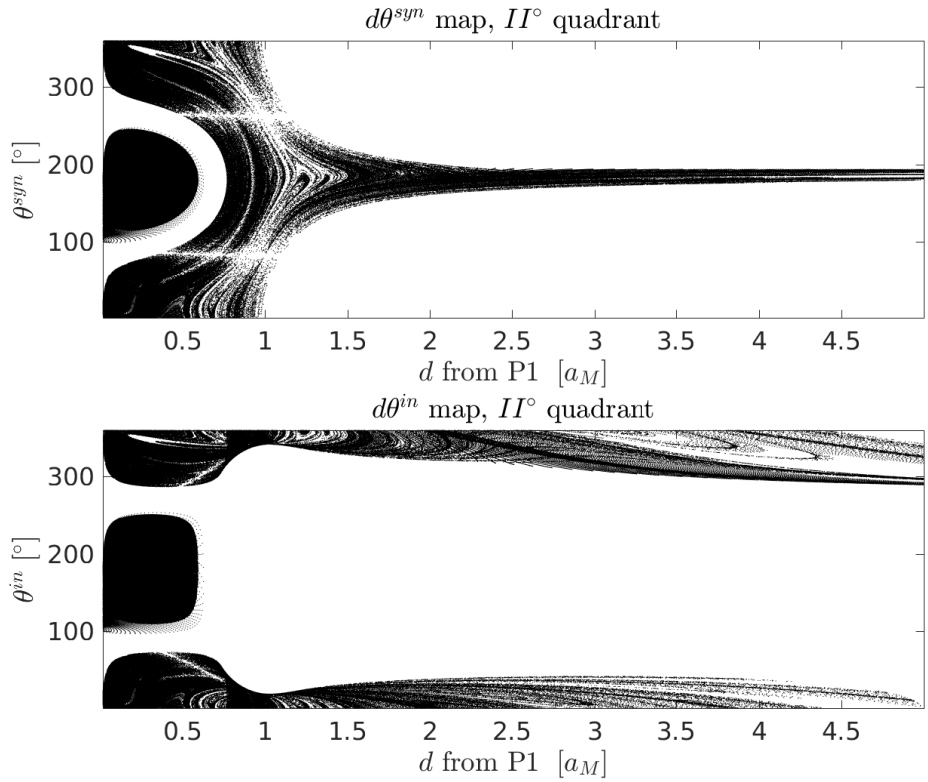

Figure 6.8: Poincaré maps used to highlight the orientation of the velocity vector in the synodic and inertial frames, V_{syn} and V_{in} respectively. The x-axis provides the distance from the primary P1, while the y-axis provides the angle of the synodic and inertial velocity with respect to the tangential velocity of the synodic frame.

Another interesting result can be observed from the maps represented in Figure 6.8. These maps represent the orientation of the synodic and inertial velocities as a function of the distance from the primary for points on the Poincaré section. The transformation equations to obtain θ^{syn} and θ^{in} are derived in Appendix E. Is important to remark that the state cannot be reconstructed in a unique way from the $d\theta^{in}$ map, that therefore is not properly a Poincaré map. Nonetheless such a graph is briefly used here to illustrate the difference between prograde and retrograde trajectories. These are separated in $d\theta^{syn}$ by a pointless region with a mirrored C shape enveloping a dense packed region of points. The latter represents all the retrograde trajectories, while all the other points are prograde ones. In the white region between them the angular momentum changes sign and generally collision trajectories with Earth are contained in this part of the map. From the shape of this region it would be possible to know which orientation to give to the synodic velocity in the SB frame on a specific point on a section to generate or avoid a collision trajectory with Earth. The distinction between prograde and retrograde trajectories is much more clear in the $d\theta^{in}$ graph, where these have respectively $\theta^{in} < 90 \wedge \theta^{in} > 270$ and $90 < \theta^{in} < 270$. From this graph it is possible to see that the only existing retrograde trajectories are constrained in the interior region of the system. This phenomenon has been observed in Figure 6.2 and is related to the properties of the Tisserand level set highlighted in Section 5.2 by Equation 5.15.

In the planar case of the CR3BP an analytic implicit relationship can be derived to describe the points in the $d\theta^{syn}$ map. This relationship is illustrated in appendix E by Equation E.19. From these expressions it has been found that the points in the $d\theta^{syn}$ map are distributed following a specific relationship that is dependent on the set of r_a and r_p values used. In practice Figure 6.9 represents different points in the $d\theta^{syn}$ map that can be obtained with this relationship using different sets of r_a and r_p on the Tisserand level set of the EM system.

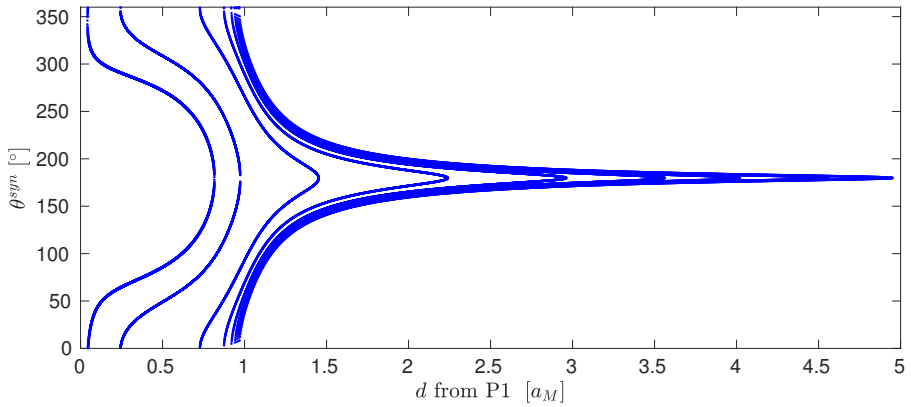

Figure 6.9: Analytic representation of the curves reproduced in the $d\theta^{syn}$ map. Each curve is obtained by choosing a value of r_a and r_p on the Tisserand level set at the energy level considered. For this representation C_{SB} = 2.91200302955986.

The presence of such a relationship makes it possible to generate these structures in a very organized way and in principle can also be used in substitution of the map to patch trajectories together. Each curve in Figure 6.9 is obtained by choosing a set of r_a and r_p values on a Tisserand level set. These two values can be recognized from the graph from the minimum and maximum distance of each of the curves in the graph. The curves also show that in the synodic frames for any distance there exist two directions of the synodic velocity that would generate a Keplerian orbit with the desired r_a and r_p, introducing an ambiguity if only the position and the osculating orbital elements are used. The only time this ambiguity is solved occurs when the distance considered is exactly equal to r_a or r_p, as in this case only one point exists, as it is possible to see in the figure. A similar phenomenon will be illustrated for the spatial case in Chapter 7.

6.2. SUN-EARTH SYSTEM

The same analysis that has been performed in the Earth-Moon system using the Poincaré section about the primary is now briefly repeated for the Sun-Earth system using the section about the secondary. An example of an $\dot{x}\dot{y}$ map of this system is given in Figure 6.10.

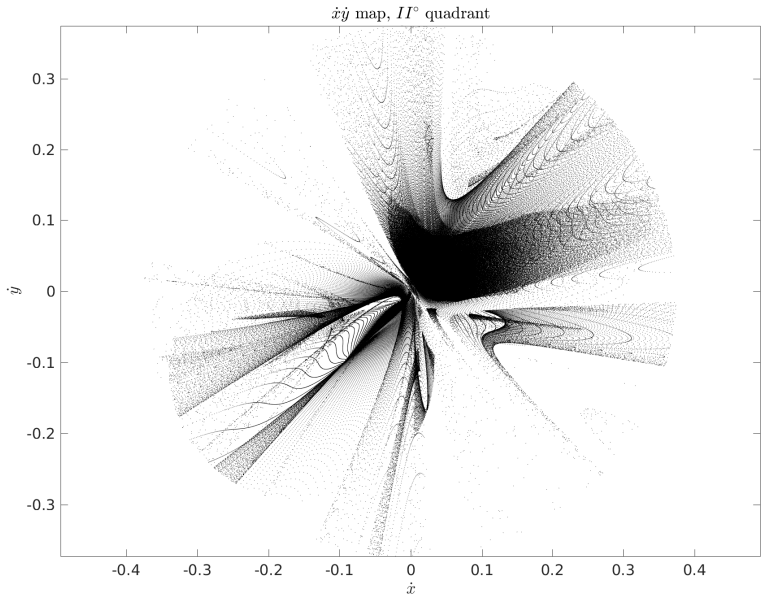

Figure 6.10: $\dot{x}\dot{y}$ map obtained with $C = 3.00075300347189$ and $P_1 = 3(1-\mu)$, considering the Poincaré section in the II° quadrant of the SP2 frame of the SE system.

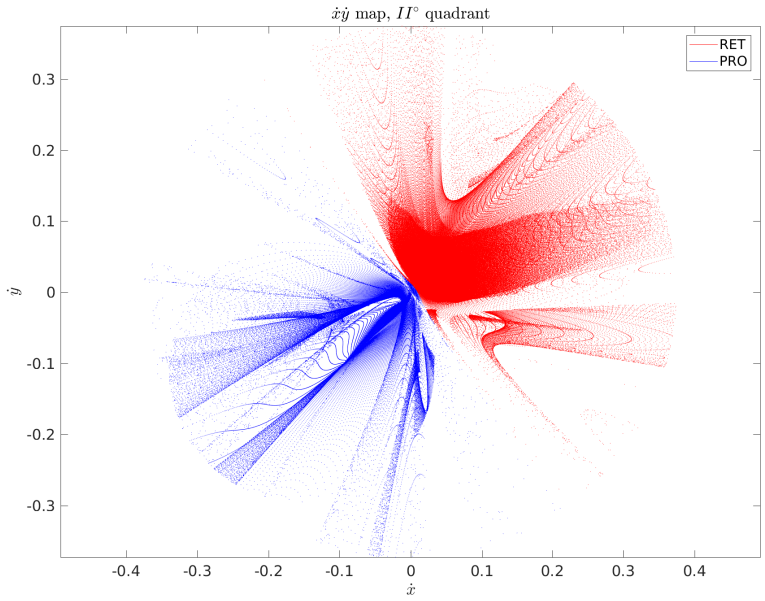

Figure 6.11: Subdivision between retrograde and prograde points in the map illustrated in Figure 6.10. Red points represent retrograde trajectories while blue ones prograde ones.

In this case it is not necessary to distinguish between interior and exterior regions, as the points chosen on the

section (within $5a_M$ distance from Earth) are all considered in the interior region of the system for the energy level considered. In the map in Figure 6.10 the distinction between prograde and retrograde trajectories is not clearly visible as in Figure 6.1. To better understand it Figure 6.11 represents this distinction with colors.

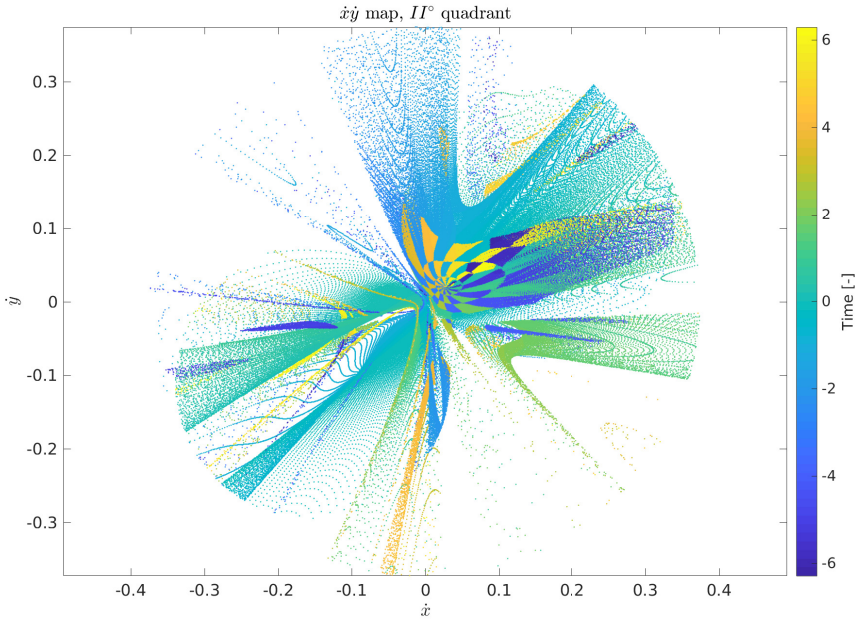

Figure 6.12: $\dot{x}\dot{y}$ map obtained with $C = 3.00075300347189$ and $P_1 = 3\left(1-\mu\right)$, considering the Poincaré section in the II° quadrant of the SP2 frame of the SE system. Colors indicate the intersection time.

Generally speaking the map for the SE system looks much more diversified than the one obtained in the EM system. Clear structures cannot be observed apart from the ones in the retrograde region, where tori and resonance lines are identified. A close-up of this region can be observed in Figure 6.13.

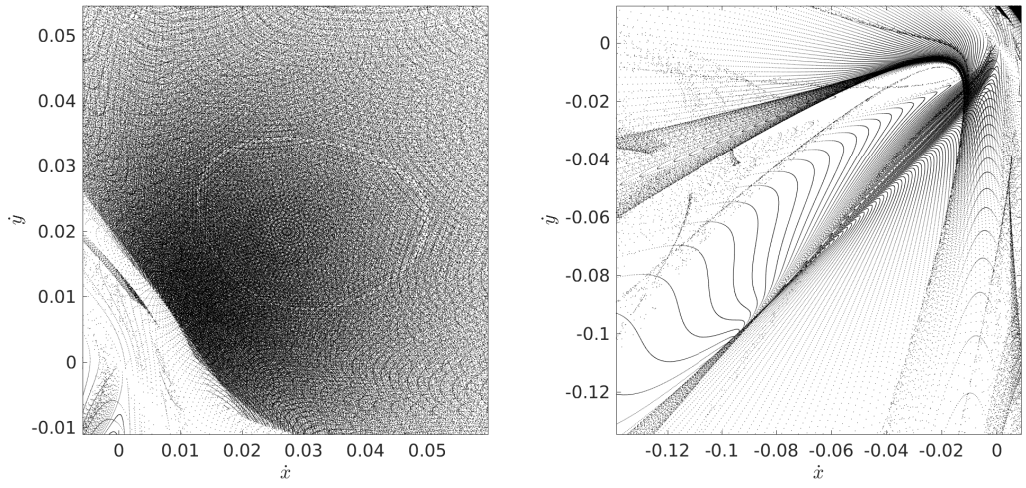

Figure 6.13: Zoom of the $\dot{x}\dot{y}$ map in Figure 6.10 in the retrograde and prograde regions, left and right respectively. On the left it is possible to see the tori structure surrounded by resonant regions. On the right it is possible to see different structures corresponding to specific types of motion in the SE system.

The explanation for this phenomenon has been discussed already in the previous section, where it was linked to a similarity between the resonance line and the Tisserand level sets in the retrograde region. The center of the tori has been identified with the circular orbit with the osculating orbital elements equal to the intersection point between the Tisserand level set and the line $r_a = r_p = r_c$ in the TP-graph. Because of the shape of the Tisserand level set in the SE system, one would expect to be able to clearly see circular orbits both in the retrograde and in the prograde regions of the map. This however does not occur, since also this time only retrograde circular orbits are the only one clearly visible. The reason why this phenomenon occurs can be explained by an inherent stability of retrograde trajectories with respect to prograde ones in the CR3BP model. Weakly stable trajectories have been observed from points in the map proper of circular orbit in the prograde region, however these temporarily captured trajectories are heavily perturbed and generally do not last more than a few revolutions about Earth in the synodic frame. An example of such a trajectory is given in Figure 6.14.

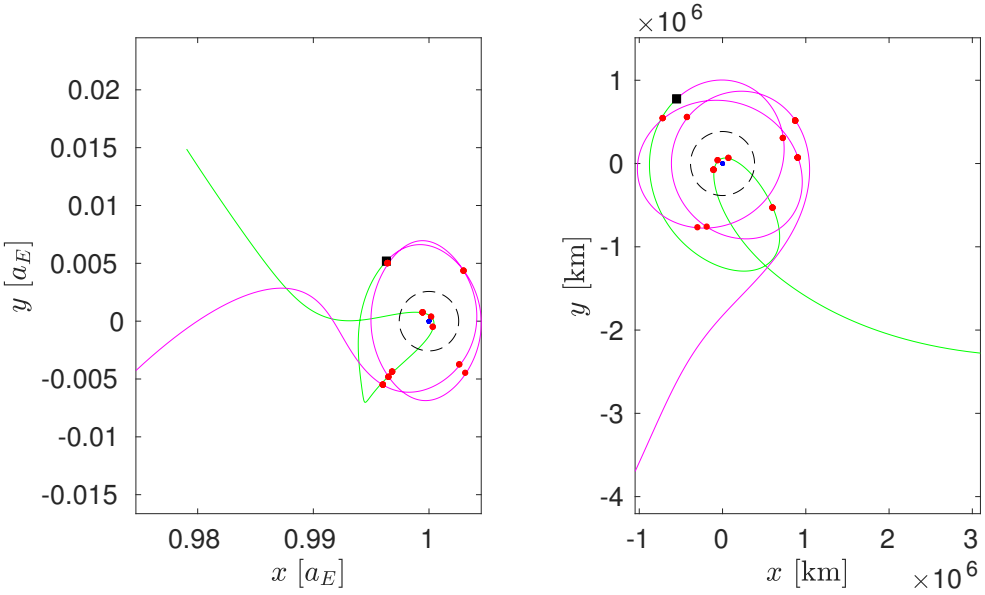

Figure 6.14: Example of a temporarily captured prograde trajectory about Earth in the SE system. On the left the trajectory in the SB frame, on the right in the IP2D frame. The initial propagation point is represented by a black square while the intersections with the Poincaré section are represented by red dots. The green and pink trajectories are propagated forward and backward from the initial state. The total TOF of the trajectory is about 480 days. Moon's orbit is represented by a black dashed circle just for reference. To obtain this trajectory the initial state considered is $X_0 = [0.9963\ 0.00519\ 0\ -0.0103\ -0.01083\ 0]^T$.

Another interesting phenomenon is the fact that generally in the SE system many more colliding trajectories with Earth have been observed than in the EM system. This is likely explained as a result of the well-known ability of the Sun's perturbation to invert the sense of motion of a trajectory, as explained in Section 3.4.

The same $d\theta^{syn}$ and $d\theta^{in}$ maps used in the EM system are now also represented for the SE system for comparison. In this case the distinction between prograde and retrograde trajectories is less clear, also because of the presence of many collision orbits with Earth. Also in this case an analytic expression can be derived to describe the distribution of the points in the map depending on the values of r_a and r_p chosen. The derivation of this analytic expression is presented in appendix E. Figure 6.16 shows the representation of points in the map that have the same sets of r_a and r_p.

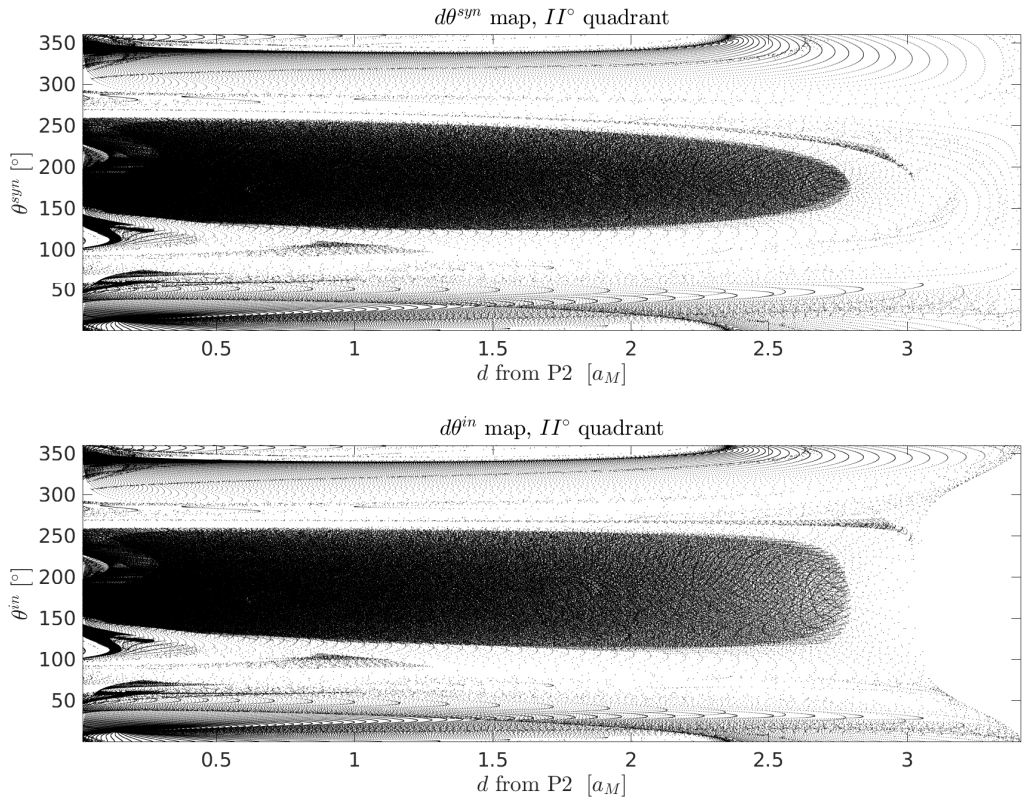

Figure 6.15: Poincaré maps used for the understanding of the direction of V_{syn} and V_{in}. The x-axis shows to the distance from the secondary P2, while the y-axis gives the angle of the synodic and inertial velocity with respect to the normal line to the distance vector.

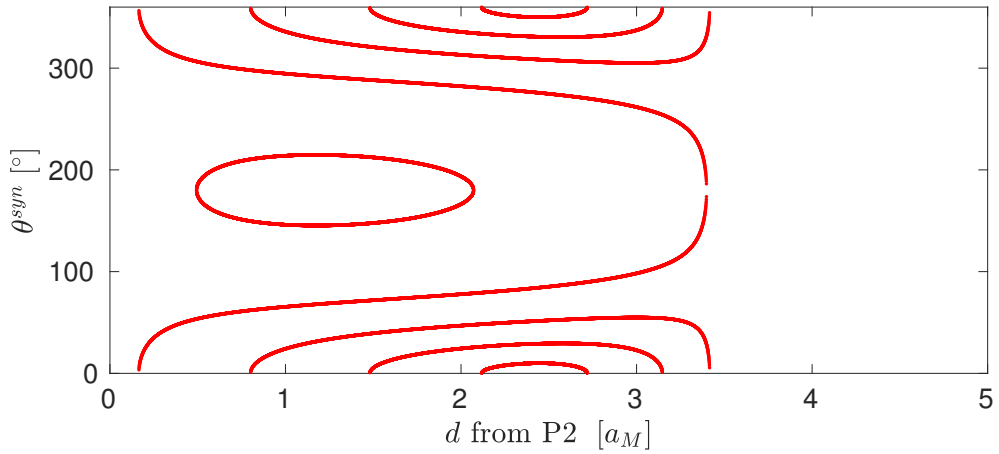

Figure 6.16: Analytic representation of the curves reproduced in the $d-\theta^{syn}$ map. Each curve is obtained in the map by choosing a value of r_a and r_p on the Tisserand level set at the energy level considered. For this representation $C = 3.00075300347189$.

6.3. CONCLUSIONS

In this chapter the Poincaré sections about the primary and secondary defined by Equations 4.51 and 4.61, respectively in the SP1 and SP2 frames, have been characterized and tested for real trajectories in the EM and SE CR3BP models. Although the characterization has been performed in the planar case of these models, it already shows numerous features of these sections that were previously unknown.

The Poincaré sections used in this chapter all have a constant value of the Jacobi constant, but also a constant value of the Tisserand parameter (depending the section considered). In this sense they are unique and their characterization has been carried out in this chapter for the very first time.

An interesting result that has been observed through the usage of these sections is the importance that is given to retrograde trajectories, whose characteristics seems to be naturally enhanced by the properties of the Tisserand level sets. Although this represent an interesting research point, it would hardly be practical for engineering applications as retrograde trajectory are generally energetically difficult to reach. This however is not difficult to achieve when considering Sun's perturbations. For this reason an interesting recommendation for future studies could be to investigate the usage of Sun's perturbed trajectory to exploit the inherent stability exhibited by retrograde trajectories for scientific orbits about a target body such as a primary or secondary.

Another interesting result was associated to collision orbits with Earth and Moon and the regions in which they are represented in the maps. These have not been investigated further in this research, however they could represent an interesting application of the maps, given their relative simplicity to represent both prograde and retrograde motions in clearly separated regions.

Note that some attempts have been made to represent similar maps for spatial trajectories, however the results did not allow a clear interpretation of the maps. The impossibility to use these maps for the spatial case is a strong limit to their application. Moreover even an application in the 2D case would be limiting, since the two Poincaré sections of the systems are defined in two different synodic frames. This would limit the possibility of intersections between the sections only at defined geometric configurations between the bodies considered.

The analyses in this chapter have been focus on specific energy levels. However Appendix E contains some Poincaré maps at other energy levels as well as the representation of particular orbits that are represented by specific points in the maps.

7

DATABASE APPROACH

In this chapter a trajectory design approach based on a database that exploits the theoretical findings of the previous chapters is developed. In Section 7.1 the structure of the database will be illustrated. In Section 7.2 some examples of trajectories designed with the database are presented. In Section 7.3 the difference between trajectories designed in the CR3BP and BR4BP are stressed to indicate what general considerations must be taken into account while applying the tool developed in this chapter. Finally in Section 7.4 the main findings of chapter are summed up. Additional material about EQUULEUS trajectory can be found in Appendix D, while its trajectory design process has been already discussed in Chapter 2.

The characteristics of solar perturbations illustrated in Chapter 3 are relevant for missions such as EQUULEUS and DESTINY, that heavily rely on them to save ΔV. Single or multiple transfer legs that traverse the solar perturbed region exterior to the Earth-Moon system can be designed for this purpose. The design of these trajectories however can be complex in a 4BP such as the BR4BP model. Since the system is non-autonomous, a trajectory designed in such a model would also be sensitive to the initial conditions chosen, that are often tailored to the specific mission considered. To avoid this, a simplified system made up by patched dynamical models can be used. The one that best approximate the Sun-Earth-Moon BR4BP is a patched model made by the EM and SE CR3BP models.

The focus of this chapter is the development of a trajectory design tool that makes use of solar-perturbed transfer legs to design trajectories in the Sun-Earth-Moon system. These transfer legs are computed in the SE CR3BP and are stored in a database. These trajectories are defined in the SE synodic frame and since they have been computed in an autonomous system the database they constitute is universal. This means that they can be used for every desired phasing configuration between the EM and SE CR3BP models. This approach is very flexible because it makes the database applicable to the specification of every mission desired. If the proper phasing is taken into consideration the transfer trajectories in the database can be also patched with trajectories obtained from different dynamical models than the EM CR3BP (such as the 2BP, BR4BP and full-ephemeris models) as it is illustrated in this chapter.

7.1. DATABASE STRUCTURE

In this section a database approach is designed that makes use of the Poincaré section defined about the secondary by Equation 4.61. The database is constructed by legs of trajectories connecting different points on the Poincaré section. The idea is that by using such a catalog of section-to-section trajectories in the SE CR3BP it would be possible to design a patched trajectory computed in different dynamical models (Earth 2BP, EM CR3BP, SEM BR4BP, full-ephemeris and so forth). The algorithm to populate the database is illustrated in the following steps:

1. A value of the Jacobi constant C in the SE system is chosen.
2. A set of points is identified on the Poincaré section within a limited region about the secondary ($a_M <$

$d_{P2} < 5\ a_M$) such that the maximal distance between any of these points is 50000 km. The coordinates that make it possible to achieve such a distribution are not affected by the value of C, however the points that are effectively considered for propagation are, as it is possible to see from Figure 7.4. This is because some points might end up within the Hill's surfaces and for this reason they are not considered for propagation. The maximal number of points on the section is 3890, while the minimal one is 388. A variable number of propagation points is preferred to a fixed one for two reasons. First of all doing so the same set of positions points are considered across the energy levels of the database. This guarantees the existence of a uniform set of entry points in the database that have the same specified distance of 50000 km. Second, this is also needed to reduce the computational effort at high values of the Jacobi constant. In this case a great number of transfer legs will derive from stable orbits about Earth generating a great number of intersections points, making it unnecessary to consider higher numbers of propagation points to populate the database.

3. The magnitude of the synodic velocities are computed from the position components and make use of the Jacobi integral expression (Equation 3.10). For each position the velocity vector is uniformly distributed in 3D space with 500 directions computed using a spherical Fibonacci mapping algorithm. This algorithm will be discussed in Chapter 8.

4. These states are then propagated backward and forward in time for one year using the Sun-Earth CR3BP. The propagation is interrupted only if the trajectory impacts Earth or travels too far from it (over a distance of 7.5 a_M). During propagation the intersection states and epochs with the Poincaré section are recorded, as well as the index of collision, escape and capture trajectories.

5. By making use of the propagation data a database is generated as a list of Sun-perturbed trajectory legs. The database structure is illustrated in Figure 7.1. The procedure is iterated from step 1 with a different value of C.

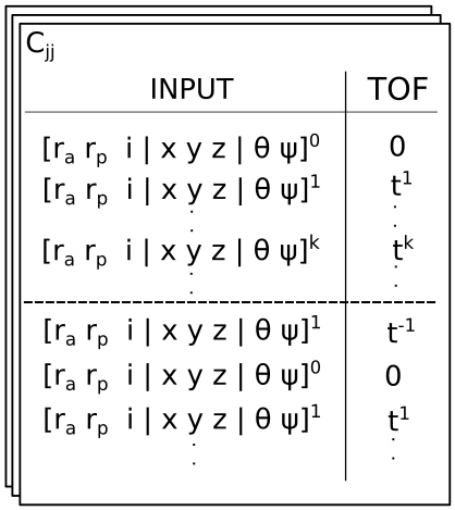

Figure 7.1: Sketch representing the structure of the database. The database is composed of an array of different matrices, each representing trajectories with the same value of the Jacobi constant. Each matrix has nine columns and a variable number of rows. A trajectory with multiple intersections is represented as a sequence of successive states and osculating orbital elements at different epochs. If the state represents a collision or escape trajectory, the value of the inclination is set to 210° and 240° respectively.

The structure of the database is illustrated in Figure 7.1 as an array of matrices, each containing trajectories propagated at the same value of C. Each matrix is composed of nine columns and a variable number of rows. The first three columns represent the osculating orbital elements r_a, r_p and i with respect to the secondary. Next to these the position in the SP2 frame is represented, followed by the azimuth and elevation angles of the synodic velocity. The last column corresponds to the time epoch in adimensional units. Since both the Jacobi constant and Tisserand parameter T_2 are automatically defined for each matrix of the array, it is immediate to compute the components of the synodic velocity from position, azimuth and elevation angles. Also the Keplerian energy and angular momentum of the trajectories with respect to Earth can be easily computed

using the osculating orbital elements as illustrated in Appendix B. The position in the database is related with a point on the Poincaré section, on Earth surface or at escape distance. In order to differentiate between these cases fictitious inclination values of 210° and 240° are used to represent collision or escape trajectories. These values have been arbitrarily chosen to represent a physically impossible condition on the inclination (limited between $0° \leq i \leq 180°$) and exploited to label these particular type of trajectories in the database in an efficient way. The database used in this report has been generated using 23 values of the Jacobi constant C. Due to the propagation settings previously explained the entire database size is approximately 28 GB, divided into smaller structures of approximately 1.2 Gb for each value of C. Figure 7.2 presents the values of C used in the database:

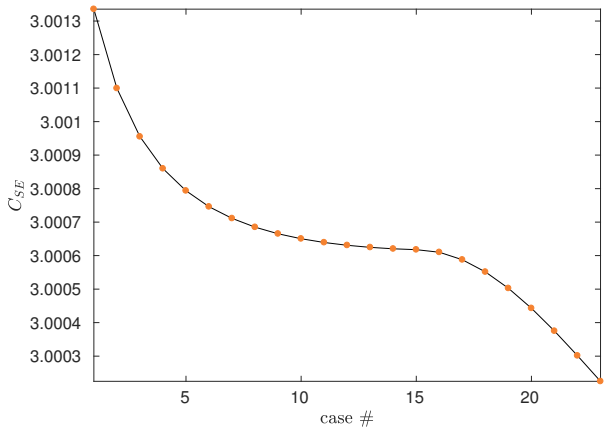

Figure 7.2: The values of the 23 Jacobi constants of the SE CR3BP model used to populate the database. These values have been chosen by geometric considerations from Figures 7.3 and 7.4.

These 23 values have been chosen such that the associated Tisserand level surfaces in the TP-graph would divide the $r_a - r_p - i$ volume into approximately uniform subsets, as it is possible to see in Figure 7.3. Note that the distribution of the energy level has been carried out by considering the spacing of the level sets on the $r_a = r_p$ and on the $r_a = r_p = 5\ a_M$ lines and it does not corresponds to a uniform spacing between the values of the Jacobi constant, as presented in Figure 7.2.

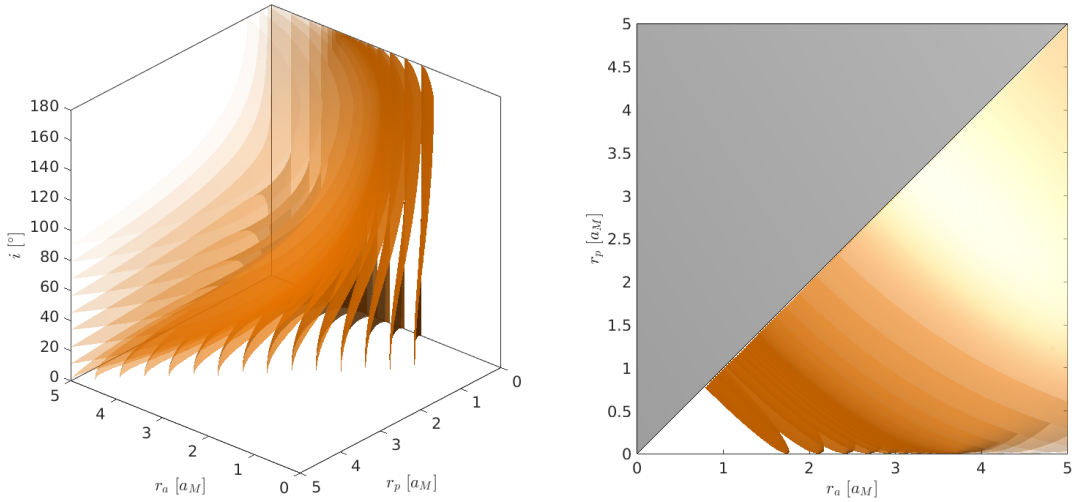

Figure 7.3: Tisserand level sets of T_2 in the TP-graph corresponding to the values of C illustrated in Figure 7.2. Darker tones correspond to higher values of C and T_2.

Note that the Poincaré section represented by Equation 4.61 corresponds to the double cone shape represented in Figure 7.4. Both the 'balloon' and planar parts of the section are not visible in the figure because we are focused on a narrow region about the secondary. This particular configuration turns out to be optimal to observe Sun's perturbation effects, that exhibit different phenomena depending on the quadrant of the SP2 frame considered as described in Section 3.4.

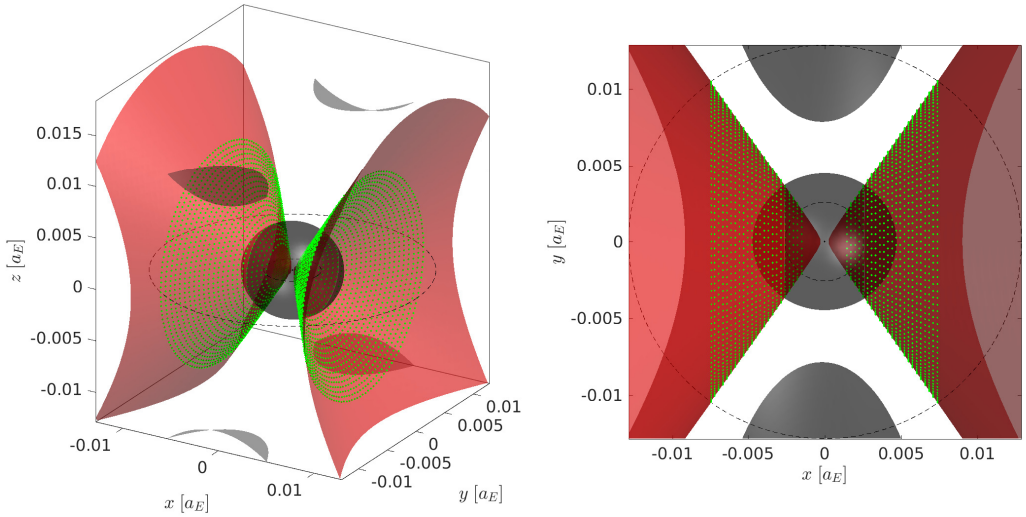

Figure 7.4: Representation of the initial propagation points used to populate the database (green) in the SP2 frame of the Sun-Earth system. The red and black surfaces represent the Poincaré section defined about the secondary and Hill's surfaces respectively. The latter is visualized only for the highest and lowest values of C. The black dashed circle is a representation of the distances at a_M and $5a_M$ in Sun-Earth coordinates.

The points considered for propagation vary depending on the value of C, the maximal number is 3890 while the minimal one is 388. The choice to distribute them uniformly such that the maximal distance between any of these points does not exceed 50000 km derives from experience with the EQUULEUS mission and with the optimization tools used to fill this position gap. The decision of the total number of propagation states to consider to populate the database have been carried out by taking into consideration the size and resolution of the database generated.

If the spacecraft state would have been represented by position and osculating orbital elements only in the database, an ambiguity would have been introduced. As it is possible to see from Figure 7.5 generally for any position chosen in space defined by a set of osculating orbital elements r_a,r_p and i there exist four different orbits. These orbits are differentiated from each other by the values of the remaining osculating orbital elements that are not considered in the database such as Ω ,ω and θ. Instead of introducing them into the database to distinguish between the four cases, the choice has been made to represent the velocity direction simply by azimuth and elevation angles. By doing so the ambiguity is solved but the full derivation of the spacecraft state in the synodic frame is guaranteed.

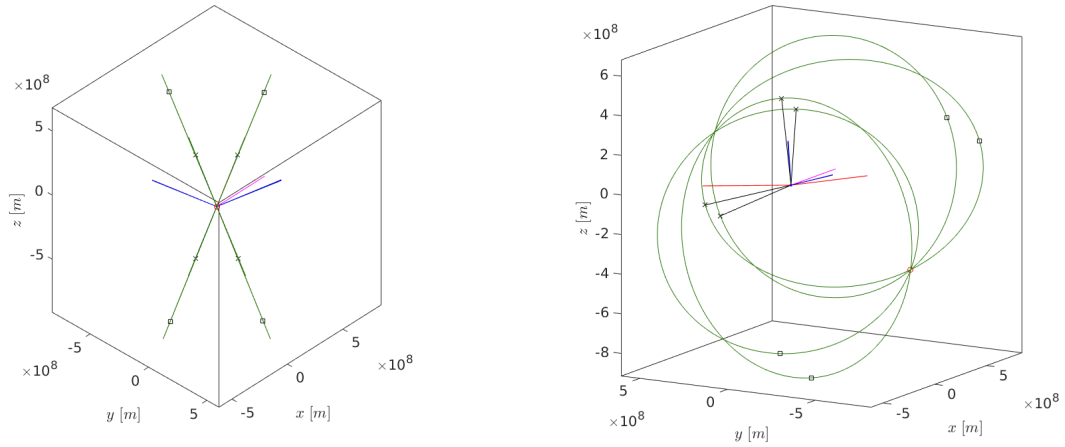

(a) (b)

Figure 7.5: Example of four orbits in the IP2D frame in the Sun-Earth system passing from the same point (red) and with the same set of osculating orbital elements r_a,r_p and i. The apogees of the trajectories are highlighted by black squares, the perigees by black crosses pointed by black arrows. Blue vectors represent the angular momentum vectors, red ones represent the line of ascending nodes. The x-axis direction is highlighted by a pink line.

The TOF epochs in the last column of the database have a dual purpose. The comparison between values in different rows makes it possible to understand the length of the considered transfer leg or to distinguish between different trajectories. In the latter case a sign change from positive to negative or a sudden change to a value of 0 signifies that another trajectory has been considered. This makes it possible to store and yet distinguish a large number of trajectories in the same matrix without the usage of additional labels. But the epochs are also fundamental when considering the phasing between different CR3BPs. Let's say that a trajectory is entering as input in the database from a computation in the EM system. In this scenario the database is used to quickly have an idea of the Sun's effect on the trajectory from the moment it is leaving the vicinity of the Earth-Moon system until it will reach again the vicinity of the Earth-Moon system. By recording the value of the phase angle at the moment when the database is queried, the TOF of a specific trajectory is used to compute the phasing angle between the two CR3BP models at the moment of patching when the trajectory will again come close to the Earth-Moon system.

In a scenario such as described above note that also dynamical models different from the EM CR3BP can be used to generate the input or output conditions to query the database. The 2BP, SEM BR4BP or full-ephemeris models can also be used to consult the database.

7.2. DATABASE TRAJECTORY DESIGN

In this section a few examples of the usage of the database are given. First a case of trajectory design using two EM CR3BP and a SE CR3BP is illustrated. In this example the arrival condition is determined by a temporarily captured trajectory about the Moon. Such a trajectory is illustrated in Figure 7.6 and has been obtained from another database of flyby trajectories with the Moon that will be introduced in Chapter 8.

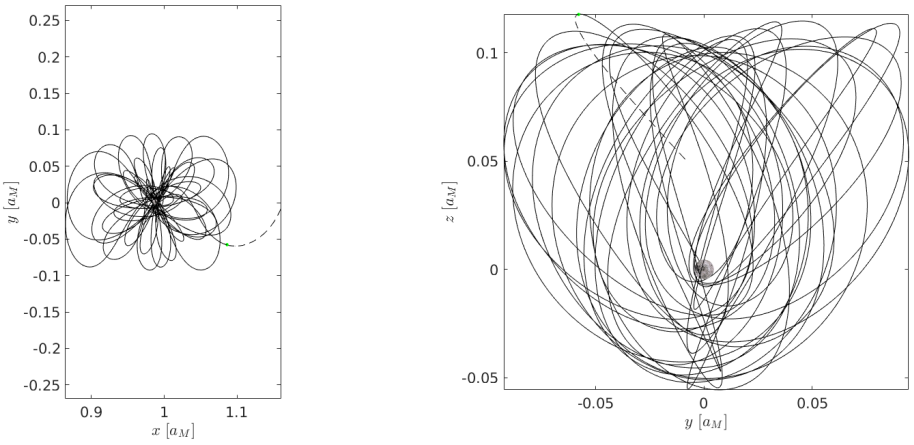

Figure 7.6: Chosen arrival trajectory in proximity of the Moon represented in the SB frame of the EM system. The continuous line is the propagation forward in time while the dashed one backward in time from a state found in the lunar flyby database for $C_{EM} = 3.1$.

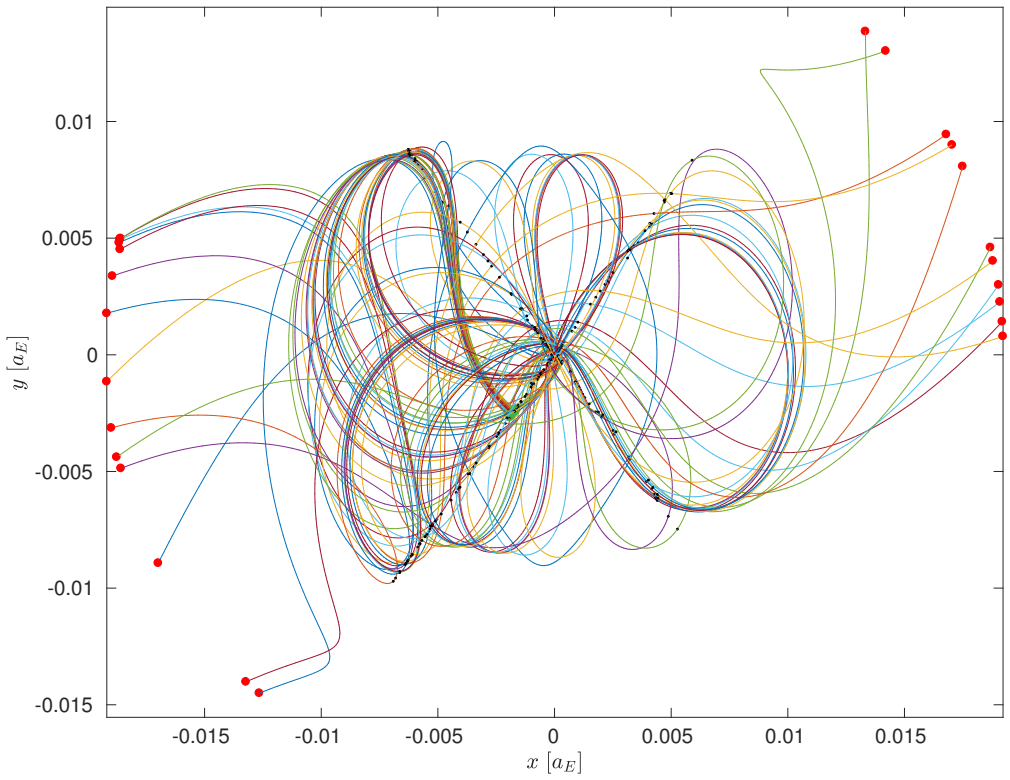

Figure 7.7: Example of section-to-section transfer legs in the SP2 frame of the SE system obtained by the query of the example discussed in this section. The intersections with the Poincaré section are represented by black points, while the starting and ending positions are represented by larger green and red points respectively.

This orbit has been chosen because it arrives from the exterior region of the EM system and stays in proximity of the Moon for about six months before colliding with the Moon. For these characteristics it is a good candidate trajectory to illustrate the usage of the database. The idea is now to investigate how we could reach

this trajectory from the EM system. In doing so the database is used. In particular the focus is put onto the portion of the trajectory emanating towards the exterior region. By changing the phasing of the two SE and EM CR3BP models different geometric configurations are investigated to understand which geometry allows a transfer in the SE system that returns to the proximity of the Earth-Moon region. By doing so we are essentially trying to understand which configurations are better for the transfer to occur considering the effects the Sun's perturbations will have on the trajectory. Once a satisfying geometric configuration is found, the intersection of the arrival trajectory with the Poincaré section in the SP2 frame of the SE system is computed. This state vector is then used to compute the value of C_{SE} and to query the matrix with the closest value in the database. A distance tolerance criterion of 50000 km and a velocity one of 100 m/s are used in this example as precision requirements for the search of solutions. With these settings we obtain 33 trajectories in the spatial SE CR3BP illustrated in Figures 7.7 and 7.8 represented by different colors.

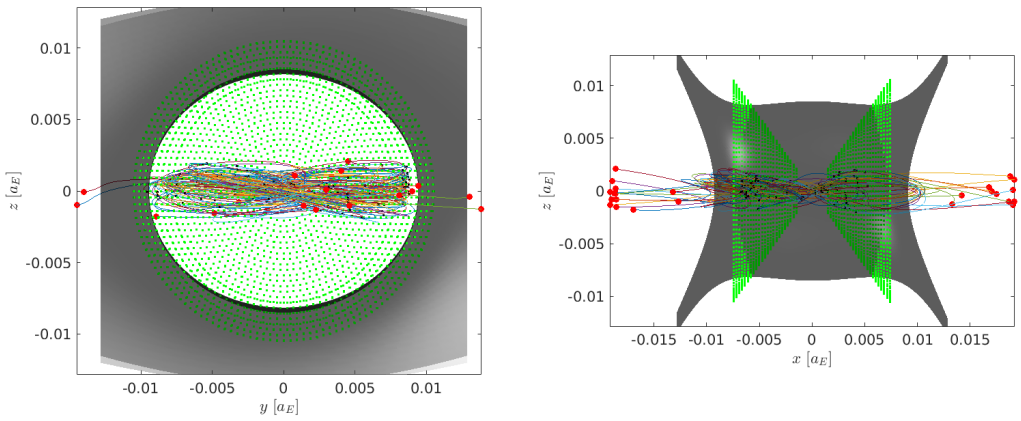

Figure 7.8: Additional views of Figure 7.7 with the visualization of the Hill's surface (black) and database initial propagation points (green) in the SE SP2 frame.

From the database all successive intersections with the Poincaré section are inspected to understand if some of them can be reached from a trajectory in the EM system. Figure 7.9 visualizes the correct position of these points in the EM system once the phasing of the intersection points with respect to the initial phasing of the two systems has been taken into account.

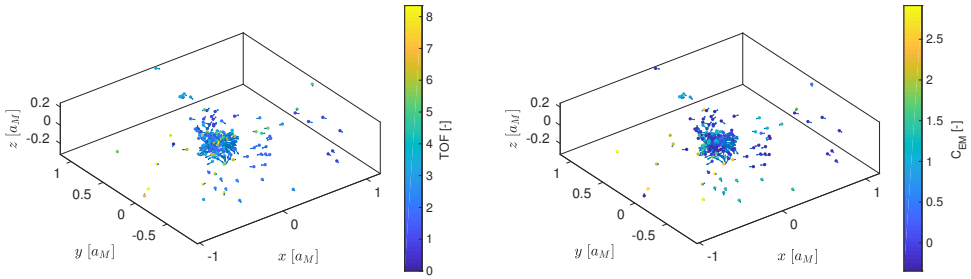

Figure 7.9: Results of the achievable states of the transfer legs in the EM system. The colors highlight the TOF in adimensional units of the SE system (left) and the value of the Jacobi constant in the EM system at the second patching condition C_{EM} (right).

From Figure 7.9 it is possible to see that all transfer legs obtained bring us within the EM system at lower values of C_{EM}. By looking at the overall trajectory design process this means that in order to arrive at the specific temporarily capture trajectory about the Moon of this example (at $C_{EM} = 3.1$), the starting point from the EM system is generally on a state with a much lower value of C_{EM}. This value will be greatly varied by the Sun perturbed leg, that will provide the necessary energy to fill this gap between the two values. From the

analysis of the initial conditions in the EM system that ends up in the final orbit thanks to Sun's perturbing effect, the designer can continue to investigate if these states are feasible or not depending on the specific mission considered. A single transfer trajectory is illustrated for clarity in Figures 7.10 and 7.11.

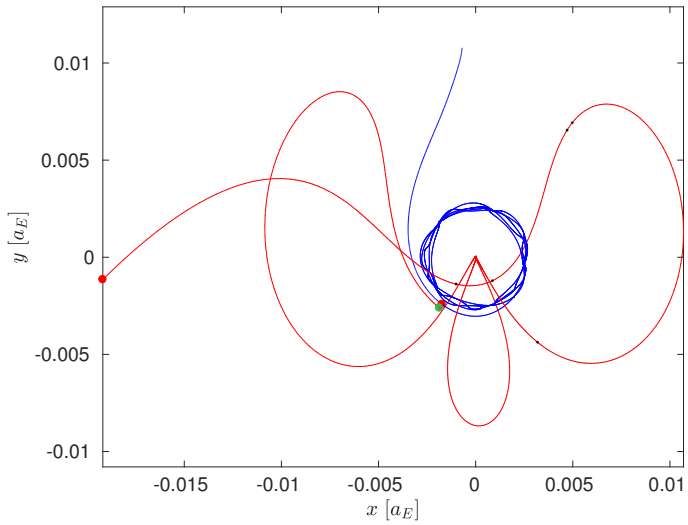

Figure 7.10: Example of patched trajectory between the EM and SE systems in the SP2 frame of the latter. The blue curve is the arrival trajectory illustrated in Figure 7.6, propagated in the EM system. The red one is the transfer leg propagated in the SE system. The patching between these two trajectories happens in the $IV°$ quadrant of the SP2 frame and occurs at a distance between the two states of about 34000 km and with a velocity difference of 54 m/s. The blue trajectory is propagated longer than needed to illustrate the shape of the trajectory without considering the solar perturbation effect.

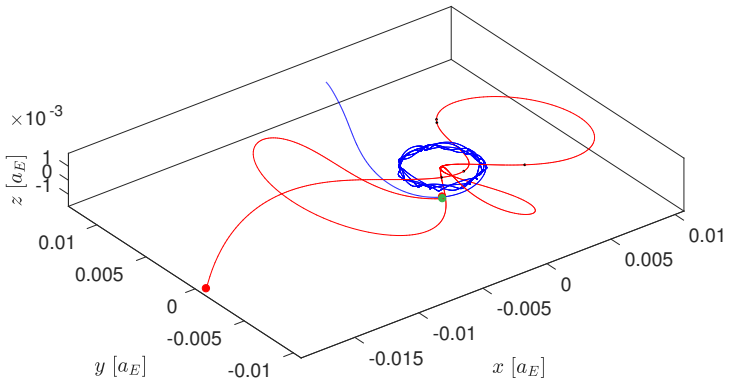

Figure 7.11: Different view of the trajectory visualized in Figure 7.10 to highlight the out-of-plane component of the trajectory that as a maximum excursion of about 300000 km. The black points represent the intersection points with the Poincaré section.

These figures show a single patched trajectory on the section that traverses the two dynamical models. The portion of the trajectory in the SE system that goes through the EM system can be considered by the trajectory designed for ulterior patching with the EM CR3BP model depending on the mission scenario considered. In such a case the database is used to identify simply and at once the main characteristics of these patching points, as illustrated in Figure 7.9. The designer may also use different dynamical models to obtain input

states for the database, as illustrated in the next examples.

The case of an example trajectory of the EQUULEUS mission is taken for discussion. The trajectory is computed in a full-ephemeris model considering the gravitational influences of the Sun, Earth and Moon. Its characterization with the usage of TP-graphs in the EM and SE systems can be seen in Appendix D. The first and last portion of this trajectory to intersect the Poincaré section about the secondary in the SE system are taken. These are the black trajectories represented in Figure 7.12. Note that in the first portion the trajectory actually does not intersect the section until 150 days after launch, excluding the possibility to study the Sun perturbed phase of the trajectory with the section designed in this report. However at a certain epoch the trajectory passes at just 40000 km from the section, below the 50000 km distance criterion used to generate the initial propagation points on the section. Instead of considering the first real intersection with the section, this point is chosen for the analysis. The values of the Jacobi constant C_{SE} for these two initial and final patching conditions are respectively 3.0006402939765 and 3.00134112130177. The latter condition corresponds to a configuration of the Hill's surface for which both $SEL1$ and $SEL2$ necks are closed, constraining the trajectory in the SE system to be located in a small region about Earth. Since we are interested in a transfer, the database related to the initial patching point is queried by using as input both the input and output conditions extracted from EQUULEUS trajectory in an attempt to design a single transfer-leg trajectory. The trajectories found in the database for such a query are illustrated in Figure 7.12.

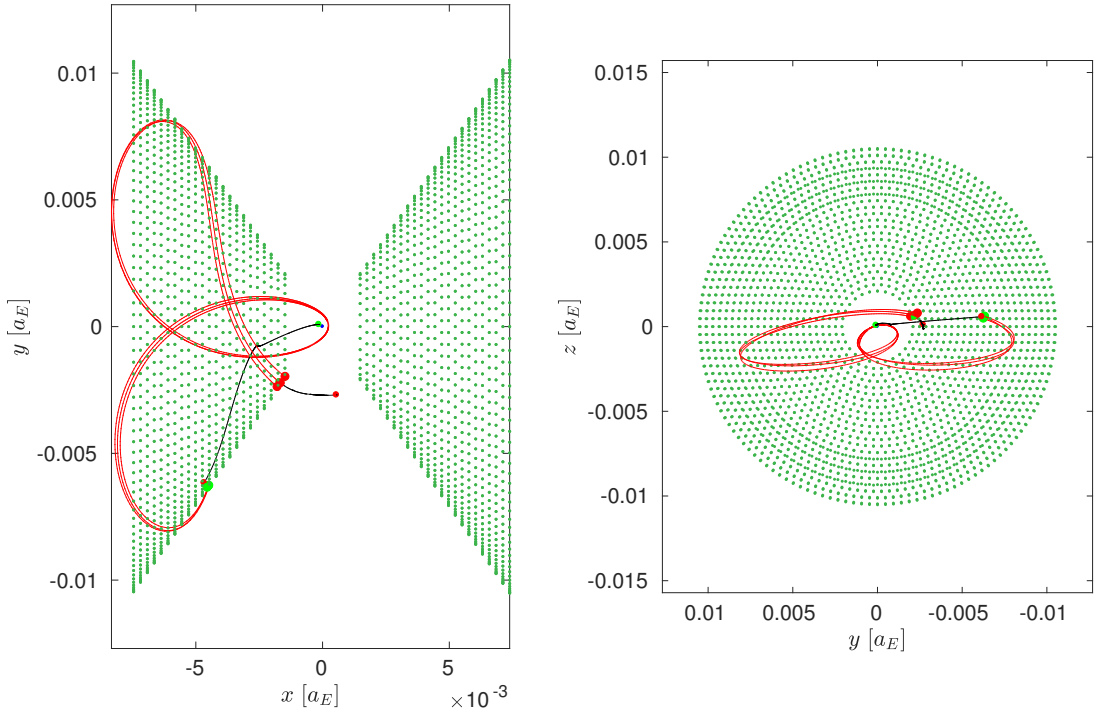

Figure 7.12: Examples of trajectories in the SP2 frame of the SE system obtained by querying the database using as initial and final conditions the states and epochs of the EQUULEUS trajectory computed in full-ephemeris model. The grid of database points is represented by green points. The trajectory in full ephemeris model is represented in black while the trajectories obtained from the database and computed in the SE system are represented in red. Initial and final conditions of each phase are represented by green and red points respectively.

In this a database there exist only three trajectories that allow a transfer between the initial and final states. These have been obtained by setting a tolerance distance for both input and output positions of 50000 km and using a ΔV criteria for the input state smaller than 200 m/s. The total ΔV of the three trajectories is about 500 m/s. However from the TOF of the trajectories it is possible to see that these geometrically correct trajectories are indeed not feasible from a timing perspective, as they reach their output state after 176 days against the required 313 days of the nominal trajectory from Appendix D considered for this example. This

shows that the usage of the database for a complex trajectory such as the one of EQUULEUS is inefficient if only a single dynamical model (the SE CR3BP) is used.

Given the difference between the Jacobi constant of the different initial and final patching conditions, it would be more efficient to include portion of the trajectories in the EM system to exploit lunar flybys in order to decrease the energy gap between initial and final values of C_{SE}. This possibility has been tested and a multi-patched trajectory for the EQUULEUS example is illustrated in Figure 7.13.

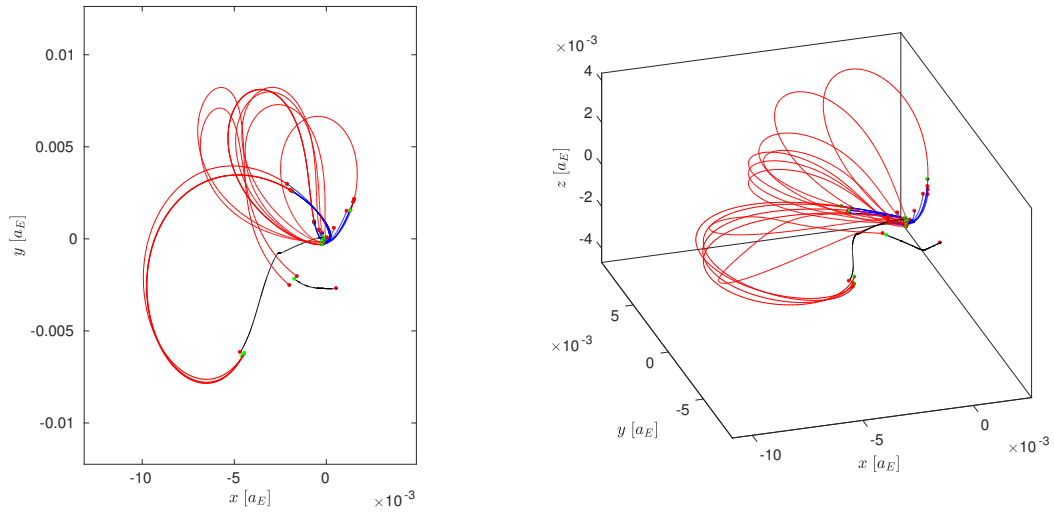

Figure 7.13: Different views in the SE SP2 frame of an attempt to generate a multi-patched trajectory using the EQUULEUS trajectory as initial and final conditions. The black curves have been computed in a full-ephemeris model, the red ones in the SE CR3BP and the blue one in the EM CR3BP. Green and red points represent initial and final position of each phase, that are also the patching points used in the database.

By using a combination of a full-ephemeris model for the initial and final parts of the EQUULEUS trajectory and by switching between database trajectories in the SE and propagated ones in the EM systems, the trajectories in Figure 7.13 are generated. The problem of such trajectories however is that they have been obtained from querying the database making use of big tolerances, especially for what concerns the patching velocities. Some of the trajectories illustrated in Figure 7.13 are the result of five successive patchings. If a ΔV tolerance at patching of 100 m/s is considered, the reader can understand how these are going to significantly build up throughout the procedure and ruin the ballistic nature of the transfers. For this reason the multi-patched trajectories just illustrated fail to realistically represents such a complex trajectory as the one computed in the full-ephemeris model for EQUULEUS.

These latter examples can be used also to understand the differences between trajectories computed in a CR3BP model and those computed in a full-ephemeris model considering Sun, Earth and Moon's influences. By comparing the first part of the trajectories in the SE CR3BP from Figures 7.12 and 7.13 with the one in Figure D.2 obtained in a full-ephemeris model and discussed in Appendix D, the differences between the trajectories in the two dynamical models are clear. As it will be illustrated in the next section, this discrepancy is not caused by the increased number of bodies considered in the model but is rather a consequence of the real motion of the bodies. In this sense it seems that the inclusion of eccentricities and inclinations in the bodies trajectories plays a fundamental role.

7.3. COMPARISON BETWEEN PATCHED CR3BP AND BR4BP

In this section a comparison is made between trajectories computed with a patched model that uses SE and EM patched CR3BP models and a BR4BP model. In the first case only two bodies at a time are considered, while in the latter the continuous influence of three bodies is considered. In a way the former dynamical system can be described as a discrete approximation of the latter continuous model. For this reason a com-

parison between the performances of these two dynamical models can give an insight into the error that is committed solely by excluding the gravitational disturbance of the fourth body. This comparison is much cleaner than the one possible to do using a full ephemeris model, as in such case the discretization effects could be masked by other factors such as the bodies eccentricity and inclinations, as well as small irregularity in their motion about the barycenter of the Solar System. For this analysis three energy levels are taken to be representative of high, medium and low-energy trajectories in the database. Multiple patching points on the Poincaré section defined about the secondary of the SE system are selected and propagated backward and forward in time using the EM or SE CR3BP. For simplicity at such points the initial phase angle between the EM line and the Sun is considered to be 0. In the patched model the backward propagation is computed in the EM system, while the forward one in the SE system. Different points on the Poincaré section are used just to understand the effect of different distances considered for the patching of the two models. In order to simplify the view only the planar case is represented here, but the results can be easily extended to the 3D case.

The trajectories patched at low,medium and high values of the Jacobi constant are represented in Figures 7.14,7.15 and 7.16 respectively.

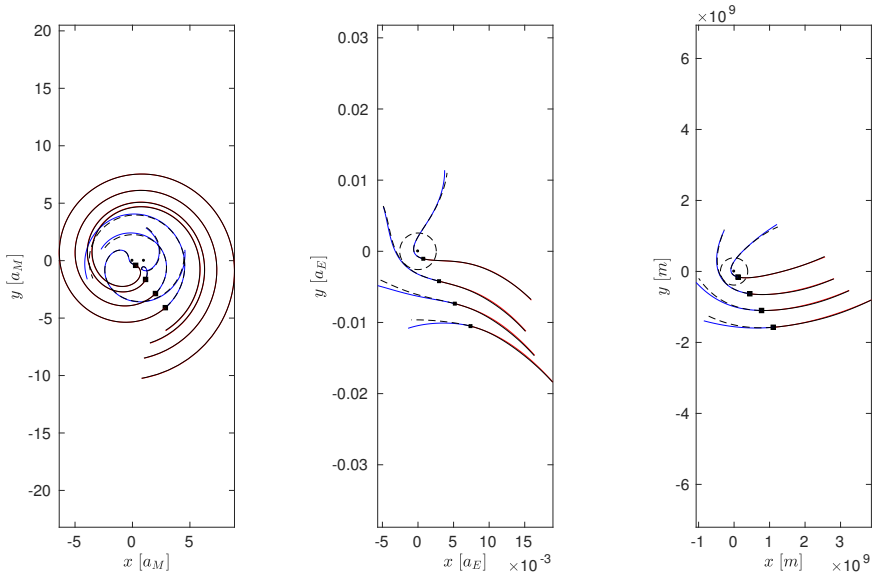

Figure 7.14: Patching simulation for 4 trajectories at $C = 3.00022476089146$ of the SE system. Trajectories are represented in EM SB frame (left), SE SP2 frame (center) and SE IP2D or EM IP1D (right). The patching point is the black square. Red and blue trajectories are propagated in the SE and EM CR3BP model respectively. The black trajectories are computed in the BR4BP model, the dashed and continuous lines are representative of the backward and forward propagations. The dashed circles in the center and right figures represent the distance of Moon's orbit.

It is possible to see in Figure 7.14 that for a low value of the Jacobi constant the patching generally gives satisfying results. Two of the four trajectories have very similar behavior in the two dynamical models. The patching is more critical for the two outermost trajectories. In these cases the portion of the trajectories computed with the EM CR3BP is exhibiting larger deviation from the reference trajectories in the BR4BP. This is due to the fact that at these patching conditions the backward trajectories are not going back towards the proximity of the EM system as in the other two cases. It can be concluded that Sun's perturbation shall be considered instead of having it substituted by the Moon's one. It is therefore necessary for the designer to understand when such a phenomenon occurs in order to patch the two dynamical models in the most efficient way possible.

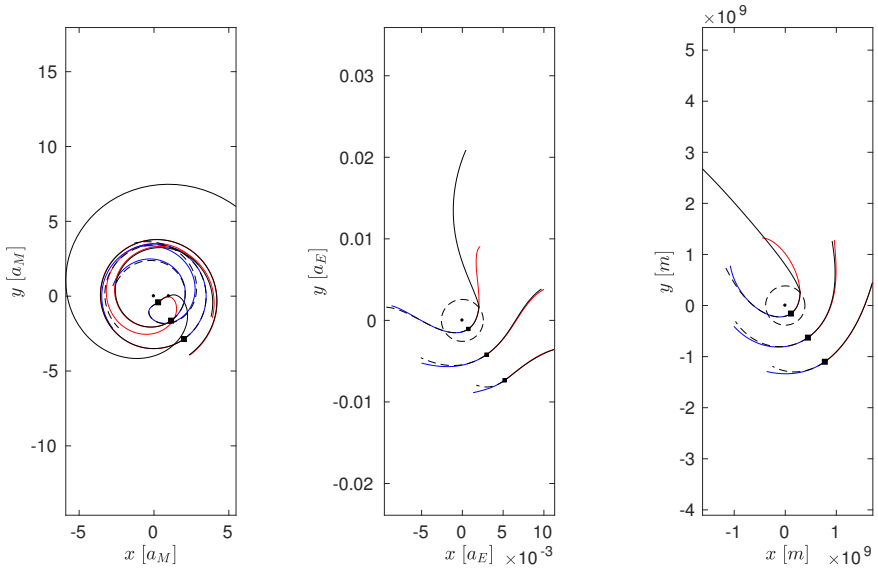

Figure 7.15: Patching simulation for 4 trajectories at $C = 3.00063909639226$ of the SE system. See caption in Figure 7.14 for details.

Similar conclusions as the one done at low values of C can be derived by looking at Figure 7.15. This time however another phenomenon can be observed for the innermost trajectory. In this case the patching happened within Moon's orbit, such that a portion of the SE trajectory is computed in this region. Since in such dynamical model the Moon is not considered the trajectory is not considering a lunar flyby event, as it is possible to see from the trajectory in the BR4BP. This difference is causing a dramatic divergence between the trajectories in the two dynamical models. Generally great care shall be put when using the SE CR3BP within the Moon's orbit that no major flyby events take place during propagation.

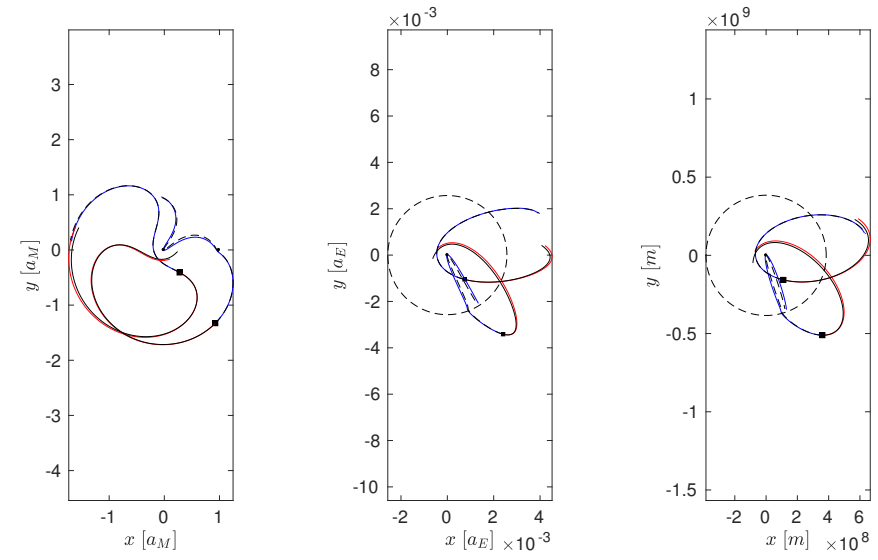

Figure 7.16: Patching simulation for 4 trajectories at $C = 3.00133554723153$ of the SE system. See caption in Figure 7.14 for details.

Inspecting Figure 7.16 is possible to see that for a high value of the Jacobi constant the precision of the patched approximation is slightly worse than the one showed in the previous cases. This case generally corresponds to lower values of the spacecraft energy with respect to Earth, thus to slower trajectories in the system. Due to

this the patching is less accurate because its not considering the influence of multiple bodies during a slow-patching event. Note that however as in the previous simulation in most of the cases the difference between the trajectories are minimals.

It is clear that the patching procedure must always be accompanied by the designer ability to avoid undesired cases as the ones described in the previous discussion. In particular the patching distance and the expected behavior of the trajectory (getting closer or further away from the Earth-Moon system) are fundamental aspects to be taken into account when patching trajectories on the Poincaré section defined in this report. For example for what concern the EM system a patching trajectory should be considered only close to the Earth-Moon system and for those trajectories that are going to enter in such a system. A SE trajectory computed close to Earth is generally a good approximation with respect to the BR4BP model if no major flyby events take place in proximity of the Moon.

Another aspect to be considered is the TOF of the trajectory. The small deviations illustrated in the examples before might diverge and cause big discrepancies between trajectories in the two models if larger TOF are considered. To avoid this, the designer shall always be cautious towards the propagation time for the single CR3BP considered.

7.4. CONCLUSIONS

In this chapter a database of section-to-section transfer legs in the SE CR3BP model has been designed to exploit the concept of the modified Tisserand parameter and the related Poincaré section about the secondary defined by Equation 4.61. Its usage has been illustrated with examples of input trajectories obtained from different dynamical models such as the EM CR3BP and full-ephemeris models.

The idea behind the database is to schematically represent the characteristics of transfer trajectories in the SE system that connect different points on a Poincaré section defined in the SP2 frame of such a system. By recording the characteristics of these transfer trajectories, it would be possible to exploit them for trajectory design purposes. Since the database is defined in an autonomous system, it can be used as a universal tool for the systematic research of patched trajectories in the SE and EM CR3BP models. Because of this the database itself is universal, since in principle it can be used to generate first-guess trajectories without being generated again for the specific case considered. An advantage of this approach is also that the database works for any type of initial and final orbits considered in the query, and it does that not in a planar assumption, often performed in literature to simplify the analysis, but in a spatial configuration.

The example of the EQUULEUS trajectory performed in this chapter however also showed certain limitations of this approach. In this example inefficient multi-patched trajectories have been generated from EQUULEUS nominal trajectory. This could be explained by several factors: the dispersion of propagation states of the database for the conditions considered, a too large difference between the Jacobi constant of the initial state and the one in the database, an initial condition not flexible enough for the case considered, and a natural limitation of the patched approach to represent a trajectory obtained in the full-ephemeris model. The latter case certainly is an important point to consider, as it is possible to see by comparing the trajectory computed in the full-ephemeris model in Figure D.2 with the one computed with a patched approach in Figure 7.13.

A double patching can be simply performed using the database, as illustrated in the first example in Section 7.2, however a multiple patching trajectory exhibit additional challenges both on the algorithmic search of trajectories and the complexity involved. The focus in this research has been put in the creation of the database itself and less time has been spent in the exploration of its usages, that might be related to other challenges not proper of the topics covered in this research. These will be illustrated in the final conclusions of the report.

The performances of the patched CR3BP model are confronted with the one of a full-ephemeris and BR4BP model. In the former case the trajectory in the two dynamical models are very different. The cause of this difference it is attributed to the real inclinations and eccentricities of the gravitational bodies considered (Sun, Earth and Moon). In the latter case the difference between the trajectories in the two dynamical models are

minimal when undesired cases are avoided. The patching distance from Earth and the expected behavior of the trajectory (getting closer or further away from the Earth-Moon system) are fundamental aspects to be taken into account during the patching procedure of the EM and SE CR3BP. When these aspects are taken into account the patched model shows to efficiently being able to represent trajectories in the BR4BP, under the assumption that short to medium propagation time are considered.

Additional material is presented in Appendix D, where an analysis of the EQUULEUS trajectory used in this chapter to obtain input and output conditions to query the database is presented and characterized through the usage of the TP-graphs.

8

3D FLYBY

In this chapter the quasi-spherical Poincaré section as defined in Section 4.5.3 is used to record flyby events in the spatial CR3BP. In particular flyby trajectories with respect to the Moon and Jupiter as secondaries of the Earth-Moon and Sun-Jupiter CR3BP respectively will be considered in the making of a database of flyby trajectories at different energy levels.

First the definition of the Poincaré section used in this chapter is given in Section 8.1. A database approach technique is developed in Section 8.2 to map the change in the osculating orbital elements caused by flyby events at different energy levels. The possible usage of the database in the Earth-Moon and Sun-Jupiter systems is illustrated in Sections 8.3 and 8.4. Section 8.5 concludes the discussion with the main findings of this chapter.

8.1. POINCARÉ SECTION DEFINITION

In Section 4.5 several Poincaré sections have been derived with the property of having constant Tisserand parameters. A representation of these sections can be seen in Figure 4.7. By looking at the family of sections about the primary with constant T_1, it is possible to see that by increasing the value of P^k the section appears first as a balloon-shaped surface and then as a quasi-spherical surface (QSS) about the secondary. Such a surface is defined in the SP1 frame by Equation 4.72, repeated here for better understanding:

$$QSS_{SP1} : \frac{1}{\sqrt{(x-1)^2+y^2+z^2}} - x + 1 + \left(R - \frac{1}{R}\right) = 0 \tag{8.1}$$

where R is the minimum radius of the QSS surface from the secondary in adimensional units. For the analysis of the 3D flyby with the Moon and Jupiter this value will be chosen to be the about the radius of the SOI of these bodies with respect to Earth and Sun, respectively 66×10^3 and 50×10^6 km. Figure 8.1 shows the QSS used about the Moon defined by Equation 8.1.

Note that although this section is defined in the SP1 frame and the trajectories taken on it have a constant T_1 parameter, it develops about the secondary. Such a property can be exploited to efficiently catalog and design flyby trajectories. In this chapter the QSS will be used to map the change in the osculating orbital elements between incoming and outgoing trajectories from the surface itself. Since the surface will not only have a constant Jacobi constant, but also a constant Tisserand parameter about the primary T_1, it will be possible to visualize the performance of the flyby trajectories at precise energy levels directly in the TP-graph.

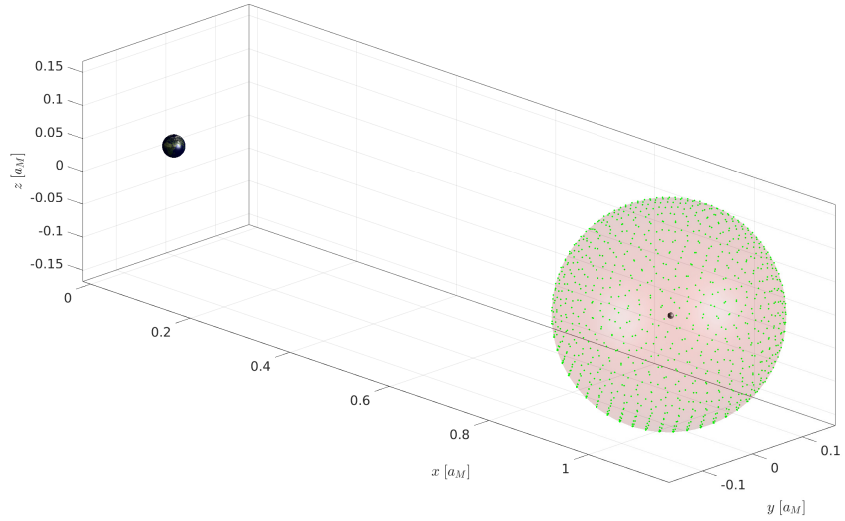

Figure 8.1: Representation of the QSS about the Moon in the SP1 frame. The green points on the QSS are the 1000 propagation points considered to populate the lunar flyby database with trajectories. Earth and Moon are also presented in the figure.

8.2. DATABASE APPROACH

In this section a database approach is designed to make use of the QSS to map the change in the osculating orbital elements caused by a flyby with the secondary. The flyby mechanism has been extensively studied in literature and has already been discussed in Section 3.3.

The T-graph has found application as a graphical tool to map in a simple way the change in the osculating orbital elements of flyby trajectories from an energy point view using a patched 2BP approximation [24]. Such a dynamical model however does not allow the representation of interesting phenomena such as temporarily capture orbits or complex flyby trajectories, since it is considering only high-energy hyperbolic trajectories. In this sense the TP-graph has successfully extended the validity of the graph to lower energy levels through the usage of the CR3BP. In particular in [11] a flyby map that combines the TP-graph and the Keplerian map is used to investigate and differentiate between flybys in the planar CR3BP. Thanks to the definition of the QSS the author of this report would like to make use of the findings from Chapters 4 and 5 to extend the study of flyby events in the spatial CR3BP by using a combination of propagation techniques and TP-graphs. A database approach inspired by the one illustrated in [9] to design Moon-to-Moon trajectories in the Sun-Earth planar CR3BP is adopted. The database developed in this chapter would like to be a simple and efficient tool to quickly investigate the set of osculating orbital elements that is possible to achieve from flyby trajectories. The idea is that such a database can be used as a tool to generate first-guess trajectories. The database is generated by propagating a set of states from the QSS and storing certain properties of the trajectories generated. The algorithm to populate the database is illustrated in the following steps:

1. A value of the Jacobi constant C is chosen to represent the energy level considered for the system.
2. A total of 1000 points are uniformly distributed on the QSS using a spherical Fibonacci mapping algorithm. This algorithm allows to reach a sub-optimal distribution of points on a spherical surface by using a Fibonacci spiral unwinding on the surface of a sphere[26]. A representation of the distribution on the QSS in the azimuth-elevation plane can be seen in Figure 8.2. Note that depending on the energy level considered some points might be positioned within the Hill's surface. If this is the case these points are ignored.
3. From the points considered the magnitudes of the synodic velocities are obtained from the Jacobi integral (Equation 3.10). For every position 500 angles in space are used to orient the velocity vector. Once again a spherical Fibonacci mapping algorithm is used to distribute the velocities uniformly in space.

4. Each initial state is propagated backward and forward in time for a maximum period of about six months in the Earth-Moon CR3BP and two years in the Sun-Jupiter CR3BP. The propagation is halted whenever the trajectory goes too far from the QSS or if a collision with the secondary occurs. The intersection states with the QSS are recorded, as well as the index of collision and capture trajectories.

5. By making use of the propagation data a database is generated that lists flyby, collision and capture trajectories that have been generated from or to the QSS. The database structure is illustrated in Figure 8.3. Once the portion of the database for the value of C specified at the beginning has been generated, the procedure is iterated from step 1 onwards with a new value of C.

Figure 8.2 shows the uniform distribution of the points on the QSS in the azimuth-elevation plane obtained by applying a spherical Fibonacci mapping algorithm. The distribution of the points on the polar regions suffer from a well known projection distortion involved when representing a spherical surface on a planar projection. Note that to distribute the points on the QSS, that is not exactly a spherical surface, a projection technique have been adopted applying a circumscribing spherical surface (with uniform points distributed on it) to the QSS.

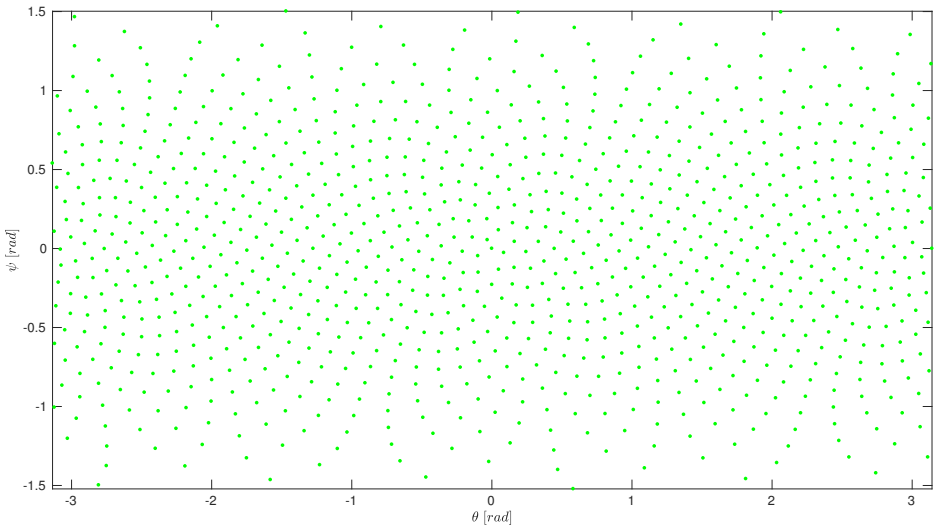

Figure 8.2: Azimuth θ and elevation ψ of the 1000 points distributed on the QSS using a spherical Fibonacci mapping algorithm.

The structure of the database is illustrated in Figure 8.3 and can be described as an array of several matrices, each defining the characteristics of the flyby trajectories at a specific energy level. Each of these matrices is composed by 17 columns and a variable number of rows; each row represents a trajectory. The columns can be divided into three categories: the first eight columns represent the input states of the database. It is followed by a column representing the time of flight (TOF) in adimensional units between the input and output states, represented by the last eight columns of the matrix. Note that in this description the notation "state" is not used to intend the Cartesian state made by position and velocity of the spacecraft but is rather intended as state vector of the database. The input and output states indeed are described by the osculating orbital elements r_a, r_p and i with respect to the primary, the position x, y, z and the azimuth and elevation angles of the synodic velocity θ and ψ. Note that since both the Jacobi constant and Tisserand parameter T_1 are automatically defined for each matrix of the array, it is immediate to compute the components of the synodic velocities from position, azimuth and elevation angles. Also the Keplerian energy and angular momentum of the trajectories with respect to Earth can be easily computed using the osculating orbital elements as illustrated in Appendix B. The input and output states can refer to points on the QSS, on the Moon's surface or points within the SOI of the secondary. To differentiate between these three conditions, fictitious inclination values of 210° and 240° are used to represent states pertaining to collision or capture trajectories. As in the database structure introduced in Chapter 7, these two values have been arbitrarily chosen to represent

a physically impossible condition on the inclination (limited between $0° \leq i \leq 180°$) and exploited to label these particular type of trajectories in the database in an efficient way.

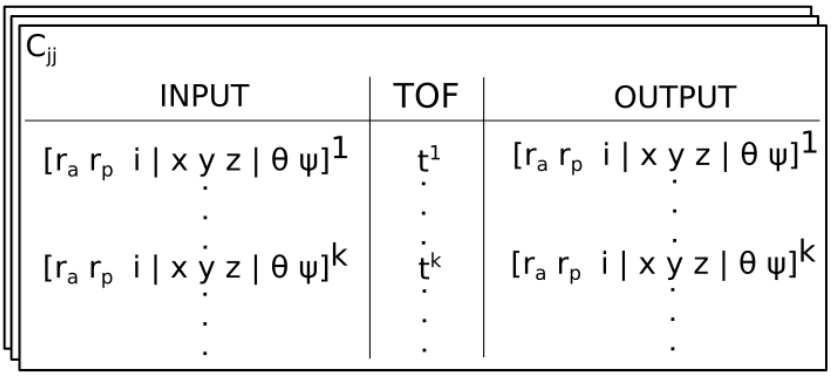

Figure 8.3: Schematic of the database structure used to record lunar and Jovian trajectories from the QSS. The database is an array of matrices; each matrix represents trajectories with the same value of the Jacobi constant and Tisserand parameter T_1. The database is structured in such a way to represent any trajectory by input-output states. These states might not be on the QSS in case they are describing a collision or capture trajectories. In the latter cases the inclination is changed to fictitious values of 210° and 240° respectively.

The database so designed is essentially a catalog of trajectories that are interacting with the secondary. Since the dynamical model used is the CR3BP these trajectories could be much more complex than simple hyperbola. Capture and collision trajectories have been considered also in the database since they can be of use in the design process. For example a temporarily capture trajectory could be used to inject the spacecraft into a stable orbit about the secondary, or depending on the TOF could be used itself as operational orbit about the secondary. Collision orbits can be used as first-guess for landing trajectories or can be transformed through ΔV maneuvers as close flyby trajectories. Since it might also be important to avoid them at all they have been saved in the database when encountered during the propagation phase. Some applications of the database will be illustrated with practical examples in Sections 8.3 and 8.4.

Note that the choice to use a database was the only one capable to capture the complex dynamics involved in the CR3BP. In doing so only the most important data about the trajectories have been saved. The author wanted to represent each trajectory, independently from its complexity, only by input and output states, in order to be able to map the flyby effects in a discrete way. In doing so a generic user may apply the database with different dynamical models. For example a pacthed 2BP problem can be used to design the trajectory before and after the motion within the QSS if the user would like to employ a simpler dynamical model than the CR3BP. On the other hand if a more sophisticated model is used the database can be used as an exceptional way to quickly investigate the capability of spatial ΔV maneuvers without the need to propagate a single trajectory.

8.3. 3D FLYBY WITH THE MOON

In this section some examples of the usage of the database about the Moon are given. The results presented are simply obtained by querying the database, which contains data on 14×10^6 trajectories distributed across 28 energy levels, from $C = 0.5$ to $C = 3.2$ with a spacing ΔC of 0.1. The total size of the database is about 1.9 Gb.

Figure 8.4 represents the intersection states with the QSS as well as the collision points with the Moon's surface of about 500000 trajectories in the database with $C = 2.9$. Note that the number of trajectories considered to populate the database has been chosen as a tradeoff between the computational time, the size of the database and the ability of the latter to have a uniform distribution of points across the QSS.

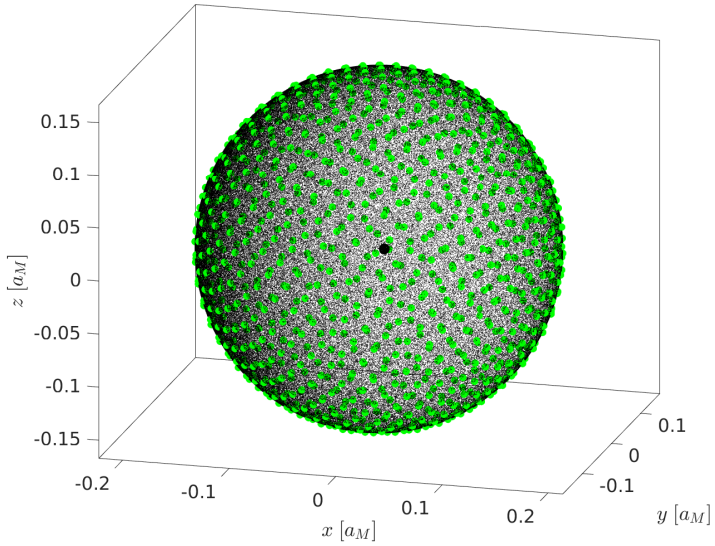

Figure 8.4: Representation in the SP2 frame of the initial propagation states (green points) and intersections with the QSS and Moon's surface (black points) for $C = 2.9$ in the database.

Figure 8.5 presents all osculating orbital elements in the range between $0 < r_a < 5$ and $0 < r_p < 5$ for $C = 2.9$ in the database. By inspecting the figure it is possible to see that the osculating orbital elements are not distributed across the whole Tisserand level set but are rather limited in a narrow region of the graph. This limitation is caused by a phenomenon involving the geometrical definition of the QSS and the specific value of the Jacobi constant considered.

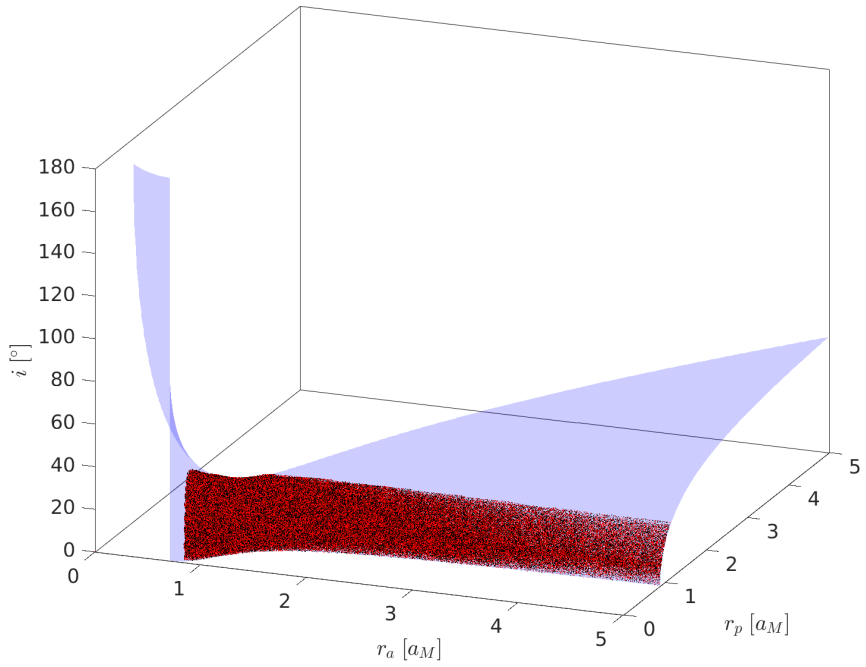

Figure 8.5: TP-graph with the Tisserand level set for $C = 2.9$ (blue) and the input (black) and output (red) osculating orbital elements from the database. It is possible to see that the points are distributed across a region of the graph limited by the two planes $r_a \approx 1 - R$ and $r_p = 1 + R$, where R is the radius defining the QSS, equal to $0.17 a_M$ for the case about the Moon.

The definition of the QSS about the secondary is naturally excluding Keplerian orbits about the primary that cannot intersect the QSS. Keplerian orbits with a pericenter higher than $1+R$ or with apocenter smaller than $1-R$ would never be able to intersect the QSS. For this reason trajectories with such osculating orbital elements cannot be recorded by the Poincaré section. This constraint is also limiting the value of the maximum inclination achievable in a flyby event. By changing the energy level of the system by varying the Jacobi constant, the Tisserand parameter would vary accordingly and the level set will have a different disposition with respect to the limit planes expressed by $r_a \approx 1-R$ and $r_p = 1+R$. In particular by decreasing the value of the Jacobi constant the Tisserand level surface will shift to the right, making it possible to reach higher inclinations. Continuing to lower the Jacobi constant, the retrograde region of the level sets, that was previously excluded for flybys, will become accessible. From Equation 5.4 it is possible to see that the retrograde region will be accessible to the level set only for:

$$T_1 < \frac{2(1-\mu)}{1-R} \tag{8.2}$$

From this phenomenon it is possible to conclude that prograde flybys are accessible at every energy level, while retrograde ones become accessible only at low values of the Jacobi constant. This phenomenon was already observed in [11], that distinguished between Type I or direct and Type II or retrograde flybys in the planar CR3BP as discussed in Section 3.3. The description of the phenomenon however is presented here for the first time with the usage of the QSS surface at constant T_1 for the spatial CR3BP, elegantly explained by the behavior of the Tisserand level set at different energy levels as characterized in Section 5.2.

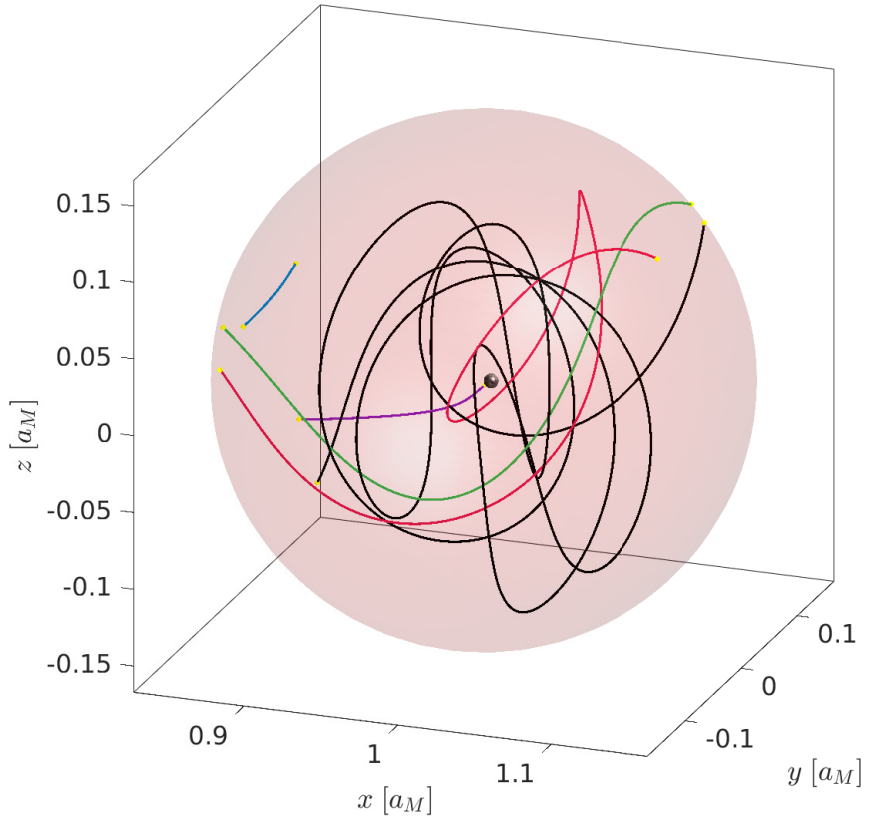

Figure 8.6: Schematic of different classes of trajectories in the SP1 frame obtained for $C = 3.1$ in the database. The green and turquoise cases are categorized as simple flybys, the first one being short while the last one being long. The red case is classified as a complex flyby, since it makes one revolution about the Moon in the SP1 frame; this trajectory lasts about 16 days. The purple trajectory is a collision orbit while the black one is a temporarily capture trajectory, as it performs multiple revolutions about the Moon, staying within the QSS for about 43 days. Yellow points represent the initial and final positions of the trajectories.

Figures 8.6 and 8.7 present different classes of trajectories stored in the database in the SP1 frame, while Figure 8.8 presents the same trajectories in the IP1D frame. A total of five types of trajectories are classified in the database. Three of them are flyby trajectories, differentiated as simple and complex, the first one being further divided into short and long flybys. These trajectories are all starting and ending on the QSS. The simple flyby is characterized by the absence of orbit revolutions about the secondary in the synodic frame. The length of the flyby arch within the QSS is used to differentiate between short and long flybys. In the first case the gravitational influence caused by the secondary on the trajectory is minimal. The second case is essentially the classical hyperbolic flyby trajectory within the SOI of the secondary. The complex flyby is characterized by a single orbit revolution about the secondary in the synodic frame. If the number of revolutions about the secondary is greater than one, the trajectory is classified as a temporarily capture trajectory. After several revolutions this trajectory could leave the system and intersect the QSS or collide with the secondary. In the latter case the trajectory is still considered as a temporarily capture trajectory, since a collision trajectory is considered only as a simple trajectory without a revolution directly connecting the QSS and the secondary's surface.

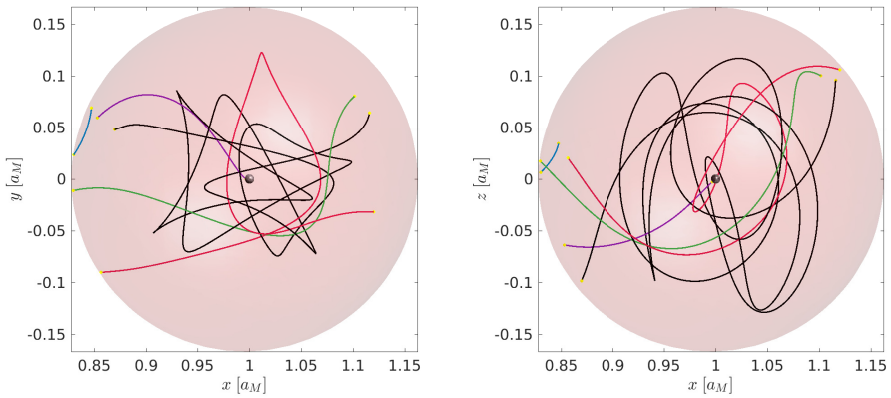

Figure 8.7: xy (left) and xz (right) views of the trajectories illustrated in Figure 8.6.

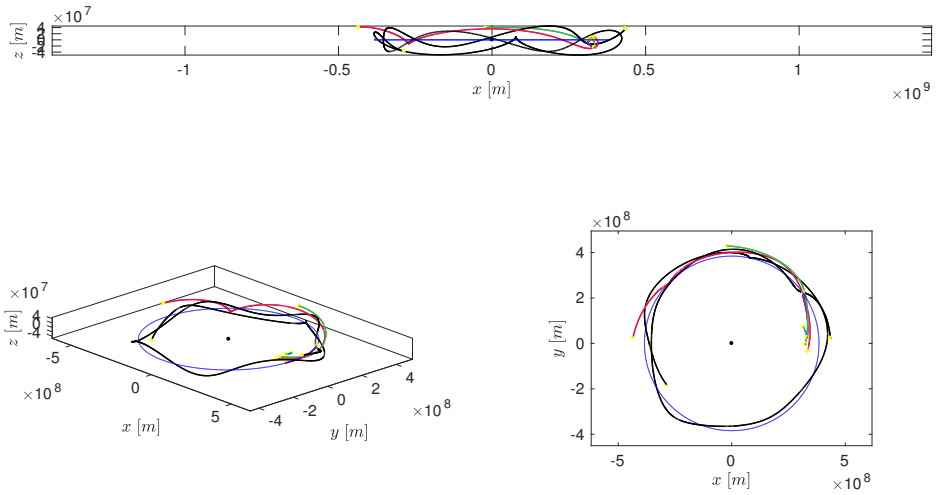

Figure 8.8: Different views in the IP1D frame of the different classes of trajectories illustrated in the SP1 frame in Figure 8.6. Moon's orbit is represented by the blue line. See the caption in Figure 8.6 for details.

Figures 8.9 and 8.10 show an example of usage of the database. In this example a Cartesian position in proximity of the QSS is defined at a specific energy level and the characteristics of the trajectories close to this position are presented. A position at $C = 2.9$ with coordinates $(-0.1673\ ,\ -0.0380\ ,\ 0.0042)$ in the SP2 frame is used. The database is therefore queried for all trajectories on the QSS that are within 1500 km from this point. Figure 8.9 shows the spatial information of the input and output positions in the database that match the condition specified in the query. The output positions are represented on the QSS with the information on the TOF of the trajectory. To complete this information with the characteristics of the osculating orbital elements before and after the flyby, the TP-graph is illustrated in Figure 8.10 with the osculating orbital elements of input and output states. Once again the information on the time of flight is represented by the color scale.

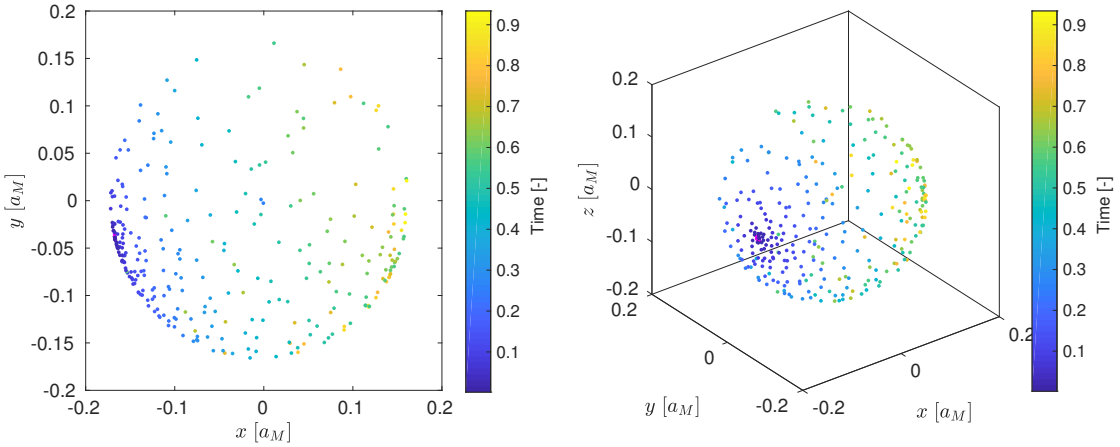

Figure 8.9: Input (pink) and output (colored) states in the database obtained from the input states within a 1500 km radius sphere centered on $(-0.1673\ ,\ -0.0380\ ,\ 0.0042)$ for the case with $C = 2.9$.

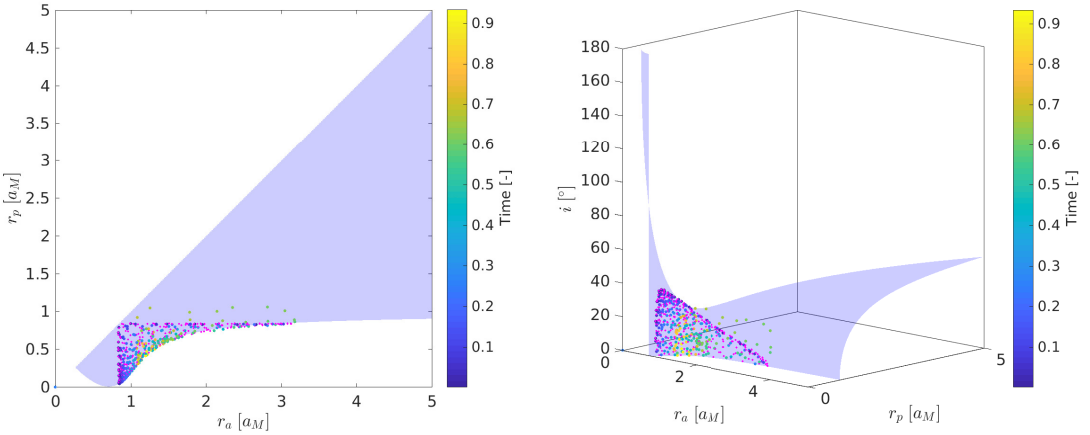

Figure 8.10: Tp-graph of the input (pink) and output (colored) osculating orbital elements in the database obtained from the input states within a 1500 km radius sphere centered on $(-0.1673\ ,\ -0.0380\ ,\ 0.0042)$ for the case with $C = 2.9$.

The information obtained from the database can be used to judge whether or not the flyby trajectory is capable to reach the desired set of osculating orbital elements or if a collision trajectory would be avoided. If the solutions are not satisfactory, the user can modify the query by looking at different energy levels or by changing other settings of the query.

8.4. 3D FLYBY WITH JUPITER

In this section an example of the usage of the database about Jupiter is provided. The results presented are simply obtained by querying the database, which contains data on about 15×10^6 trajectories distributed across 30 energy levels, from $C = 2.72859971143673$ to $C = 3.02161413943274$. The total size of the database is about 1.9 Gb.

By plotting the osculating orbital elements of the input and output states of the database at the lowest value of the Jacobi constant in Figure 8.11 it is possible to see the maximum achievable inclination from the database. The phenomenon that is constraining this value has been explained already in the previous section. Since the minimum value of C does not allow inclinations higher than 40°, retrograde flybys with Jupiter are not allowed in the database generated in this research.

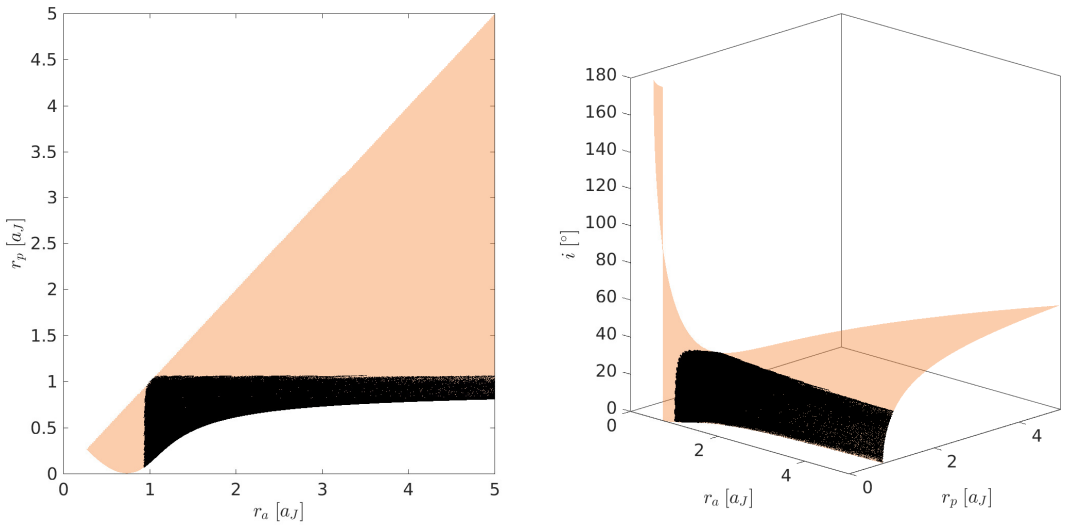

Figure 8.11: TP-graph with the osculating orbital elements of the input and output states (black dots) in the database about Jupiter for $C = 2.72859971143673$. The Tisserand level set at this level is represented by the orange surface. The maximum achievable inclination at this energy level is about 40°.

The Jupiter database can be used to investigate feasible flyby trajectories coming from Earth. In order to do so the database is queried from the osculating orbital elements of the input states. The following set for $(r_a\ ,\ r_p\ ,\ i)$ is used to simulate such flyby trajectories:

$$\begin{cases} 1-R < r_a < 1+R \\ r_p \leq 1\,AU \\ i < 5° \end{cases} \tag{8.3}$$

This example will also be used in Chapter 9 to generate feasible transfer trajectories from Earth to the Jovian system. Figure 8.12 shows the input and output osculating orbital elements in the TP-graph of this query. Two of these trajectories are selected and visualized in Figure 8.13; these are a trajectory with the maximum inclination change and a low-inclination trajectory with an aphelion increase after the flyby.

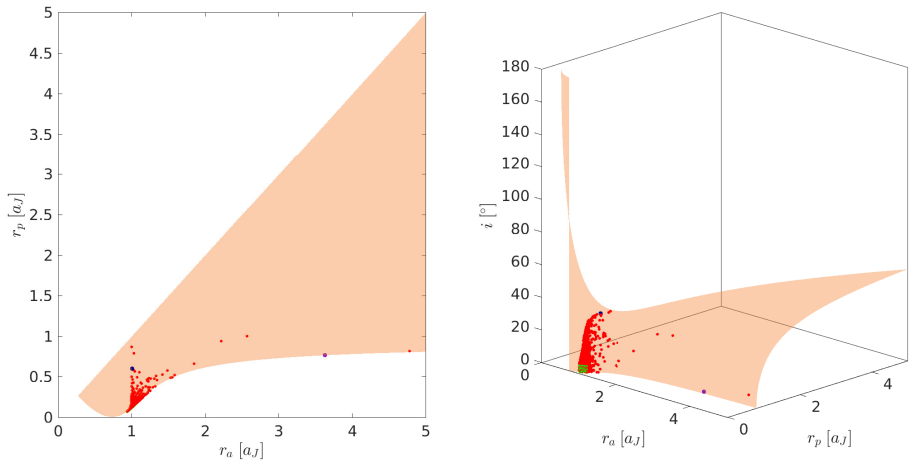

Figure 8.12: Representation of the input and output osculating orbital elements obtained by querying the database with the input expressed by Equation 8.3 at $C = 2.72859971143673$. The input elements are represented by green points, while the output ones by red points. Two trajectory cases are considered from the graph, represented by blue and purple points, whose trajectories are presented in the IP1D frame in Figure 8.13.

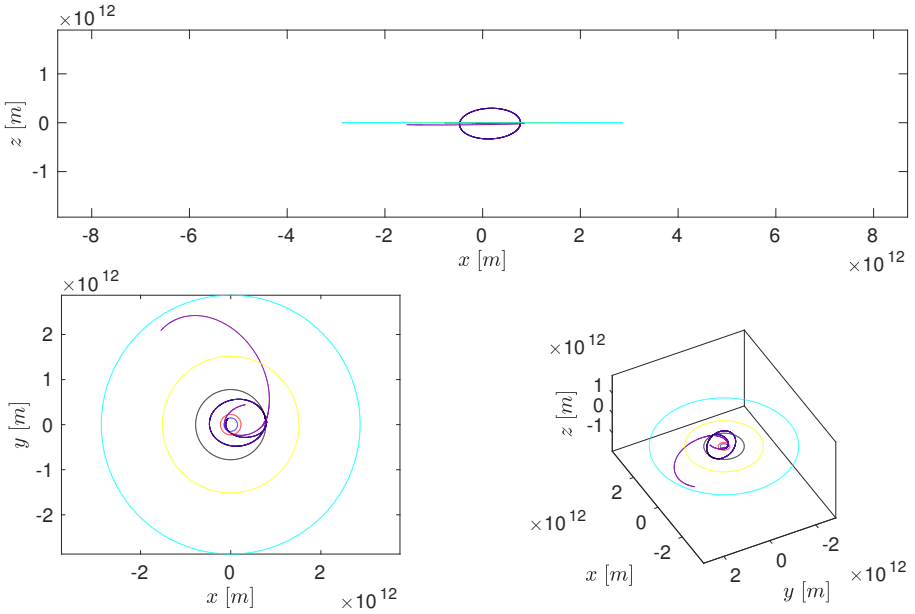

Figure 8.13: Example of two flybys with Jupiter in the IP1D frame of the SJ system for the blue and purple trajectories highlighted in Figure 8.12. Circular approximations of the orbits of Earth (blue), Mars (red), Jupiter (black), Saturn (yellow) and Uranus (cyan) are represented for comparison.

By visualizing the osculating orbital elements in the TP-graph it is possible to see that the flyby effect with Jupiter distributes most of the points at higher inclinations in a limited region with $r_a < 2$. Moreover from the visualization of the Tisserand level set in the TP-graph it is immediately possible to visualize whether or not the energy level considered is the desired one. For example it is possible to see that since the surface set is far from the osculating orbital elements $(1,1,0)$, the trajectory after the flyby will never be circularized on the same orbital plane of Jupiter, suggesting that another value of C might be considered if this is the scenario the user has been looking for. Just from the visualization of the Tisserand level set, simple conclusions can

be derived about the value of the Jacobi constant that shall be considered to achieve the desired effects in terms of osculating orbital elements of the trajectory after the flyby. The spatial configuration of the flyby trajectories illustrated in Figure 8.13 is presented in Figure 8.14.

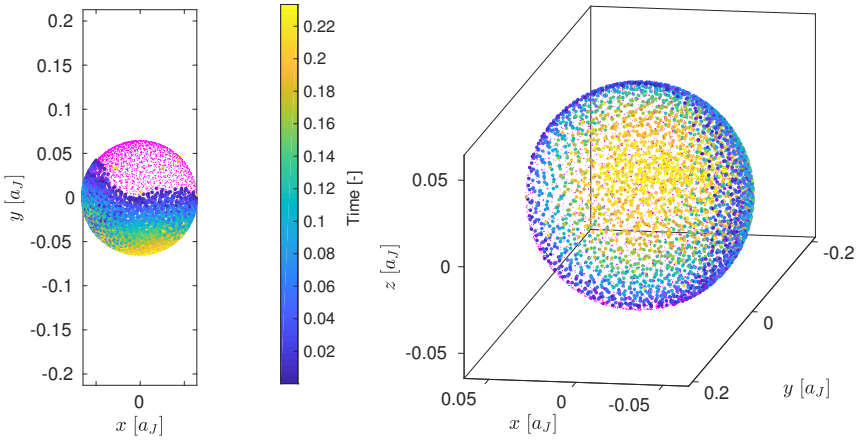

Figure 8.14: The input (pink) and output (colored) states from the database query used to generate Figure 8.13. The colors of the output states correspond to the TOF of the trajectories within the QSS. Note that input and output positions occupy opposite sides of the QSS as a result of the high energy considered.

8.5. CONCLUSIONS

In this chapter a database approach has been developed to record, catalog and design trajectories interacting with the secondary in the CR3BP model. This has been possible due to a specific Poincaré section derived in Section 4.5.3 with the shape of a quasi-spherical surface about the secondary.

By applying the spatial case of the CR3BP model five different types of trajectories have been cataloged that can be used for trajectory design purposes. By following the procedure described in Section 8.2 two databases using the QSS about the Moon and Jupiter have been generated. Examples of the usage of these databases have been presented in Sections 8.3 and 8.4.

Another important result of this chapter has been the demonstration of a graphical relationship in the TP-graph between the prograde and retrograde flybys and the value of the Jacobi constant considered. This relationship is caused by limitations imposed by the geometry of the Poincaré section considered, distributing the points on the energetic surface of a Tisserand level set only on a limited region defined by the planes $r_a \approx 1-R$ and $r_p < 1+R$. Depending on the value of the Jacobi constant, these constraints limit the maximum achievable value of the inclination and can preclude the possibility for retrograde flybys to exist.

By visualizing the Tisserand level sets and the osculating orbital elements they connect, important consideration upon the value of the Jacobi constant to consider can be done. Basically the visualization of the level sets in the TP-graph allow an easy interpretation of the performance of a flyby trajectory in terms of osculating orbital elements before and after the flyby. If these performances are not satisfactory for the case considered by the user, then the value of the Jacobi constant shall be changed accordingly to the shape of the Tisserand level set in the TP-graph that is satisfying the desired requirements. If input and output requirements are not achievable by the same Tisserand level set, then a ballistic trajectory connecting the two conditions does not exist under the assumptions of the CR3BP model considered.

Lastly the author would like to point out that the definition of the QSS proves that by computing the osculating orbital elements of a body before and after a flyby with the secondary at approximately the same distance from the flyby body would cause the Tisserand parameter T_1 to be approximately constant. This could explain the successful usage of the parameter for astronomical purposes to observe Jupiter's flyby comets before and after the flyby, as originally intended by Tisserand.

9

SUN-JUPITER-EUROPA TRAJECTORY DESIGN

In this chapter the Sun-Jupiter and Jupiter-Europa CR3BP models will be used to design a transfer trajectory that will make use of Sun's perturbations and Europa flyby effect to facilitate the insertion from an interplanetary trajectory into a science orbit about Jupiter. This specific example will be used to show an alternative application of the Poincaré section designed in Chapter 4. Instead of opting for a database approach as in Chapters 7 and 8, in this chapter a combination of propagation technique and patching technique on the Poincaré section is used.

The trajectory design process in the two CR3BP models is divided into five phases. First a reasonable transfer trajectory from Earth to Jupiter will be designed in Section 9.1 making use of the Jupiter flyby database defined in Chapter 8. The result of this section will be the definition of an arrival state to the Jovian system. This state will be manipulated in Section 9.2 to generate multiple intersection states with the Poincaré section defined about Jupiter in the Sun-Jupiter CR3BP. The science orbit about Jupiter is designed in Section 9.3 in the Jupiter-Europa CR3BP. The intersections with the Poincaré section of the operational orbit will be computed in Section 9.4. Finally the trajectories obtained in the two CR3BP models will be patched and the results will be presented in Section 9.5. To conclude the chapter Section 9.6 will sum up the main findings.

9.1. TRANSFER EARTH-JOVIAN SYSTEM

In this section a reasonable transfer trajectory from Earth to the Jovian system is designed following these steps:

- Select a value of the Jacobi constant of the Sun-Jupiter system such that the following (r_a, r_p, i) could be approximately connected by the same Tisserand level set:

$$(r_a, r_p, i)_{input} = (DU_{SJ}, DU_{SE}, 0) \tag{9.1}$$

$$(r_a, r_p, i)_{output} = \left(DU_{SJ}, DU_{SJ}, < \frac{\pi}{2}\right) \tag{9.2}$$

  where DU_{SJ} and DU_{SE} are respectively the Sun-Jupiter and Sun-Earth distances while the osculating orbital elements are intended with respect to the Sun. For the example illustrated in this chapter $C = 2.72955248581335$.

- Consult the Jupiter database defined in Section 8.4 using the two sets expressed by Equations 9.1 and 9.2 as input and output conditions respectively.

The osculating orbital elements after the flyby with Jupiter have been selected such to generate a reference trajectory that is naturally using the flyby with Jupiter to circularize the trajectory about the Sun. This should be helpful in putting the spacecraft at the right energy level for an orbit insertion about Jupiter. Moreover in

order to facilitate the insertion into a high-inclination science orbit, only prograde trajectories with a high inclination after the flyby have been considered. Figure 9.1 shows the reference trajectory considered to simulate the transfer from Earth to Jupiter. Note that in the design process the phasing of Earth has not been considered since the trajectory is just the representation of an energy-wise realistic transfer to the Jovian system. This assumption is done to simplify the analysis.

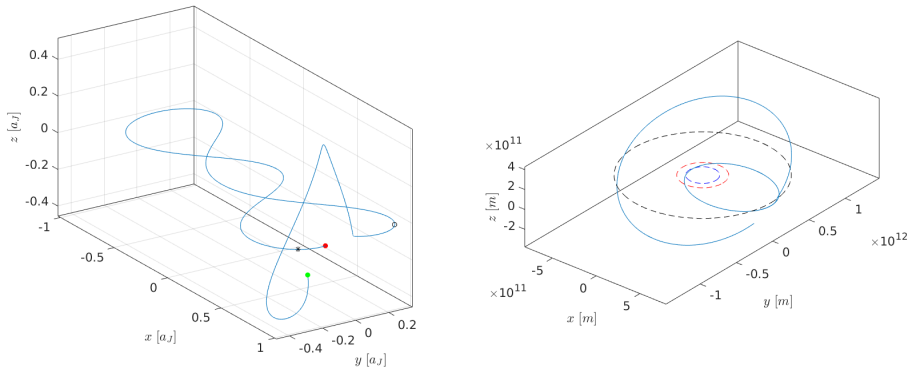

Figure 9.1: The Earth to Jupiter transfer trajectory. Left: Trajectory represented in the SP1 frame. Red and green points are initial and final propagation states, while the black points represent the intersection with the SOI of Jupiter. Right: The trajectory in the IP1D frame. Also the approximation of Jupiter (black), Mars (red) and Earth (blue) orbits are presented for reference.

9.2. SUN-JUPITER CR3BP ANALYSIS

From the reference transfer trajectory designed in Section 9.1 the state and epochs of the trajectory at a distance of $5R_{SOI}$ from Jupiter are taken as initial conditions. The analysis continues focusing on the characteristics of the trajectory in the vicinity of Jupiter. To obtain a large number of flyby trajectories close to the reference one, the following steps are executed:

- A ΔV_1 maneuver with a magnitude between 10 and 200 m/s (with increments of 10 m/s) and with a random orientation in space is executed. A total of 100 combinations of azimuth and elevation angles are taken into account for each value of ΔV_1.
- The manifold of trajectories propagated from the initial condition is intersected with the Poincaré section defined about the secondary in the SP2 frame expressed by Equation 4.61.
- The states and osculating orbital elements of these intersections are stored and will be used for patching in Section 9.5.

The reason why the initial condition is shifted at $5R_{SOI}$ from Jupiter is to give time to Sun's perturbing effect in the CR3BP to play a role in spreading the manifold generated by a relatively low ΔV_1 maneuver. In such a way an important part of the trajectory is computed by taking into consideration the gravitational influence of both Jupiter and the Sun.

9.3. SCIENCE ORBIT ABOUT JUPITER

In this section a high-inclination high-eccentricity operational orbit about Jupiter is designed making use of a flyby with Europa to decrease the energy of the spacecraft arriving from the interplanetary phase designed in Section 9.2. Because of the complexity of designing a trajectory with the proper characteristics that is also having a flyby with Europa, the process is performed backward by choosing the proper flyby trajectory with Europa that is also satisfying the characteristics of a science orbit about Jupiter. The science orbit is therefore selected following this procedure:

- The same approach used in Sections 8.3 and 8.4 is now applied to Europa as flyby body. In particular a Jacobi constant $C = 1.775$ of the Jupiter-Europa system is used to generate a small database of flyby trajectories from a QSS of radius $0.05DU_{JE}$ about Europa.
- Consulting such a database, only those trajectories that exhibit the greatest variation in the apojove and that have high inclinations after the flyby are considered. This is done to maximize the Europa flyby effect.
- Lastly only that trajectory for which the final orbit about Jupiter after the flyby with Europa satisfies the desired characteristics of a stable science orbit about Jupiter is selected.

Such a stable reference operational orbit about Jupiter that makes use of a Europa flyby is illustrated in Figure 9.2.

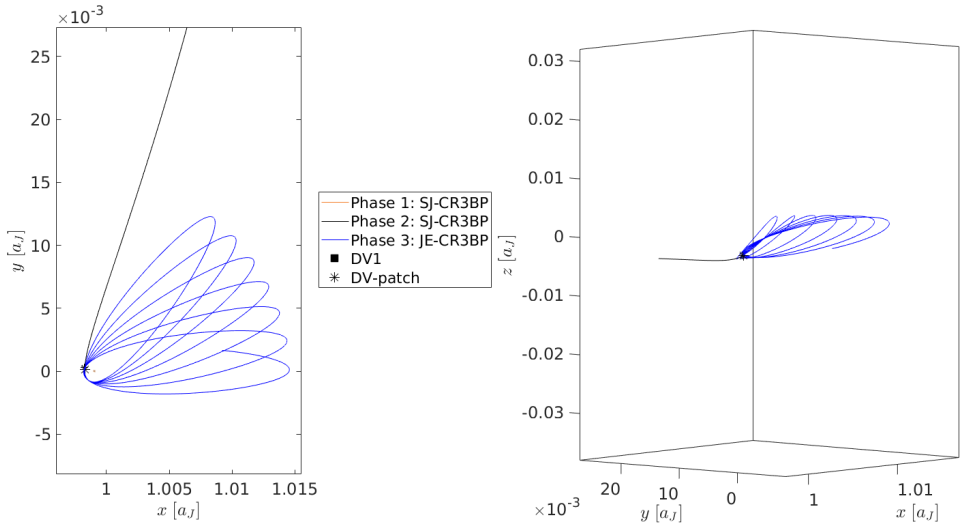

Figure 9.2: The trajectory in the Sun-Jupiter SP1 frame designed in the Sun-Jupiter-Europa system making use of patched CR3BP models. The science orbit about Jupiter is represented by the blue curve. The interplanetary trajectory designed in Section 9.2 is represented in black. The location of the patching ΔV maneuver is represented by a $*$ while ΔV_1 is not visible in this figure.

9.4. JUPITER-EUROPA CR3BP ANALYSIS

The reference science orbit about Jupiter defined in Section 9.3 is now confronted with the Poincaré section defined in the SP2 frame of the Sun-Jupiter CR3BP. To do so the reference trajectory is transformed from the SB to the IP2D frame of the Jupiter-Europa system. From this the trajectory is transformed to the SB frame of the Sun-Jupiter system. The chain of transformations depends on the phasing angle between the two systems. In order to simplify the analysis, the correct phasing between the systems is not considered and this angle is varied to random values to generate multiple intersections of the reference orbit about Jupiter with the Poincaré section. The intersection states and epochs recorded in this section will be used in the next section to patch the trajectories in the two models.

Note that in this analysis it also would have been possible to locate a ΔV_2 maneuver to generate multiple intersections with the Poincaré section by considering the proper phasing of the systems. Although this would have resulted in a much more realistic trajectory, the complexity of the proper tuning between these parameters and the unsatisfying results obtained have pushed to assume this simplification.

9.5. PATCHING BETWEEN CR3BP MODELS

From Sections 9.2 and 9.4 the intersection states from the trajectories computed in the Sun-Jupiter and Jupiter-Europa CR3BP models have been recorded on the Poincaré section about Jupiter in the SP2 frame

of the Sun-Jupiter system. The difference between the positions and velocity components of these intersections are then compared to select the trajectory with the lowest ΔV_{patch}, illustrated in Figures 9.2 to 9.4.

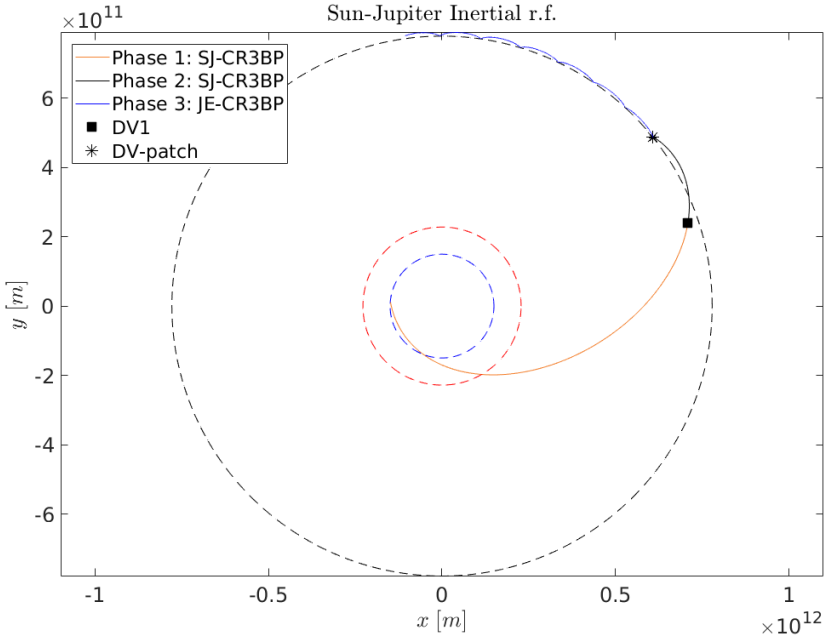

Figure 9.3: Complete trajectory designed in the Sun-Jupiter-Europa patched CR3BP model represented in the IP1D of the SJ system. Jupiter (black), Mars (red) and Earth (blue) orbits are presented for comparison. ΔV_1 and ΔV_{patch} are represented by square and asterisk symbols.

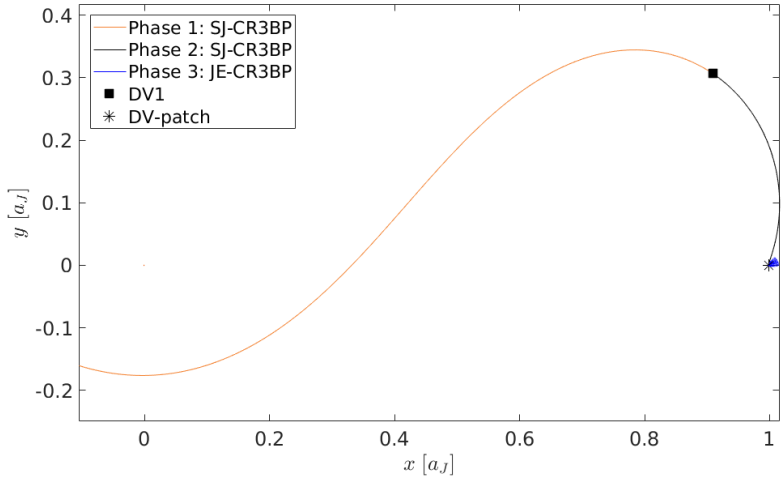

Figure 9.4: Complete trajectory designed in the Sun-Jupiter-Europa patched CR3BP model represented in the SP1 frame of the Sun-Jupiter system. ΔV_1 and ΔV_{patch} are represented by square and asterisk symbols. A zoom of this figure in the vicinity of Jupiter can be seen in Figure 9.2.

The trajectory illustrated in these figures has been obtained with ΔV_1 = 50 m/s and a patching velocity ΔV_{patch} of 2.1971 km/s, at a patching distance Δr_{patch} of 144000 km.

9.6. CONCLUSIONS

In this chapter an alternative procedure that makes use of numerical propagation and Poincaré sections is used to design a trajectory in the Sun-Jupiter-Europa patched CR3BP model. The specific example taken into consideration in this chapter allowed to design a trajectory from Earth's orbit to Jupiter that is directly exploiting Jupiter's flyby, Sun's perturbation and Europa's flyby effects.

Although these effects have been taken into account, no ballistic transfers have been found. The lowest value of ΔV_{patch} found in this analysis (2.1971 km/s) is relatively high. Considering also ΔV_1 the overall mission ΔV considered for this trajectory is 2.2471 km/s. Note that in this computation the initial ΔV_0 necessary to put the spacecraft into the interplanetary transfer trajectory is not computed as in the focus of this analysis is in the multi-body dynamical effects in proximity of Jupiter to ensure a capture.

The author believes that this large value to connect the two ballistic trajectories is the result of a natural gap existing between the energy levels considered in the two systems. To visualize this gap Figure 9.5 represents the TP-graph of the level sets of the two systems, together with the osculating orbital elements of the patch points.

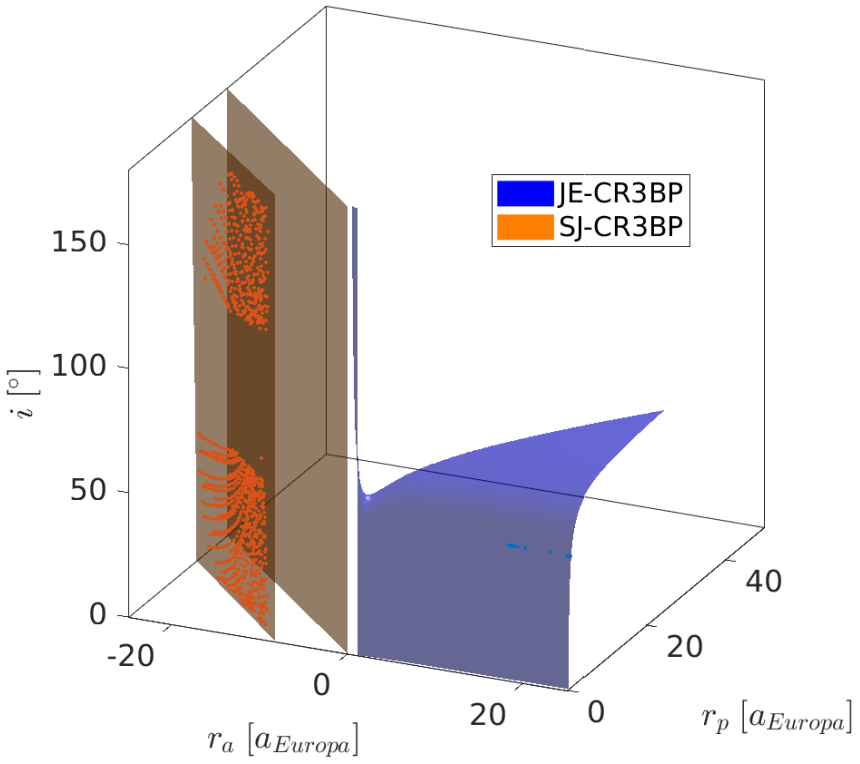

Figure 9.5: TP-graph obtained with the two values of the Jacobi constant of 2.72955248581335 and 1.775 respectively for the Sun-Jupiter and Jupiter-Europa CR3BP. The Tisserand level surface of the first system is represented in orange, while the one of the Jupiter-Europa system is represented by the blue surface. The patch points are plotted in darker blue and orange on the corresponding surfaces.

As it is possible to see from Figure 9.5, the values chosen for the Jacobi constants of the two systems it is not adequate to generate an overlap between the Tisserand level sets in the TP-graph. In particular is possible to see that the Tisserand level set of the Sun-Jupiter system develops entirely in the region with $r_a < 0$. This region, that has never been explored in this report, describes hyperbolic trajectories with the correct value of pericenter, but with a wrong r_a parameter. For hyperbolic trajectories $r_a = +\infty$, so negative finite values of r_a are physically wrong, since they do not represent apocenter radius. Nonetheless these values, computed applying the usual expression $r_a = a(1+e)$ are mathematically consistent for both systems.

The representation of the region with $r_a < 0$ therefore illustrates very clearly in the ETP-graph the energetic bridge existing between the trajectories considered in the two systems. From this the high ΔV_{patch} found in the analysis can be explained by the attempt to patch elliptic and hyperbolic trajectories in the ETP-graph. For comparison it is possible to determine the values of the Jacobi constants of the Sun-Jupiter system that make the Tisserand level sets described by T_2 to pass through the points $(r_a, r_p, i) = (a_{Europa}, a_{Europa}, 0)$ and $(18a_{Europa}, a_{Europa}, 0)$. By imposing these conditions it is found that the Jacobi constants of the Sun-Jupiter CR3BP should be 4.1042 and 3.1151 respectively. These values however correspond to a situation where both $L1$ and $L2$ necks of the system are closed and a transfer trajectory from Earth as the one designed in Section 9.1 is simply not possible. It becomes clear from this scenario that it is necessary to perform a compromise on the value of the Jacobi constant of the Sun-Jupiter system by taking into account both the characteristics of the transfer trajectory to Jupiter from Earth and the patching conditions in the vicinity of Jupiter. In this sense a trade-off solution might be seeked by increasing the apojove distance of the patching condition such to open the L1 neck of the Sun-Jupiter system. An alternative would be to work on the patching conditions between hyperbolic trajectories in both systems. In case of the Jupiter-Europa system the trajectory would be a hyperbolic trajectory performing a close flyby with Europa that transforms it into an highly-elliptic and high-inclination stable orbit about Jupiter. Both alternatives could be investigated in future studies to overcome this issue in the Sun-Jupiter-Europa patched CR3BP.

10

CONCLUSIONS AND RECOMMENDATIONS

This chapter concludes the research presented in this report performed at ISAS/JAXA. The most important findings are summarized in Section 10.1, while recommendations for future studies are presented in Section 10.2.

10.1. CONCLUSIONS

The work presented in this report has been divided into two parts following the research questions highlighted in Section 1.2.

Chapters 4, 5 and 6 are dedicated to the extension of the theoretical framework related to the Tisserand parameters, TP-graphs, ETP-graphs and Poincaré sections used to obtain them, answering the first research question and sub-questions. The main findings can be summarized as follows:

- **Modified Tisserand parameter:** A modified Tisserand parameter exists that can be defined using the osculating orbital elements with respect to the secondary of a CR3BP system:

$$T_2 = \frac{\mu_2}{a} + 2\frac{1}{TU}\sqrt{\mu_2 a\left(1-e^2\right)}cos(i) \tag{10.1}$$

  The formulation of this parameter turns out to be identical to the one of the classical Tisserand parameter T_1, with the only difference that the osculating orbital elements are expressed with respect to the secondary of the system. This parameter derives from a fundamental decomposition of the Jacobi integral J as the sum of two functions T_2 and P_2, the first one referred to as modified Tisserand parameter and the latter as a residual function:

$$J\left(x,y,z,\dot{x},\dot{y},\dot{z}\right) = T_2\left(a,e,i\right) + P_2\left(x,y,z\right) \tag{10.2}$$

  The Tisserand parameter T_2 is a function of the osculating orbital elements while the residual function P_2 is a potential function depending only on the position components. This exact relationship has been derived both for T_1 and T_2, with the definition of a residual function P_1.

- **Poincaré sections:** Because the residual functions P_1 and P_2 depend only on spacecraft position, they define families of equipotential surfaces in the CR3BP. Such surfaces are defined in the synodic frames centered on the primaries and make the Tisserand parameters local integrals when the osculating orbital elements of a trajectory are computed for points positioned on such surfaces. This is of fundamental importance especially for T_2, that otherwise would not exhibit the same homogeneous properties of T_1. Three of these surfaces have been chosen for the research illustrated in this report to generate TP-graphs and ETP-graphs. These are often constructed with arbitrarily chosen Poincaré sections far from the secondary however thanks to P_1 and P_2, in this report they are constructed following a mathematically rigorous definition that guarantees constant values of T_1 and T_2.

- **ETP-graph:** By applying the definitions of T_1 and T_2 the corresponding Tisserand level sets in the TP-graph and ETP-graph have been thoroughly characterized both from a geometric and mathematical point of view. It has been discovered that by combining the level sets of the EM and SE systems obtained by T_1 and T_2 in the ETP-graph, it is possible to described solar perturbation effects under existing frameworks. In particular the ETP-graph characterized in this report complies with the findings of a qualitative analysis existing in literature about solar perturbation effects in the ETP-graph [9]. These are proven to act on lines of slope -1 in the graph and suggests that an inversion of motion from prograde to retrograde regions and vice-versa is simpler to achieve than in the EM system. The ETP-graph also shows the existence of energy connections between $SEL1$ and $SEL2$ with all the energy levels of the Lagrange points of the EM system (within $3a_M$). The effects of the level sets describing solar perturbation is explained by the different time normalization parameters of the CR3BP considered. This difference acts as a scaling factor in the representation of the Tisserand level sets, generating an overlapping of energetic levels in a useful region of the EM and SE systems.

- **Poincaré maps:** The Poincaré sections defined by the Tisserand parameters have been characterized both in the EM and SE systems to understand their performances and what type of dynamics they are able to represent in Poincaré maps. Classical maps turned out to be inefficient in describing the complexity of the motions captured by these sections, for this reason $\dot{x}\dot{y}$ maps have been adopted. In certain cases it is important to distinguish whether these refer to the interior or exterior regions in order to avoid ambiguity and guarantee the full state reconstruction of any point taken from the maps. With the usage of these sections it has been observed that the way in which retrograde and prograde motions are represented in the maps by the sections is different. In particular it has been observed that great importance seems to be given to retrograde trajectories, whose characteristics seem to be naturally enhanced by the properties of the Tisserand level sets associated to the Poincaré sections. Stable regions of periodic motion exist for both regions. However the stable motion for retrograde trajectories can be found at any energy level through the sections, while stable motion for prograde trajectories is more rare and appears with distinctive features in the maps only at high values of the Jacobi constant. Another interesting result is associated to collision trajectories both with Earth and Moon, that in the first case are easily represented in the interface region in the map between retrograde and prograde motion, while in the latter are distributed in different specific regions of the maps.

In Chapters 7, 8 and 9 three different technical approaches have been developed in order to exploit the theoretical findings illustrated in the previous chapters. The main findings can be summarized as follows:

- **Database approach:** A database approach has been developed to design Sun's perturbed trajectories in the SE CR3BP. This approach exploited section-to-section transfer legs with constant T_2 in the SE system using a Poincaré section defined about the Earth in the SP2 frame. The idea behind the database is to enable the storing of fundamental characteristics of transfer trajectories in the SE system that connect different points on a Poincaré section in order to use these trajectories as a way to increase or decrease the value of the Jacobi constant of the EM system for trajectory design purposes. Since the database is defined for an autonomous system, it can be used as a universal tool for the systematic research of patched trajectories in the SE and EM CR3BP models. Few examples have been illustrated about the usage of such database, in particular a two-point patched trajectory in the EM-SE-EM system. The approach also showed some limitations regarding the complexity in designing a multiple-point patched trajectory, especially regarding the significant build-up in the necessary ΔV for patching and in the complexity of the query structure to obtain a trajectory. These issues have not been addressed in this research and remain open for further activities in the future since the research has been focused more on the generation of the database itself and on the demonstration of its application.

- **Flyby database:** Exploiting a particular Poincaré section at constant T_1 that develops about the secondary as a quasi-spherical surface, a database approach has been developed to record, catalog and design trajectories interacting with the secondary in the CR3BP. Two database have been generated considering the Moon and Jupiter cases. Such catalogs of trajectories mapped the input-output states from the Poincaré sections mostly affected by the influence of the secondary. These databases are referred to as flyby databases, but are much more than this since they also collect informations on collision and temporarily capture trajectories. Indeed, five different categories of trajectories have been cataloged in these databases, that demonstrated to be really useful during the technical analysis performed in these

chapters. These databases also elegantly demonstrated on the TP-graph a phenomenon that cause an energetic distinction between retrograde and prograde flybys. The latter exist basically at all energy levels, while the former ones only exist for low values of the Jacobi constant. Generally speaking on the TP-graph the effect of the maximum inclination that is possible to achieve from a flyby event can be simply visualized since it is a function of the energy level considered; thus it is a function of the value of the Tisserand parameter considered to represent a level set. From the shape of the level sets in the TP-graph it is possible to determine the necessary value of the Jacobi constant that allows to reach the desired output or input conditions after a flyby event.

- **Sun-Jupiter-Europa trajectory:** Finally, a technique that is solely relying on numerical propagation and representation of the intersection points both on the Poincaré section and on the TP-graph is illustrated for a patched trajectory in a SJ and JE CR3BP. This system is theoretically the same of the SE and EM CR3BP and it was interesting to investigate it through the new tools derived in this report. In such a system however a trajectory design process would rather be focused on the reduction of the mission ΔV through the usage of multi-body dynamical effects. This is investigated through the usage of Jupiter and Europa flybys and by exploiting solar perturbation for a portion of the trajectory. The overall design is not successful in designing a ballistic transfer trajectory from Earth because of the existence of an energetic 'wall' between the SJ and JE systems due to choices done concerning both the transfer phase from Earth and the science orbit about Jupiter. This example however illustrates that the choice of the correct energy levels is fundamental for the trajectory design. In this process the Tisserand level surfaces can be exploited to obtain indications upon the energy required by certain transfers. A possibility that is highlighted in this analysis is that, although elliptic patching trajectories cannot be found because of the arrangement of the Tisserand level sets in the graph, there could be a possibility for ballistic patching in the hyperbolic realm. This possibility however has not been investigated and is left for further studies.

- **Patched CR3BP vs BR4BP vs full-ephemeris:** In chapter 7 and Appendix D the performances of these three dynamical models are briefly confronted. The patched CR3BP model resulted in a good approximation of the BR4BP whenever considering a short to medium propagation time and with a particular care to avoid undesired patching conditions. In this sense the patching distance from Earth and the expected behavior of the trajectory (getting closer or further away from the Earth-Moon system for example) are fundamental aspects to be taken into account. The comparison between the results obtained in the patched CR3BP and full-ephemeris model highlights important discrepancies between the trajectories. These are attributed to the real inclinations and eccentricities of the gravitational bodies considered, since such discrepancies have not been observed in the BR4BP with the introduction of a coplanar 4th perturbing body. The usage of a Bicircular Elliptic Four-Body Problem in which the Earth and Moon move in elliptic orbits that do not share the same plane shall overcome this limitation.

- **3D description:** The techniques developed in the research have been used in the 3D case in order to be realistically applicable for mission design purposes. In the flyby database this has proven to be important to understand the relationship existing between prograde and retrograde flybys and the energy level considered in the TP-graph. In the Moon and Jupiter flyby databases this is fundamental in the design of trajectories whose inclinations is greatly changed during the flyby event. No particular phenomena have been observed about the SE transfer legs database rather than an oscillating behavior of the trajectories along the z-axis. This suggests that the usage of coplanar systems do not generate particular phenomena in the 3D case. Nonetheless from an engineering point of view is important to take into account the oscillating behavior in order to ensure a proper patching. It can be concluded that a 3D description complicates the analysis, but ultimately allows to use more interesting arrival orbits such as Halo, temporarily capture or simple high-inclination and high-eccentricity orbits useful for observation and/or scientific activities.

- **Optimization:** The research has been focused on the generation of first-guess solutions and optimization tasks have not been considered in this report. Further study shall be pursued in order to match the first-guess generation step with an optimization step that takes the output of this research as an input to improve the speed of the overall trajectory design process.

10.2. RECOMMENDATIONS

Following these conclusions, recommendations and ideas for future studies that have not been pursued in this research are briefly collected:

- The Tisserand level sets in the ETP-graph that are describing the effects of solar gravitational perturbation could in principle be used to describe also solar radiation pressure effects. Since both forces would be modeled by the primary, they could be united in the same dynamical model in a modified CR3BP. A modified Tisserand parameter that takes into consideration the combined effect of gravitational and SRP effects could in principle be expressed. Since many expressions make use of the normalization parameters defined for a gravitational system, it is not sure that the derivation can be successful.
- The Poincaré maps have shown incredible stable structures for retrograde trajectories at any energy levels. This inherent stability can be exploited for mission observation purposes considering as target bodies both primaries. Although it would hardly be practical to directly reach such retrograde trajectories, it could be possible to investigate the usage of solar perturbation to reach this type of orbits with ballistic trajectories.
- The SJ and JE CR3BP showed that in some cases patching conditions might be sought in the hyperbolic region of the TP-graph. This region has been completely ignored in this research, since the focus has been put on low-energy elliptic trajectories.
- The Poincaré maps highlighted the regions of collision trajectories with Earth in a simple way in the interface region between prograde and retrograde motion. On the other hand the structure of the collision orbits with the Moon in the maps has not been characterized in this research.
- Since the database approach of the SE perturbed trajectories is defined in an autonomous system, in principle it could be possible to patch trajectories modeled between EM and SE systems that are not coplanar with respect to each other. In order to do that it is just necessary to keep track of the relative inclination of one of the models with respect to the other and to change the query in the database. This should affect only the inclination parameter and shall not have repercussions on r_a and r_p, once the proper Ω and ω for the specific patching considered are taken into account by the user. This possibility would increase the precision of this model in representing the different orbital planes in which Sun, Earth and Moon move.
- The possibility to generate Poincaré maps in the 3D case has been briefly explored in this research with unsatisfactory results. The huge amount of data collected in the generation of the database of SE trajectories can be used in this sense for the interested reader that would like to try to seek a clear interpretation of these data in a multi-dimensional Poincaré map.

A

TISSERAND PARAMETERS

In this appendix the different expressions of the Tisserand parameters and residual functions are summarized for a better understanding of the report. The classical and modified Tisserand parameters are referred for simplicity as Tisserand parameters or as Tisserand parameter about the primary (T_1) and Tisserand parameter about the secondary (T_2). These are defined in dimensional units as:

$$\begin{cases} T_1(a,e,i) = \dfrac{\mu_1}{a} + 2\dfrac{1}{TU}\sqrt{\mu_1 a\left(1-e^2\right)}cos(i) \\ T_2(a,e,i) = \dfrac{\mu_2}{a} + 2\dfrac{1}{TU}\sqrt{\mu_2 a\left(1-e^2\right)}cos(i) \end{cases} \tag{A.1}$$

where μ_1 and μ_2 are the gravitational parameters of the primaries, TU is the time normalization parameter of the CR3BP considered and a,e and i are the osculating semi-major axis, eccentricity and inclination. By using the pericenter and apocenter radius r_p and r_a instead of a and e, the following expressions can be written:

$$\begin{cases} T_1\left(r_a,r_p,i\right) = \dfrac{2\mu_1}{r_a+r_p} + \dfrac{2}{TU}\sqrt{2\mu_1\dfrac{r_a r_p}{r_a+r_p}}cos(i) \\ T_2\left(r_a,r_p,i\right) = \dfrac{2\mu_2}{r_a+r_p} + \dfrac{2}{TU}\sqrt{2\mu_2\dfrac{r_a r_p}{r_a+r_p}}cos(i) \end{cases} \tag{A.2}$$

These Tisserand parameters can also be expressed in the adimensional units of the CR3BP considered as:

$$\begin{cases} T_1(\tilde{a},e,i) = \dfrac{1-\mu}{\tilde{a}} + 2\sqrt{\left(1-\mu\right)\tilde{a}\left(1-e^2\right)}cos(i) \\ T_2(\tilde{a},e,i) = \dfrac{\mu}{\tilde{a}} + 2\sqrt{\mu\tilde{a}\left(1-e^2\right)}cos(i) \end{cases} \tag{A.3}$$

where the semi-major axis in these equations is expressed in normalized units as $\tilde{a} = \frac{a}{DU}$. These expressions can be written as a function of $\tilde{r}_a = \frac{r_a}{DU}$ and $\tilde{r}_p = \frac{r_p}{DU}$ in normalized units as:

$$\begin{cases} T_1\left(\tilde{r}_a,\tilde{r}_p,i\right) = \dfrac{2\left(1-\mu\right)}{\tilde{r}_a+\tilde{r}_p} + 2\sqrt{2\left(1-\mu\right)\dfrac{\tilde{r}_a\tilde{r}_p}{\tilde{r}_a+\tilde{r}_p}}cos(i) \\ T_2\left(\tilde{r}_a,\tilde{r}_p,i\right) = \dfrac{2\mu}{\tilde{r}_a+\tilde{r}_p} + 2\sqrt{2\mu\dfrac{\tilde{r}_a\tilde{r}_p}{\tilde{r}_a+\tilde{r}_p}}cos(i) \end{cases} \tag{A.4}$$

Once the CR3BP considered is specified by the mass parameter μ, the residual functions defined in this report are depending only on the position vector in the $SP1$ or $SP2$ frames. The residual function associated to T_1 is expressed as P_1, while the one associated to T_2 as P_2.

$$P_1\left(\mathbf{r}_{SP1}\right) = \frac{2\mu}{\sqrt{(x-1)^2+y^2+z^2}} - 2\mu x + \mu^2 + \mu\left(1-\mu\right) \tag{A.5}$$

$$P_2\left(\mathbf{r}_{SP2}\right) = \frac{2\left(1-\mu\right)}{\sqrt{(x+1)^2+y^2+z^2}} + 2(1-\mu)x + (1-\mu)^2 + \mu\left(1-\mu\right) \tag{A.6}$$

where $\mathbf{r}_{SP1} = \left[x\ y\ z\right]^T$ and $\mathbf{r}_{SP2} = \left[x\ y\ z\right]^T$ are the position vectors from the origins of the $SP1$ and $SP2$ frames. The relationships existing between the Tisserand parameters, the Jacobi integral and the residual functions can be expressed as:

$$J\left(\mathbf{X_{SP1}}\right) = T_1(\tilde{a}, e, i) + P_1(\mathbf{r}_{SP1}) \tag{A.7}$$

$$J\left(\mathbf{X_{SP2}}\right) = T_2(\tilde{a}, e, i) + P_2(\mathbf{r}_{SP2}) \tag{A.8}$$

B

DERIVATIONS

In this appendix the derivations of the expressions used in this report to compute the Keplerian energy and angular momentum vector with respect to the main attracting body are presented together with the algorithms used to compute the osculating orbital elements.

An important part of the derivations presented in this appendix rely on the coordinate transformation equations presented in Section 3.2.2. In the particular the relationship between the state $\mathbf{X}_{IP_i} = [\xi\ \eta\ \varsigma\ \dot{\xi}\ \dot{\eta}\ \dot{\varsigma}]^T$ expressed in IP_i frame and $X_{SB} = [x\ y\ z\ \dot{x}\ \dot{y}\ \dot{z}]^T$ in SB frame will be used:

$$\begin{bmatrix} \xi \\ \eta \\ \varsigma \\ \dot{\xi} \\ \dot{\eta} \\ \dot{\varsigma} \end{bmatrix} = \begin{bmatrix} cos\theta & -sin\theta & 0 & 0 & 0 & 0 \\ sin\theta & cos\theta & 0 & 0 & 0 & 0 \\ 0 & 0 & 1 & 0 & 0 & 0 \\ -sin\theta & -cos\theta & 0 & cos\theta & -sin\theta & 0 \\ cos\theta & -sin\theta & 0 & sin\theta & cos\theta & 0 \\ 0 & 0 & 0 & 0 & 0 & 1 \end{bmatrix} \begin{bmatrix} x-(P_i)_x \\ y \\ z \\ \dot{x} \\ \dot{y} \\ \dot{z} \end{bmatrix} \tag{B.1}$$

where $(P_i)_x$ denotes the coordinate of the origin of the inertial frame and θ is the angle between the x-axes of the synodic and inertial frames. From this expression each component of the inertial state can be computed as a function of the SB components of the state as:

$$\begin{cases} \xi = (x-(P_i)_x)\,cos\theta - y sin\theta \\ \eta = (x-(P_i)_x)\,sin\theta + y cos\theta \\ \varsigma = z \\ \dot{\xi} = -(x-(P_i)_x)\,sin\theta - y cos\theta + \dot{x} cos\theta - \dot{y} sin\theta \\ \dot{\eta} = (x-(P_i)_x)\,cos\theta - y sin\theta + \dot{x} sin\theta + \dot{y} cos\theta \\ \dot{\varsigma} = \dot{z} \end{cases} \tag{B.2}$$

B.1. KEPLERIAN ENERGY

The specific energy of the spacecraft with respect to the main attractor body P_i with a gravitational parameter μ_i is computed in the inertial reference frame as:

$$(E_i)_{IP_iD} = \frac{V^2}{2} - \frac{\mu_i}{r} \tag{B.3}$$

where V and r are the spacecraft velocity and position in such a frame, $V = \sqrt{\dot{\xi}^2 + \dot{\eta}^2 + \dot{\varsigma}^2}$ and $r = \sqrt{\xi^2 + \eta^2 + \varsigma^2}$. By substituting the components of these expression with the terms in Equation B.2 these can be written in SB coordinates as:

$$r = \sqrt{(x-(P_i)_x)^2 + y^2 + z^2} \tag{B.4}$$

$$V^2 = \left(x - (P_i)_x + \dot{y}\right)^2 + \left(\dot{x} - y\right)^2 + \dot{z}^2 \tag{B.5}$$

By applying the normalization parameters of the CR3BP model and after some simplifications the expressions of the Keplerian energy with respect to the primaries in SB coordinates are obtained. Note that the energy with respect tot the primary $(E_1)_{SB}$ is obtained by substituting $(P_i)_x = -\mu$, while the one with respect to the secondary $(E_2)_{SB}$ is obtained by substituting $(P_i)_x = 1-\mu$.

$$(E_1)_{SB} = \frac{\left(x+\mu+\dot{y}\right)^2 + \left(\dot{x}-y\right)^2 + \dot{z}^2}{2} - \frac{1-\mu}{\sqrt{\left(x+\mu\right)^2 + y^2 + z^2}} \tag{B.6}$$

$$(E_2)_{SB} = \frac{\left(x+\mu-1+\dot{y}\right)^2 + \left(\dot{x}-y\right)^2 + \dot{z}^2}{2} - \frac{\mu}{\sqrt{\left(x+\mu-1\right) + y^2 + z^2}} \tag{B.7}$$

B.2. ANGULAR MOMENTUM

The angular momentum vector with respect to the main attractor P_i is computed in the inertial frame IP_i as:

$$(\mathbf{H_i})_{IP_i} = \mathbf{r} \wedge \mathbf{V} = \begin{bmatrix} \eta\dot{\xi} - \varsigma\dot{\eta} \\ \varsigma\dot{\xi} - \xi\dot{\tau} \\ \xi\dot{\eta} - \eta\dot{\xi} \end{bmatrix} \tag{B.8}$$

The magnitude of such a vector is referred to as h_i. By substituting the terms in Equation B.2 the general expression of the angular momentum vector in SB coordinates with respect to the body P_i can be written as:

$$(\mathbf{H}_i)_{SB} = \begin{bmatrix} y\dot{z} - z\left(\dot{y} + x - (P_i)_x\right) \\ z\left(\dot{x} - y\right) - \dot{z}\left(x - (P_i)_x\right) \\ \left(x - (P_i)_x\right)\left(\dot{y} + x - (P_i)_x\right) - y\left(\dot{x} - y\right) \end{bmatrix} \tag{B.9}$$

By substituting $(P_i)_x = -\mu$ and $(P_i)_x = 1-\mu$ this expression is specified with respect to the primary $(\mathbf{H}_1)_{SB}$ or secondary $(\mathbf{H}_2)_{SB}$ of the system:

$$(\mathbf{H}_1)_{SB} = \begin{bmatrix} y\dot{z} - z\left(\dot{y} + x + \mu\right) \\ z\left(\dot{x} - y\right) - \dot{z}\left(x + \mu\right) \\ \left(x + \mu\right)\left(\dot{y} + x + \mu\right) - y\left(\dot{x} - y\right) \end{bmatrix} \tag{B.10}$$

$$(\mathbf{H}_2)_{SB} = \begin{bmatrix} y\dot{z} - z\left(\dot{y} + x - 1 + \mu\right) \\ z\left(\dot{x} - y\right) - \dot{z}\left(x - 1 + \mu\right) \\ \left(x - 1 + \mu\right)\left(\dot{y} + x - 1 + \mu\right) - y\left(\dot{x} - y\right) \end{bmatrix} \tag{B.11}$$

In the planar case these vectors are defined only by their third component, since $z = \dot{z} = 0$. In this case the magnitude of these vectors can be simply computed as $h_1 = \left(x+\mu\right)\left(\dot{y}+x+\mu\right) - y\left(\dot{x}-y\right)$ and $h_2 = \left(x-1+\mu\right)\left(\dot{y}+x-1+\mu\right) - y\left(\dot{x}-y\right)$. The value of h_1 and h_2 in the 3D case are not as simple and for this reason are rarely used in their extended form.

B.3. OSCULATING ORBITAL ELEMENTS

In this section the algorithm to obtain the osculating orbital elements from the state expressed in SB frame is presented. The elements of interest in this report are the semi-major axis a, the eccentricity e and the inclination i, from which the pericenter and apocenter r_p and r_a can be easily derived for elliptic trajectories. The algorithm illustrated here is used to obtain the osculating orbital elements with respect to the primary, the expressions however can be simply adapted to express the elements with respect to the secondary. The starting point of the algorithm is the vis-viva equation in inertial frame:

$$\frac{V^2}{2} - \frac{\mu_1}{r} = -\frac{\mu_1}{2a} = E_1 \tag{B.12}$$

In the previous section the expression of the energy with respect to the primary (E_1) in SB components has been derived in Equation B.6. By substituting this expression into the vis-viva equation the semi-major axis can be computed in adimensional units as:

$$a_1 = -\frac{1-\mu}{2\,(E_1)_{SB}} = \frac{1-\mu}{\frac{2(1-\mu)}{\sqrt{(x+\mu)^2+y^2+z^2}} - \left(x+\mu+\dot{y}\right)^2 - \left(\dot{x}-y\right)^2 - \dot{z}^2} \tag{B.13}$$

The Angular momentum vector with respect to the primary $\mathbf{H}_1$ derived in Equation B.10 is then computed from the state components. From this vector the inclination is computed as:

$$i_1 = acos\left(\frac{(\mathbf{H}_1)_{SB}|_z}{h_1}\right) = acos\left(\frac{\left(x+\mu\right)\left(\dot{y}+x+\mu\right) - y\left(\dot{x}-y\right)}{h_1}\right) \tag{B.14}$$

The eccentricity vector is then computed by using the following expression [1], adapted to be expressed in SB components:

$$\mathbf{e_1} = \frac{1}{1-\mu}\left(\begin{bmatrix}\dot{x}-y\\ \dot{y}+x+\mu\\ \dot{z}\end{bmatrix} \wedge (\mathbf{H}_1)_{SB}\right) - \frac{1}{r_1}\begin{bmatrix}x+\mu\\ y\\ z\end{bmatrix} \tag{B.15}$$

from which the scalar value of the eccentricity is obtained by computing the magnitude of such vector $e_1 = ||\mathbf{e_1}||$. By following these simple steps and by using these expressions in SB coordinates the osculating orbital elements a_1,e_1 and i_1 have been computed with respect to the primary. By following the same steps it would be very easy to derive the expressions to obtain these osculating orbital elements with respect to the secondary:

$$\begin{cases} a_2 = -\dfrac{\mu}{2\,(E_2)_{SB}} \\ i_2 = acos\left(\dfrac{(\mathbf{H}_2)_{SB}|_z}{h_2}\right) \\ e_2 = \|\mathbf{e_2}\| \end{cases} \tag{B.16}$$

To represent the pericenter and apocenter for elliptic trajectories the following formulas are used substituting a_1 and e_1 or a_2 and e_2:

$$\begin{cases} r_a = a\,(1+e) \\ r_p = a\,(1-e) \end{cases} \tag{B.17}$$

C

VALIDATION AND VERIFICATION

In this appendix the validation and verification of several fundamental blocks of the code is illustrated.

DYNAMICAL MODELS, JACOBI INTEGRAL EXPRESSIONS, COORDINATE TRANSFORMATIONS

Figure C.1 shows a trajectory propagated in the Earth-Moon system using the BR4BP and CR3BP models. Since the latter is a particular case of the first one when $m_S = 0$, the propagation shall results in two identical trajectories and so it does as it is possible to see from Figure C.1. The trajectory is propagated from the initial state $X_0 = [0.8\ 0.3\ 0.1\ 0\ 0.2\ 0]^T$ in SB frame using Matlab *ode113* with absolute and relative tolerances of 10^{-12}. The initial time is set to $t_0 = 0$ while the final one to $t_f = 150.8$. With such configuration the Jacobi constant of the system is $C_{SB} = 3.03496787622864$.

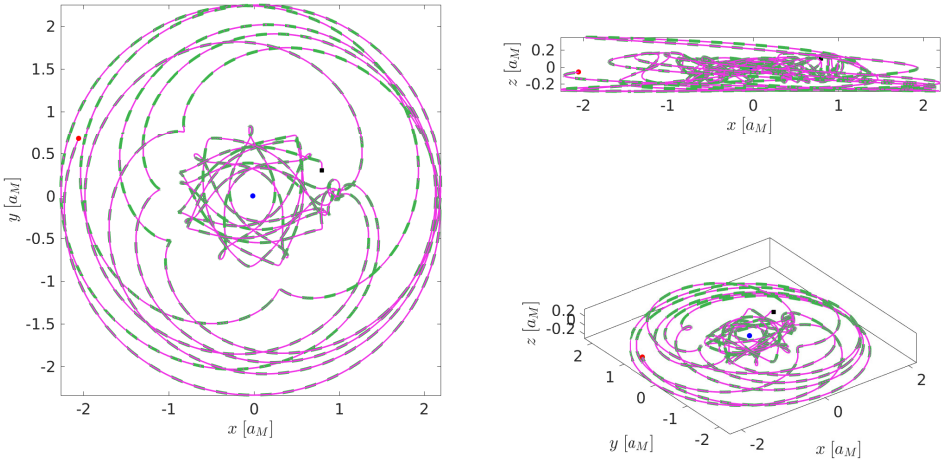

Figure C.1: Different views of the reference trajectory propagated from $X_0 = [0.8\ 0.3\ 0.1\ 0\ 0.2\ 0]^T$ with $t_0 = 0$ and $t_f = 150.8$ in Earth-Moon SB frame. The trajectory in the CR3BP is green, while the one in the BR4BP with $m_S = 0$. Earth and Moon are represented by blue and black points, while starting and ending points by a black square and red dot respectively.

The reference trajectory is computed in SB frame, however by applying coordinate transformations the states and epochs are transformed into other frames such as SP1, SP2, IB, IP1, IP2, SBD, SP1D, SP2D, IBD, IP1D and IP2D. The expressions of the Jacobi integral in such frames are then applied by using Equation 4.23. By doing so both the coordinate transformation equations between frames and the expressions of the Jacobi integral in Equation 4.23 are validated. Independently from the frame considered the Jacobi constant shall remain the same during the propagation, so its change is a good indicator of the error committed during the propagation procedure. Figure C.2 shows two error functions err_1 and err_2 of the Jacobi integrals for the

trajectory expressed in several frames. err_1 is defined as the difference between the mean Jacobi constant of the trajectory in SB frame and the Jacobi constant of the trajectory in the frame considered. err_2 is used to enhance the difference between err_1 in different frames, that is not clearly visible from Figure C.2, and is defined as the difference between err_1 in SB frame and err_1 in another frame.

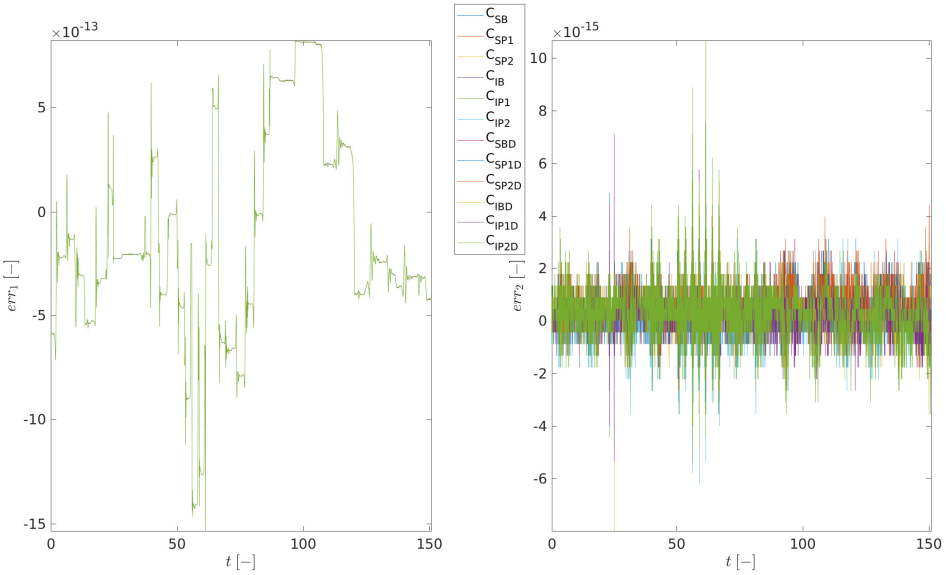

Figure C.2: On the left: Plot of err_1 for the frames indicated in the legend for the trajectory illustrated in Figure C.1. On the right: Plot of err_2 for the same frames indicated in the legend.

Since the values of err_1 and err_2 are considerably small in every frame considered, the propagation scheme, the coordinate transformation equations and the Jacobi integral expressions are considered validated. To further validate the BR4BP uses is made of the electronic supplement material in [4]. In particular trajectory $VIII$ In Figure 8 of [4] is used to validate the planar case of the BR4BP.

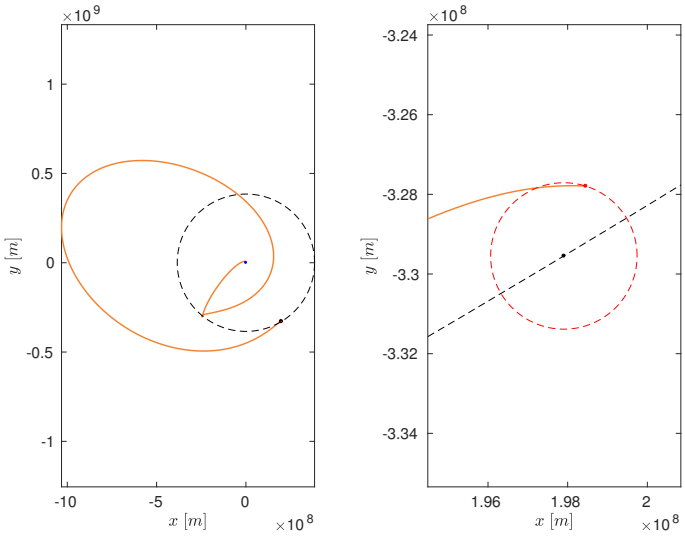

Figure C.3: Trajectory $VIII$ from [4] in the planar BR4BP: $X0 = [-0.019048265996746\ -0.015566582598150\ 09.751858086858906\ -4.321076476149917\ 0]^T$, $t_0 = 2.932062269968396$, $t_f = 17.819572739337175$ and $\theta_{S0} = 0$. Earth and Moon are represented by blue and black dots respectively. The dashed black line represents Moon's trajectory while the dashed red line is a 100km altitude orbit about the Moon. The figure on the right is a zoom of the one on the left in proximity of the Moon at the final epoch.

The shape of the trajectory represented here is the same of the one illustrated in [4]. Moreover such a trajectory is characterized by a final state reaching a circular orbit about the Moon at a 100 km altitude. Since the trajectory represented here reach such orbit with an error of 1.35 m the code of the BR4BP is considered validated.

PROPAGATION SCHEME

The software used in the report for the computations is MATLABR2017a and the propagation scheme adopted is *ode113*. There are important properties that make this propagator preferable for the tasks in this report. For what concern the speed and precision of the computation it is overall better than oder propagators such as *ode45*. Figure C.4 shows the values of errors on the Jacobi constant for the trajectory illustrated in Figure C.1 computed with these propagators. By repeating the propagation for 1000 cases *ode113* perform much better than *ode45*, taking on average 0.538561s against the 3.002009s average time of *ode45*. The reason why other propagation schemes other than the ones in Matlab have not been considered is because of the event functionality in Matlab's ode solvers. This has proven to be particularly easy to use and extremely useful in detecting trajectory intersections with Poincaré sections.

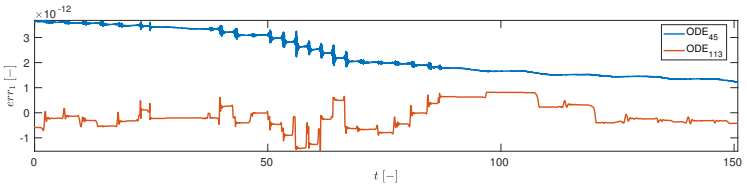

Figure C.4: Visualization of the errors on the Jacobi integral of the trajectory illustrated in C.1 propagated with different propagation scheme. It is possible to see that different schemes correspond to different behaviors of the error function.

The computations for the databases have been performed with a high-performance working station with the following performance characteristics: Intel® Xeon® Processor E5-2640 v4 @ 2.4GHz × 16, 3.4GHz × 16 Turbo with a 61.6 GiB memory. The other computations have been performed on a device with the following performances: Intel® Core™ i7-4510U CPU @ 2.00GHz × 4 with a 7.7 GiB memory. SPICE has been a tool actively used in the computation, as well as MEX functions and parfoor loops, that greatly enhanced the computational speed of the codes, allowing to efficiently exploit the multi-processing capabilities of the working station at ISAS/JAXA.

OSCULATING ORBITAL ELEMENTS

Two algorithms are used throughout the report to compute the osculating orbital elements from the state expressed in cartesian components. The first one is a the classical algorithm used to compute them from the state expressed in an inertial reference frame about the main attractor. As this is a well known algorithm it is nor presented in this report. The second technique makes use of the vis-viva equation and angular momentum expressions directly in the SB, SP1 or SP2 frames to compute the osculating orbital elements in such frames. The latter technique is preferred because it does not involve the coordinate transformation of the whole trajectory state and epoch history to an inertial frame, resulting in a faster computation of the osculating orbital elements directly from the frame in which the trajectory is propagated. These two techniques are tested with the *oscelt* SPICE function that perform the same task. For this testing $\mu_{Earth} = 398600.441\ \mathrm{km}^3/\mathrm{s}^2$ and the state considered in the Earth-Moon system is:
As is possible to see the errors between the osculating orbital elements obtained from the SPICE function and the two techniques are quite small, hence both techniques are validated.

POINCARÉ SECTION

To record the intersections between the Poincaré sections and the trajectory two techniques are used. One makes use of MATLAB event function and can be easily set from the ode solver's options. The event function only requires the implicit function of the event, that can be taken for example from Equations 4.51 and 4.61, and by using a combination of propagation and interpolation techniques can retrieve the epochs and states intersecting the Poincaré section. The second technique is used for those times where the trajectory is propagated in a different system than the one in which the Poincaré section is defined. In such a case an interpolation technique is used to record the intersection states and epochs. Figure C.5 shows the correctness of these techniques to record the intersection points for the trajectory illustrated in Figure C.1.

Component	IP1D	SP1
x	363873007.386024	0.946587602622297
y	203431556.873759	0.52921152657681
z	-415856411.869599	-1.08181842553973
$\dot{x}$	-84.5338561559273	0.446702462229068
$\dot{y}$	119.680804650645	-0.829773444826218
$\dot{z}$	-195.694014560301	-0.191006666134343

Table C.2: The state in IP1D is written in m and m/s while the one in SP1 in dimensional units of the Earth-Moon system. The angle θ between SP1 and IP1D frame is set to 0.

Orbital element	*oscelt*	error from IP1D	error from SP1
r_a [m]	596462153.879926	$2.38418579101562 \times 10^{-7}$	0
r_p [m]	19565206.480481	$3.35276126861572 \times 10^{-8}$	$3.72529029846191 \times 10^{-9}$
i [rad]	1.0537594370071	$2.22044604925031 \times 10^{-16}$	$2.22044604925031 \times 10^{-16}$
e [−]	0.936479423676785	$1.11022302462516 \times 10^{-16}$	0
a [m]	308013680.180204	$5.96046447753906 \times 10^{-8}$	0

Table C.4: The first column represents the osculating orbital elements obtained from SPICE function *oscelt* used for reference. The second column represent the error between the osculating orbital elements obtained from the IP1D state and the reference one. The third column is the error between the osculating orbital elements obtained directly from the SP1 state and the reference one.

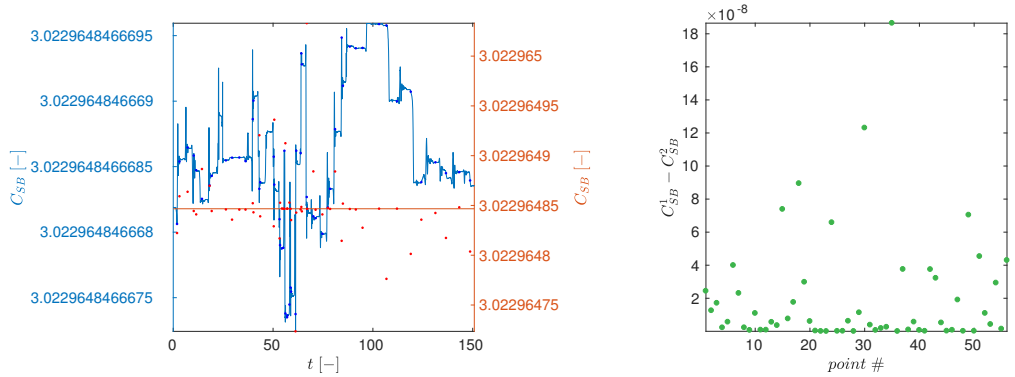

Figure C.5: On the left: Representation of the Jacobi constant in SB frame and its evaluation for the intersection points with the Poincaré section about the primary obtained with the event function technique (blue points) and the interpolation technique (red points). The graph is represented on two y-axis to stress the difference in scale between the two techniques. On the right: Visualization of the difference between the Jacobi constant of the intersection points of the two techniques.

Note that the event function technique is more precise because it makes use of propagation and interpolation, while the other uses interpolation only. Both techniques however give a small error on the Jacobi constant, thus can be considered validated for the purposes of this report.

D

ANALYSIS OF EQUULEUS TRAJECTORY WITH TP-GRAPH

An old case of EQUULEUS trajectory can be seen in Figures D.1 and D.2 in J2000-Earth centered frame and SP2 frame of the SE system respectively. This trajectory is an example of transfer trajectory computed in a full ephemeris model considering Sun, Earth and Moon gravitational influences alongside with thrust maneuvers.

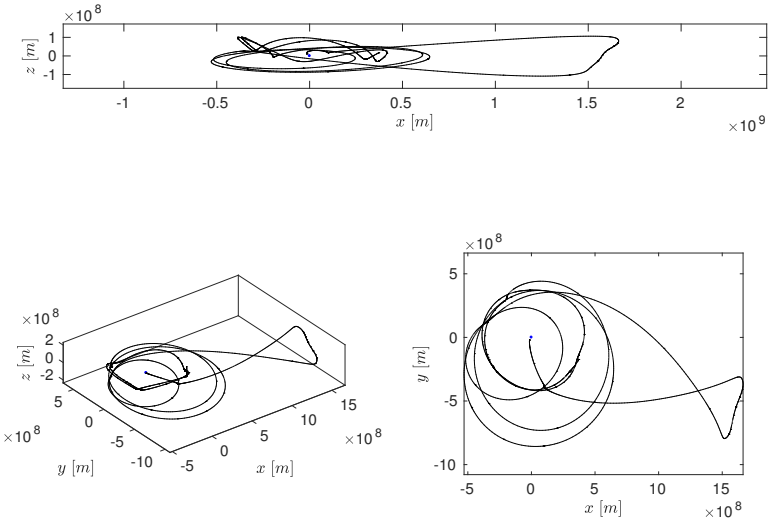

Figure D.1: Example of EQUULEUS trajectory in the J2000-Earth centered frame. The Sun perturbed phase is clearly visible, as well as the retrograde portion of the trajectory. Such effect is common in trajectories that are highly perturbed by the Sun.

Reference frame transformations are performed and the intersection of these trajectories with the Poincaré sections defined by Equations 4.51 and 4.61 are computed. Figure D.3 displays the behavior of the Tisserand parameter and Jacobi constant of the trajectory at different epochs. Note that since a full ephemeris model has been used as dynamical model, the Jacobi constant is not constant. The value of the Tisserand parameter with respect to Earth evaluated on the Poincaré section defined in the EM synodic frame are highlighted by red points.
From Figures D.3 is possible to see that the Tisserand parameter presents spikes when the spacecraft is closer to the Moon, at the beginning and end of the trajectories, and that overall it approximates in a more regular

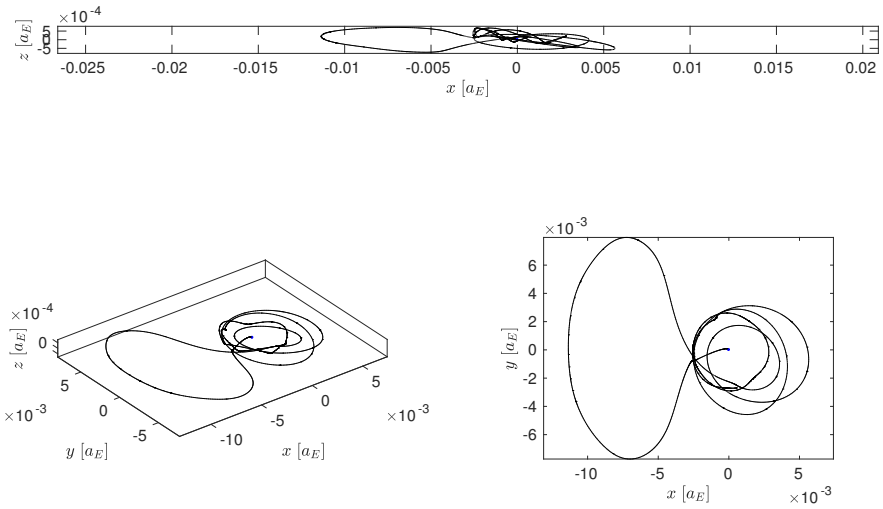

Figure D.2: Example of EQUULEUS trajectory in the SP2 frame of the SE system. The Sun perturbed phase is clearly visible on the left, this time however the retrograde portion of the trajectory is not clearly identifiable.

way the behavior of the Jacobi constant. Note also that since the final phase of the trajectory takes part about the Moon, these phase is not visible to the section defined by Equation 4.51.

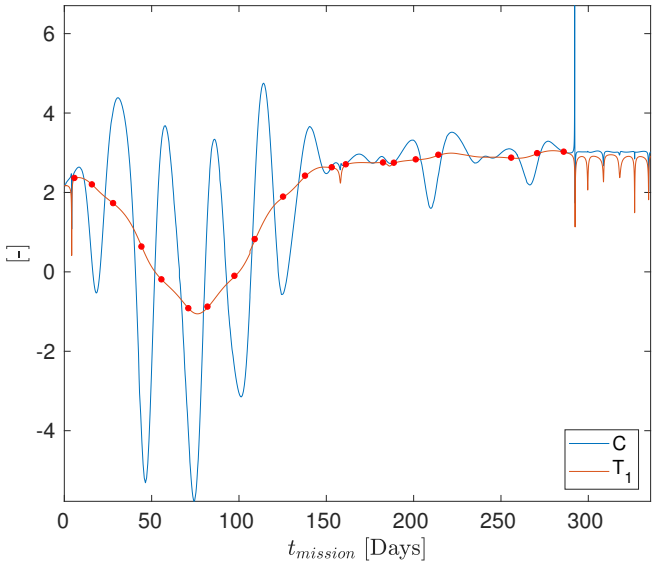

Figure D.3: Jacobi constant (blue) and Tisserand parameter with respect to Earth (orange) of the trajectory in the SP1 frame of the Earth-Moon system. The red points are the intersection points with the Poincaré section defined about the primary in the Earth-Moon synodic frame.

Figure D.4 shows the behavior of the Tisserand parameter defined about the secondary in the Sun-Earth synodic frame. Unfortunately for this specific case due to the way the Poincaré section is defined by Equation 4.5.2 the first intersection with the section occurs only after 150 days. As it is possible to see also from Figure

D.2 most of the trajectory takes place in the Sun-Earth system and for this reason the behavior of the modified Tisserand parameter is relatively smooth. This is true until the last phase of the trajectory, when several lunar flybys contribute to cause the peaks visible in the figure.

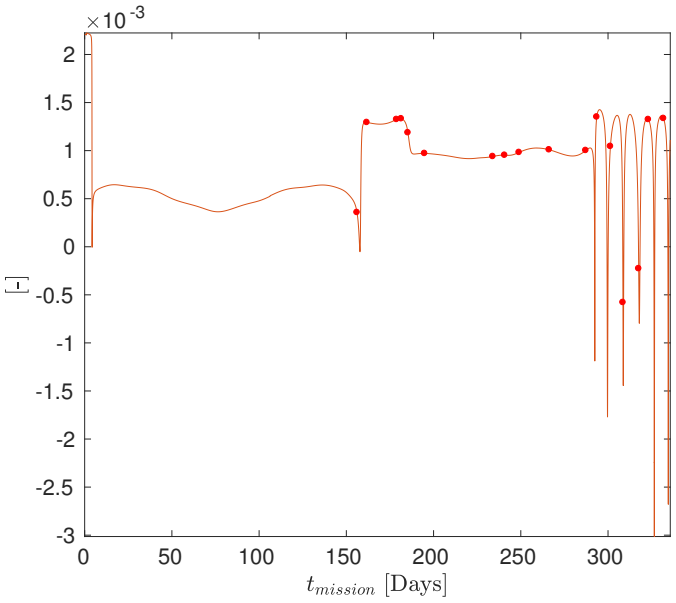

Figure D.4: Tisserand parameter with respect to Earth (orange) of the trajectory in the SP2 frame of the Sun-Earth system. The red points are the intersection points with the Poincaré section defined about the secondary in the Sun-Earth synodic frame.

Finally the values of the osculating orbital elements of the intersection points highlighted by the red points in Figures D.3 and D.4 are represented in the TP-graph. The analysis of the trajectory in the TP-graph can give insight into the trajectory designed in the full-ephemeris model. From Figure D.5 is possible to see that the trajectory sensed by the section is divided into 4 phases, that constitute 4 different groupings of points in the TP-graph. Right after the first point the trajectory inclination increases rapidly and the trajectory becomes retrograde, many intersection points are recorded in this phase as the trajectory slowly proceed in the exterior part of the EM system being heavily perturbed by the Sun. During this phase the EM synodic frame rotate relatively faster than the spacecraft, generating multiple intersection points with the section. After this first phase the trajectory return in the vicinity of the EM system with a high apogee. After a second lunar flyby event however such apogee quickly decrease. Such decrease however does not seems to happen casually, as it successfully locates the trajectory on a 1:1 resonance level with the Moon. Shortly after, some additional Sun-perturbed phases move the spacecraft up to the 11:6 resonance level. On such level the spacecraft climb-up to reach the portion of the graph with an energy level just between the one associated to $EML2$ and $EML3$. This happens just before multiple lunar flybys that result in a temporarily captured trajectory. As it is possible to see from Figure D.3, this phase is not sensed by the section due to geometric considerations. These flybys probably are exploited by the spacecraft to reach the precise energy state to enter into the final Halo orbit about the EML2 point. A much porer dynamic can be seen in the TP-graph of the SE system in Figure D.5 due to the fact that the Poincaré section fails to intersect the trajectory in the first 150 days of the mission. The only phenomenon that is visible is a sudden decrease of the apogee due to the second lunar flyby event, right after the end of the highly perturbed phase of the Sun.

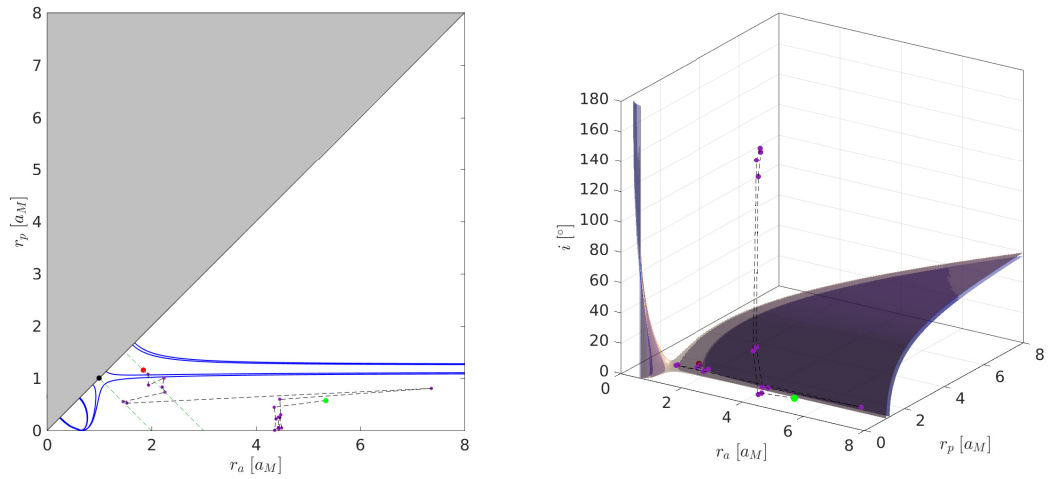

Figure D.5: On the left: 2D TP-graph of the Earth-Moon system with the Tisserand level sets associated to the Lagrange points in dark blue. The 11:6 and 1:1 resonance levels are represented by green dashed lines. On the right: 3D TP-graph of the Earth-Moon system with the Tisserand level surfaces associated to the Lagrange point in dark blue. The osculating orbital elements of all but the first and last intersection points with the Poincaré section about the primary are represented in purple and connected by a black dashed line. The first and last points are represented in green and red respectively.

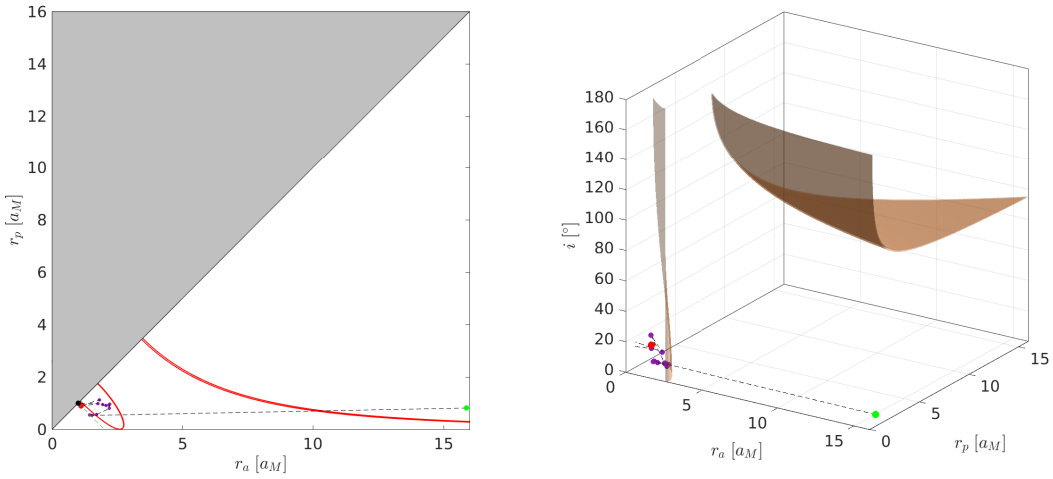

Figure D.6: On the left: 2D TP-graph of the Sun-Earth system with the Tisserand level sets associated to the Lagrange points in dark red. The 1:1 resonance is represented by a green dashed line. On the right: 3D TP-graph of the Sun-Earth system with the Tisserand level surfaces associated to the Lagrange point in Orange. The osculating orbital elements of all but the first and last intersection points with the Poincaré section about the secondary are represented in purple and connected by a black dashed line. The first and last points are represented in green and red respectively.

As it is possible to see in this case the TP-graphs can be used to give a quick insight into complex phenomena that generated the trajectory. Once these are understood in principle a better design can be achieved by focusing on refining the way these phenomena are used.

E

POINCARÉ MAPS

E.1. DERIVATIONS

In this section the relationships to obtain the $d-\theta$ maps introduced in Chapter 6 are illustrated. These are illustrated for the EM-system but they can be easily adapted to be valid in the SE system. First the transformations to obtain these maps are illustrated.

$(x, y, \dot{x}, \dot{y}) \rightarrow (C_{SP1}, P_1, d, \theta)$

The state of the spacecraft in SP1 frame is now transformed into an alternative set to be used in the $d-\theta$ Poincaré map. The Jacobi integral in SP1 frame is considered:

$$J_{SP1} = 2\frac{1-\mu}{r_1} + 2\frac{\mu}{r_2} + (x^2+y^2) - (\dot{x}^2+\dot{y}^2+\dot{z}^2) - 2x\mu + \mu^2 + \mu(1-\mu) \tag{E.1}$$

The domain of the Jacobi integral is $D = \left\{\forall (x,y,z,\dot{x},\dot{y},\dot{z}) \in \mathbb{R}^6 \,|(x,y,z) \neq (0,0,0) \wedge (x,y,z) \neq (1,0,0)\right\}$. The singularity points are in the primaries positions. The value of C_{SP1} is computed from this expressions. The Poincaré section in the SP1 frame is the one defined by Equations 4.51 and 4.57, obtained by imposing the value $P_1^k = 3\mu$ on the residual function P_1. The explicit function of the Poincaré section can be written as:

$$y(x) = \sqrt{\frac{1}{(x+1)^2} - (x-1)^2} \tag{E.2}$$

The domain of $y(x)$ is $D = \left\{\forall (x,y) \in \mathbb{R}^2 \,| x > -1 \wedge (x,y) \neq (1,0)\right\}$. By considering the section branch in the $II°$ quadrant of the SP1 frame $x < 0 \ \wedge \ y > 0$. From the spacecraft position the distance is simply computed as $d = \sqrt{x^2+y^2}$, however as the spacecraft is constrained on the Poincaré section this can be computed as:

$$d = \sqrt{x^2 + \frac{1}{(x+1)^2} - (x-1)^2} \tag{E.3}$$

Now the angle θ is computed. This angle can be expressed as the angle of the inertial velocity (θ_{in}) or synodic velocity (θ_{syn}) w.r.t. to the normal line of the distance vector. The reason this angle is taken from the normal line is to facilitate the patching between maps of different systems. To compute θ_{syn} the following expression can be applied from geometric considerations:

$$\theta_{syn} = atan2(\dot{y},\dot{x}) - atan2(y,x) - \frac{\pi}{2} \tag{E.4}$$

In order to compute θ_{in} it is first necessary to transform the state of the spacecraft from the synodic reference frame $(x,y,\dot{x},\dot{y})$ to the inertial reference frame $(\xi,\eta,\dot{\xi},\dot{\eta})$. Assuming that the phase angle between inertial and synodic reference frame is null, the following equations can be used:

$$\begin{cases} \xi = x \\ \eta = y \\ \dot{\xi} = \dot{x} - y \\ \dot{\eta} = \dot{y} + x \end{cases} \tag{E.5}$$

So θ_{in} is computed as:

$$\theta_{in} = atan2(\dot{y}+x, \dot{x}-y) - atan2(y,x) - \frac{\pi}{2} \tag{E.6}$$

The transformation between the two sets is successful when avoiding the singularities highlighted in the derivation.

$(C_{SP1}, P_1, d, \theta) \rightarrow (x, y, \dot{x}, \dot{y})$

The procedure is now reversed to show that the state of the spacecraft can be uniquely reconstructed from the $d-\theta_{syn}$ and $d-\theta_{in}$. The procedure is not successful for the latter case, as an ambiguity in the reconstruction procedure exist for this map. Both C_{SP1} and P_1 are fixed by assumption. By choosing a point in the (d, θ_{syn}) map the x-component of the state can be computed by inverting Equation E.3:

$$x^2 + \frac{1}{(x+1)^2} - (x-1)^2 - d^2 = 0 \tag{E.7}$$

further simplifying this equation it will be possible to arrive to the following cubic form:

$$x^3(2) + x^2(3-d^2) + x(-2d^2) + (-d^2) = 0 \tag{E.8}$$

The roots of such equation can be founded applying numerical techniques. Note that only the solution that satisfy $-1 < x < 0$ is taken, since this correspond to the domain of the Poincaré section considered. The y-component of the state is easily obtained by an evaluation of the section expression in Equation E.2. By inverting Equation E.1 is possible to obtain the magnitude of the velocity in the synodic reference frame as a function of the spacecraft position and C_{SP1} of the system:

$$V_{syn} = \sqrt{2\frac{1-\mu}{r_1} + 2\frac{\mu}{r_2} + (x^2+y^2) - C_{SP1} - 2x\mu + \mu^2 + \mu(1-\mu)} \tag{E.9}$$

To compute $\dot{x}$ and $\dot{y}$ the angle between these two components with respect to the x-axis is used. This angle is indicated as θ^x_{syn} and is in relationship with the angle w.r.t. the normal line θ_{syn} as:

$$\theta^x_{syn} = \theta_{syn} + atan2(y,x) + \frac{\pi}{2} \tag{E.10}$$

this relationship can be simply derived from Equation E.4. The velocity components of the state are then computed as:

$$\begin{cases} \dot{x} = V_{syn} cos\theta^x_{syn} \\ \dot{y} = V_{syn} sin\theta^x_{syn} \end{cases} \tag{E.11}$$

Assuming the angle expressed in the Poincaré map is the angle of the inertial velocity θ_{in} the procedure needs to take into account a coordinate transformation. A null initial angle between inertial and synodic frames is assumed.

$$\theta^x_{in} = \theta_{in} + atan2(y,x) + \frac{\pi}{2} \tag{E.12}$$

Now is necessary to transform θ^x_{in} into θ^x_{syn}. The definition of θ^x_{syn} and the velocity transformation equation from synodic to inertial frame are used:

$$\begin{cases} \dot{\xi} = V_{in} cos\theta^x_{in} \\ \dot{\eta} = V_{in} sin\theta^x_{in} \\ V^2_{syn} = V^2_{in} + (\eta^2 + \xi^2) + 2(\eta\dot{\xi} - \dot{\eta}\xi) \end{cases} \tag{E.13}$$

It follows that V_{in} can be computed by solving a second order equation:

$$V^2_{in} + V_{in}\left(2\eta cos\theta^x_{in} - 2\xi sin\theta^x_{in}\right) + \left(\xi^2 + \eta^2 - V^2_{syn}\right) = 0 \tag{E.14}$$

The problem now is that there exists an ambiguity between the two solutions of V_{in}. If this ambiguity is solved then it would be possible to compute:

$$\theta^x_{syn} = atan2(V_{in} sin\theta^x_{in} - \xi, V_{in} cos\theta^x_{in} + \eta) \tag{E.15}$$

From which it would be possible to compute $\dot{x}$ and $\dot{y}$ as in Equation E.11.

ANALYTIC EXPRESSION

As illustrated in Figures 6.9 and 6.16 the $d-\theta$ map can be obtained from an analytic expression that is now presented. First is necessary to select a value for r_a and r_p of the trajectory. These should be decided by taking into consideration the Tisserand level set at the energy level for which the map holds. By selecting a range of distances from r_p to r_a that lay on the section, Equation E.9 can be used to compute V_{syn}. By using Equation B.3 V_{in} is computed as:

$$V_{in} = \frac{1}{VU}\sqrt{2\mu_1\left(\frac{1}{\sqrt{x^2+y^2}} - \frac{1}{r_a+r_P}\right)} \tag{E.16}$$

where r_a, r_p ,x and y are expressed in dimensional units while V_{in} is adimensional. By expressing the relation between V_{in} and V_{syn} from coordinate transformation we obtain:

$$V_{syn}^2 = V_{in}^2 + (\eta^2+\xi^2) + 2(\eta\dot{\xi} - \dot{\eta}\xi) \tag{E.17}$$

Assuming that the initial phase angle between synodic and inertial reference frame is null, from Equations E.5 we can rewrite Equation E.17 as:

$$\begin{cases} \frac{V_{syn}^2 - V_{in}^2 + d^2}{2} = y\dot{x} - x\dot{y} \\ \dot{x}^2 + \dot{y}^2 = V_{syn}^2 \end{cases} \tag{E.18}$$

Assuming $A = \frac{V_{syn}^2 - V_{in}^2 + d^2}{2}$ and after some simplification we arrive to express the synodic components of the velocity as:

$$\begin{cases} \dot{x} = \frac{A + x\dot{y}}{y} \\ \dot{y}^2\left(1+\frac{x^2}{y^2}\right) + \dot{y}\left(\frac{2Ax}{y^2}\right) + \left(\frac{A^2}{y^2} - V_{syn}^2\right) = 0 \end{cases} \tag{E.19}$$

From the solutions of this system we can compute θ_{syn}, θ_{in} given x,y, C_{SP1} and P_1. The set of solutions of this system describes the analytic relationship observed in Figure 6.8 and reproduced in Figure 6.9. The same expressions can be derived for the secondary in the SE system.

E.2. ADDITIONAL MAPS EARTH-MOON SYSTEM

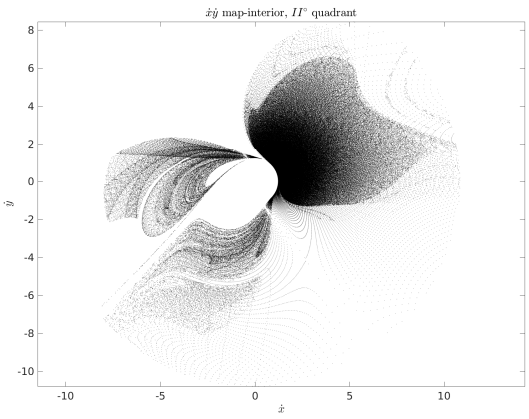

(a)

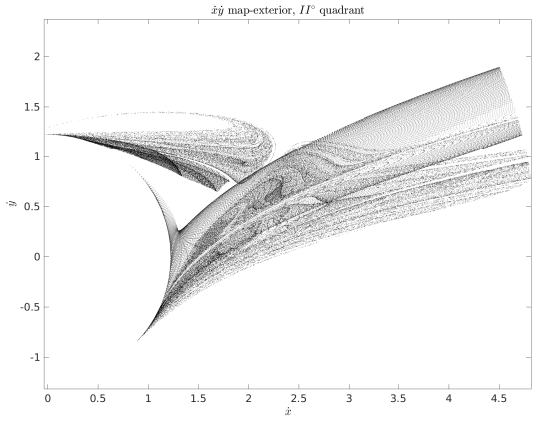

(b)

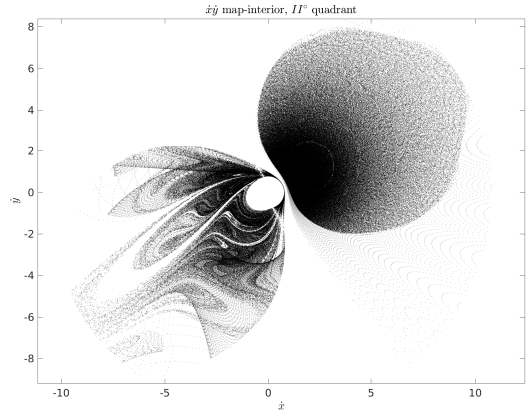

(c)

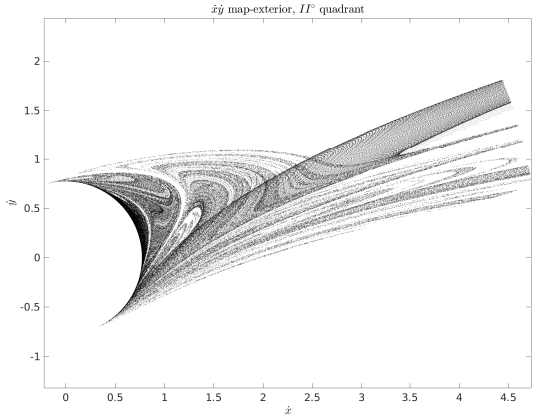

(d)

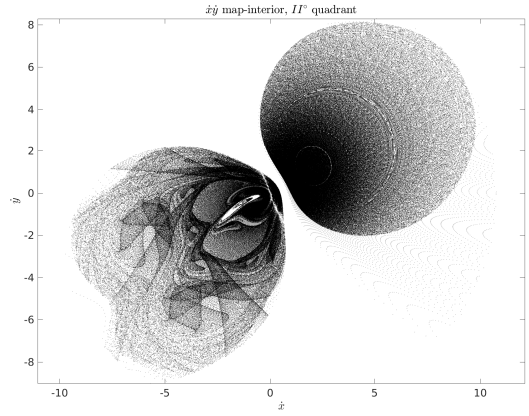

(e)

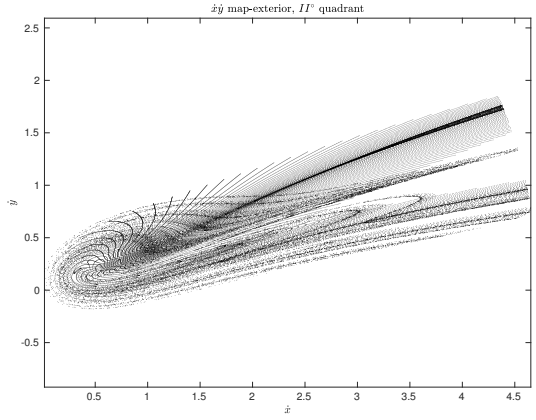

(f)

Figure E.1: Various $\dot{x}\,\dot{y}$ maps, from top to bottom C is: 1.5, 2.4, 3.1

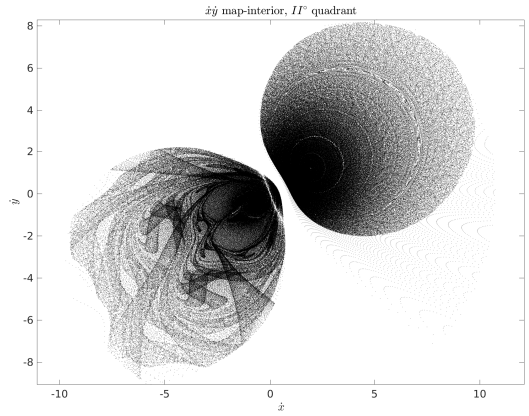

(a)

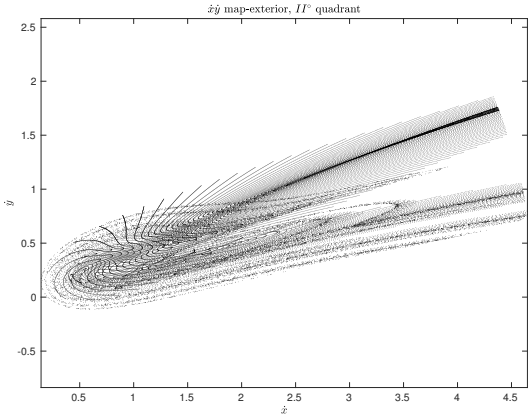

(b)

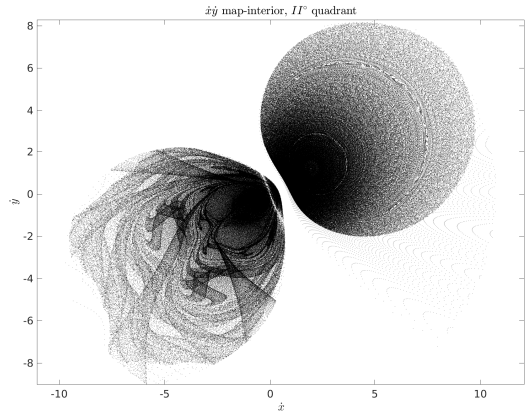

(c)

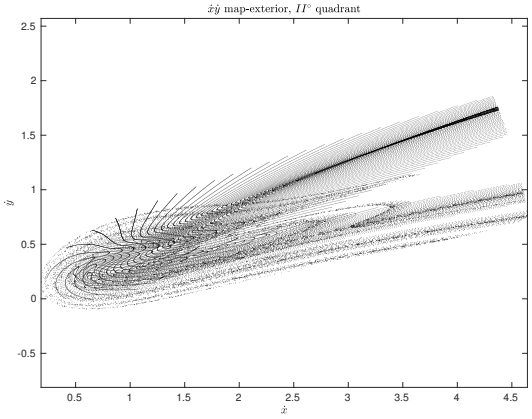

(d)

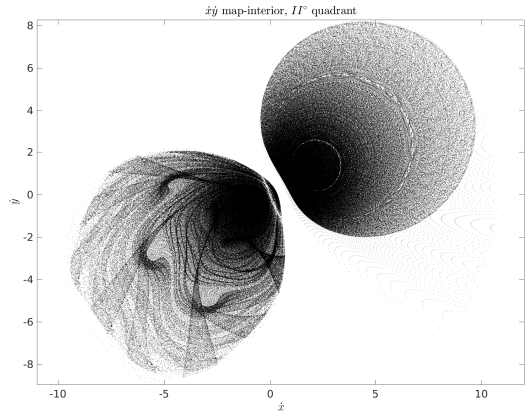

(e)

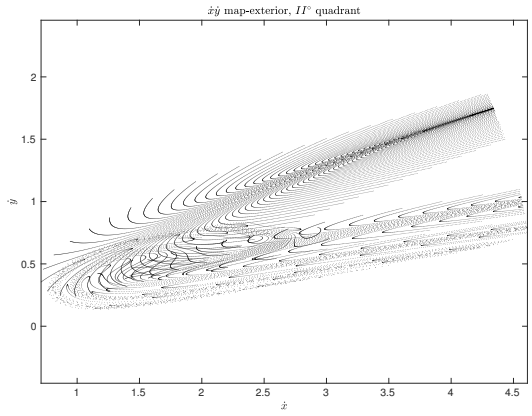

(f)

Figure E.2: Various $\dot{x}\,\dot{y}$ maps, from top to bottom C is: 3.18, 3.2, 3.5

E.3. ADDITIONAL MAPS SUN-EARTH CR3BP

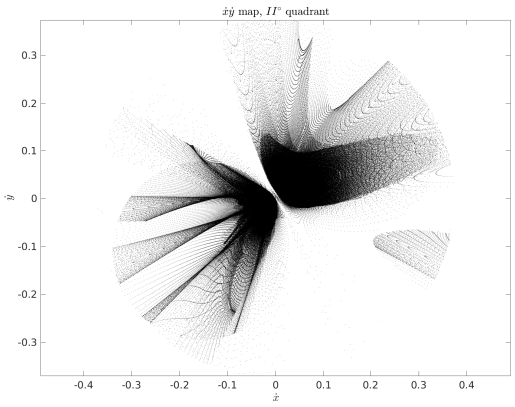

(a)

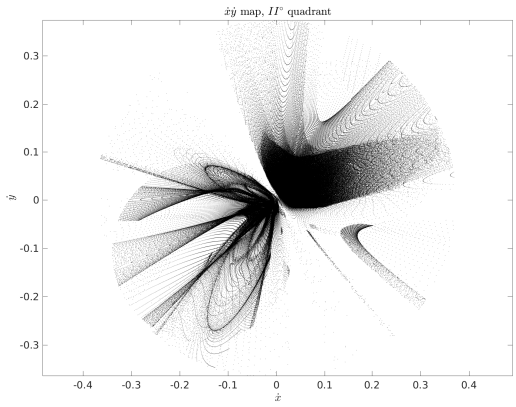

(b)

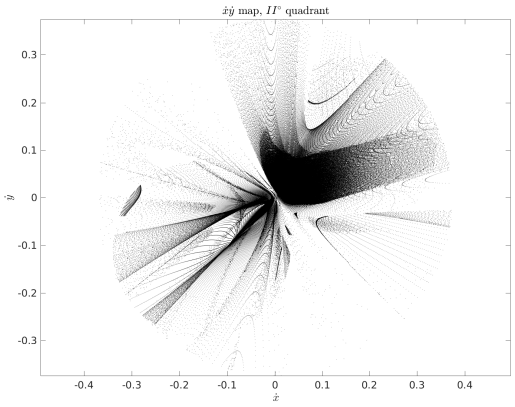

(c)

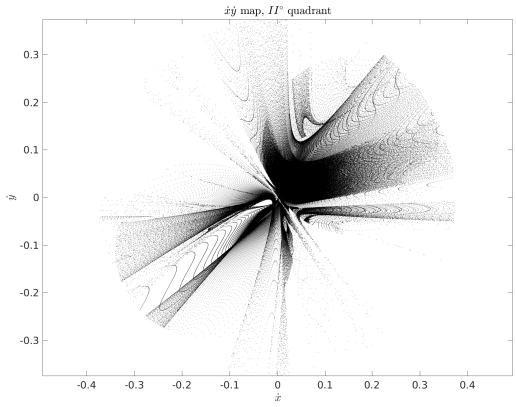

(d)

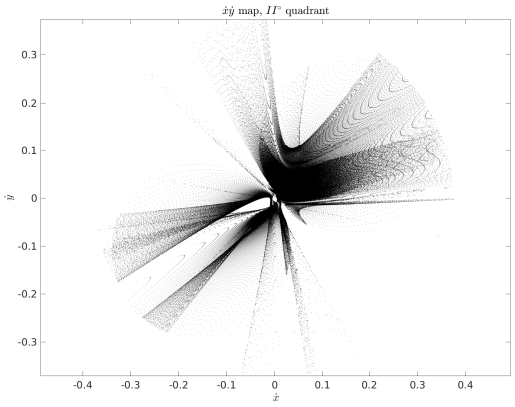

(e)

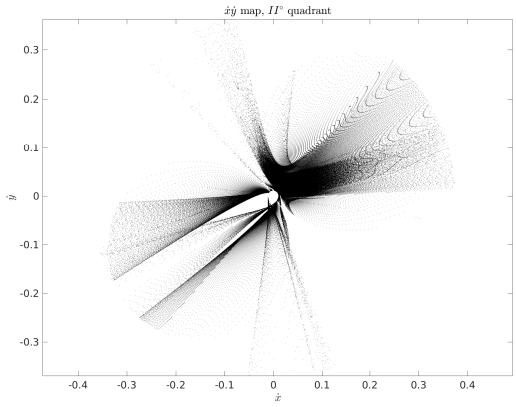

(f)

Figure E.3: Various $\dot{x}\dot{y}$ maps. The values of C are from a to f: 3.00090300347189, 3.00085300347189, 3.00080300347189, 3.00070300347189, 3.00060300347189,3.00050300347189.

E.4. EXAMPLES OF TRAJECTORIES

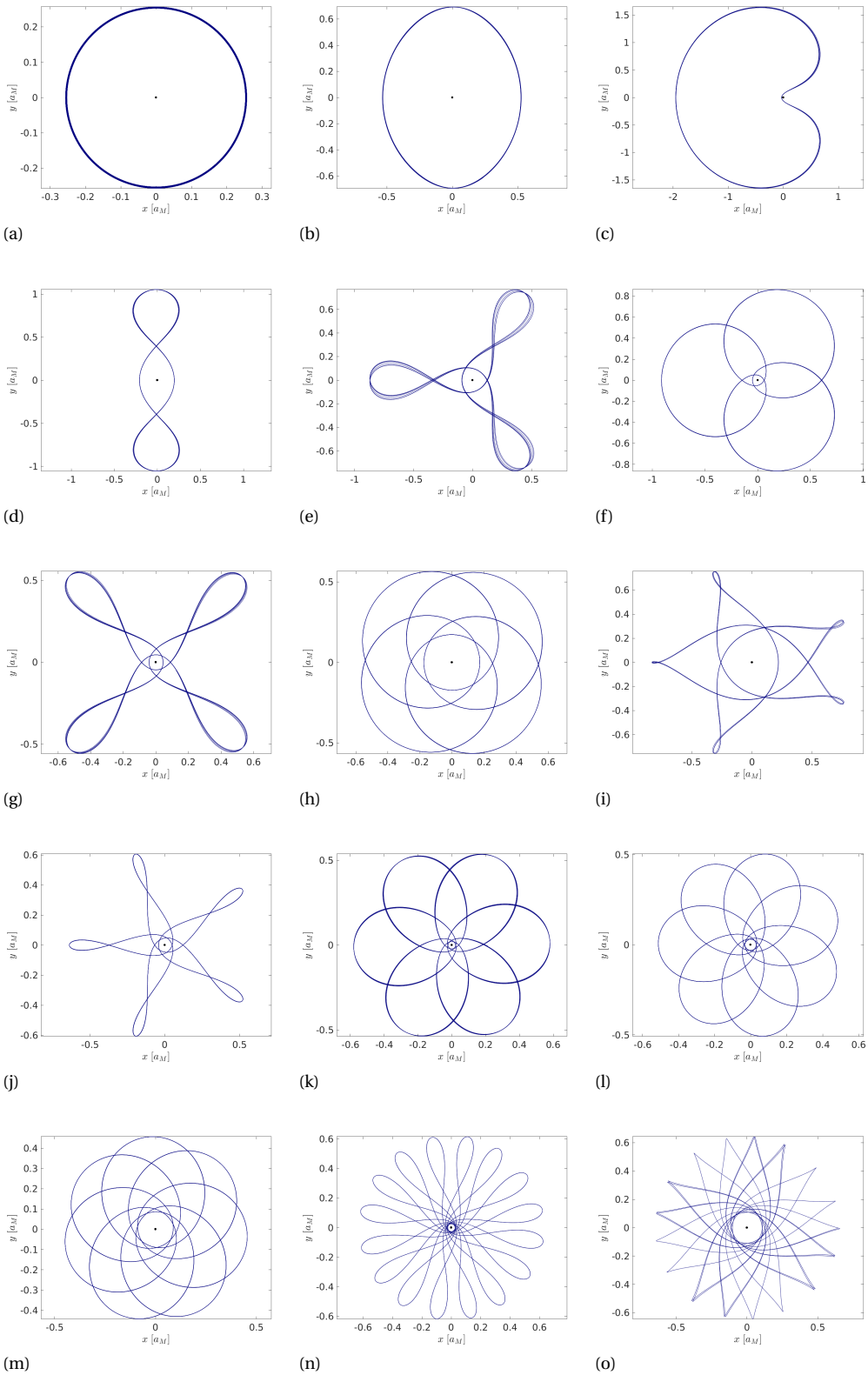

Figure E.4: Example of multi-revolutionary periodic orbits (prograde and retrograde) in SP1 frame of the EM system. The coordinates used to obtain these orbits are presented in the table next page. The x-axis represent the x-component while the y-axis the y-component, both expressed in a_M units.

index	x	y	$\dot{x}$	$\dot{y}$	C
a	-0.1450	0.2157	1.8955	1.1808	2.9
b	-0.3007	0.5616	-0.4526	-0.4092	3.18
c	-0.0342	0.0319	-3.3072	-6.2069	1.5
d	-0.2195	0	0	-2.6165	2.75
e	-0.0761	0.0965	-1.9113	-3.2477	2.9
f	-0.04768	0.0521	0 2.7498	4.7229	1.5
g	-0.04030	0.04096	-5.7525	-1.8939	3.1
h	-0.1105	0.1538	0 2.8460	1.1321	1.5
i	-0.1863	0.2960	-1.6381	-0.3355	3.1
j	-0.03862	0.0384	-5.5652	-2.8087	3.5
k	-0.02532	0.01888	6.1946	6.6776	2.9
l	-0.02956	0.02505	6.3603	4.6008	3.18
m	-0.0630	0.07567	4.0156	1.6376	2.9
n	-0.02811	0.02293	-6.2370	-5.3246	3.5
o	-0.0825	0.1069	-1.8487	-2.9257	3.5

Table E.2: States components for the orbit illustrated in previous page. Note that the value of the Jacobi constant C in this table is computed without the term $\mu(1-\mu)$ illustrated in Equation 3.10.

BIBLIOGRAPHY

[1] K. Wakker, *Fundamentals of Astrodynamics*, 1st ed. (Institutional Repository Library, Delft University of Technology, 2015).

[2] J. Jack and I. de Pater, *Fundamental planetary science*, 1st ed. (Cambridge University Press, 2013).

[3] R. Wertz, H. Meissinger, L. Newman, and G. Smit, *Orbit & Constellation Design & Management*, 2nd ed. (Microcosm, 2009).

[4] F. Topputo, *On Optimal two-impulsive Earth-Moon transfers in a four-body model,* Celestial Mechanics and Dynamical Astronomy **117**, 279 (2013).

[5] W. Koon, M. Lo, J. Marsden, and S. Ross, *Dynamical Systems, the Three-Body Problem and Space Mission Design* (Marsden Books, 2011).

[6] K. Oshima, S. Campagnola, C. Yam, Y. Kayama, Y. Kawakatsu, N. Ozaki, Q. Verspieren, K. Kakihara, K. Oguri, and R. Funase, *EQUULEUS Mission Anlysis: Design of the Transfer Phase,* (2017) 31st International Symposium on Space Technology and Science (ISTS), Matsuyama, Japan.

[7] S. Campagnola, N. Ozaki, K. Oguri, Q. Verspieren, K. Kakihara, K. Yanagida, R. Funase, C. Yam, L. Ferella, T. Yamaguchi, Y. Kawakatsu, and D. Yarnoz, *Mission Analysis for EQUULEUS, JAXA's Earth-Moon Libration Orbit Cubesat,* (2016) 67th International Astronautical Congress, Guadalajara, Mexico.

[8] Y. Kawakatsu, K. Nishiyama, I. Funaki, and T. Iwata, *DESTINY Mission Description and its Value,* (2013) 29th International Symposium on Space Technology and Science (ISTS), Nagoya-Aichi, Japan.

[9] D. Yarnoz, C. Yam, S. Campagnola, and Y. Kawakatsu, *Extended Tisserand-Poincare' graph and multiple lunar swingby design with Sun perturbation,* (2016) 6th ICATT conference, Darmstadt, Germany.

[10] S. Campagnola and R. Russel, *Endgame Problem Part 2: The Multi-Body Technique and the T-P Graph,* Journal of Guidance, Control and Dynamics **33**, 476 (2010).

[11] S. Campagnola, P. Skerritt, and P. Russel, *Flybys in the planar, circular, restricted, three-body problem,* Celestial Mechanics and Dynamical Astronomy **113**, 343 (2012).

[12] N. Strange and J. Longuski, *Graphical Method for Gravity-Assist Trajectory Design,* Journal of Spacecraft and Rockets **39**, 9 (2002).

[13] K. Uesugi, H. Matsuo, J. Kawaguchi, and T. Hayashi, *Japanese First Double Lunar Swingby Mission, "Hiten"* , Acta Astronautica **25**, 347 (1991).

[14] K. Uesugi, *Results of the MUSES-A "Hiten" mission,* Advances in Space Research **18**, 69 (1996).

[15] E. Belbruno, *Lunar Capture Orbits, a Method of Constructing Earth Moon Trajectories and the Lunar Gas Mission,* (1987) 19th AIAA/DGLR/JSASS International Electric Propulsion Conference, Colorado Springs, Colorado.

[16] T. Sweetser, S. Broschart, V. Angelopoulos, G. Whiffen, D. Folta, M.-K. Chung, S. Hatch, and M. Woodard, *ARTEMIS Mission Design,* Space Science Review **165**, 27 (2012).

[17] K. Oguri, K. Kakihara, S. Campagnola, N. Ozaki, K. Oshima, T. Yamaguchi, and R. Funase, *EQUULEUS Mission Anlysis: Design of the Science Orbit Phase,* (2017) 31st International Symposium on Space Technology and Science (ISTS), Matsuyama, Japan.

[18] R. Broucke, *The celestial mechanics of the gravity assist.* (1988) AIAA/AAS Astrodynamics Conference, Minneapolis, Washington, DC.

[19] G. Felipe and A. Prado, *Classification of out of plane swing-by trajectories,* Journal of Guidance Control Dynamic **22**, 643 (1999).

[20] Y. Qi and S. Xu, *Mechanical anlysis of lunar gravity assist in the Earth-Moon system,* Astrophysics and Space Science **360**, 55 (2015).

[21] J. Kawaguchi, H. Yamakawa, T. Uesugi, and H. Matsuo, *On making use of Lunar and Solar gravity assists in LUNAR-A, PLANET-B missions,* Acta Astronautica **35**, 633 (1995).

[22] F. Verhulst, *Nonlinear Differential Equations and Dynamical Systems*, 2nd ed. (Springer, 2006).

[23] F. Tisserand, *Traité de mécanique céleste*, Vol. 4 (Gauthier-Villars eet fils, 1896).

[24] A. Labunsky, O. Papkov, and K. Sukhanov, *Multiple Gravity Assist interplanetary trajectories* (Gordon and Breach publishers, London, 1998).

[25] S. Campagnola and R. Russel, *Endgame Problem Part 1: V_∞-Leveraging Technique and the Leveraging Graph,* Journal of Guidance, Control and Dynamics **33**, 463 (2010).

[26] E. Saff and A. Kuijlaars, *Distributing many points on a sphere,* The Mathematical Intelligencer **19**, 5 (1997).